Sensitivity Studies for the $\mu^+ \rightarrow e^+e^+e^-$ Search with the Mu3e Experiment and Performance of the Pixel Tracker Detector

Doctor in Philosophy

Has been carried out by

Afaf Wasili

Afaf.Wasili@liverpool.ac.uk

Under the supervision of

Prof. Joost Vossebeld

Dr. Helen Hayward

School of Physical Sciences

University of Liverpool

October 6, 2022

Abstract

The Mu3e experiment is a novel experiment to search for the lepton flavour violating (LFV) decay $\mu^+ \rightarrow e^+e^+e^-$, with an ultimate sensitivity to a branching ratio of one in 2 $\times 10^{15}$ in phase-I and one in 10^{16} muon decays for phase-II. This is an improvement in sensitivity by four orders of magnitude compared to previous searches by the SINDRUM experiment. Since this decay is suppressed to unobservable levels in the Standard Model of particle physics, any measurement of this decay would be a clear sign of new physics. The experiment is currently under construction and will take place at the Paul Scherrer Institute in Switzerland. In order to achieve this number of muon decays, the Paul Scherrer Institute (PSI) is utilizing the worlds most intense proton beam, which is used to produce $10^8 \mu/\mathrm{s}$ at the πE5 beamline (phase-I) and a new proposal high-intensity muon beamline HiMB will provide $10^9 \mu/\mathrm{s}$ (phase-II). To achieve the proposed sensitivity, the Mu3e experiment requires excellent vertex, timing, and momentum resolutions. These are needed to reduce the main background processes, internal conversion and accidental coincidences caused by two or more Michel decays. Using kinematics, such as energy and momentum conservation with a common vertex for three particles emitted at the same time allows the signal muon decays to be distinguished from the background categories.

In the context of this thesis, I am presenting an overview of the Mu3e experiment with the performance of the phase-I Mu3e detector, and how this sensitivity is achieved using high voltage monolithic active pixel sensors for high spatial resolution and scintillating fibres and tiles providing precise timing information at high particle rates. For discriminating signal and background events, energy and momentum conservation must be exploited. The signal decay is identified by two positrons and one electron originating from the same vertex appearing coincidentally in time in which the energy of the three emitted particles will therefore sum to the total mass of the muon. Through analysis of the reconstructed tracks from signal decays, the properties of tracks, momentum, mass, vertex position, and timing resolution for fibre and tile timing detector were studied. Furthermore, in simulation, tracking performance with an imperfect detector has been studied considering the different effects of missing hits, noise, and misalignment. The performance of a realistic detector with sensor inefficiencies, noise and misalignment is presented together with a refined tracking selection that can be used alongside a conditions database to help recover some of the physics sensitivity of the experiment. In addition, this thesis presents a description of the path towards the chosen chip for the pixel tracker, and a study of the projected sensitivity of the experiment is presented as well as work preparing for quality assurance measurements that will take place as part of the assembly work on the MuPix-HV-MAPS pixel tracker in Liverpool. On the hardware side, test-beam data has been analyzed for two prototypes which are MuPix8 and MuPix9. The readout design, DAQ concept, monitoring, efficiency, noise calculation, and alignment are discussed.

Contents

1 Outline of the Thesis

The Mu3e experiment is a dedicated search for a lepton flavour violating (LFV) decay in the charged sector, $\mu^+ \rightarrow e^+e^-e^+$. Such a decay has not been observed to date and would be a clear indication of new physics beyond the Standard Model (BSM). In Chapter 2, the Standard Model (SM) of elementary particle physics which describes the constituents of matter as well as their interactions is presented with a particular focus on flavour violating decays of the muon within the SM. In this context, possible muon decays based on BSM physics are also discussed. Also, previous, current and planned experiments searching for charged lepton flavour violation (CLFV) are presented.

In Chapter 3, an overview of the planned Mu3e experiment is given. The signal properties, as well as expected background processes, are discussed. There are two categories of background processes that can mimic the signal decay in the Mu3e experiment. These are internal conversion (irreducible) and combinatorial (accidental) background. In phase I Mu3e detector, we have the capability of suppressing the types of backgrounds events to a level that allows for a background free measurement for at least 2.5×10^{15} muon stops. The rate of background events is significantly greater than the expected signal with 10 billion events. The aim is to use selection cuts to remove the background events. From these, the experimental requirements on the Mu3e detector are derived. The Mu3e detector concept of a low mass tracker containing pixel, fibre and tile timing components is presented.

In Chapter 4, the Mu3e simulation, track and vertex reconstruction are discussed. The Mu3e track candidate classification with 4-hit, 6-hit, 8-hit tracks, is discussed. Furthermore, in Chapter 5, simulated samples of signal and background events with specific selection cuts on the frames and vertex are studied to optimize the vertex, momentum and mass requirements to suppress the internal conversion background. Timing selection cuts are also investigated to suppress combinatorial backgrounds. A detailed description of the timing in the reconstruction and analysis framework is given.

In Chapter 6, an improved track reconstruction and selection is presented that can be used for realistic detector conditions where pixel sensors could be masked due to inefficiency or large noise. The studies of the Mu3e tracking performance for different categories of particle tracks will be presented. The tracking selection is optimized by studying artificially introduced inefficiencies into the pixel layers in the central station. The ultimate goal is to allow the tracking algorithm to access sensor information in a conditions database so that the alternate tracking selection can be involved when a track is extrapolated to pass through a known dead, inefficient or noisy sensor. In Chapter 7, the tracking performance for different pixel detector scenarios is presented. These include studies on the impact of misalignment, detector inefficiencies and the impact of noise. The impact of the sensitivity of the Mu3e experiment under these conditions is presented.

In addition to using simulation to study the expected tracking and physics performance of the Mu3e detector, the performance of prototype MuPix sensors has been studied. Chapter 8 is dedicated to the readout hardware for some of the latest MuPix sensor prototypes, such as MuPix8, MuPix9 and MuPix10, covering the chip characteristics and features as well as the setups that are used to operate the chip. In this context, a detailed description of the required hardware and software is given, measurements and analysis of the calibration of the MuPix temperature sensor are shown. The ability to monitor the temperature is important in the Mu3e experiment to verify the cooling performance of the detector since thermal runaway is most often caused by failure of the cooling system.

In Chapter 9, the MuPix Telescope, a particle tracking telescope consisting of four of MuPix sensors for tracking and two additional scintillating tiles in the front for precise timing information is discussed. The telescope is used for efficiency and noise measurements as well as measurements of the spatial and time resolution of sensor prototypes at the test-beam. In this chapter, the particle track reconstruction method for the telescope is discussed and test-beam results are presented in Chapter 10.

Finally, a summary and conclusion with an outlook on further optimization is presented in Chapter 11.

2 Theoretical Background

Today's understanding of the particle physics field is captured by the Standard Model (SM), the most condensed theory in physics history which is able to explain many experimental observations with good precision. Despite its success, the SM is incomplete. For example, it lacks an explanation for dark matter and it does not incorporate gravity. Experiments are searching in a large area of observables for new physics beyond the Standard Model (BSM).

In this chapter, the SM of elementary particle physics and forces is reviewed and it is discussed how the violation of lepton flavour is a promising signature of new physics BSM. Selected models BSM are presented, focusing on lepton flavour violating (LFV) muon decays. In addition, previous, current and planned experimental searches for charged lepton flavour violation (CLFV) are summarized.

2.1 The Standard Model of Elementary Particle Physics and Forces

The SM of particle physics describes all known elementary particles as well as three of the four known fundamental interactions which are the strong, electromagnetic and weak interactions. These interactions are explained by the exchange of the gauge bosons between particles [24]. The gravitational force is not part of the SM, it is very weak compared with other forces and can be ignored in the interactions of fundamental particles. Although gravitational effects are negligible at typical energy scales in high energy physics, they dominate the interactions at cosmological scales. Many astrophysical observations cannot be explained by the amount and distribution of ordinary luminous matter in the universe and thus hint at the existence of another form of matter, the dark matter, which interacts gravitationally and has only very weak interactions with photons [40].

In the SM, the elementary particles that make up matter can be split into quarks and leptons, which are all fermions with spin 1/2. The gauge interactions are mediated by the exchange of gauge bosons with spin 1. Mathematically, the SM is a gauge quantum field theory (QFT) containing the internal symmetries of the unitary product group $\mathrm{SU}(3)_\mathrm{C} \times \mathrm{SU}(2)_\mathrm{L} \times \mathrm{U}(1)_\mathrm{Y}$, with $\mathrm{SU}(3)_\mathrm{C}$ corresponding to the strong interaction and $\mathrm{SU}(2)_\mathrm{L} \times \mathrm{U}(1)_\mathrm{Y}$ being the group for the electroweak interaction. The theory is described by a Lagrangian, containing 26 free parameters whose numerical values are established by experiments. The Higgs particle is a scalar boson with spin 0, it is separated because it is neither a matter particle nor does it mediate a gauge interaction. In 2012, the ATLAS and CMS experiments at the LHC at CERN observed a new particle consistent with the Higgs boson at $(125 - 126)$ GeV [45].

Particles in the SM are defined by their mass and quantum numbers (spin, electric charge, colour charge and flavour quantum number). Figure 2.1 provides an overview of all matter particles and force-carrying boson. For every matter particle, there is a corresponding anti-matter particle with identical properties, but opposite quantum numbers.

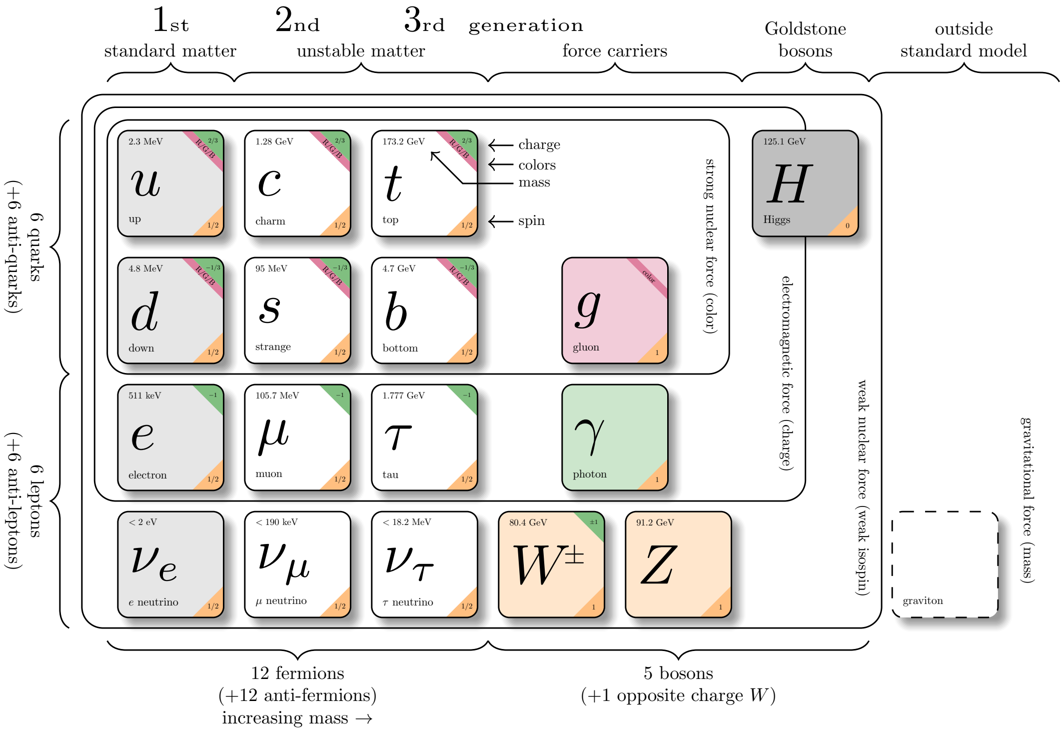

FIGURE 2.1: Particles described by the SM. Figure adapted from [18].

Fermions are divided into 6 quarks and 6 leptons based on their quantum numbers.

These are separated over 3 generations. Quarks are the only fermions that have a property colour charge and thus are the only particles that interact strongly. Gluons themselves carry the color charge of the strong interaction giving triple-gluon and quartic-gluon couplings. This is unlike the photon, which mediates the electromagnetic interaction which are electrically neutral. This process is known as gluon self-interaction, it causes the potential between quarks to increase with distance, so to pull them apart, more energy is required. The possible colour charges are red, green, and blue, while anti-quarks carry anti-colour. Quarks also interact via the electromagnetic and the weak forces. They do not exist as free particles in nature but only appear bound inside Hadrons in nature.

The quarks (see table 2.1), the quarks include the up quark (u) and a down quark (d), which together form one quark generation and which are the constituents of protons and neutrons, the second generation is made up of the charm quark (c) and strange quark (s), and the third by the top quark (t) and the bottom quark (b).

	Particle	Electric Charge	Mass/GeV
1st Generation	up (u)	-1/3	0.003
	down (d)	2/3	0.005
2nd Generation	strange (s)	-1/3	0.1
	charm (c)	2/3	1.3
3rd Generation	bottom (b)	-1/3	4.5
	top (t)	2/3	174

TABLE 2.1: Quarks in the standard model.

The leptons (see table 2.2) only interact via the weak and the electromagnetic force, they do not have a colour charge and cannot interact with gluons, so they do not interact via the strong force. The first generation of leptons, are formed of the negatively charged electron $e^{-}$and the uncharged electron-neutrino ν_e characterised by the electron lepton flavour number $Ł_e$. The electron has the lowest mass of all charged leptons and is stable whilst the other leptons with higher mass can decay into lower-energy particles. Although the neutrinos are massless in the SM, recent neutrino mixing experiments have established that this is not in fact the case as will be discussed in the next section. The second generation of leptons consists of the muon μ^{-} and muon-neutrino ν_{μ}, and the third generation of the tau τ^{-} and tau-neutrino ν_{τ}. These are given the muon lepton flavour number L_{μ} and the tau lepton flavour number L_{τ}, respectively.

In all interactions, the total lepton number is conserved as defined in Table 2.3, whenever a lepton interacts with a W boson, it just changes a lepton to its corresponding lepton

	Particle	Electric Charge	Mass/GeV
1st Generation	electron (e^-)	-1	0.005
	neutrino (ν_e)	0	<10^{-9}
2nd Generation	muon (μ^-)	-1	0.106
	neutrino (ν_μ)	0	<10^{-9}
3rd Generation	tau (τ^-)	-1	1.78
	neutrino (ν_τ)	0	<10^{-9}

TABLE 2.2: Leptons in the Standard Model.

neutrino or the other way around.

Quantum number	e^-	ν_e	μ^+	ν_μ	τ^+	ν_τ	e^+	$\overline{\nu_e}$	μ^+	$\overline{\nu_\mu}$	τ^-	$\overline{\nu_\tau}$
L$_e$	+1	+1	0	0	0	0	-1	-1	0	0	0	0
L_μ	0	0	+1	+1	0	0	0	0	-1	-1	0	0
L_τ	0	0	0	0	+1	+1	0	0	0	0	-1	-1

TABLE 2.3: Assignment of lepton flavors, L$_e$, L_μ, and L_τ.

The particles of the SM interact through the three fundamental forces of the SM. All interactions in the SM are mediated through the exchange of gauge bosons with spin 1. The strong interaction is described by QCD, as mentioned above, only quarks can interact through the strong force in which they exchange gluons. Gluons couple to colour charge, and they are massless.

The gauge boson of the EM interaction is the photon γ, described by QED. The photon has no invariant mass. All electrically charged particles have electromagnetic interactions.

The weak interaction, which affects all fermions of the SM as well as the Higgs boson, is mediated by the three gauge bosons: two W bosons with a mass of about 80.4 GeV and the Z boson with a mass of about 91.2 GeV. The W bosons have an electric charge of ±1 whilst the Z boson is a neutral particle. Table 2.4 is summarized the fundamental forces between particles.

Force	Strength	Boson	Spin	Charge	Mass/GeV
Strong	1	gluon (g)	1	0	0
Electromagnetism	10^{-2}	photon (γ)	1	0	0
Weak	10^{-13}	Z boson (Z)	1	0	91.2
	10^{-13}	W boson ($W^{\pm}$)	1	±1	80.4

TABLE 2.4: Fundamental forces between particles.

2.2 Flavour Violating Decay of the Muon within the Standard Model

The muon is the charged lepton of the second generation within the SM, it is more than 200 times heavier than the electron with a mass of $(105.658367 \pm 0.000004)\mathrm{MeV}/c^2$ [24] and decays with a lifetime of $(2.197034 \pm 0.000021)\mu s$ via the weak interaction into electrons, neutrinos and sometimes photons. There are different decays of muons in the SM, the decay mode with a BR of almost 100 % is the Michel decay $\mu^+ \rightarrow \mathrm{e}^+\overline{\nu}_\mu\nu_\mathrm{e}$. With a BR of about 1.4 % an additional energetic photon is emitted $\mu^+ \rightarrow \mathrm{e}^+\gamma\overline{\nu}_\mu\nu_\mathrm{e}$ ($\mathrm{E}_\gamma > 10$ MeV). With a BR of $3.4 \cdot 10^{-5}$ this photon converts internally to an e^+ e pair with $\mathrm{P}_e^T > 17MeV$, $\mu^+ \rightarrow \mathrm{e}^+\mathrm{e}^-\mathrm{e}^+\overline{\nu}_\mu\nu_\mathrm{e}$. The branching fractions for various decay modes of the muon are summarized in table 2.5 and corresponding Feynman diagrams are shown in figure 2.2.

Measurements of the Michel decay parameters are tests of the EW theory. The radiative and internal conversion decay have been measured by the TWIST collaboration [44]. No deviation from the SM has been found in these measurements.

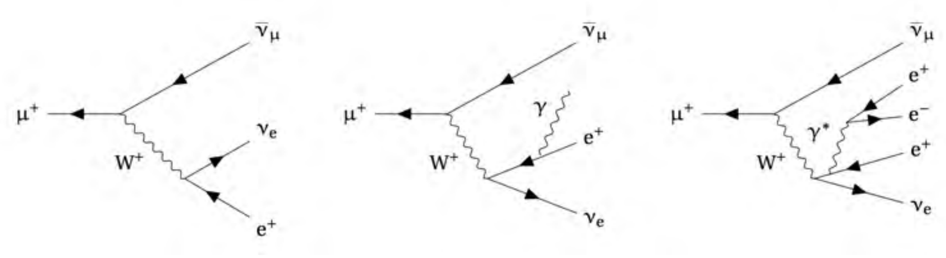

FIGURE 2.2: Decays of the muon in the SM. Michel decay of the muon $\mu^+ \rightarrow \mathrm{e}^+\overline{\nu}_\mu\nu_\mathrm{e}$, radiative muon decay $\mu^+ \rightarrow \mathrm{e}^+\gamma\overline{\nu}_\mu\nu_\mathrm{e}$, and radiative muon decay with internal conversion $\mu^+ \rightarrow \mathrm{e}^+\mathrm{e}^-\mathrm{e}^+\overline{\nu}_\mu\nu_\mathrm{e}$, respectively.

Decay modes	Branching Fraction
$\mu^+ \rightarrow \mathrm{e}^+\overline{\nu}_\mu\nu_\mathrm{e}$	$\approx 100\%$[37]
$\mu^+ \rightarrow \mathrm{e}^+\gamma\overline{\nu}_\mu\nu_\mathrm{e}$	$(1.4 \pm 0.4)\%$ [37]
$\mu^+ \rightarrow \mathrm{e}^+\mathrm{e}^-\mathrm{e}^+\overline{\nu}_\mu\nu_\mathrm{e}$	$(3.4 \pm 0.4) \cdot 10^{-5}$[37]

TABLE 2.5: Branching fraction of SM muon decay modes.

Many BSM models include flavour violating processes in the charged lepton sector. An example of a CLFV process is the muon decay $\mu^+ \rightarrow e^+e^+e^-$. In the SM including neutrino masses, LFV can only occur via neutrino mixing. Neutrinos as discovered in experiments such as Super-Kamiokande [51], SNO [48] and KamLAND [46], from one generation can turn into neutrinos of another generation through neutrino oscillations. This indicates that neutrinos have a small mass. Furthermore, this process is lepton flavour violating. Neutrinos oscillate between all three states of flavour, as the eigenstates of flavour are not the eigenstates of mass. As a consequence ν_e, ν_μ and ν_τ are not fundamental particle states but a mixture of the mass eigenstates ν_1, ν_2 and ν_3. Neutrino mixing is described by the mixing matrix which can be parameterized through the PMNS parameterization:

$$\begin{pmatrix} \nu_e \\ \nu_\mu \\ \nu_\tau \end{pmatrix} = \begin{pmatrix} U_{e_1} & U_{e_2} & U_{e_3} \\ U_{\mu_1} & U_{\mu_2} & U_{\mu_1} \\ U_{\tau_1} & U_{\tau_2} & U_{\tau_3} \end{pmatrix} \begin{pmatrix} \nu_1 \\ \nu_2 \\ \nu_3 \end{pmatrix} \tag{1}$$

$$= \begin{pmatrix} c_{12}c_{13} & s_{12}c_{13} & s_{13}e^{-i\delta} \\ -s_{12}c_{23} - c_{12}s_{23}s_{13}e^{i\delta} & c_{12}c_{23} - s_{12}s_{23}s_{13}e^{i\delta} & s_{23}c_{13} \\ s_{12}s_{23} - c_{12}c_{23}s_{13}e^{i\delta} & -c_{12}s_{23} - s_{12}c_{23}s_{13}e^{i\delta} & c_{23}c_{13} \end{pmatrix} \begin{pmatrix} \nu_1 \\ \nu_2 \\ \nu_3 \end{pmatrix}$$

where s$_{ij}$ and c$_{ij}$ are used to denote $\sin\theta_{ij}$ and $\cos\theta_{ij}$, respectively. $\left(U_{ij}\right)$ which describes the rotation between the mass eigenstates v_1, v_2, v_3 relevant for free propagation and the flavour eigenstates v_e, v_μ, v_τ relevant for weak interactions. As a result, neutrinos[1] propagate as a superposition of all mass eigenstates. The PMNS matrix describe this mixing through three mixing angles θ_{12}, θ_{13} and θ_{23} and a complex phase δ[2]. The electron superposition looks like this:

$$\mid \nu_e\rangle = U_{e_1}|\nu_1\rangle e^{-i\Phi_1} + U_{e_2}|\nu_2\rangle e^{-i\Phi_2} + U_{e_3}|\nu_3\rangle e^{-i\Phi_3} \tag{2}$$

Where $\Phi_i = E_i \times t$. The probability for a neutrino to transition from flavour α to β can be calculated:

$$\begin{aligned} P\left(\nu_\alpha \to \nu_\beta\right) &= 2\,\mathrm{Re}\left(U_{\alpha_1}U^*_{\beta_1}U^*_{\alpha_2}U_{\beta_2}e^{-i(\Phi_1-\Phi_2)}\right) \\ &+ 2\,\mathrm{Re}\left(U_{\alpha_1}U^*_{\beta_1}U^*_{\alpha_3}U_{\beta_3}e^{-i(\Phi_1-\Phi_3)}\right) \\ &+ 2\,\mathrm{Re}\left(U_{\alpha_2}U^*_{\beta_2}U^*_{\alpha_3}U_{\beta_3}e^{-i(\Phi_2-\Phi_3)}\right) \end{aligned} \tag{3}$$

---

[1] The mass difference between neutrinos is non zero: $m_i - m_j = \Delta m_{i,j} \neq 0, \forall j \neq i$

[2] Measurements: $\theta_{12} \approx 35°, \theta_{13} \approx 10°, \theta_{23} \approx 45°$[49],[47]

An important thing to note is, that if any elements of the PMNS matrix are complex, this process is not invariant under time reversal[3] $(t \to -t)$ $P\left(\nu_\alpha \to \nu_\beta\right) \neq P\left(\nu_\beta \to \nu_\alpha\right)$

Lepton family number is violated through neutrino oscillations. However, why should flavour oscillation be exclusive to neutrinos? Maybe there are ways for the charged leptons also transition to another lepton family.

2.3 Lepton Flavour Violating Decays of the Muon Beyond Standard Model

The BR for lepton flavour violating muon decays that stem from the neutrino mixing (see figure 2.3) alone is extremely small [19].

$$\mathrm{B}\ _{SM}(\mu \to \mathrm{e}\gamma) \approx \frac{3\alpha}{32\pi}\left|\sum_{i=2,3} U^*_{\mu i} U_{ei} \frac{\Delta m^2_{i1}}{m^2_{\mathrm{W}}}\right|^2 < 10^{-54} \tag{4}$$

where α is the fine structure constant, m_W the mass of the W-boson [19], $U_{\alpha i}$ the elements of the neutrino mixing matrix, Δm^2_{i1} the differences of the squared neutrino masses. Such branching fractions are far beyond the reach of any present day experiments. The large suppression is caused by the smallness of Δm^2_{i1} $\left(O\left(10^{-3}\mathrm{eV}^2\right)\right)$ and the comparably large W boson mass $(M_{\mathrm{W}} = 80.4\mathrm{GeV})$.

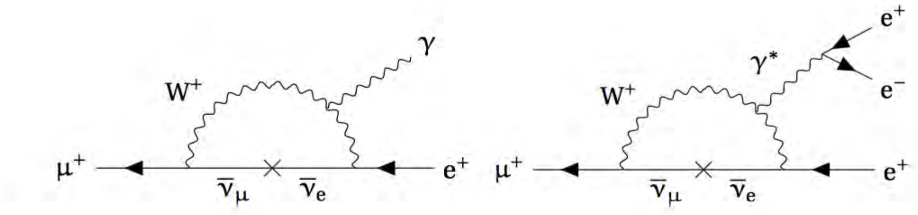

FIGURE 2.3: Lepton flavour violating muon decays in the SM with neutrino mixing and masses for $\mu \to e^+\gamma$ and $\mu \to e^+e^-e^+$. As a result of neutrino oscillation, the lepton flavour is a broken symmetry. CLFV is strongly suppressed because the mass difference between neutrinos is tiny compared to the W boson mass.

Many new physics models introduce possible diagrams for LFV reactions in the charged sector and any observation of $\mu \to e^+e^-e^+$ would provide an unique opportunity to explore physics BSM. There are two different approaches to introduce CLFV processes in BSM models, through loop contributions or new tree couplings as shown in figure 2.4.

---

[3] The probability does not change, if a complex phase adds to the PMNS matrix, just if one of the elements has a phase different from the others

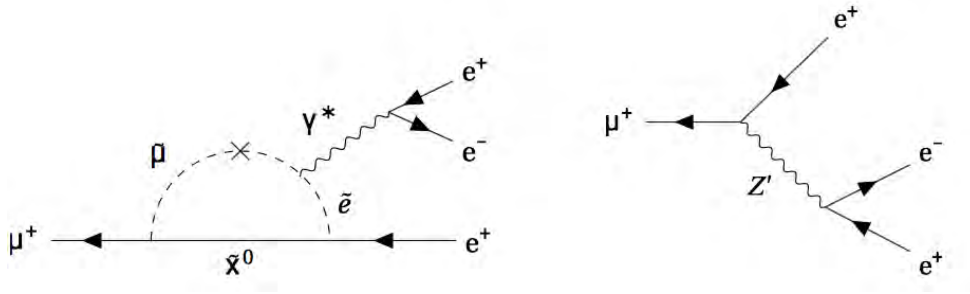

FIGURE 2.4: Left: The diagram is the $\mu^+ \to e^+e^-e^+$ via penguin loop diagram involving new heavy particles in the super-symmetric models. Right: The diagram $\mu \to e^+e^-e^+$ decay at tree level involving new particles in super-symmetric models BSM.

The CLFV effects are enhanced and potentially experimentally accessible in many extensions of the SM, such as left-right symmetric models [15], grand unified models [36], models with an extended Higgs sector [14] [26] and neutral Z′ models [12]. One example for such a family of BSM models would be SUSY in which $\mu^+ \to e^+e^-e^-$ can occur via γ/Z-penguin loops involving new heavy particles [4] in models BSM. Briefly, CLFV seems to be natural. However, does CLFV exist? Some experiments have made it their goal to answer this question.

2.4 Previous and Current Experiments Searching for Charged Lepton Flavour Violation

The search for LFV in the charged lepton sector has been a topic of interest for various experiments in the past or planned in the near future. The history of experimental LFV searches is shown in figure 2.5. The most recent upper limits on the LFV decay modes are summarized in table 2.6.

In the years from 1983 to 1986, the **SINDRUM** experiment at the Paul Scherrer Institute in Switzerland (PSI) was operated to search for the decay $\mu^+ \to e^+e^-e^+$. During the run time of SINDRUM, no signal decay was found and an upper limit was set on the BR of 1×10^{-12} at 90 % C.L. [50]. This was mainly limited by accidental backgrounds. In SINDRUM, the incoming muon beam was stopped on a hollow double cone target made of a thermoplastic foam, placed inside a solenoidal magnetic field of 0.33 T. An arrangement of multiwire proportional chambers were used to measure the electrons from the muon

---

[4] In super-symmetric models, every particle has a super-symmetric partner particle, its super-partner with opposite spin-statistics. For example, the superpartners of leptons are called “sleptons”. In some SUSY models, the mass matrix of these sleptons has off-diagonal elements, allowing for LFV via the mixing of sleptons

decays, and the timing was measured with a plastic scintillator hodoscope read-out with photo-multipliers. The timing and momentum resolution were used to suppress the accidental background. Figure 2.6 shows a schematic layout of SINDRUM in which the incoming muons are stopped on the target (T). The multiwire proportional chambers (C) measure the momentum and the hodoscope (M) the timing of the decay products.

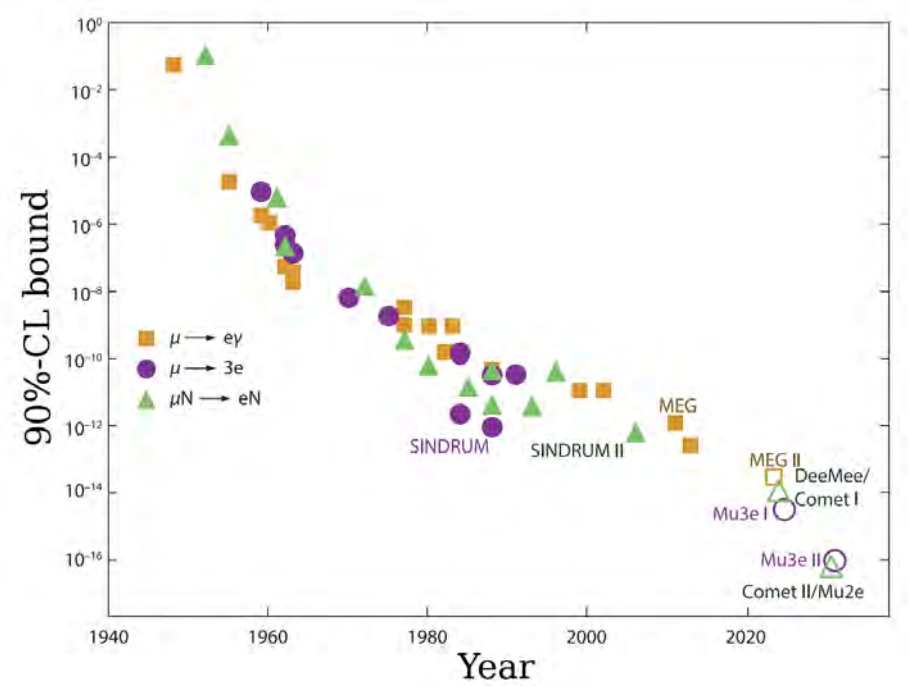

FIGURE 2.5: Previous and future experiments searching for LFV. Hollow markers denote upcoming experiments that are under development, solid markers represent currently running or already finish experiments. Adapted from [34].

The **MEG** experiment has been searching for CLFV $\mu^+ \to e^+\gamma$. It ran at PSI from 2008 until 2013. A muon beam of about $3 \cdot 10^7 \mu/s$ was stopped on a small thin target [7]. A drift chamber system was used to measure the single positron momenta from the bending radius of the tracks in the magnetic field. A timing counter system made of scintillating bars measured the time. A liquid Xenon calorimeter read out via photo-multiplier tubes was used to detect the photon. MEG set the current best upper limit on the BR of $4.2 \cdot 10^{-13}$ at 90 % C.L.. The main background comes from the accidental coincidence of high energy photons and single positrons from Michel decays. Figure 2.7 shows the longitudinal and transverse views of the MEG detector.

Decay modes	Branching Fraction	Experiment
$\mu^+ \to e^+\gamma$	$< 1.2 \cdot 10^{-11}$ [16]	MEGA
$\mu^+ \to e^+\gamma$	$< 4.2 \cdot 10^{-13}$ [7]	MEG
$\mu^+ \to \mathrm{e}^+e^-e^+$	$< 1.0 \cdot 10^{-12}$ [50]	SINDRUM

TABLE 2.6: Limits on branching ratios on the LFV muon decays.

In the **MEG II** experiment, the positron tracker and the liquid Xenon calorimeter have been upgraded to improve the resolution and to operate with higher muon rates [8]. The upgraded experiment restarted in 2021 and aims to achieve a sensitivity of $5 \cdot 10^{-14}$ in the BR after 3 years of data taking [21].

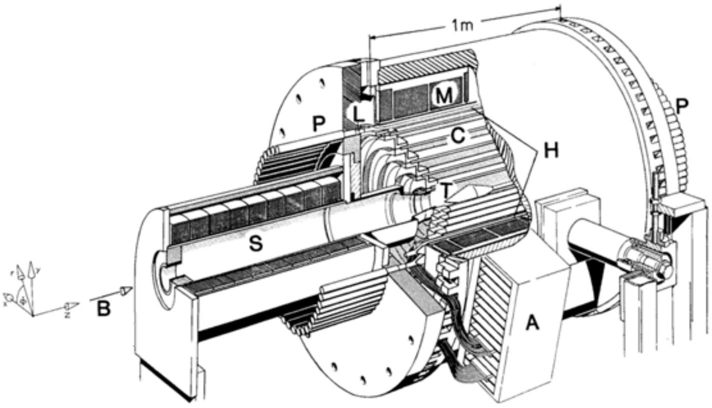

FIGURE 2.6: Sketch of the SINDRUM experiment [80]. The incoming muons are stopped on the target (T). The multiwire proportional chambers (C) measure the momentum and the hodoscope (M) the timing of the decay products. Adapted from [13].

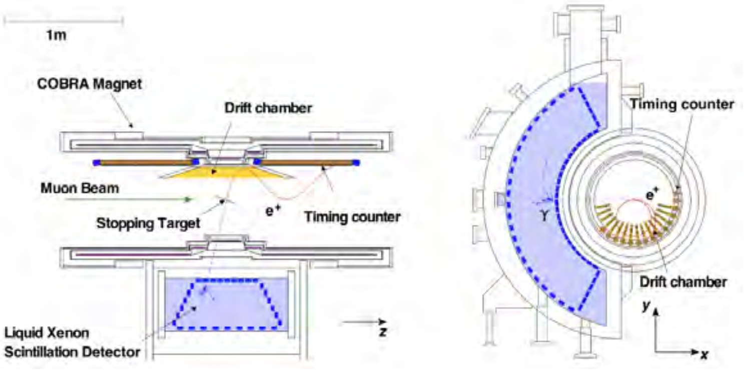

FIGURE 2.7: Longitudinal and transverse view of the MEG detector. Adapted from [7].

3 The Mu3e Experiment

The Mu3e experiment is a new search for the lepton-flavour violating decay of a positive muon into two positrons and one electron. The Mu3e experiment is designed to be able to place a limit on the branching fraction of $\mu^+ \to e^+e^+e^-$ of 10^{-16} or above at a 90% C.L., which is higher than the sensitivity of the previous experiment, SINDRUM. This will be achieved by using the design and technology presented in this chapter.

3.1 Muon Decays: Signal and Background Typologies

The **signal decay** $\mu^+ \to e^+e^+e^-$ produces two positrons and one electron from a common vertex, coincidentally in time as depicted in Figure 3.1 (First). In the Mu3e experiment, incident muons from a muon beam are stopped in the target to decay at rest. Therefore, through conservation of momentum, the sum of the momentum of the three decay particles is vanishing:

$$\vec{p}_{\text{tot}} = \sum_{i=1}^{3} \vec{P}_i = 0 \qquad (1)$$

with $\vec{p}_{\text{tot}}$ denoting the three-momenta of the muon and $\vec{p}_i$ is the three-momentum of each of the decay products. This also means that the momenta are in a plane. From the conservation of energy the 4-vectors $\mathbf{P}_i$ must fulfil:

$$m_\mu^2 = \left| \sum_{i=1}^{3} \mathbf{P}_i \right|^2 \qquad (2)$$

In the center of mass for the system of the muon, energy conservation dictates that the summed energy of the three decay particles be equal to the rest mass of the muon:

$$E_{tot} = \sum_{i=1}^{3} E_i = m_\mu \cdot c^2 \approx 105.7 MeV \tag{3}$$

where $E_i (i = 1, 2, 3)$ is the energy of the three decay particles. The momentum for a single decay particle can not be more than half the muon mass, $1/2 \cdot m_\mu \approx 53 MeV/c$. In the Mu3e experiment, all of these conditions as stated earlier are valid also in the laboratory frame since the muons decay at rest.

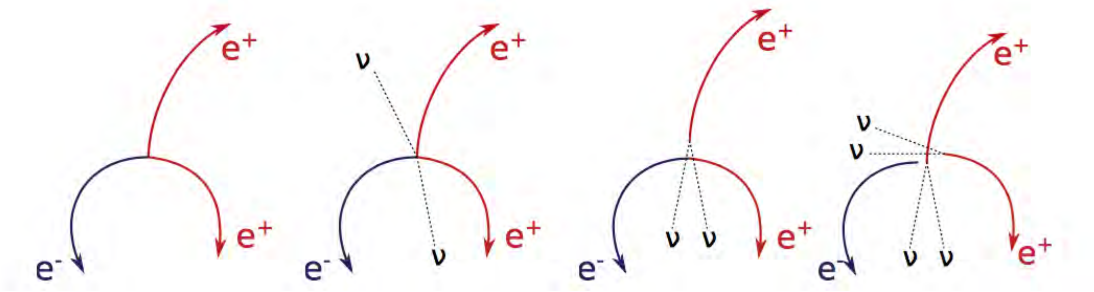

FIGURE 3.1: Illustration signal and background topology. From left to right Signal decay; internal conversion in which the neutrinos are unobserved; combinatorial background with an additional e+e- pair and a positron from Michel decay; and accidental background with two Michel decays and an electron track.

The Mu3e experiment aims to be a zero background experiment, which means that the rate of background events is below one expected event. Therefore, the elimination of backgrounds is essential. There are two categories of background processes to the signal decays that are of importance in the Mu3e experiment. These are **internal conversion events (irreducible)** and **combinatorial (accidental) backgrounds**. The signal can be distinguished from background processes as described in the following and summarised in Table 3.1.

Internal conversion background arises from decay $\mu^+ \rightarrow e^+e^-e^+\overline{v}_\mu v_e$, and has a BR of $(3.4 \pm 0.4) \cdot 10^{-5}$ [37]. This background is not easily distinguishable from the signal decay since this background decay emerges from a common vertex and is coincident in time, but it can still be differentiated from the signal decays as the sum of the momenta for the three detected electrons does not vanish, and the sum of the energies are not equal to the muon mass. The reason for this, is that a part of the rest mass of the original muon is given to the two neutrinos. By kinematic constraints, as in equations 1 to 3, this type of background can be suppressed. An energy resolution of better than 1 MeV/c is needed to suppress this background (see section 5.3, Chapter 5).

	signal	combinatorial background	internal conversion
Common vertex	yes	no	yes
Coincidence in the time	yes	no	yes
Total momentum $\sum \vec{P}$	0	any	$\neq 0$
Total energy $\sum E$	m_μ	any	$< m_\mu$

TABLE 3.1: Specifications of signal and background processes.

Combinatorial background is accidental background from, in most cases, two uncorrelated vertices, one providing a single positron track from a Michel decay and the other an additional e^+e^- pair. The e^+e^- pair can be produced either from Bhabha scattering of an e^+ in the muon stopping target or from pair production of a photon which can originate from the radiative muon decay $\mu^+ \to e^+\gamma\nu_e\overline{\nu}_\mu$. Precise timing measurements to better than 500 ps/track are required to discriminate the signal decay from combinatorial background and hence suppress this backgrounds sufficiently (see subsection 5.2.4, Chapter 5).

Figure 3.1 shows the signal and all types of background with properties.

3.2 The Detector Concepts

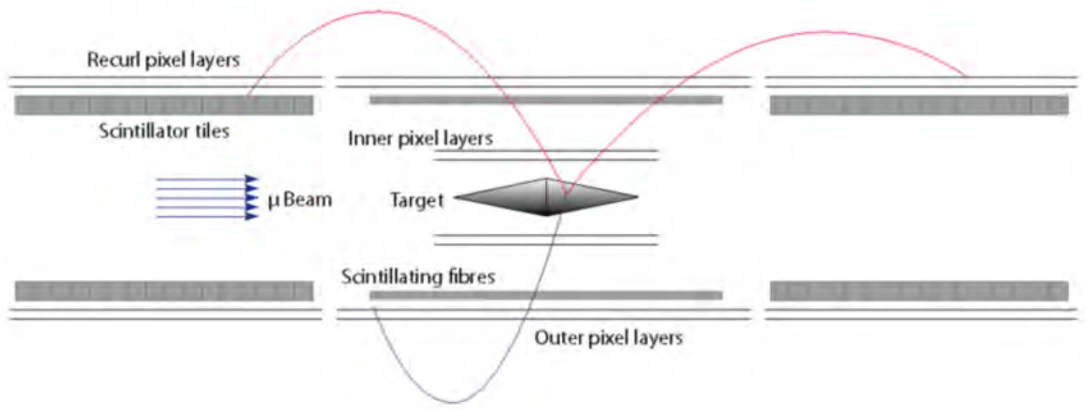

FIGURE 3.2: Schematic view of the phase I Mu3e detector, which is comprised of a central part with recurl stations. The central station contains two double silicon pixel tracker layers and a scintillating fibre layer. The two recurl stations shown, each contain one double silicon pixel tracker and a tile timing detector [1].

The Mu3e experiment will be operated at PSI in Switzerland. In order to reach its target sensitivity, it needs extremely high incident muon rates, and the detector must provide accurate spatial and timing resolution measurements. Figure 3.2 illustrates the main components of the phase I detector. The muons are stopped in a thin target in the central detector. The whole detector is placed in a solenoid magnetic field of 1 T so that all tracks from the muon decay products are bent through a full helix inside the detector. The curvature in the magnetic field is used to determine a track candidate's charge and momentum.

3.2.1 The Muon Beam

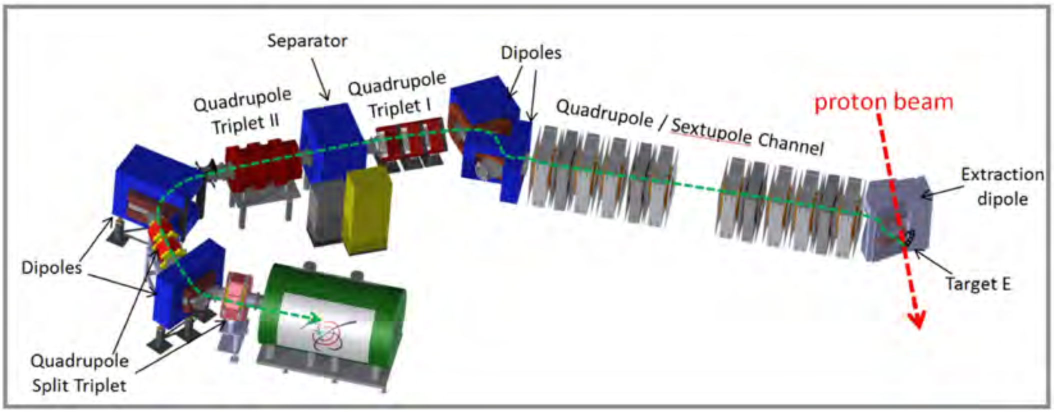

FIGURE 3.3: The CMBL in the experimental area of Mu3e. Figure taken from [1].

A high intensity muon beam stopped on a target is used to produce the muon decays. The first phase (Phase-I) of experiment which aims to reach a sensitivity to a BR $\sim \mathcal{O}\left(10^{-15}\right)$ requires a muon stopping rate of about 10^8 μ/s. Such a high muon rate is available at PSI which operates the world's most powerful proton beam with up to 2.3 mA of 590 MeV/c protons. The proton beam is used to produce pions decays in a production target, then muons created from the decays of pions stopped very close to the target surface, are extracted via the $\pi E5$ beamline shown in figure 3.3. It is also used by the MEG II experiment and provides a muon rate of $O\left(10^8\mu/s\right)$ with muon momenta of 28 MeV. This momentum of the muon is determinated by the momentum of pion and the angle of decay in the pion rest frame.

In the second phase (Phase-II) of the Mu3e experiment, the aim is to reach a sensitivity to a BR $\sim \mathcal{O}\left(10^{-16}\right)$. This will be achieved with muon stopping rates up to $2{\times}10^9\mu/s$ through the construction of a new muon beamline [1].

3.2.2 The Stopping Target

In the Mu3e experiment, the muons from the beam are stopped in the target. The target is required to be low mass. The target has a hollow double cone design out of Mylar foil with a thickness of about 70 μm in the upstream and 80 μm in the downstream part (see figure 3.4). The target is 10 cm long with a radius of 1.9 cm. The target is supported by a carbon tube from the downstream side. The material in the target is enough to achieve a high stopping ratio of about 90% for the low momentum muons. The shape of target is similar to that used in the SINDRUM experiment.

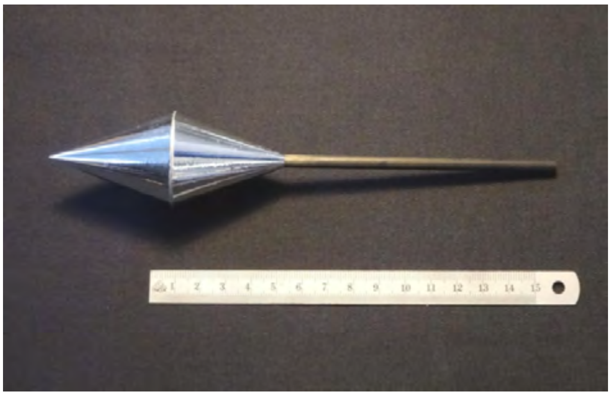

FIGURE 3.4: Hollow double-cone muon stopping target made of aluminized Mylar foil. It is adapted from [1].

3.2.3 The Pixel Tracker

The Mu3e detector consists of a central station, surrounding the stopping target, and two recurl stations. The central pixel tracker has four layers, two inner layers at small radii and two outer layers at larger radii. The recurl stations have two outer pixel layers which are identical to the outer pixel layers in the central tracker. The inner tracking layers consist of 8 and 10 overlapping ladders of 12 cm in length, where each ladder consists of 6 chips, as shown in figure 3.5. The outer layers have a length of 34 cm for layer 3 and 36 cm for layer 4, and host 17 and 18 MuPix chips, respectively. To achieve a large acceptance for low momentum tracks and in order to help with the alignment of the pixel tracker, the MuPix ladders are mounted with a small overlap of 0.5 mm. The recurl layers are critical to select high quality tracks with an excellent momentum resolution and to provide a high acceptance for downstream and upstream particles. The momentum resolution is limited by multiple scattering (MS) in the Mu3e detector material, as the electrons have very low momenta. As a result, the material budget must be minimized to below 0.190 of a radiation length per layer [1]. Figure 3.5 shows the

pixel layer	1	2	3	4
number of modules	2	2	6	7
number of ladders	8	10	24	28
number of MuPix sensor per ladder	6	6	17	18
in instrumented length [mm]	124.7	124.7	351.9	372.6
minimum radius [mm] [1]	23.3	29.8	73.9	86.3

TABLE 3.2: Summary table for pixel tracker geometry parameters of the central station.

layers, modules and ladders of the central tracking station including the target. Table 3.2 lists the main geometry parameters of the central tracking station.

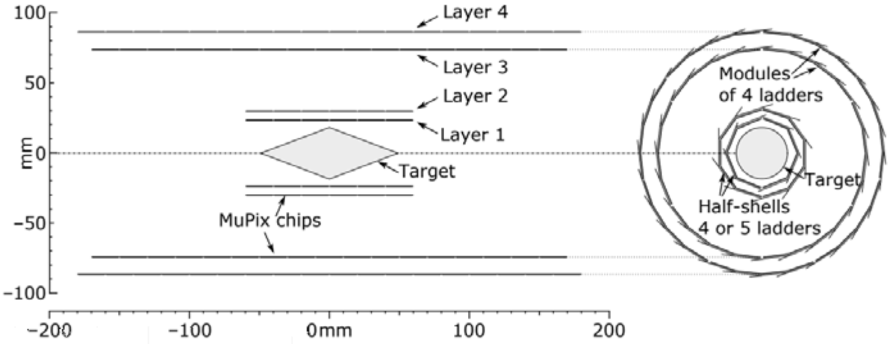

FIGURE 3.5: Geometry of the inner and outer pixel layers in the central station illustrate the layers, modules and ladders and the target. Ladders are the smallest mechanical unit in the tracker, it is adapted from [1].

The pixel tracking detector consists of thinned silicon pixel sensors and a mechanical support structure made of Kapton designed to be low mass, to reduce multiple scattering.

An upper limit on the resolution of the pixel sensors, σ_x, can be derived from the variance of a uniform distribution of hit positions over the area of a single pixel, and it is given by:

$$\begin{aligned} \sigma_x^2 &= \int_{-a/2}^{a/2} x^2 f(x)dx \\ &= \frac{a^2}{12} \\ \Rightarrow \sigma_x &= \frac{a}{\sqrt{12}} \end{aligned} \tag{4}$$

Where (a) is the pixel pitch, and with the corresponding residual distribution is a uniform distribution with width $f(x) = 1/a($ for $0 \leq x \leq a)$. Therefore, the resolution is directly correlated to the pixel size.

The pixel detectors proposed for the Mu3e experiment are HV-MAPS sensors with a pixel size of 80 × 80 (μm^2). The sensors are thinned to 50 μm to limit the impact of multiple scattering on the momentum resolution.

The vertex resolution of the Mu3e detector, is limited by the amount of MS in the target and in the inner pixel layers, so multiple scattering at the innermost pixel layer is the only uncertainty considered. To achieve an accurate vertex position resolution, the innermost pixel layers, known as vertex layers, are situated close to the target, reducing the distance between the vertex and the closest track measurement to minimise the impact of scattering. The minimum radius is determined by the target dimensions. A moderator and two collimators must be used to match the target radius with the beam pipe radius in order to stop the high rate of muon beams at the target.

Electrical connections for power, readout of the pixel chips, slow control and high-voltage are provided through a thin aluminium-kapton flex-circuit [1].

3.2.4 HV-MAPS Technology

The pixel tracker of the Mu3e detector is designed with High-Voltage Monolithic Active Pixel Sensors (HV-MAPS). Monolithic means the sensor and the readout electronics are integrated on a single silicon chip. A high voltage is used for fast charge collection and a larger depleted area. The chosen chip is from the MuPix chip family, Chapter 8 describes the design in more details. A schematic view of an HV-MAPS is illustrated in figure 3.

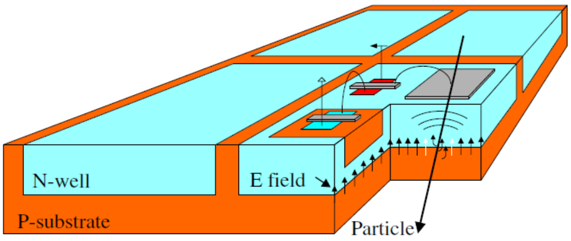

FIGURE 3.6: Schematic view of an HV-MAPS. Figure adapted from [38].

There are differences between MAPS and HV-MAPS technology. Mu3e is the first particle physics experiment to employ HV-MAPS in a tracker. Mu3e would not be possible without this new technology with sensitivity $\sim (X\backslash X_0)^3$.

In **MAPS**, small n-wells in the p-substrate are used for the electronics to form diodes. Electron-hole pairs are created when charged particle passes through or photons are absorbed. The charges then are separated by diffusion and collected [30].

For **HV-MAPS**, deep n-wells are implemented inside the p-substrate to form a depletion zone, the high voltage of O(100V) is applied with a high electric field passing the diode. This high voltage ensures the charge collection is via drift, and not diffusion, which is a faster process. Diodes are implemented inside the deep n-well, avoiding parasitic charge collection by the readout electronics.

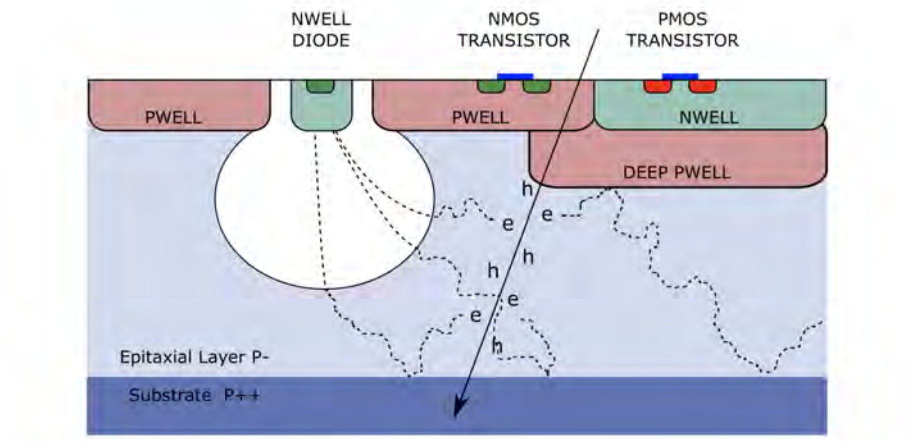

FIGURE 3.7: A deep p-well shields the n-well which contains the PMOS transistors, preventing it from collecting signal charge from the epitaxial layer instead of the n-well as charge collection electrode [52].

The deep p-well shields the other n-wells different from the collection electrode from the epitaxial layer, preventing them from collecting signal charge, which then would be lost for readout. This allows implementing PMOS transistors and hence full CMOS in the in-pixel circuit. The p-well allows to integrate NMOS transistors while the epitaxial layer serves as detection volume as shown in figure 3.7. Charges generated in this layer diffuse until they eventually reach the depleted area at the diode. The pixel detectors have a timing resolution of 15-30 ns.

3.2.5 The Timing Detector

A good timing resolution is required to reduce the combinatorial background and to facilitate event reconstruction. As the pixel sensors do not have adequate timing resolution, additional dedicated timing detectors are used to provide time resolution measurements on reconstructed tracks, so accidental background can be suppressed. The Mu3e detector includes scintillating tiles and fibres.

The **Scintillating fibre** detector is placed between the inner and outer double layers of pixel sensors at a radius of 6.4 cm and has a timing resolution of 500 ps per fibre(see subsection 5 .2.4, Chapter 5). The design of Scintillating fibre tracker consists of 12 ribbons, where each ribbon has 3 layers of 126 fibres each. The fibre detector has a length of about 29 cm. The fibres are connected to a silicon photo-multipliers array (SiPM) and read out via a custom readout chip called MuTRiG [20].

The **Scintillating tile** detector has a length of 36.4 cm with an outer radius of 6.3 cm and an expected time resolution better than 100 ps (see subsection 5 .2.4, Chapter 5). The tiles have a size of about of $6.5 \cdot 6.5 \cdot 5.0$ (mm^3). The detector in each recurl station is segmented into 56 tiles in z direction and 56 tiles along the azimuthal angle. The readout uses 3 mm · 3 mm single channel SiPMs. Signals are digitised by the same MuTRiG ASIC as in the fibres detector. Each tile is connected to an individual SiPM. No further measurements of the particles are performed after particles reach the tiles.

3.2.6 Readout data concept

The Mu3e experiment will operate without a hardware trigger. Due to the life times of the muon and pion, the muon decays are quasi-continuous, overall Mu3e readout scheme is shown in figure 3.8. Data from the whole Mu3e detector are combined on front end FPGA boards into time slices and sent to a filter farm with GPUs in which fast tracking and vertex algorithms are implemented to select interesting events which are then sent to storage for offline analysis. The FPGA is programmed to sort and group the hit information in frames of 50 ns. The information regarding the particle tracks are read out from the detectors into objects called reconstruction frames. These overlapping frames with time-length 50 ns contain all the information about the muon decay products. The particle track information is stored in respect to a frame number in the experiment, and so at a particular time, with the first frame's position representing the starting point of the experiment. The vertices of these decays are reconstructed using the information stored within these frames. A true time is measured at the beginning of a experiment when the π^+ beam creates muons for the first time, whereas the propagated times are measured in frames, where one muon decay occurs per frame, with the first frame beginning at the beginning of the experiment and each frame lasting 50 ns. The filter farm reduces the incoming data from 100 Gbits/s to 50-100 MB/s [1].

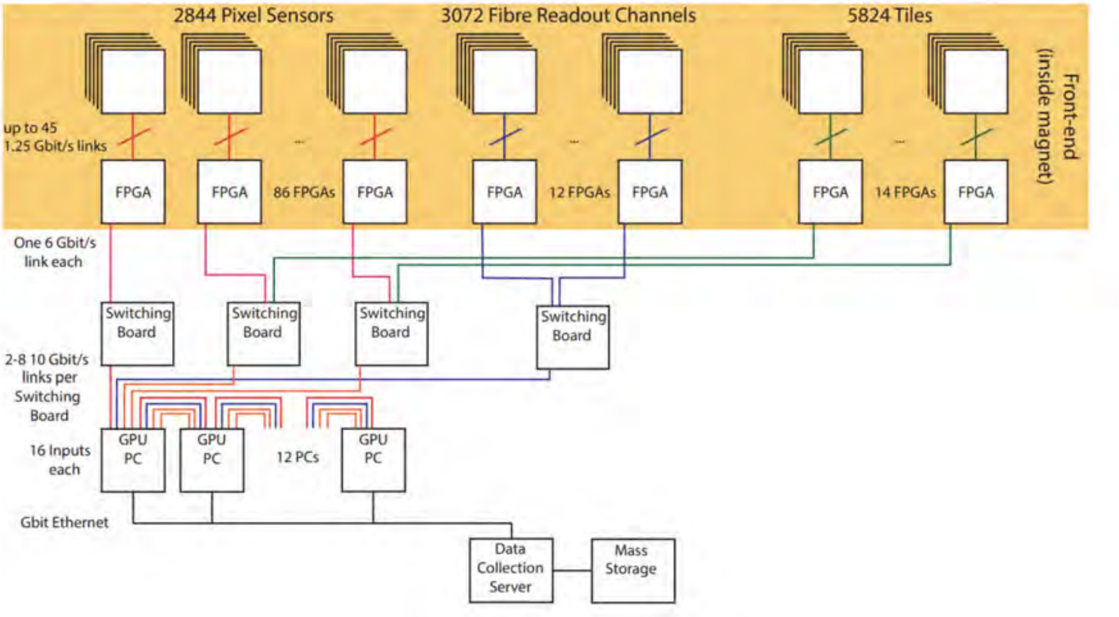

FIGURE 3.8: Overall Mu3e readout scheme.

3.2.7 Cooling

Most of the active detector components can produce significant amounts of heat, so the cooling performance is a very important aspect of the Mu3e detector. Elements located outside the active volume, such as the front-end readout electronics and the readout of the scintillating detectors are cooled using water. To reduce MS, gaseous helium is used for cooling inside the active detector. The gaseous helium flows in the volumes in between the pixel layers and fibre detector and through the rest of the magnet bore. A heat dissipation of 300 mW/cm^2 is expected for the silicon sensors. Lab studies and simulations have shown that the cooling system is able to restrict the temperature gradient over the inner and outer pixel layers to less than 70 K and 40 K, respectively [35].

4 Reconstruction and Simulation

The Mu3e track reconstruction is based on a simple geometric vertex algorithm that uses triplets of hits in the central pixel tracker. It is implemented on graphical processing units (GPUs) and will run as part of the online data acquisition (DAQ) chain.

4.1 Track Reconstruction

Track reconstruction is based on combining overlapping triplets of pixel hits in the inner and outer pixel layers. A triplet consists of three hit positions. Triplets are fitted independently, before they are combined to make track segments as illustrated in figure 4.1 (left). Due to the low particle momentum, there are significant tracking uncertainties from multiple scattering (MS) that must be taken into account.

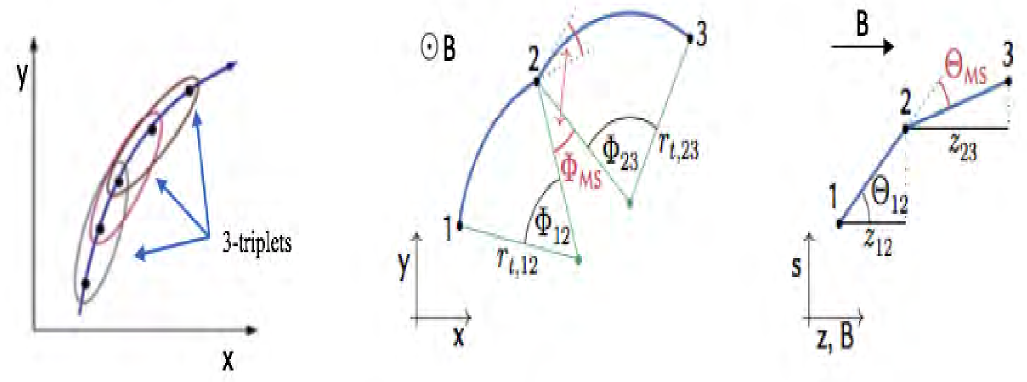

FIGURE 4.1: Left: this shows the triplets which are the basic building blocks of tracks. Middle: two helices in the x-y plane describing a triplet with scattering angle ϕ_{MS} in the material in the plane of the central hit. Right: projection on the z-s plane with scattering angle θ_{MS}, where s is the path length along the trajectories. Adapted from [10].

The parameters that are needed to reconstruct a triplet are shown in figure 4.1. For each individual triplet candidate, two helices are constructed. The middle hit position is expressed by the two angles ϕ_{MS} and θ_{MS} in the transverse and longitudinal plane to the magnetic field, respectively. Particles bend in the homogeneous magnetic field with bending radius R_{3D}, so the track reconstruction in the magnetic field is a helical trajectory:

$$R_{3D}^2 = r_{t,12}^2 + \frac{z_{12}^2}{\Phi_{12}^2} = r_{t,23}^2 + \frac{z_{23}^2}{\Phi_{23}^2} \tag{1}$$

R_{3D} is conserved since MS in the thin material of tracking layers changes the direction of a particle but not substantially the amplitude of momentum. During the reconstruction, the energy loss in the pixel detector is neglected because the loss due to ionization is small. However, energy loss correction can be made retrospectively taking the path length between layers into account.

A helix fit is used in the triplet reconstruction, taking into account the MS by minimizing the scattering angles at the central hit of the triplet.

$$\chi_{triplet}^2 \left(R_{3D}\right) = \frac{\Phi_{\mathrm{MS}} \left(R_{3D}\right)^2}{\sigma_\phi^2} + \frac{\Theta_{\mathrm{MS}} \left(R_{3D}\right)^2}{\sigma_\theta^2} \tag{2}$$

In MS theory, because the polar and azimuthal angles distribute around zero, the scattering angles have a mean of zero with variances $\sigma_\theta^2 = \sigma_{\mathrm{MS}}^2$ and $\sigma_\phi^2 = \sigma_{\mathrm{MS}}^2 / \sin^2\theta$. Due to the two triplets sharing two hits on a single track, and the independence of the scattering in each layer, this can be implemented by minimising the sum of the χ_i^2

$$\chi_{\text{track}}^2 \left(\overline{R}\right) = \sum_{i=1}^{n_{\text{ triplets}}} \chi_i^2 \left(R_i\right) \tag{3}$$

$$\overline{R} = \sum_{i}^{n_{hit}-2} \frac{R_i^3}{\sigma \left(R_i\right)^2} / \sum_{i}^{n_{hit}-2} \frac{R_i^2}{\sigma \left(R_i\right)^2} \tag{4}$$

A weighted average of the resulting radii $\overline{R}$ of the individual fits is given in equation 4. The number of triplets is defined as $n_{\text{ triplets}} = n_{\text{ hits}} - 2$. R_i and $\sigma(R_i)$ are the curvature radius and the uncertainty estimate on R_i for triplet [11]. A triplet has three pixel hits with two helices. If a particle traverses two chips from adjacent ladders in a single layer, the relative distance between the associated hits is less than 3 mm, and the hits are combined to a single hit.

In mu3e, the minimization problem is non-linear and there is no an analytic solution. However, the problem can be linearized such that both ϕ_{MS} and θ_{MS} are linear functions of the curvature radius (r). For small scattering angles, the trajectory that is circular in the xy-plane can be taken as the initial solution. In this case the scattering angle in the xy-plane is zero and the parameters of both helices can be calculated from the positions of the hits. To combine multiple triplets into a track, it can be shown that the solution to the minimization of the track χ_i^2 is a weighted average of the radii R_i of the individual triplets [10].

4.1.1 Vertex Reconstruction

One obvious characteristic of the signal muon decay $\mu^+ \to e^+e^+e^-$ is a common vertex from the two positron tracks and one electron track. This feature can be used to suppress accidental backgrounds. The reconstruction of a common vertex by extrapolating the three tracks into the vertex region is not trivial. This is because the MS of the tracks results in the three tracks not coinciding in a single space point. Furthermore, the bending of the tracks in the magnetic field causes a non-linear problem. Here, the spatial uncertainties are neglected and only MS in the inner pixel detector layer is considered.

The best estimate for the vertex position $\vec{x}_\mathrm{v}$ is obtained by minimization of the scattering angles, in the first tracking layer of each particle track [2][41].

$$\chi^2(\vec{v})_{\text{ vertex}} = \sum_{i=1}^{\text{tracks = 3}} \frac{\Phi_{\mathrm{MS},i}(\vec{v})^2}{\sigma_{\phi,i}^2} + \frac{\Theta_{\mathrm{MS},(\vec{v})^2}}{\sigma_{\theta,i}^2} \tag{5}$$

Vertex fits are performed with all possible combinations of one negative and two positive tracks.

4.2 Track Classification

The tracks in the pixel tracker detector are taken into consideration if they have 4-pixel hits, or if they consist of 6 or 8-pixel hits either recurling back into the central station or into two recurl stations of the detector. The properties of each type are as follow:

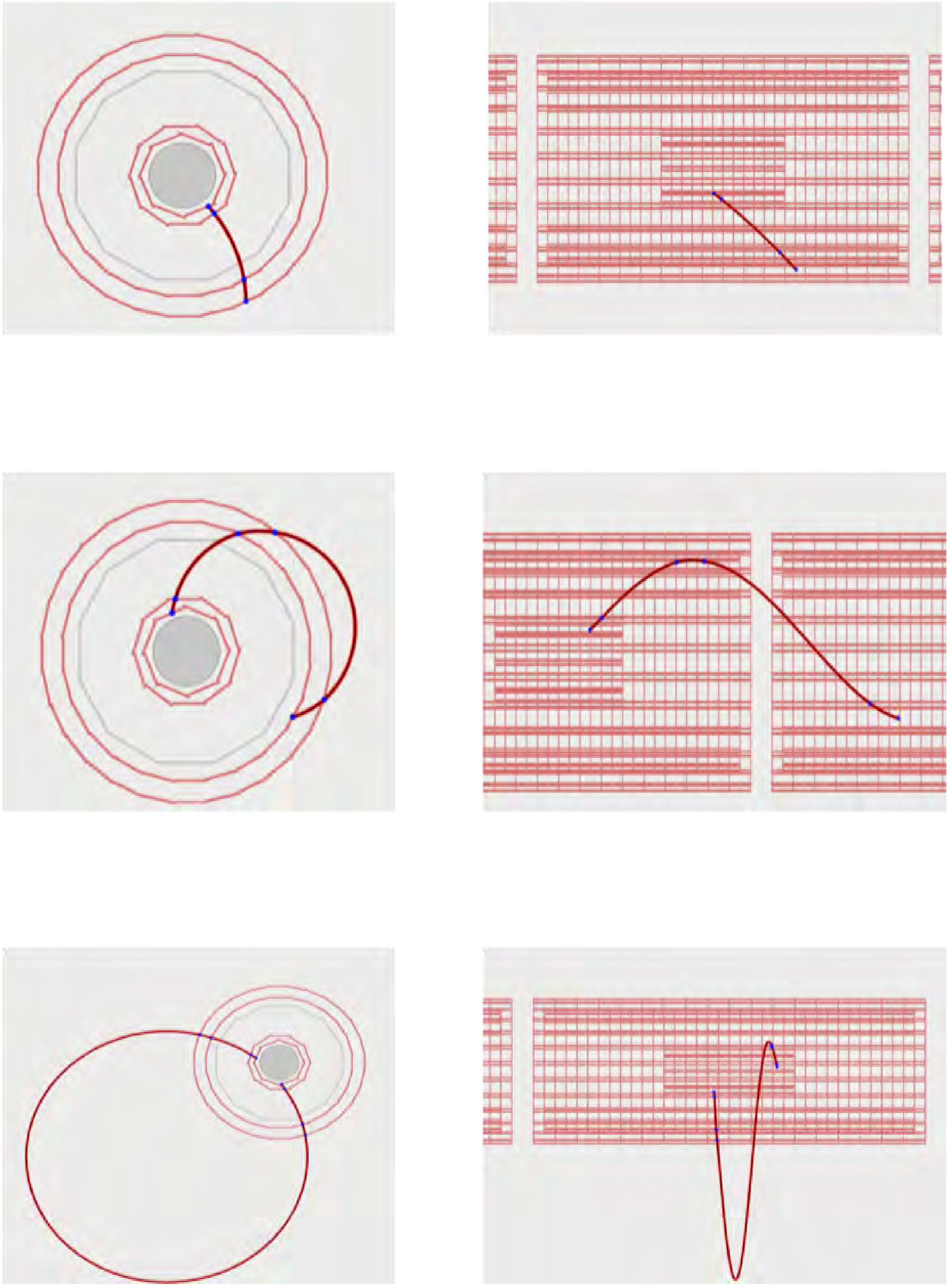

FIGURE 4.2: Track candidate classification by the number of pixel tracking layers, they contain hits into short 4-hit, long 6-hit, and 8-hit track candidates, respectively. A transverse (left) and longitudinal (right) cut through the detector is shown.

Short 4-hit tracks: Short tracks consisting of 4-pixel hits corresponding to an outgoing track passing all inner and outer pixel tracking layers in the central station. They are seeds for long tracks as shown in figure 4.2 (top).

Long 6-hit tracks: Long tracks with 6-pixel hits are tracks that pass 6 pixel layers. The first 4 layers are similar to short tracks and the other 2 layers are the outer layers of the recurl or central stations. These tracks are shown in figure 4.2 (middle).

Long 8-hit tracks: These are tracks with 8-pixel hits (4 layers on the way out, and 4 layers on the way back in to the central detector).

Long tracks with 6 or 8-pixel hits have superior timing and momentum resolution compared to short tracks.

4.3 Simulation of Signal and Background Events

A simulation of the Mu3e detector [1] has been developed to optimize the detector design and study the performance. In the simulation, reconstructed results can be compared with the true variables in order to evaluate the resolution and efficiency. The simulated events are reconstructed using the MS track and vertex fit outlined in section 4.1.

The simulation of the experiment uses the current simulation framework supplied by the Mu3e collaboration based on GEANT4 [4]. GEANT4 is the library used to model scattering and energy loss effects within the materials of the detector. The simulation can be configured according to settings such as frame length, decay mode and other settings to generate signal or background events. The resultant trajectories of the decay particles are propagated through the detector, and the hits in the different layers are recorded.

Generated event samples used in this thesis have been simulated for the signal and for backgrounds events using the Liverpool HEP computing facility and version v4.5 of the Mu3e collaboration simulation software [1] . Analysis of the data is done using the ROOT data analysis framework [17]. The mu3e software also provides an event display to visualise what is happening in simulated events. For example, figure 4.2 shows event display for single positron tracks.

4.4 Alignment Software

Alignment software is essential to study the effects of detector misalignment, and to correct such misalignments. Therefore, the Mu3e experiment has developed alignment software. The Mu3e's alignment software MU3EPIXEL [9] is based on the track fitting library WATSON [28].

In order to study the alignment algorithm, detector misalignments can be introduced using the misalignment tool MU3EMISAL [9]. This tool provides various misalignment modes for the pixel and timing detectors. More information on this procedure is presented in Chapter 7.

5 The Search for $\mu^+ \to e^-e^+e^+$ with the Mu3e Experiment

In this chapter, a description of the event selection and the characteristics of $\mu^+ \to e^-e^+e^+$ events are presented. Search for signal muon decays is given in section 5.1, and tracks selection cuts with a way of choosing the best cuts are presented in section 5.2. The event selection is studied in section 5.3, and the resultant detector acceptance and efficiency are presented in section 5.4. Finally, a description of the selected signal event kinematics is given in section 5.5. Finally, the predicted background and sensitivity for the (phase-I) Mu3e experiment is given in section 5.5.

5.1 Search for $\mu^+ \to e^-e^+e^+$ Events

In order to reach a sensitivity to a branching ratio of 1 in 10^{16} muon decays, high background suppression is required. The dominant background events, internal conversions and combinatorial backgrounds are discussed in section 3.1. Simulation studies will explore combinatorial backgrounds, which result from the decay particles of multiple muon decay modes that combine into signal-like vertex. We also consider the irreducible background resulting from muon internal conversion decays.

With an expected rate of 10^8 muon decays per second during phase I, yielding a large number of tracks and vertices, signal identification and background suppression will be a monumental challenge. Owing to the special kinematics of the $\mu^+ \to e^-e^+e^+$ decay, several quantities that describe the interaction can be used to separate the signal decay from the ever-present background, whilst also suppressing the combinatorial background present in the experiment. Quantities such as the summed particle track momentum can be used to distinguish a signal decays from the backgrounds.

The following sections will describe the particular properties that are used in the frame selection process. A pre-selection for candidate triplets is discussed in section 5.5.1. Sections 5.2.1 and 5.2.2 describe the cut optimisation based on tracking efficiency × purity and resultant optimised track selection respectively. Section 5.1.4 describes the criteria for selecting frames with 3 tracks, and finally, the vertex selection cuts are given in section 5.1.5. Signal and background decays are generated using the latest build v4.5 of the Mu3e collaboration simulation software.

5.2 The Track Selection Cuts

The standard track reconstruction for the Mu3e experiment is based on triplets of hits. For 3 consecutive layers and n hits per layer, the number of possible triplets to be fitted scales as n^3. The number of hits per layer in the central tracker, for a single positron track, is shown in figure 5.1. The length of the time window or frame length used for simulation and reconstruction is defined to be 64 ns. It is determined from the time resolution of the pixel sensors with pixel size $80{\times}80\ \mu\text{m}^2$ which was measured to be $\approx$ 14 ns.

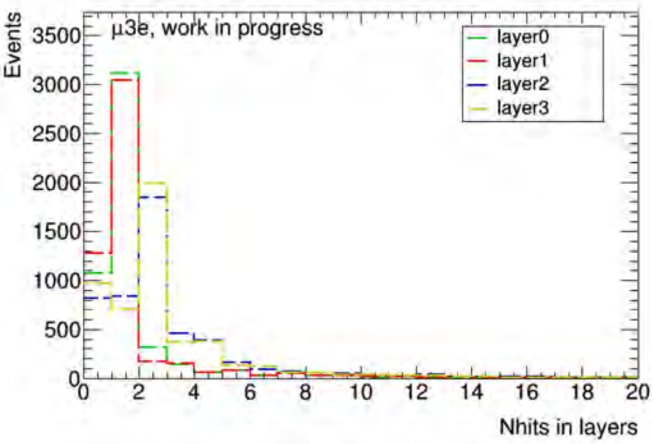

FIGURE 5.1: Number of hits in the 4 layers of the central tracker for a single positron track.

A pre-selection of hits for the triplets is required because processing all combinations of hits would take too long. Pre-selection cuts are based on geometrical variables such as Z, ϕ angles and transverse radius between each three-pixel layer as shown in figure 5.2.

The criteria are as follows: The first selection criterion is on the difference in the z-coordinate of hits between layers one and two ($|z_{01}| = |z_0 - z_1|$). The alignment of hits in layers one and two, and two and three respectively ($\delta\lambda$=$|z_{12}/r_{12} - z_{01}/r_{01}|$) can be calculated because of the large distance between layers two and three, while a fourth hit in the second triplet is optimized as ($|z_{23}|$ = $|z_2 - z_3|$). The second criterion is the difference of angles in the plane transverse to the beam direction, ϕ, between subsequent layers. A third selection criterion is the radius of curvature of the track R_t based on an initial momentum of the particle. Combining Lorentz and centripetal force leads to a relation between the momentum P and transverse radius R_t of a helix track:

$$P[MeV] = 0.3 \times R_t[mm] \times B[T] \tag{1}$$

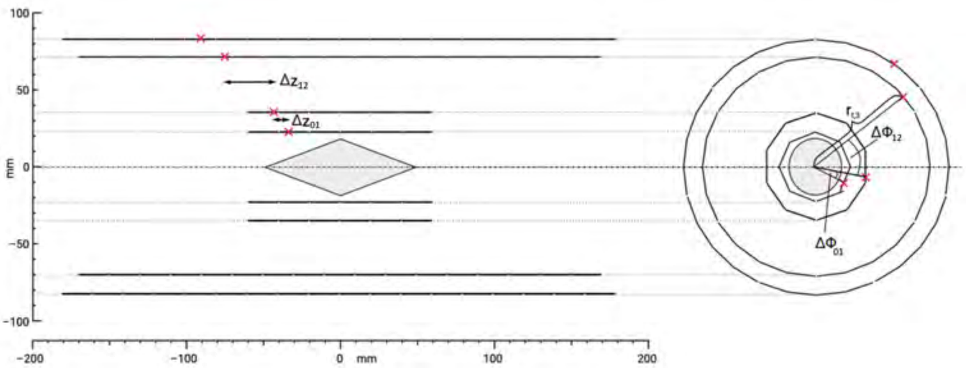

FIGURE 5.2: Illustration of the geometric variables used for the selection of 3-hit combinations for a single triplet.

Since a circle can be placed through any three points, this is done with the three hits using only the xy-coordinates spanning the plane transverse to z-direction to obtain the transverse radius R_t [27] [11]:

$$R_t = \frac{d_{12}d_{23}d_{31}}{\sqrt{-d_{12}^4 - d_{23}^4 - d_{31}^4 + 2d_{12}^2d_{23}^2 + 2d_{23}^2d_{31}^2 + 2d_{31}^2d_{12}^2}} \tag{2}$$

where the d_{ij} is defined as a relative distance between each two-pixel layer. Figure 5.3 shows a circle defined by three points in which the radius R_t is defined by the three distances between the points. After producing every possible triplet in the central station, the assumption is made that the track is travelling from the inside of the detector in an outwards direction. The 3 hits on the triplet are numbered accordingly as shown in figure 4.1 (Chapter 4). A cut is then placed to ensure that only triplets with a curvature such that the track intercepts the outer most layer of the pixel detector. This cut is [-1.5, 1.5] rad on the λ angle.

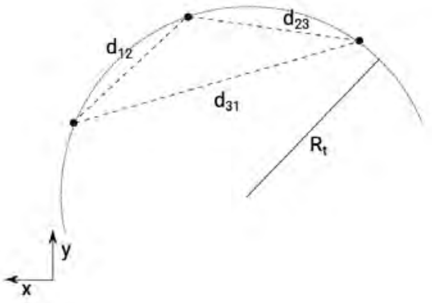

FIGURE 5.3: Circle defined by three points in which the radius R_t is defined by the three distances between the points.

Figures 5.4, 5.5 and 5.6 show the distributions in Z, ϕ and the transverse radius distribution between 4 layers in the central station of the detector for signal muon decay short tracks. In figure 5.5 B, the reason for the offset in $\delta\lambda_{12}$ is due to the large relative distance between layer 1 and 2.

For long tracks, either with 6 or 8-pixel hits the corresponding distributions are shown in the appendix B.8 and B.9. Table 5.1 summarises the maximized pre-selection geometric cut values chosen for each variable for short and long tracks.

5.2.1 A Way of Choosing the Best Cut

Tracking efficiency and purity: Once the triplet selection tracks have been fitted as described in Chapter 4, A study is conducted on the efficiency and purity of track reconstruction parameters in order to optimise the track selection criteria. For example, the efficiency of the χ^2 selection can be checked as follows (where χ^2 of a track describes the quality of a track fit):

$$\varepsilon\left(\chi^2_{\mathrm{max}}\right) = \frac{T_{\mathrm{cut}}\left(\chi^2_{\mathrm{max}}\right)}{T_{\mathrm{total}}}, \quad 0 \leq \varepsilon \leq 1 \tag{3}$$

where T_{total} is the number of all true tracks that are matched with reconstructed MC tracks, and T_{cut} is the number of true tracks after eliminating tracks with $\chi^2 > \chi^2_{\mathrm{max}}$. A true reconstructed track is a reconstructed track that matches the generated hits produced by the truth particle propagation by checking hit id, track id and correct direction of rotation. Track ID is an identifier used to associate tracks with MC information from the simulated particle. The matching criteria between reconstructed and MC tracks, they must reconstruct from the first turn with a correct hit along with the same track id as MC tracks. Figure B.6 in the appendix shows the corresponding hit id along with the same track id for four layers in the central station of the detector in which a positive hit id indicates that the track is outgoing and the negative hit id is for the in-going track. A fake track is defined as the track that does not match the truth track properties, more discussion on the cuts to reject fake tracks can be found in the section 5.2.2.

In addition track purity must be considered in the cut optimization. The purity is defined as:

$$P\left(\chi^2_{\text{max}}\right) = \frac{T_{\text{cut}}\left(\chi^2_{\text{max}}\right)}{T_{\text{cut}}\left(\chi^2_{\text{max}}\right) + F_{\text{cut}}\left(\chi^2_{\text{max}}\right)}, \quad 0 \leq P \leq 1 \tag{4}$$

A related variable is the fake tracks rejection:

$$R\left(\chi^2_{\text{max}}\right) = \frac{F_{\text{total}} - F_{\text{cut}}\left(\chi^2_{\text{max}}\right)}{F_{\text{total}}}, \quad 0 \leq R \leq 1 \tag{5}$$

where F_{total} and F_{cut} are the number of fake tracks before and after cuts, respectively.

5.2.2 Optimised Track Selection Cuts for Fake Track Rejection

There are a few spatial variables that can be used to help separate correctly reconstructed tracks of signal muon decays from fake tracks during the track reconstruction. The χ^2 of the track fit, the dip angle λ_{01}, the intersection of the track with the target region z_0, the reconstructed curvature radius, and timing cuts. Figures 5.7, 5.8, 5.9, 5.10 and 5.11 show the distribution of λ_{01}, χ^2 and Z_0 of the track fit as well as the efficiency ϵ, purity p and their product $(\epsilon \cdot p)$ of the signal muon decays as a function of the applied cut value, for different categories of tracks.

Table 5.2 lists the optimized selection cuts for short and long tracks in the nominal detector based of the high product between the purity and efficiency as was given for each reconstructed variables in figures from 5.6 to 5.11. Tables 5.3 and 5.4 summarize the efficiency and purity for different categories of positron tracks before and after applying

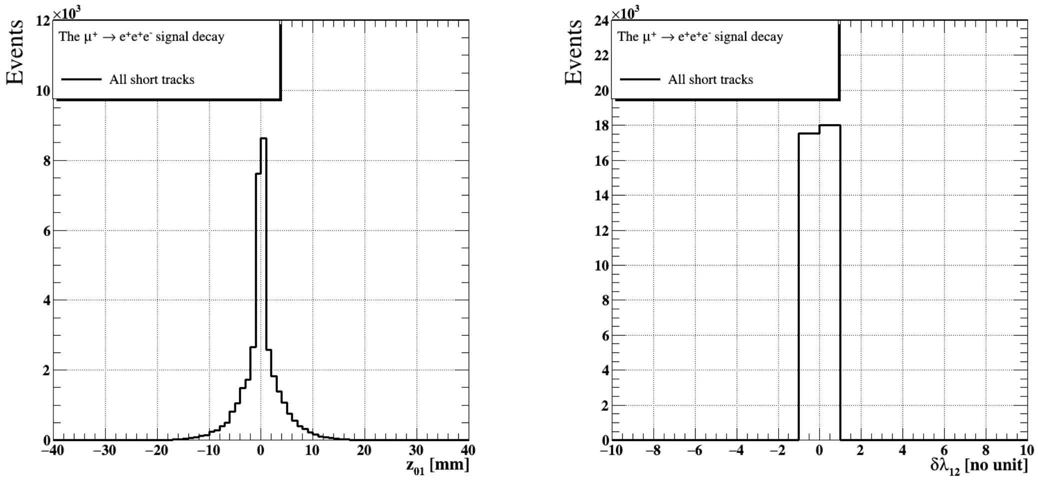

(A) Z distribution between layers 0 and 1 in the central station of the detector.

(B) $\delta\lambda_{12}$ distribution between layers 1 and 2 in the central station of the detector.

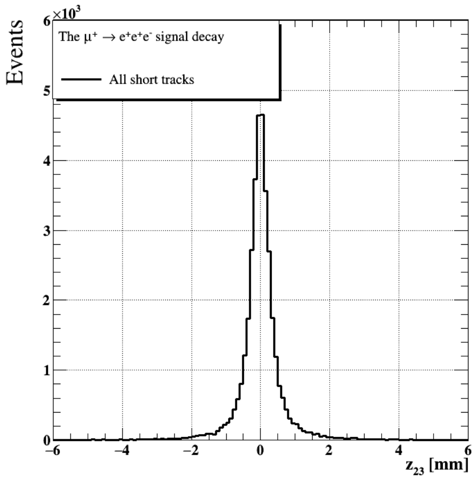

(C) Z distribution between layers 2 and 3 in the central station of the detector.

FIGURE 5.4: Z distribution between 4 layers in the central station of the detector for signal muon decays for short tracks.

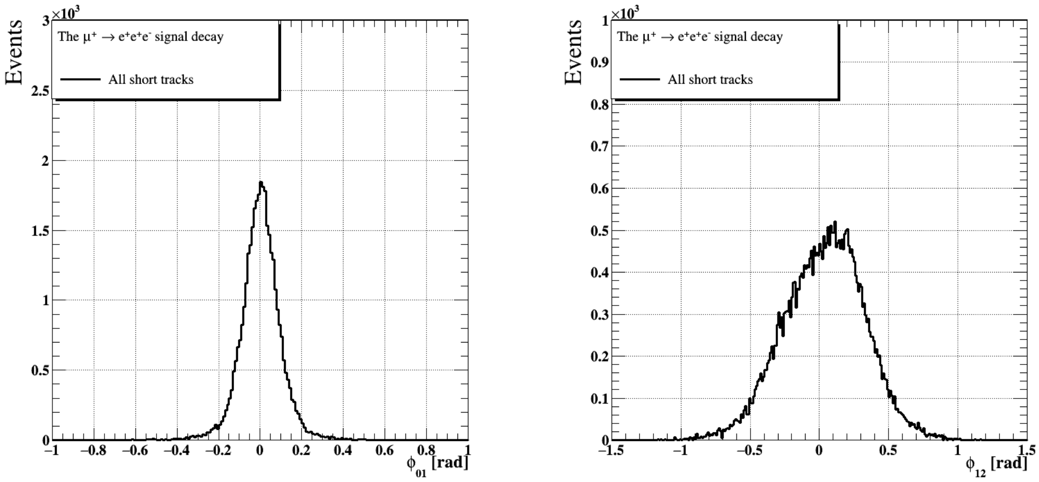

(A) ϕ distribution between layers 0 and 1 in the central station of the detector.

(B) ϕ distribution between layers 1 and 2 in the central station of the detector.

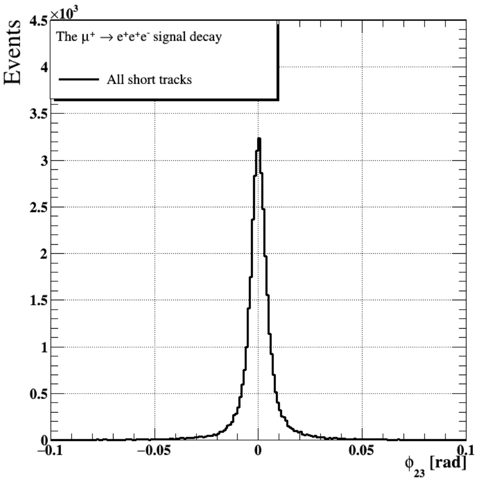

(C) ϕ distribution between layers 2 and 3 in the central station of the detector.

FIGURE 5.5: ϕ distribution between 4 layers in the central station of the detector for signal muon decays for short tracks.

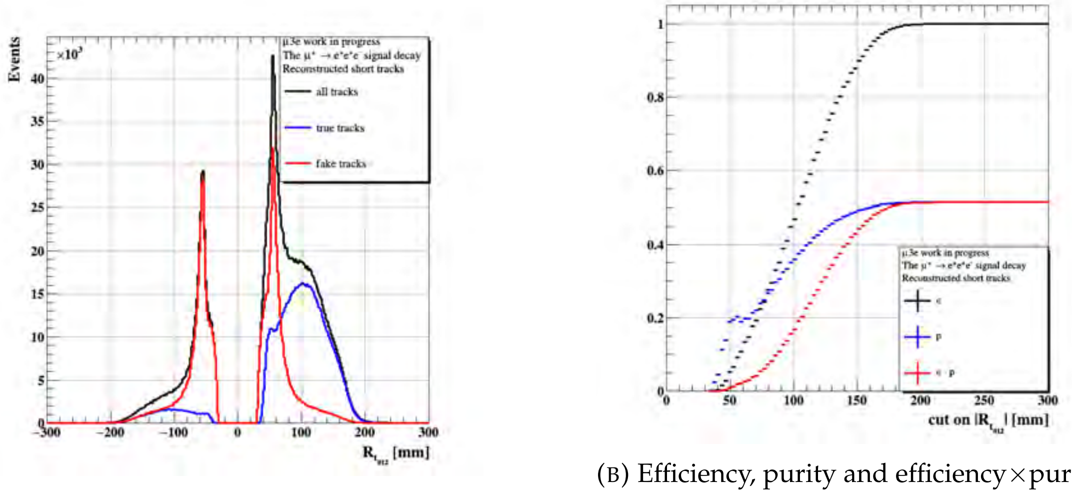

(A) Distribution of the transverse radius based on 3 hits in layers 0, 1 and 2.

(B) Efficiency, purity and efficiency × purity as a function of the cut applied on the transverse radius going through three hits in layers 0, 1 and 2.

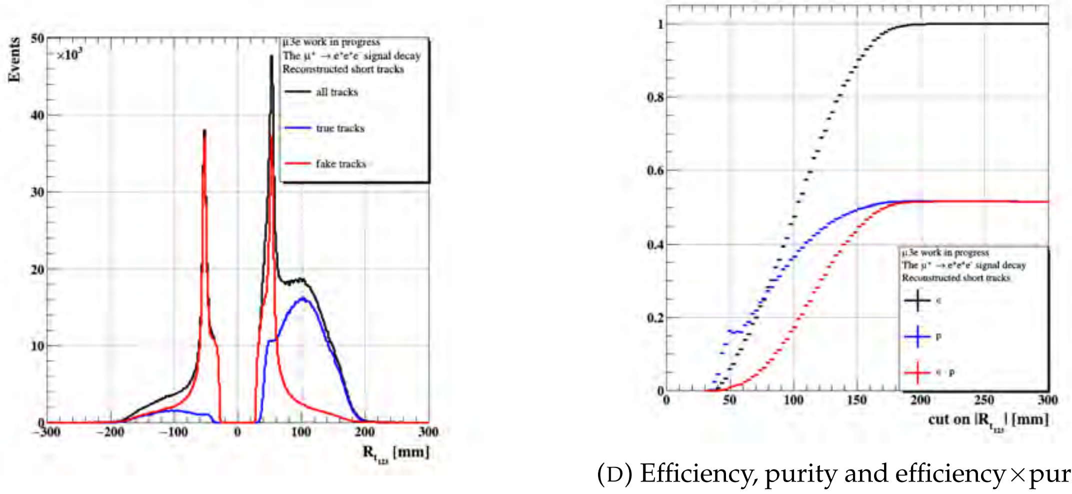

(C) Distribution of the transverse radius based on 3 hits in layers 1, 2 and 3.

(D) Efficiency, purity and efficiency × purity as a function of the cut applied on the transverse radius going through three hits in layers 1, 2 and 3.

FIGURE 5.6: The transverse radius of a circle going through three points in layers 0, 1 and 2 or 1, 2 and 3.

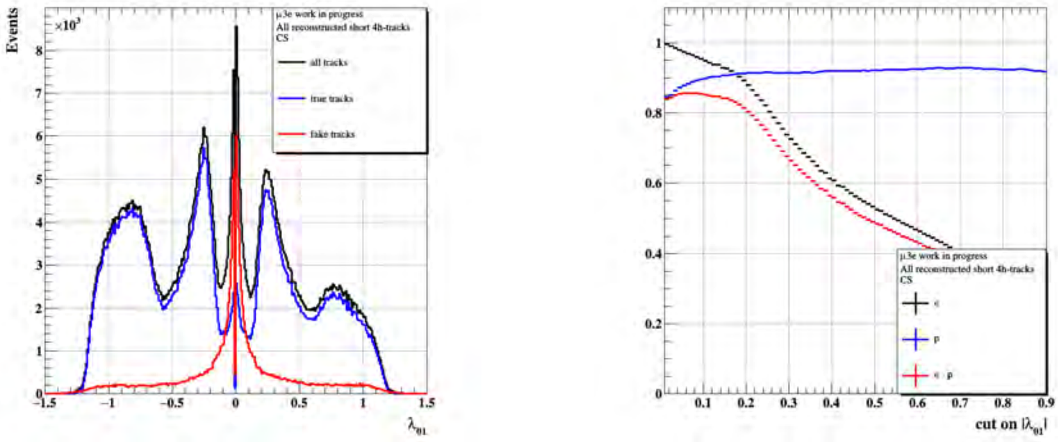

(A) Distribution of λ_{01} for short tracks with 4-pixel hits.

(B) Efficiency and purity as a function of the applied cut on λ_{01} using short tracks.

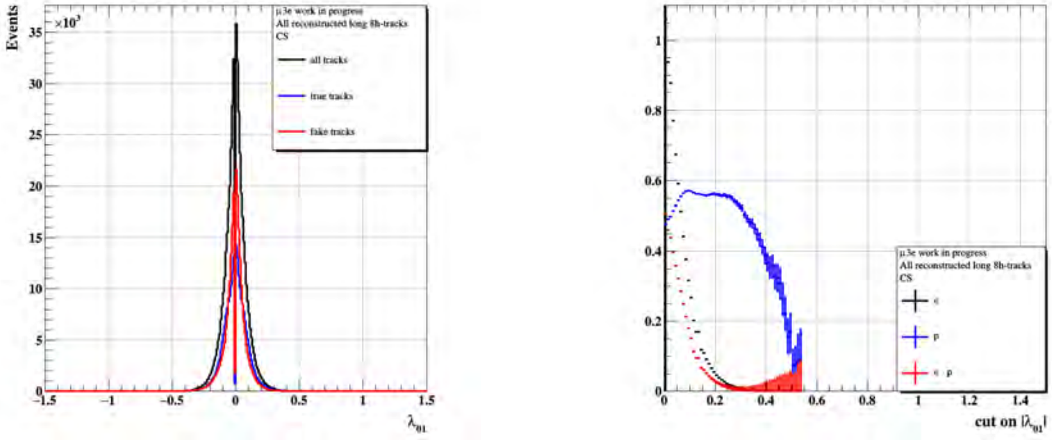

(C) Distribution of λ_{01} for long tracks with 8-pixel hits.

(D) Efficiency and purity as a function of the applied cut on λ_{01} using long tracks.

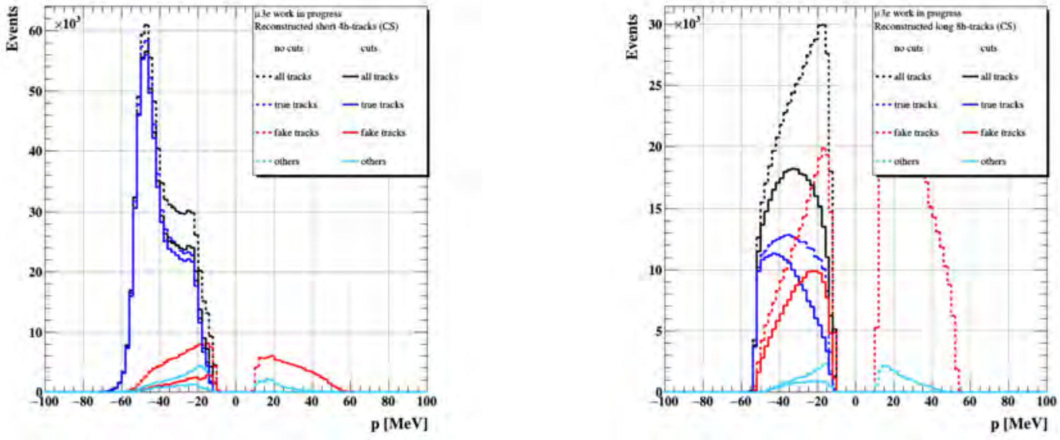

(E) Reconstructed momentum of short tracks.

(F) Reconstructed momentum of long tracks.

FIGURE 5.7: On the left-hand side (A and C), the λ_{01} distribution is shown for short and long tracks, and on the right-hand side (B and D) the resulting efficiency, purity, and the product between them as a function of the applied cut. The sample contains positrons from muon decays. Figures E and F show the distribution of the reconstructed momentum of positron candidates before and after applying cuts.

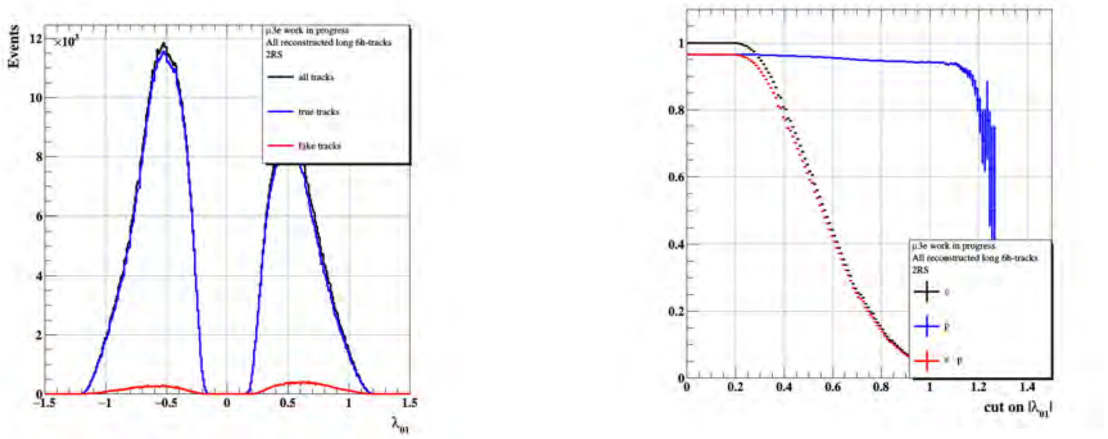

(A) Distribution of λ_{01} for long tracks with 6-pixel hits that are recurled into two recurls stations.

(B) Efficiency and purity as a function of the applied cut on λ_{01} using long tracks with 6-pixel hits that are recurled into two recurls stations.

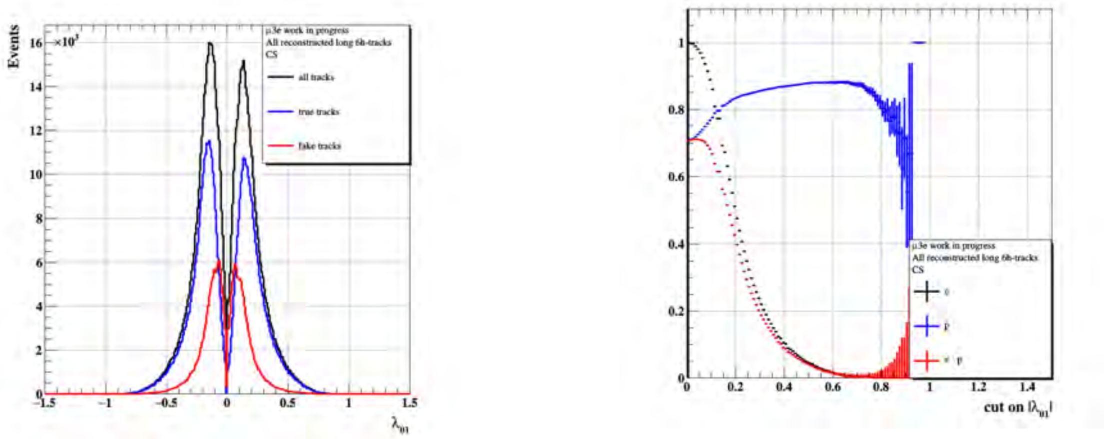

(C) Distribution of λ_{01} for long tracks with 6-pixel hits that are extrapolated back into the central station.

(D) Efficiency and purity as a function of the applied cut on λ_{01} using long tracks with 6-pixel hits that are extrapolated back into the central station.

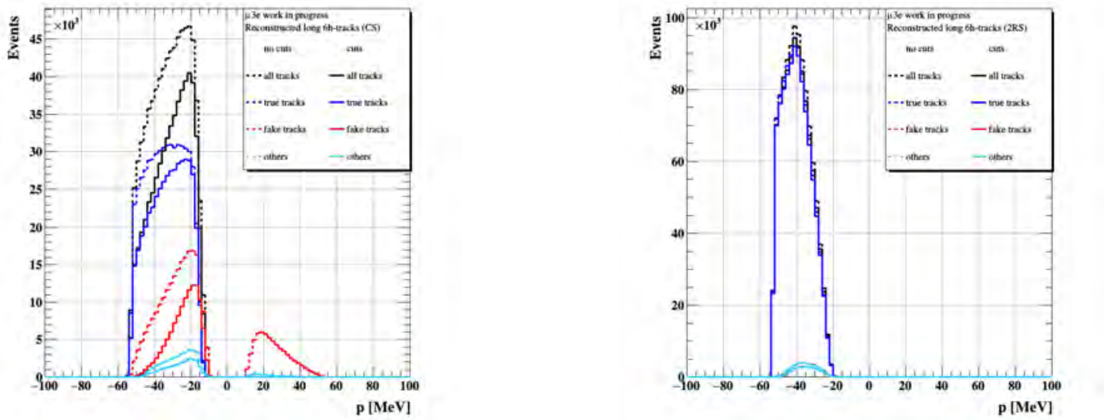

(E) Reconstructed momentum of long tracks with 6-pixel hits in the central station.

(F) Reconstructed momentum of long tracks with 6-pixel hits in the recurl stations.

FIGURE 5.8: On the left-hand side (A and C), the λ_{01} distribution for 6 hits long tracks in the central and recurl stations is shown, and on the right-hand side (B and D) the resulting efficiency, purity, and the product between them as a function of the applied cut. The sample contains positrons from muon decays. Figures E and F show the distribution of the reconstructed momentum of positron candidates before and after applying cuts.

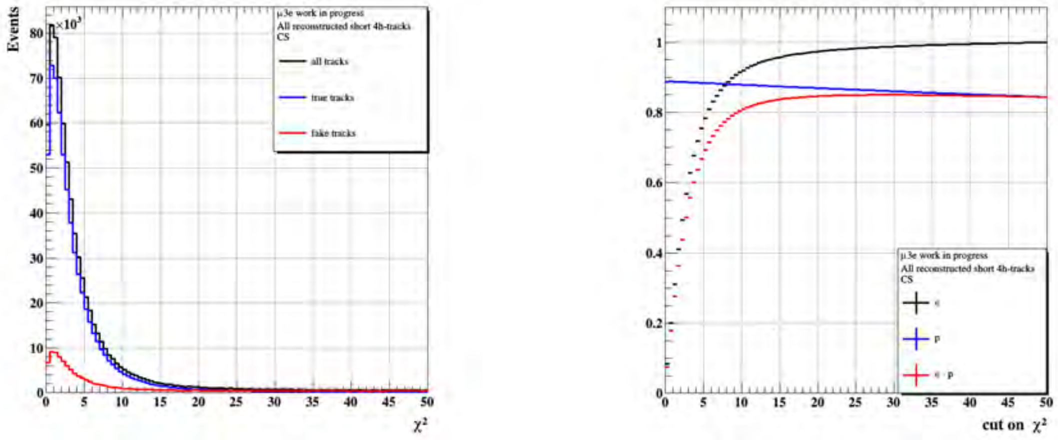

(A) Distribution of χ^2 for short tracks with 4-pixel hits.

(B) Efficiency and purity as a function of the applied cut on χ^2 using short tracks.

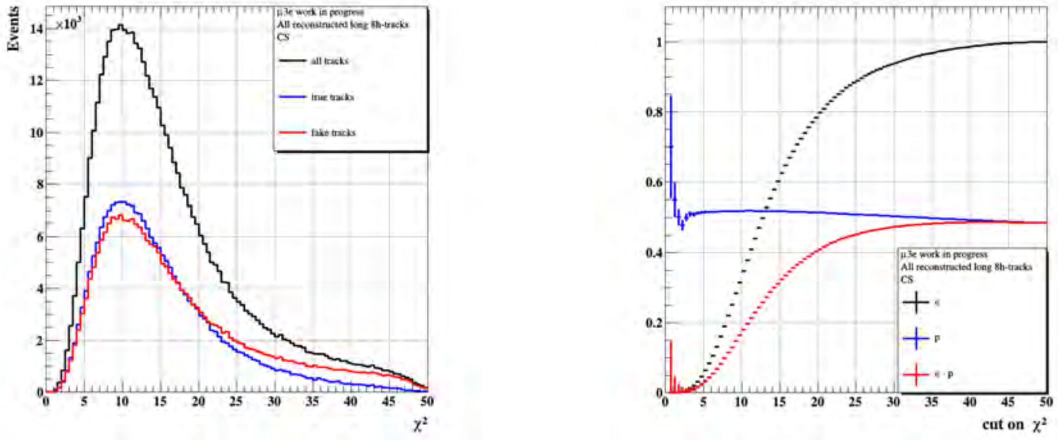

(C) Distribution of χ^2 for long tracks with 8-pixel hits.

(D) Efficiency and purity as a function of the applied cut on χ^2 using long tracks.

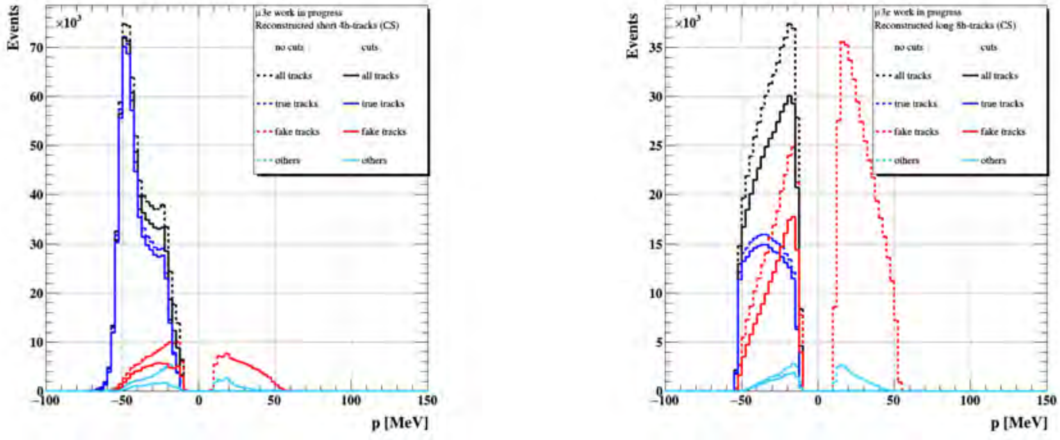

(E) Reconstructed momentum of short tracks.

(F) Reconstructed momentum of long tracks.

FIGURE 5.9: On the left-hand side (A and C), the χ^2 distribution is shown for short and long tracks, and on the right-hand side (B and D) the resulting efficiency, purity, and the product between them as a function of the applied cut. The sample contains positrons from muon decays. Figures E and F show the distribution of the reconstructed momentum of positron candidates before and after applying cuts.

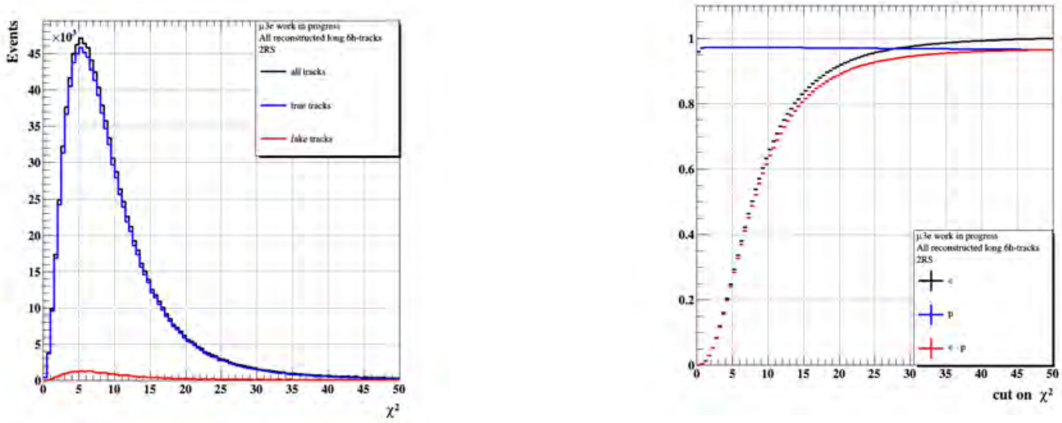

(A) Distribution of χ^2 for long tracks with 6-pixel hits that are recurled into two recurls stations.

(B) Efficiency and purity as a function of the applied cut on χ^2 using long tracks with 6-pixel hits that are recurled into two recurls stations.

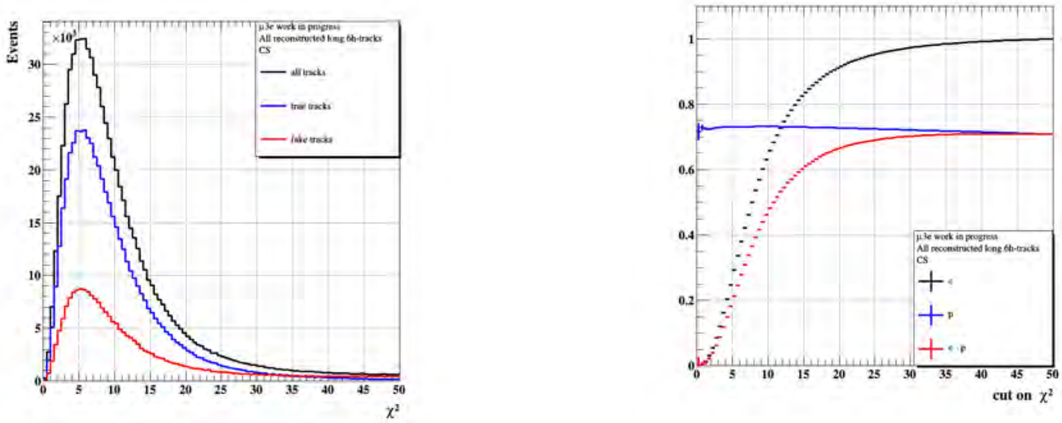

(C) Distribution of χ^2 for long tracks with 6-pixel hits that are extrapolated back into the central station.

(D) Efficiency and purity as a function of the applied cut on χ^2 using long tracks that are extrapolated back into the central station.

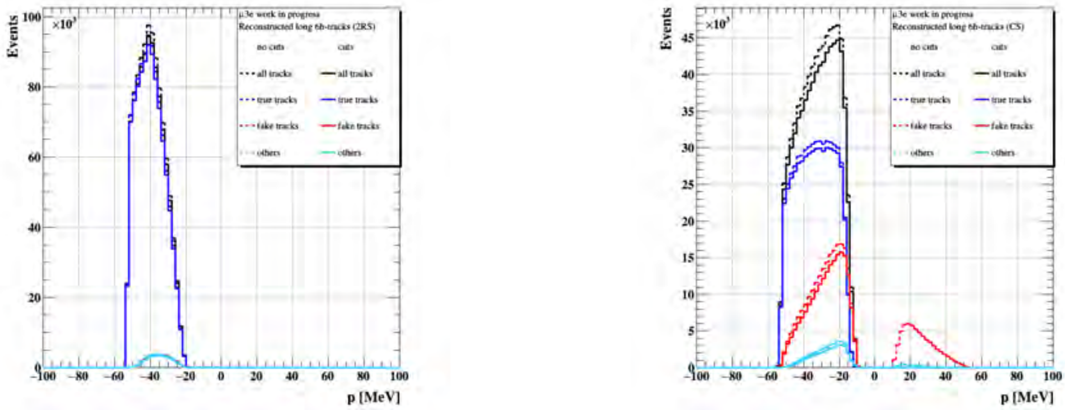

(E) Reconstructed momentum of long tracks with 6-pixel hits in the central station.

(F) Reconstructed momentum of long tracks with 6-pixel hits in the recurl stations.

FIGURE 5.10: On the left-hand side (A and C), the χ^2 distribution for 6 hits long tracks in the central and recurl stations is shown, and on the right-hand side (B and D) the resulting efficiency, purity, and the product between them as a function of the applied cut on χ^2. The sample contains positrons from muon decays. Figures E and F show the distribution of the reconstructed momentum of positron candidates before and after applying cuts.

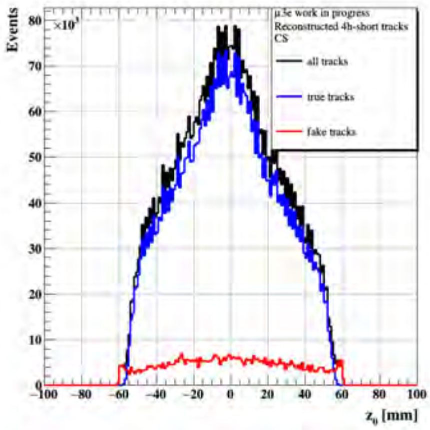

(A) Distribution of Z_0 of the track fit for 4-hit short tracks for the signal muon decays.

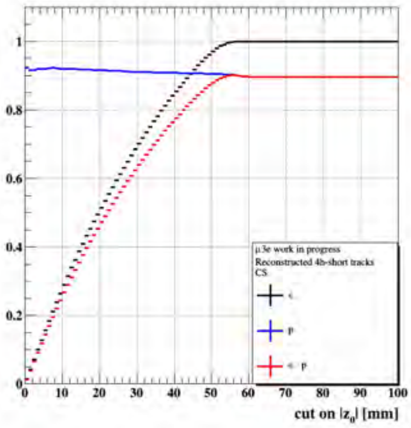

(B) Efficiency, purity and efficiency·purity as a function of the applied cut on the Z_0 of the track fit for 4-hit short tracks for the signal muon decays.

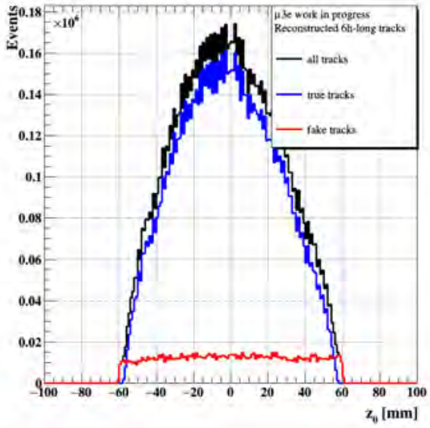

(C) Distribution of Z_0 of the track fit for 6-hit long tracks for the signal muon decays.

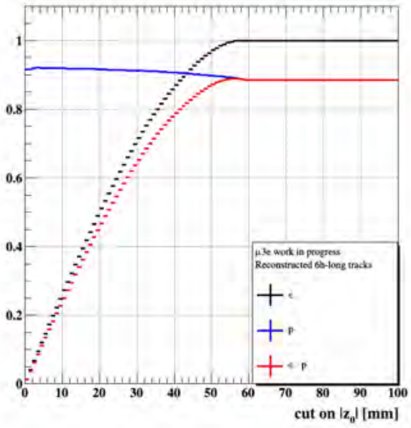

(D) Efficiency, purity and efficiency·purity as a function of the applied cut on the Z_0 of the track fit for 6-hit long tracks for the signal muon decays.

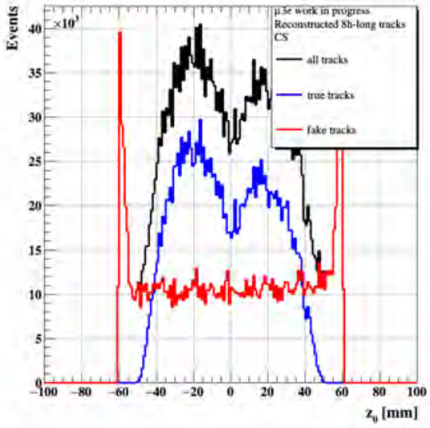

(E) Distribution of Z_0 of the track fit for 8-hit long tracks for the signal muon decays.

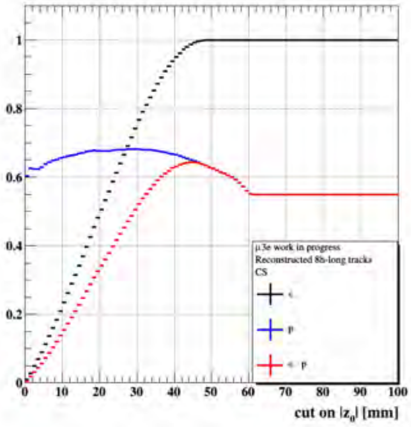

(F) Efficiency, purity and efficiency·purity as a function of the applied cut on the Z_0 of the track fit for 8-hit long tracks for the signal muon decays.

FIGURE 5.11: Z_0 of the track fit for muon decays.

variable	cut value
Short tracks (4-hits)	
$\lvert z_{10} \rvert$	< 30 mm
$\delta\lambda_{12}$	< 1 no unit
$\lvert z_{32} \rvert$	< 5 mm
$\lvert \phi_{01} \rvert$	< 0.8 rad
$\lvert \phi_{12} \rvert$	< 0.8 rad
$\lvert \phi_{23} \rvert$	< 0.05 rad
$\lvert R_t \rvert$	30 mm $< R_t <$ 250 mm
long tracks (6-hits)	
$\lvert z_{34} \rvert$	< 100 mm
$\lvert z_{45} \rvert$	< 3 mm
$\lvert \phi_{34} \rvert$	< 0.35 rad
$\lvert \phi_{45} \rvert$	< 0.035 rad
long tracks (8-hits)	
$\lvert z_{3oi} \rvert$	< 100 mm
$\lvert z_{0oi} \rvert$	< 10 mm
$\lvert \phi_{3oi} \rvert$	< 0.35 rad
$\lvert \phi_{0oi} \rvert$	< 0.2 rad

TABLE 5.1: Summary of the chosen pre-selection cuts for short tracks and for long 6-hit and 8-hit tracks. The pre-selection cuts for the 8-hit tracks are applied to the measurements on layer 3 (z_{30i} and ϕ_{3oi}) and layer 0 (z_{0oi} and ϕ_{0oi}) of the track in the incoming direction or return path of the long track.

Z_0 (mm): 4- ; 6-; 8- hits	< 50
λ_{01} (rad): 4- ; 6-; 8- hits	> 0.1
$\chi^2 : 4-;6-;8-hits$	15, 30, 30

TABLE 5.2: Optimized selection cuts for short and long tracks in the nominal detector. In these cuts, the purity is improved with suppression of the most fake tracks; they are chosen based on the highest value for efficiency× purity.

these cuts. Figure 5.12 shows the reconstructed momentum for tracks from signal muon decays before and after applying all cuts in table 5.2 for short and long tracks.

In addition to the spatial tracking selection cuts, timing cuts can be used to remove incorrectly reconstructed 6-hit and 8-hit tracks, where the wrong direction of propagation could be assigned to a track. Long 8 hit or central 6 hit track will be detected by the fibre layer twice, and will thus have two timing measurements. Plotting a 2-dimensional histogram of the difference in time between these measurements and the path length of the track can show how incorrectly reconstructed tracks can be removed using these measurements. This is shown in figures 5.13A and 5.14A, for 8-hit and 6-hit (central station) respectively, where the left 'branch' of the histogram outlines the density of tracks with the wrong direction and hence the wrong charge assigned. This is mostly an important effect for the long 8-hit tracks. Figure 5.15A shows the same figure for 6-hit tracks that

Reconstruction		No cuts	Cuts applied
Short 4-hit tracks	ϵ	1	0.948(1)
	p	0.754(6)	0.947(3)
	$\epsilon \cdot p$	0.754(6)	0.898(3)
Long 8-hit tracks	ϵ	1	0.757(1)
	p	0.266(5)	0.549(2)
	$\epsilon \cdot p$	0.266(5)	0.416(2)
Long 6-hit tracks (CS)	ϵ	1	0.844(1)
	p	0.653(3)	0.794(1)
	$\epsilon \cdot p$	0.653(3)	0.670(1)
Long 6-hit tracks (RS)	ϵ	1	0.974(1)
	p	0.965(3)	0.974(3)
	$\epsilon \cdot p$	0.965(3)	0.949(3)

TABLE 5.3: Efficiency ϵ, purity p and $\epsilon \cdot p$ before and after applying cuts for positrons from muon decays.

Reconstruction		No cuts	Cuts applied
Long 4-hit tracks	ϵ	1	0.956(1)
	p	0.754(3)	0.892(2)
	$\epsilon \cdot p$	0.754(3)	0.853(2)
Long 8-hit tracks	ϵ	1	0.936(1)
	p	0.266(3)	0.557(3)
	$\epsilon \cdot p$	0.266(3)	0.521(3)
Long 6-hit tracks (CS)	ϵ	1	0.972(1)
	p	0.653(3)	0.721(2)
	$\epsilon \cdot p$	0.653(3)	0.701(2)
Long 6-hit tracks (RS)	ϵ	1	0.974(1)
	p	0.965(2)	0.969(1)
	$\epsilon \cdot p$	0.965(2)	0.944(1)

TABLE 5.4: Efficiency ϵ, purity p and $\epsilon \cdot p$ before and after applying cuts for positrons from muon decays with choosing the proper χ^2 and z_0 cut value.

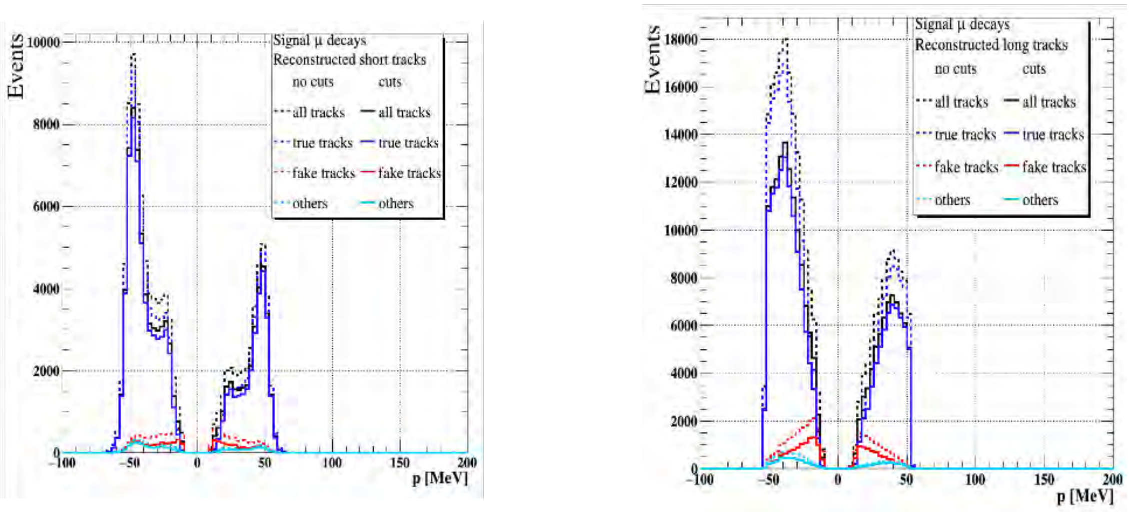

(A) Reconstructed momentum before and after applying the track reconstruction cuts for short tracks.

(B) Reconstructed momentum before and after applying the track reconstruction cuts for long tracks with 6-pixel hits.

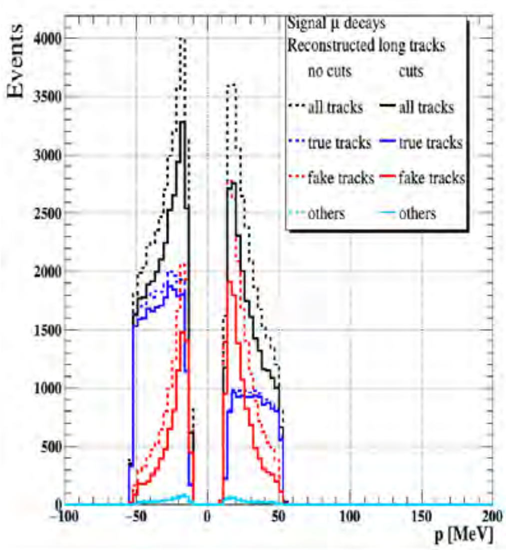

(C) Reconstructed momentum before and after applying the track reconstruction cuts for long tracks with 8-pixel hits.

FIGURE 5.12: Reconstructed momentum for signal muon decays before and after applying the track reconstruction cuts for the nominal detector.

recurl into the recurl station, where no such mis-identification occurs. Figure 5.15 shows the timing information in the two recurl stations of the detector in which the purity is high with fewer fake tracks compared with others.

To check how many tracks with an incorrect charge assignment there are, table 5.5 lists the efficiency ϵ, purity p and $\epsilon \cdot p$ before and after applying timing cuts by cutting on the time difference between two fibre hits or one fibre and one tile hit, requiring this to be greater than 0. This constrained can be applied in this study as the used event sample contains essentially only positively charged (positron) tracks. Finally, table 5.6 lists efficiency ϵ, purity p and $\epsilon \cdot p$ before and after applying spatial and timing cuts together. More information on the sources of fake tracks is presented in appendix B.3.

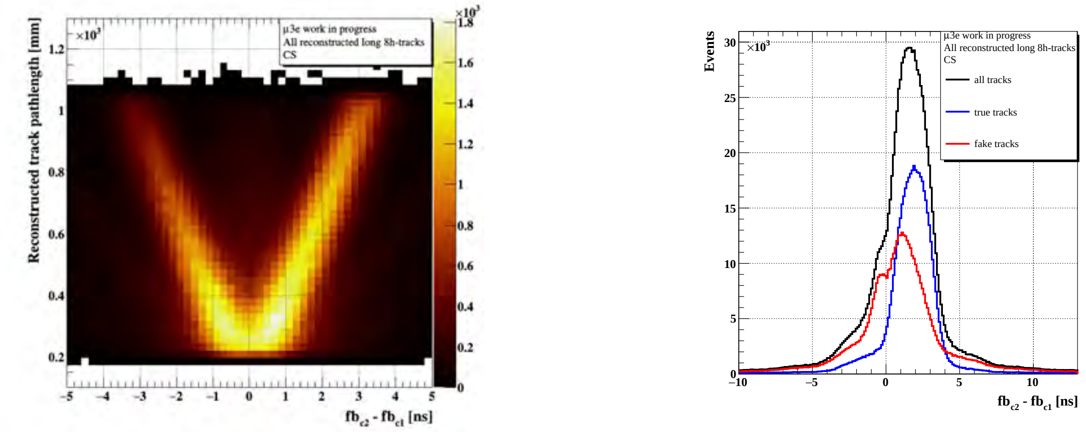

(A) The path length of 8-hit tracks between two fibre hits plotted against the measured time difference.

(B) Distribution of the time difference between two fibre hits of recurling track.

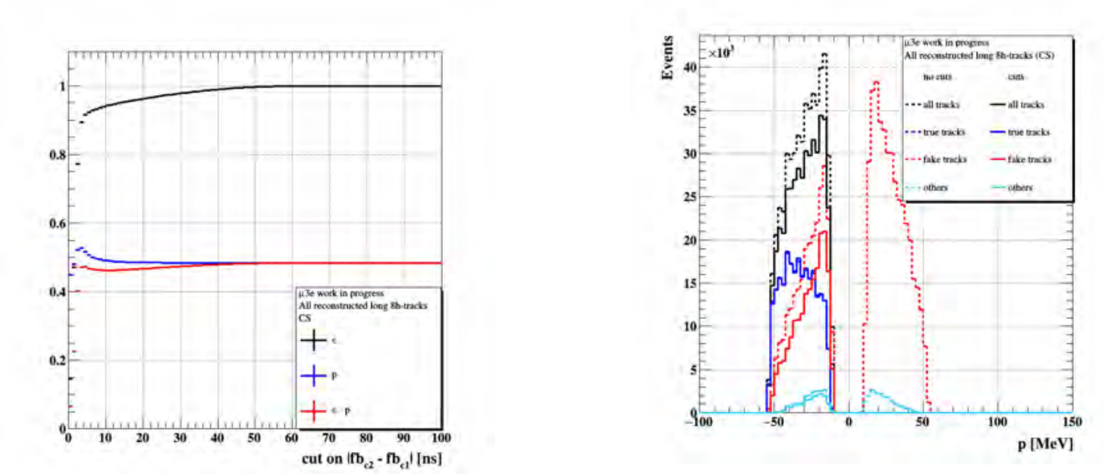

(C) Efficiency and purity as a function of the cut applied on the timing difference for long 8-hit tracks.

(D) Distribution of the reconstructed momentum of positron candidates before and after applying the cut on the time difference.

FIGURE 5.13: Plots relating to the selection cuts on timing for reconstructed as long 8-hit tracks. The sample contains positrons from muon decays.

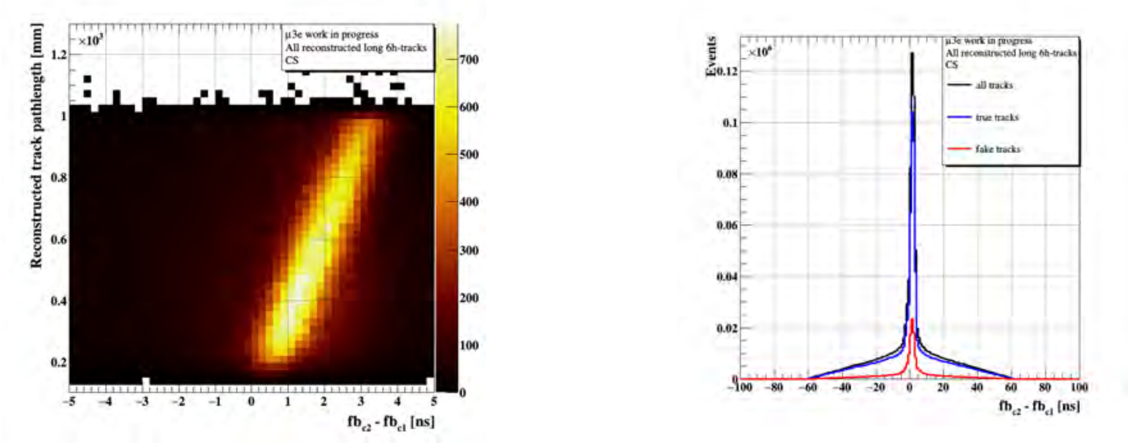

(A) The path length of 8-hit tracks between two fibre hits plotted against the measured time difference.

(B) Distribution of the time difference between two fibre hits of recurling track.

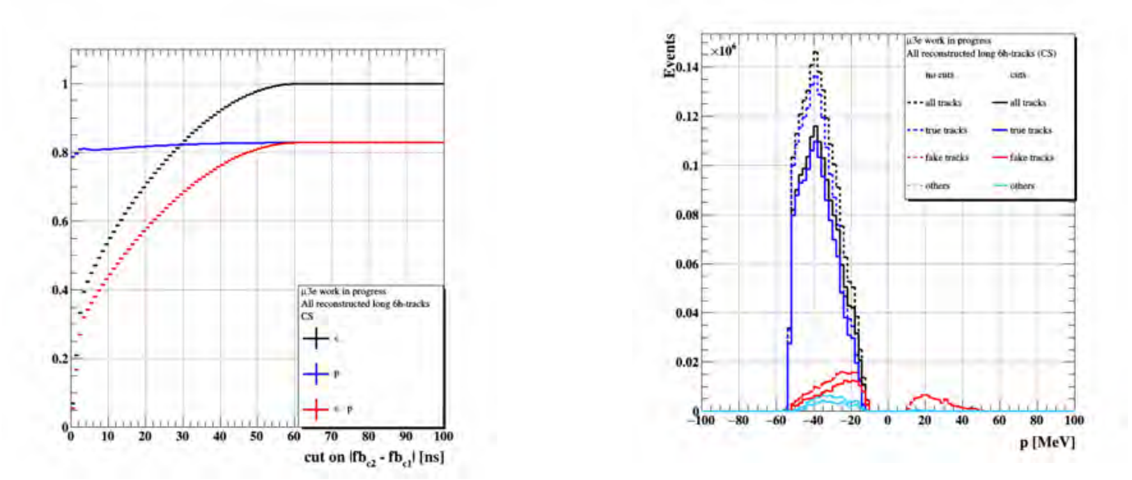

(C) Efficiency and purity as a function of the cut applied on the timing difference for long 6-hit tracks.

(D) Distribution of the reconstructed momentum of positron candidates before and after applying the cut on the time difference.

FIGURE 5.14: Plots relating to the selection cuts on timing for reconstructed as long 6-hit tracks in the central station. The sample contains positrons from muon decays.

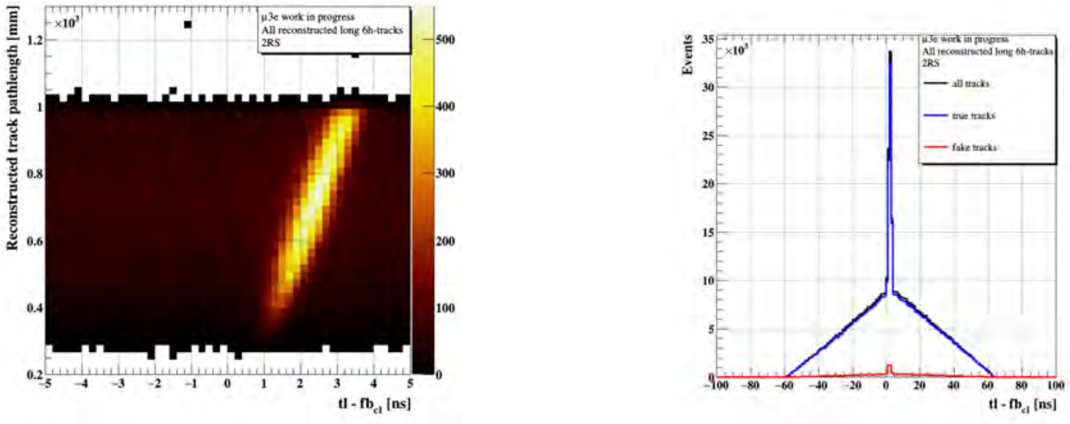

(A) The path length of 6-hit tracks between one fibre hit with one tile hit crossings plotted against the measured time difference.

(B) Distribution of the time difference between one fibre hit with one tile hit of recurling track.

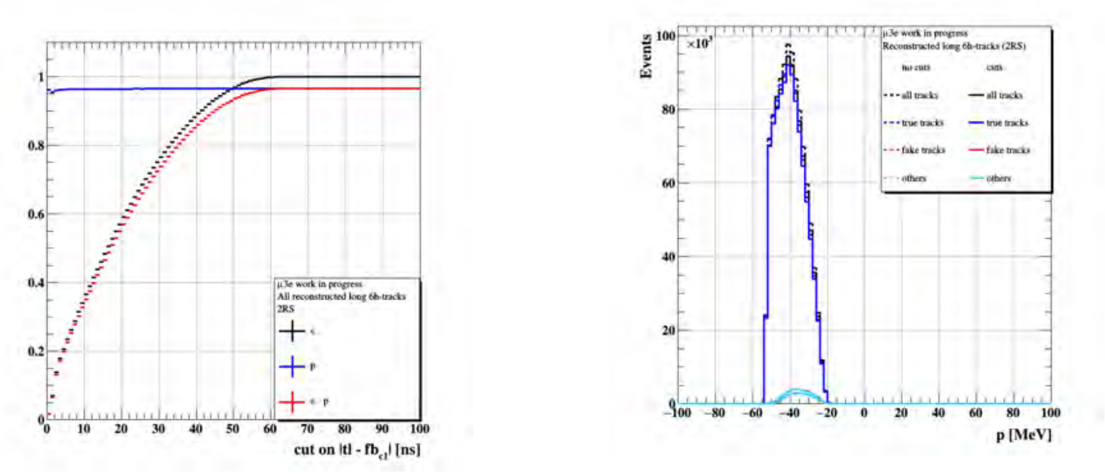

(C) Efficiency and purity as a function of the cut applied on the timing difference for long 6-hit tracks

(D) Distribution of the reconstructed momentum of positron candidates before and after applying the cut on the time difference.

FIGURE 5.15: Plots relating to the selection cuts on timing for reconstructed as long 6-hit tracks in the recurl stations. The sample contains positrons from muon decays.

5.3 Frame Selection Cuts

In order to select the frames[1] that contain two positron tracks and one electron track originating from the same decay, a number of selection cuts are applied to frames that

---

[1] The particle track information is stored in respect to a frame number in the experiment, and so at a particular time, with the first frame's position representing the starting point of the experiment. The vertices of these decays are reconstructed using the information stored within these frames. A true time is measured at the beginning of a experiment when the π^+ beam creates muons for the first time, whereas the propagated times are measured in frames, where one muon decay occurs per frame, with the first frame beginning at the beginning of the experiment and each frame lasting 50 ns

Reconstruction		No cuts	Cuts applied
Long-8 hits tracks	ϵ	1	0.881(8)
	p	0.551(6)	0.788(8)
	$\epsilon \cdot p$	0.561(6)	0.694(8)
Long-6 hits tracks (CS)	ϵ	1	0.793(7)
	p	0.796(5)	0.851(7)
	$\epsilon \cdot p$	0.796(5)	0.675(1)
Long-6 hits tracks (RS)	ϵ	1	0.984(5)
	p	0.967(3)	0.969(4)
	$\epsilon \cdot p$	0.967(3)	0.953(6)

TABLE 5.5: Efficiency ϵ, purity p and $\epsilon \cdot p$ before and after applying a timing cut, $\Delta t > 0$.

Reconstruction		No cuts	Cuts applied
Long-8 hits tracks	ϵ	1	0.88(8)
	p	0.561(6)	0.891(8)
	$\epsilon \cdot p$	0.561(6)	0.785(8)
Long-6 hits tracks (CS)	ϵ	1	0.788(7)
	p	0.796(5)	0.904(7)
	$\epsilon \cdot p$	0.796(5)	0.713(1)
Long-6 hits tracks (RS)	ϵ	1	0.984(5)
	p	0.967(3)	0.987(4)
	$\epsilon \cdot p$	0.967(3)	0.971(6)

TABLE 5.6: Efficiency ϵ, purity p and $\epsilon \cdot p$ before and after applying spatial and a timing cut, $\Delta t > 0$.

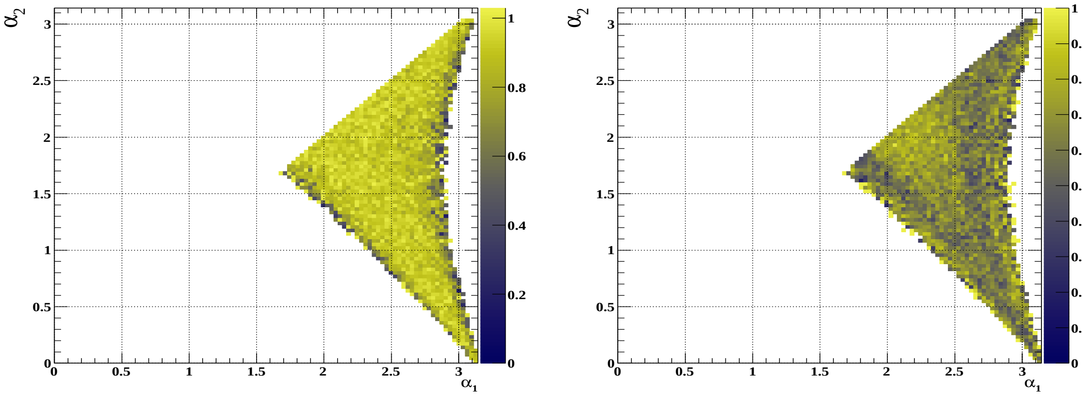

FIGURE 5.16: The efficiency with respect to generated events of opening angles of a positron track with respect to electron track. (α_1) is denoted to an electron track and a positron track for the (α_2). All correctly reconstructed tracks and only long correctly reconstructed tracks are shown from left to right, respectively. The unit is given in radian for both angles, and the all the expected background events are rejected after applying the signal properties as shown in table 5.7.

contain a reconstructed vertex before applying cuts on the reconstructed vertices themselves. These are as follows:

Frames must include at least one vertex: this cut is applied to remove any empty frames.

At least one reconstructed vertex must lie within a defined acceptance region of the detector: The reconstructed vertex in the frame should be located within a cylinder of radius 1.9 cm and length 10 cm centred in the target region. This selection helps remove muon decays in flight or vertices from Bhabha scattering or pair conversions in the detector.

5.3.1 Vertex Selection Cuts

The vertex selection cuts are based on the spatial and timing properties of the signal muon decays that are described in Chapter 3. The selection cuts are as follows:

Removal of duplicate tracks from the same particle: Multiple tracks can be reconstructed per particle, if a particle has high transverse momentum and performs several loops in the central station of the detector, resulting in more than one same sign track. If the track recurls back into the target, this can also produce an opposite sign track.

In order to remove tracks that originate from the same particle, selection cuts are made on the opening angles and momentum difference. Same-sign tracks from the same vertex that differ by less than 1 MeV in momentum are required to have an opening angle

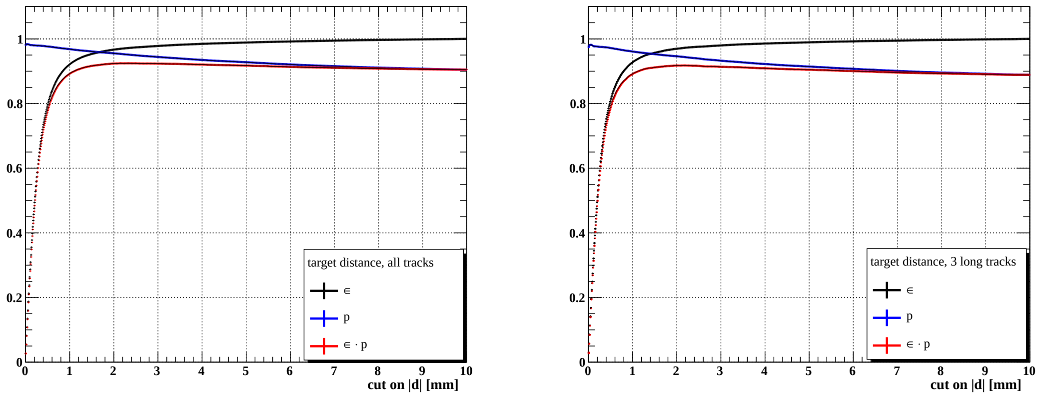

FIGURE 5.17: Efficiency, purity, and the product between efficiency and purity as a function of the cut applied on the distance of the reconstructed vertex of the signal muon decays to the target region, for all correctly reconstructed tracks (left) and for three correctly reconstructed long tracks (right).

larger than $\Delta\omega > 0.14$ rad. For opposite sign tracks, the opening angle has to be less than $\Delta\omega < 3$ rad (see figure 5.16). Track ID is an identifier used to associate tracks with MC information from the simulated particle. A tracking ID of 0, is used to indicate no association is possible and the track is therefore considered a fake track and does not correspond to a particle from the target. It could be produced from noise or unconnected hits. A track id of less than 0 indicates a duplicate track, which shares the same collection of hits with another track.

Vertex-target distance:

If the distance between the reconstructed vertex and the target is greater than 3 mm, the vertex is discarded. This cut is used to reduce combinatorial backgrounds. Efficiency, purity, and their product as a function of the cut on the distance of the reconstructed vertex of the signal muon decays to the target for all correctly reconstructed tracks (truth-matched) and for only three long tracks are shown in figure 5.17.

Momentum of the three-track system: As described in section 3.1, for signal events the momentum of the three-track system must vanish. A cut is applied to require that the momentum of the 3-track system is less than 8 MeV. This cut is an efficient selection to suppress internal conversion backgrounds. In figure 5.18, reconstructed energy of the two positron tracks of the signal muon decays for all correctly tracks and for three long tracks are shown. Efficiency, purity, and their product as a function of the reconstructed momentum cut of the signal muon decay for all correctly reconstructed tracks and only three recurl long tracks are shown in figure 5.19.

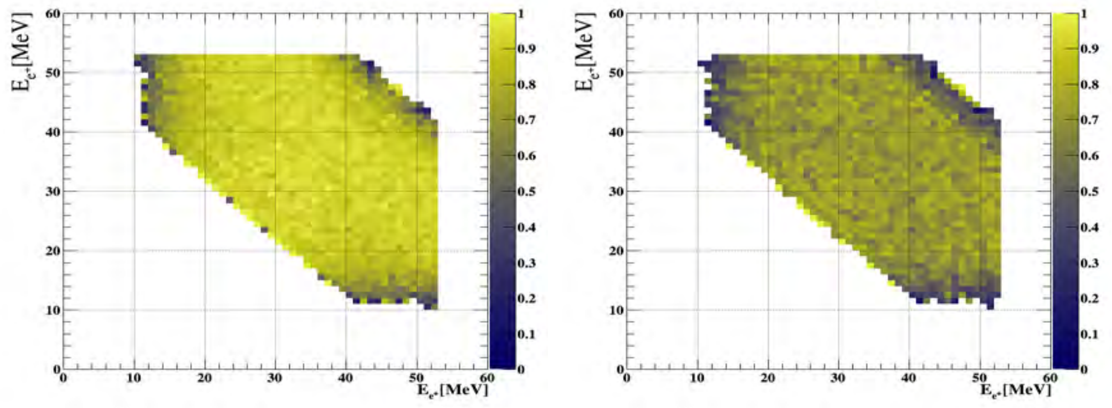

FIGURE 5.18: The reconstructed energy efficiency with respect to generated events in acceptance of two positron tracks of the signal muon decays for all correctly reconstructed tracks (left) and only long tracks (right).

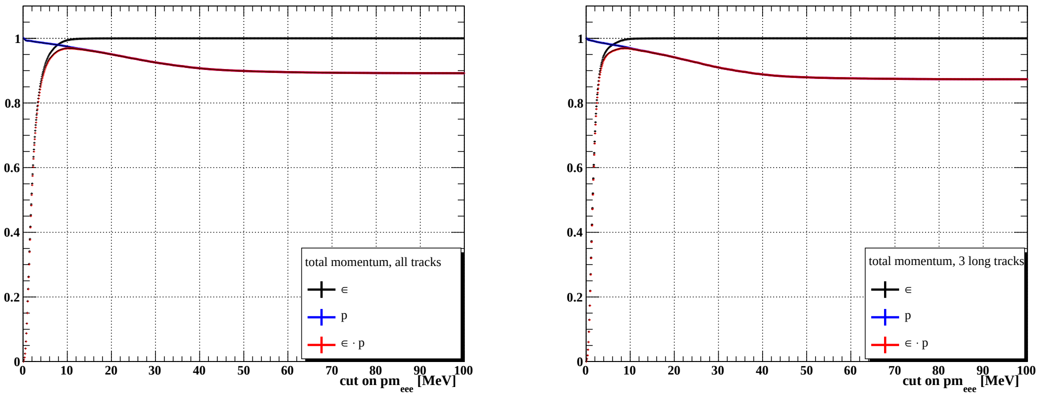

FIGURE 5.19: Efficiency, purity, and the product between efficiency and purity for reconstructed momentum cut of the signal muon decay for all correctly reconstructed tracks (left) and the three long correctly reconstructed tracks (right).

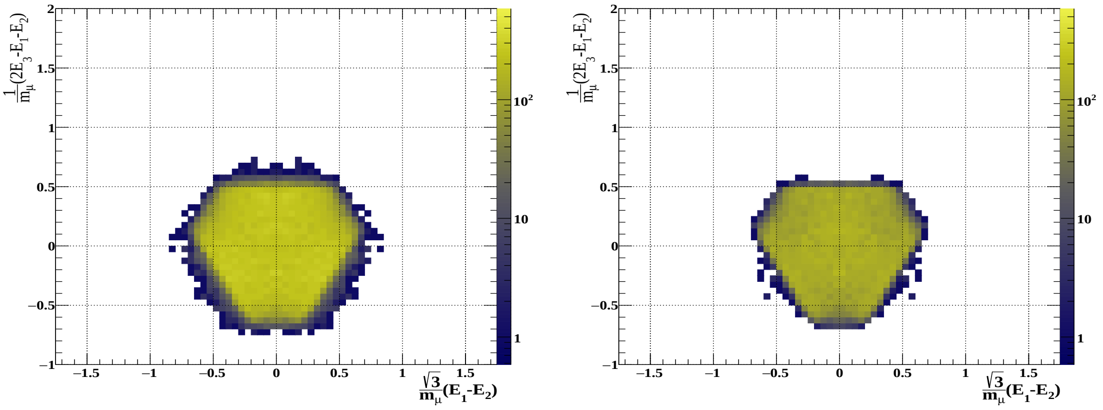

FIGURE 5.20: Dalitz plot in acceptance for $\frac{\sqrt{3}}{m_\mu}(E_1 - E_2)$ and $\frac{1}{m_\mu}(2E_3 - E_1 - E_2)$ of the signal muon decays in the reconstruction step for all correctly reconstructed tracks (left) and only ingoing long tracks (right).

Invariant mass of the three-track system: As the muon decays at rest, the energy of the three-track system is expected to be equal to the rest mass of the muon (106 MeV). A selection cut on the mass is applied where the system mass window is 103.5 MeV $\leq$ m $\leq$ 115 MeV. The Dalitz plots for $\frac{\sqrt{3}}{m_\mu}(E_1 - E_2)$ and $\frac{1}{m_\mu}(2E_3 - E_1 - E_2)$ of the signal muon decays for all correctly reconstructed tracks and three long tracks show in the figure 5.20, respectively. E_1, E_2 and E_3 are the energy for the three emitted particles which are two positrons and electron. Efficiency, purity, and the product between them is plotted as a function of the lower cut on the reconstructed invariant mass, for all correctly reconstructed tracks and three long tracks in figure 5.21 in which black line is denoted to efficiency, blue line is for purity and the product between purity and efficiency is shown with red line. A similar plot for the upper invariant mass cut is shown in figure 5.22. It is observed that the upper invariant mass cut does not provide much background rejection power. An upper cut of $m_{eee} \leq 115$ MeV is chosen in order to remove potential mis-reconstructed vertices, without loss to the signal selection efficiency. An lower cut of $m_{eee} \geq 103.5$ MeV is not suppression high fraction of internal conversion samples as upper limit as shown in figure 5.41.

Cut on the vertex χ^2 and vertex timing χ^2_{timing}: The signal decay has three tracks originating from a common vertex resulting in a small χ^2 of the vertex fit. Events with a χ^2 greater than 30 are removed. The three tracks of the signal decay should also coincide in time, so $\chi^2_{timing}(v)$[2] must be small (χ^2_{timing} < 6). Both cuts suppress combinatorial background where an e^+e^- pair originating from an internal conversion decay or a Bhabha scattering, is combined with an e^+ track from a Michel decay. Efficiency, purity and their

---

[2] Equation 8 in this chapter is defined $\chi^2_{timing}(v)$

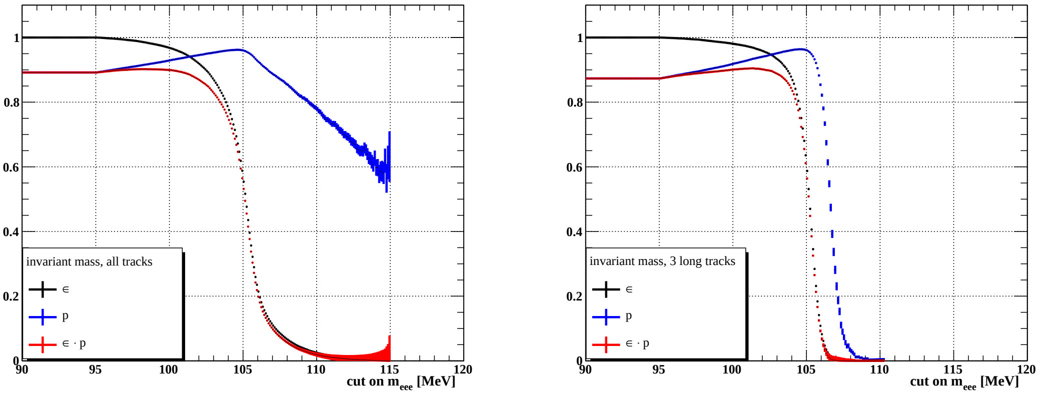

FIGURE 5.21: Efficiency, purity, and the product between efficiency and purity as a function of the lower cut on the reconstructed invariant mass for signal muon decay, for all correctly reconstructed tracks (left) and the three long 8 or 6 hit tracks (right).

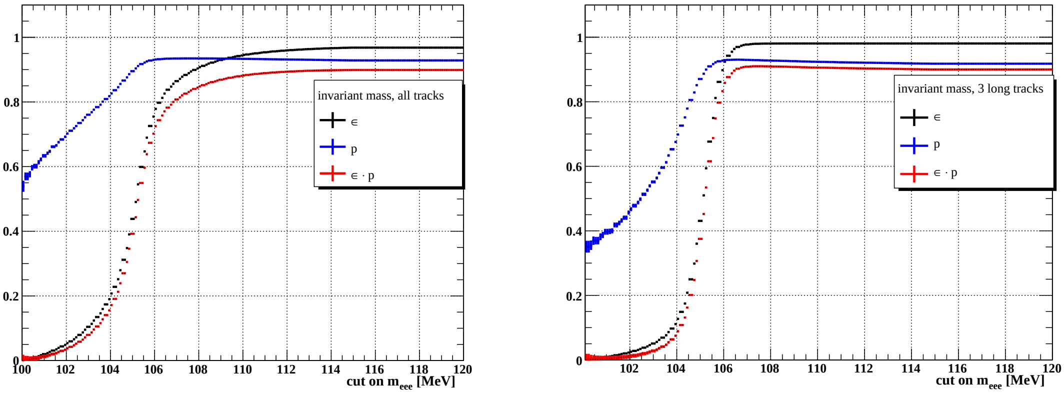

FIGURE 5.22: Efficiency, purity, and the product between efficiency and purity as a function of the upper cut on the reconstructed invariant mass for signal muon decay, for all correctly reconstructed tracks (left) and the three long 8 or 6 hit tracks (right).

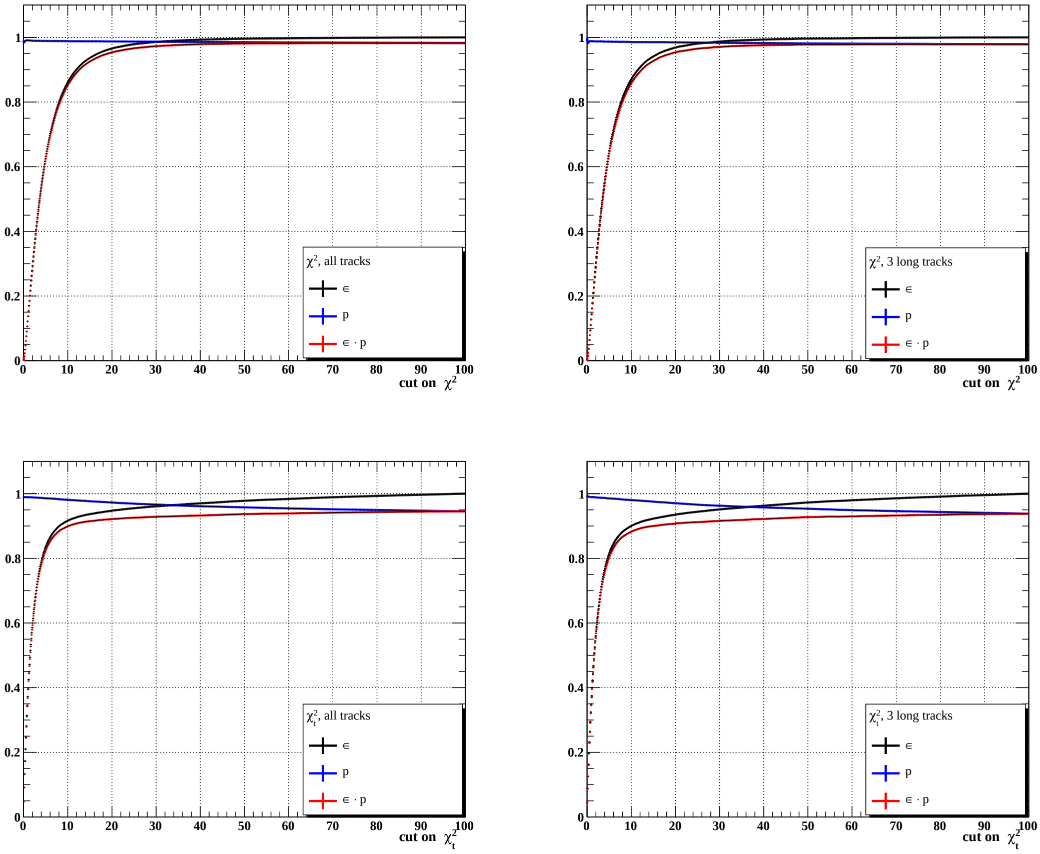

FIGURE 5.23: Efficiency, purity, and their product as a function of the cut applied on the vertex χ^2 (top) or vertex timing χ^2_{timing} cut (bottom) of the signal muon decays, for all correctly reconstructed tracks (left) or long tracks only (right). Black line is denoted for efficiency, blue line is for purity and the product between purity and efficiency is red line.

product for the vertex χ^2 and vertex timing χ^2_{timing} cuts for all correctly reconstructed tracks and only three long tracks are shown in figure 5.23. More discussion on the timing information of the signal muon decays is coming in section 5.2.4.

A summary table for the discussed selection cuts applied to select $\mu \to e^+e^+e^-$ events and suppress different background categories is given in table 5.7.

Variable	Value Cut	Comment
χ^2_{vertex}	<30	3 degrees of freedom
$\lvert\vec{p}_{eee}\rvert = \lvert\sum \vec{p}_i\rvert$	<8 Mev/c	
distance: $\vec{v}$ to target	<3 mm	closest approach
m_{eee}	103.5 Mev $\leq$ m $\leq$ 115 Mev	
crossed tracking layers	≥ 4	4,6,8 hits tracks
χ^2_{timing}	< 6	

TABLE 5.7: Default selection cuts applied to select $\mu \to e^+e^+e^-$ events and suppress different background categories.

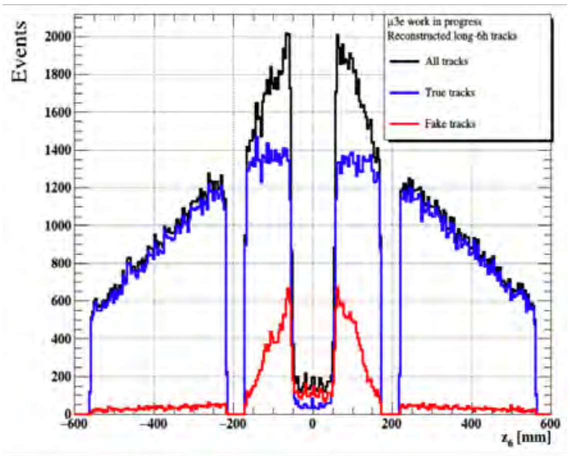

FIGURE 5.24: Distribution of the z-position of the 6th silicon hit, in the outer layers of the central or recurl station (z_6).

5.4 Detector Performance, Acceptance and Efficiency

The Mu3e experiment is designed to search for the decay $\mu^+ \to e^- e^+ e^+$ with high efficiency and an excellent resolution. The final sensitivity of the experiment depends on the rejection of backgrounds that originate from various sources and thus on vertex, momentum, and timing resolution, as well as on the efficiency to reconstruct tracks and the vertex. The geometrical acceptance and efficiency of the detector for the proposed experiment are determined by its angular and momentum coverage. In order to get a high acceptance and efficiency in all regions of phase space, the detector must reconstruct tracks with momenta up to half the muon mass and up to large angles. There are acceptance losses arising from the gap between the central and recurl stations and from the total length of the detector.

To study the efficiency and purity of tracks, it is helpful to define central long tracks and forward long-6 tracks based on a cut on the z position of the 6th silicon hit z_6, in the outer recurl stations. Figure 5.24 shows the z_6 distribution. Long tracks with 6-pixel hits that are extrapolated into one of the two recurl stations have $z_6 > 200$ mm. These have high purity and fewer fake tracks. Table 5.8 lists the efficiency ϵ for different categories of long tracks.

The total reconstruction efficiency for signal events, after the discussed selection cuts, including geometrical acceptance as a function of reconstructed momentum and inclination angle $\lambda = \frac{\pi}{2} - \theta$ [rad], is shown in figure 5.25 for correctly reconstructed events with three any tracks, long-6 tracks, long-8 tracks, any long tracks, central long-6 tracks and forward long 6 tracks. The acceptance of the detector is limited by the outer radius

Reconstruction		CS (z6 < 200 mm)	RS (z6 > 200 mm)	CS and RS
All tracks	ϵ			0.837(2)
All long-6 tracks	ϵ			0.885(3)
Long-6 central tracks	ϵ	0.767(5)		
	ϵ relative to all long-6 tracks	0.365(3)		
Long-6 recurl tracks	ϵ		0.962(4)	
	ϵ relative to all long-6 tracks		0.578(2)	
long-8 tracks	ϵ	0.549(5)		

TABLE 5.8: Efficiency ϵ for different categories of correctly reconstructed tracks. CS and RS indicate the central and recurl stations.

of the pixel tracker. Given the magnetic field of 1 T, tracks must have a minimum p_T of approximately 12 MeV/c in order to reach the outer pixel layer of the central region. Further losses in acceptance are due to the limited length of the detector and the gaps between the central and recurl stations.

5.4.1 Momentum Resolution

The invariant mass resolution in Mu3e depends directly on the momentum resolution of the tracks and it is required to be excellent in order to reject internal conversion backgrounds.

For the study of the momentum resolution, simulated signal events are used, after applying the previously discussed selection cuts. The short and long tracks are split into different bins between 10 to 55 MeV/c, and the resolution is estimated for each single bin by fitting the distribution of the difference between the true and reconstructed momenta to a double-sided crystal ball (see section B.1 in the appendix for more details about this function). Figure 5.26 shows the momentum resolution for short tracks with 4 hits, long tracks with 6-hits, and long tracks with 8-hits. The fit results are summarized in figure 5.27. In these plots, it can be seen that the resolution steadily deteriorates as the momentum of the tracks increases in which $\frac{\sigma_p}{p}$ proportional with $\frac{\Theta_{MS}}{\Omega}$, where Ω the amount of track deflection, the multiple scattering angle Θ_{MS}, σ_p is the momentum resolution and P is the momentum of track. It can be seen that the resolution for long tracks is much better than for short tracks. This is because short tracks have fewer hits on track and a reduced lever arm for the measurement. A lever arm with a large size is therefore necessary to achieve high momentum precision. Increasing tracking station radii can achieve this, but may compromise particle acceptance if low momentum particles are detected. The muon decay tracks will curl back towards the magnet axis if the

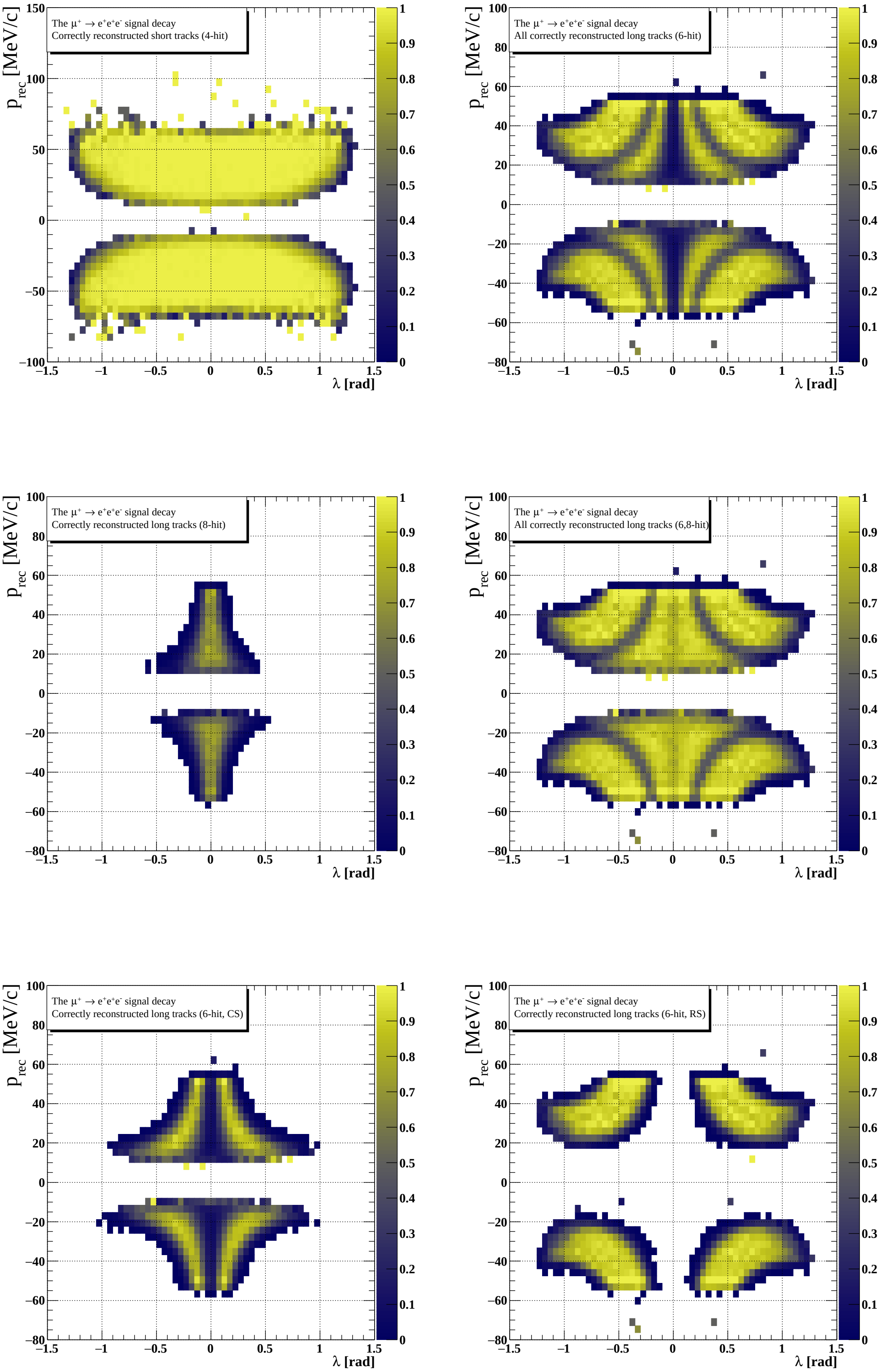

FIGURE 5.25: Track reconstruction efficiency, including geometrical acceptance, of the detector as a function of the reconstructed momentum, p_{rec}, and the dip angle $\lambda = \frac{\pi}{2} - \theta$ from top left to bottom right the figures show the efficiency for correctly reconstructed tracks with 4-hits, 6-hits, 8-hits, combination all long tracks with 6- or 8-hits, long tracks with 6-hits that recurl back into the central station and long tracks with 6-hits that recurl into one of the two recurl stations.

magnet bore is sufficiently large since all track moments are below 53 MeV. During a half turn, multiple scattering cancels out in first order on momentum measurements. A narrow, long tube layout was designed specifically to measure recurling tracks in order to exploit this feature. Recurling particles with mostly transverse momentum cause the tail towards larger numbers of hits. Many hits are created in one sensor if these particles perform many loops in the detector. The best momentum resolution is achieved around momenta of 20 MeV since multiple scattering uncertainties cancel to first order if the particle has performed about a half turn in between the two crossings of the outer layers. A significantly improved momentum resolution is observed for long tracks. A DSCB was chosen over a gaussian fit, that was used in previous studies [5] in order to fully fit the tail of the distribution. It is acknowledged that the fit is not optimal but due to time constraints this was not fully optimised. However the form is good enough to observe the behaviour of the resolution. A comparison of the fits can be seen in the appendix B (figure B.21).

Also, observing a shift in momentum is an indication of total energy loss for long tracks. Taking into account the energy loss during track fitting, which requires an understanding of the trajectory and the material passed, is one way to correct for this shift. In figures 5.26 and 5.28, there is a tail to the lower values of the invariant mass, due to individual particles losing energy in the detector due to bremsstrahlung or ionization. As it is shown in figure 5.41, for the Internal Conversion events there is a drop off just before the muon mass as expected. When considering all tracks including short and long tracks, the distribution does extend above the muon mass. This is due to the poorer mass resolution. The standard criterion used is $103.5\text{MeV} \leq \text{m}_{\text{eee}} \leq 115\text{MeV}$. It is proposed that the simulation could be validated using real data by studying a background control region of $\text{m}_{eee} < 90$ MeV (see figure 5.41).

5.4.2 Mass Resolution

After the track and vertex reconstruction, the mass of the 3-track system (M) can be calculated by using the sum of the 4-momenta of the tracks (P_{sum}):

$$M = |P_{\text{sum}}| = |\sum_{i=1}^{3} P_i| = |\sum_{i=1}^{3} \left(\sqrt{\vec{p}_i^{\,2} + m_e^2}, \vec{p}_i \right) | \tag{6}$$

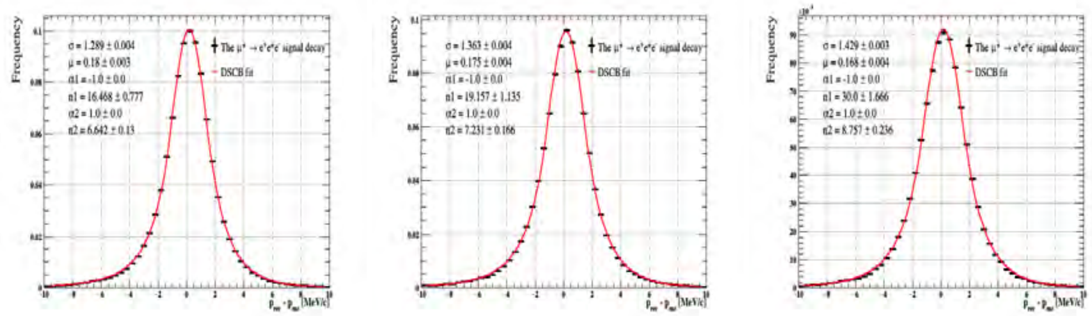

(A) 4-hits; 18-20 MeV

(B) 4-hits; 20-22 MeV

(C) 4-hits; 22-24 MeV

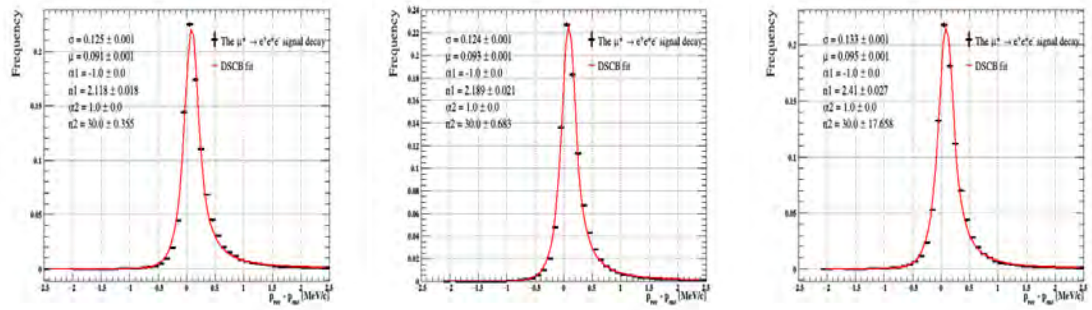

(D) 6-hits; 18-20 MeV

(E) 6-hits; 20-22 MeV

(F) 6-hits; 22-24 MeV

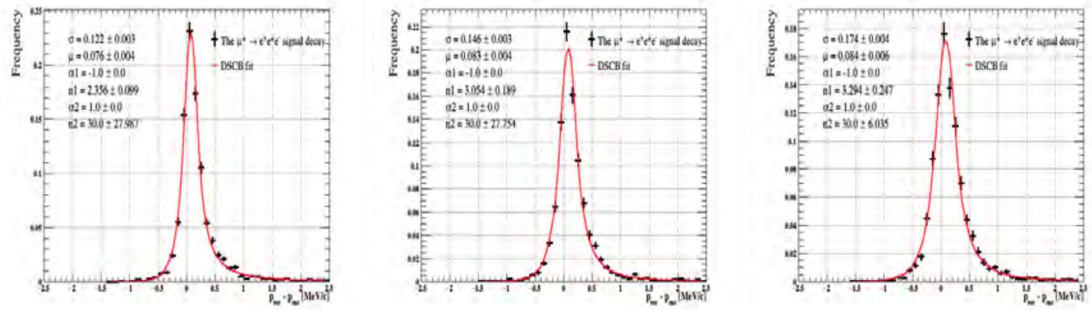

(G) 8-hits; 18-20 MeV

(H) 8-hits; 20-22 MeV

(I) 8-hits; 22-24 MeV

FIGURE 5.26: Momentum resolution for track momenta, 18-20, 20-22, 22-24 MeV for short tracks with 4-hit, long tracks with 6-hit, and long tracks with 8-hit. The fitting function is a Double-sided crystal ball function (DSCB).

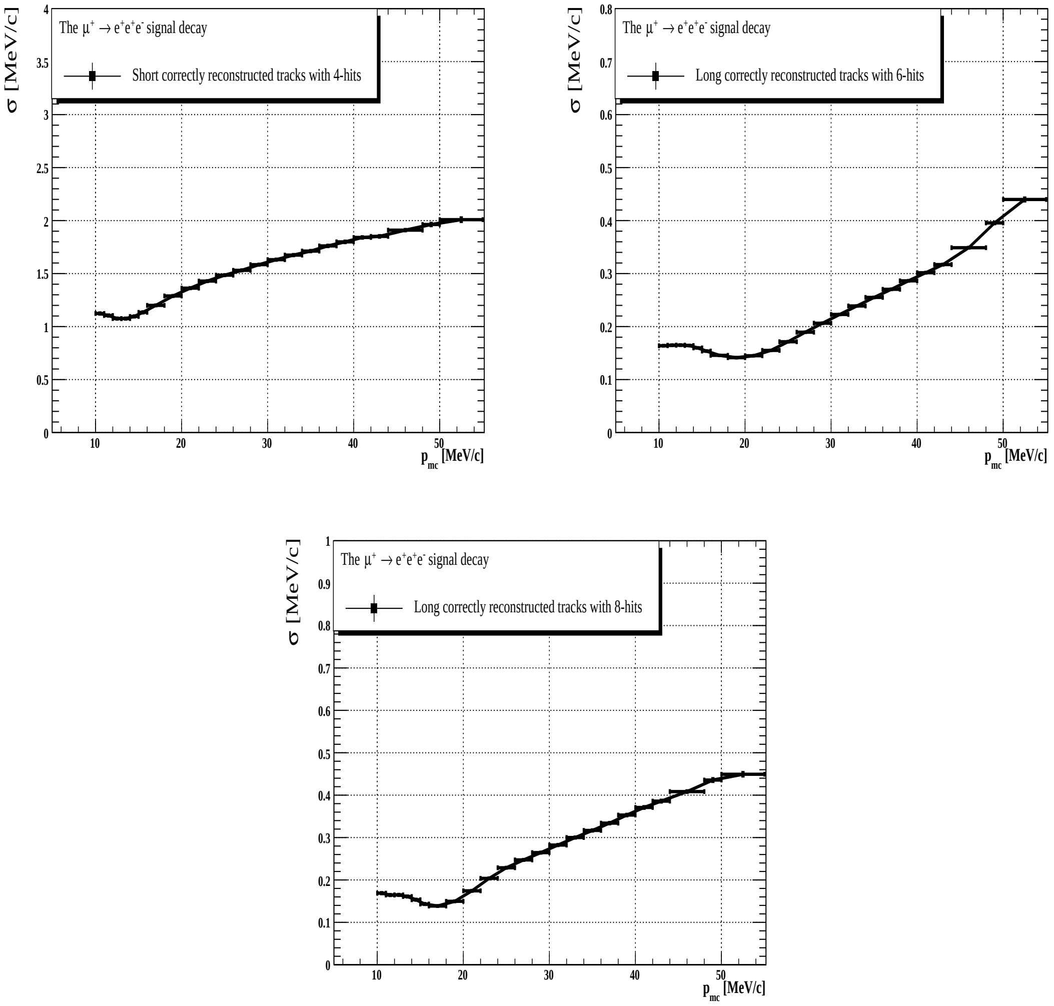

FIGURE 5.27: Summary plots for the variations of the momentum resolutions obtained using a Double-sided crystal ball fit as a function of the true track momentum for short tracks with 4-hits, long tracks with 6-hits, and long tracks with 8-hits, respectively from left to right (with track momenta 20-22 MeV).

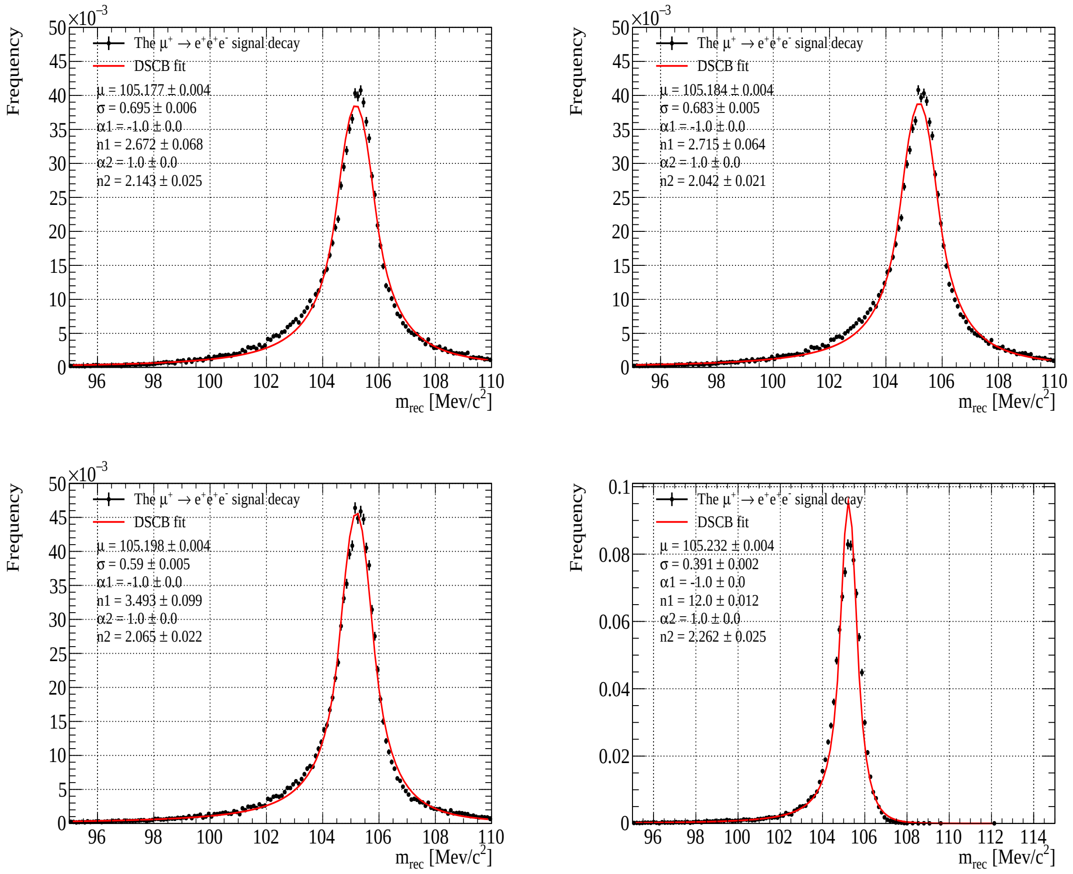

FIGURE 5.28: Reconstructed 3-track mass for all tracks (top left), at least one long track (top right), at least two long tracks (bottom left), and three long tracks (bottom right). The fits are based on a double-sided crystal ball functions.

The invariant mass resolution of the signal muon decays must be high in order to reject backgrounds that occur in the Mu3e experiment. The reconstructed muon mass in Mu3e phase 1 simulation is shown in figure 5.28 for all tracks, at least one long track, at least two long tracks, and three long tracks, respectively. A double-sided crystal ball function is used to fit the distributions. The invariant mass resolution is best with 3 long tracks, with a resolution around $\sigma = 0.391\ MeV/c^2$. Those with three long tracks fall off sharply at around 107 MeV, and they have a tail toward m_{eee} smaller than m_{μ}. There is a tail as a result of the energy loss of the individual particles within the detector. As the material amount in the detector is low, the energy loss follows a Landau distribution, characterized by rare events of large energy losses by bremsstrahlung or ionization. It is found that a smaller invariant mass can be measured because the energy loss in the individual particles is transferred to the three electron system. In the m_{eee} spectrum of all track events, the tail is less pronounced due to the larger invariant mass resolution.

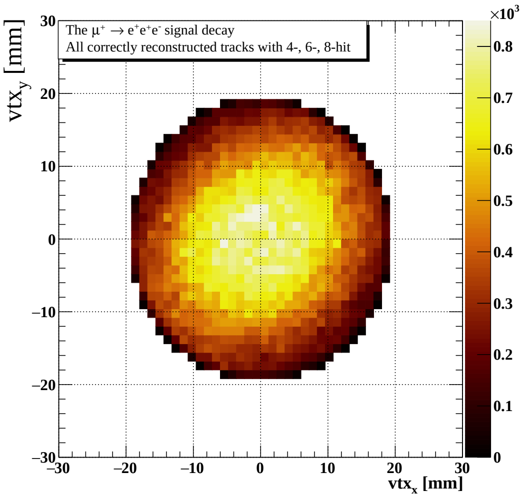

FIGURE 5.29: The reconstructed vertex position distribution in the x and y-direction for signal muon decays. The target region is clearly visible.

5.4.3 Vertex Resolution

The properties of the vertex fit are studied in simulated signal events to check how well the vertex fit performs. Figure 5.29 illustrates the vertex position distribution in the x and y directions for the signal muon decays within the target region after applying the frame selection cuts described in section 5.1.3. Figure 5.30 shows the distance between the reconstructed and true vertex position in x, y, z and the distance to the target in 3 dimensions for events with 3 reconstructed long tracks. For the latter, the sign is negative if the reconstructed vertex is inside the target. The distribution is highest at small d_{target} and decreases towards larger target distances. For signal muon decays, this is expected from the common vertex. The tail towards larger d_{target} in signal events stems from decays in flight.

5.4.4 Timing Resolution of the Fibre and Tile Timing Detector

The time information of all silicon, scintillating fibre or scintillating tile hits associated to a track, propagated back to the first-pixel tracker layer, is labelled ${t_i}^{(1)}$ where i identifies the given layer. Once a vertex is found, the track can be propagated back to find the track's vertex time for hits in different layers ${t_i}^{(v)}$ with error $\sigma_{t,i}^{(v)}$. The track vertex time is given by the weighted mean of hits in the silicon tracker, scintillating fibre and tile

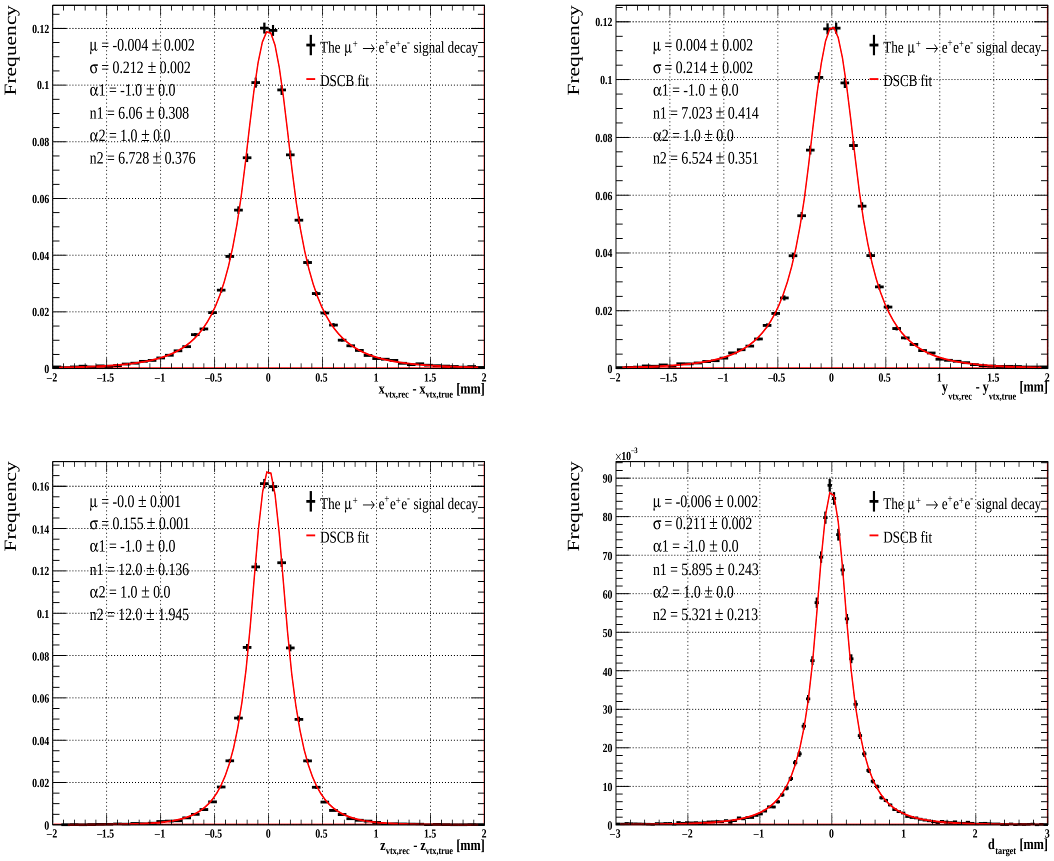

FIGURE 5.30: Vertex resolution of the signal muon decays in the Mu3e phase 1 simulation in x (top left), in y (top right), in z (bottom left) and the distance from the reconstructed vertex to the target region (bottom right). The d_{target} is negative if the vertex is inside the target. For events with 3 long tracks. The fits are based on a double-sided crystal ball function. The peak of the fit is not consistent with the data due to the effects on the vertex selection cuts and track fit quality in table 5.7.

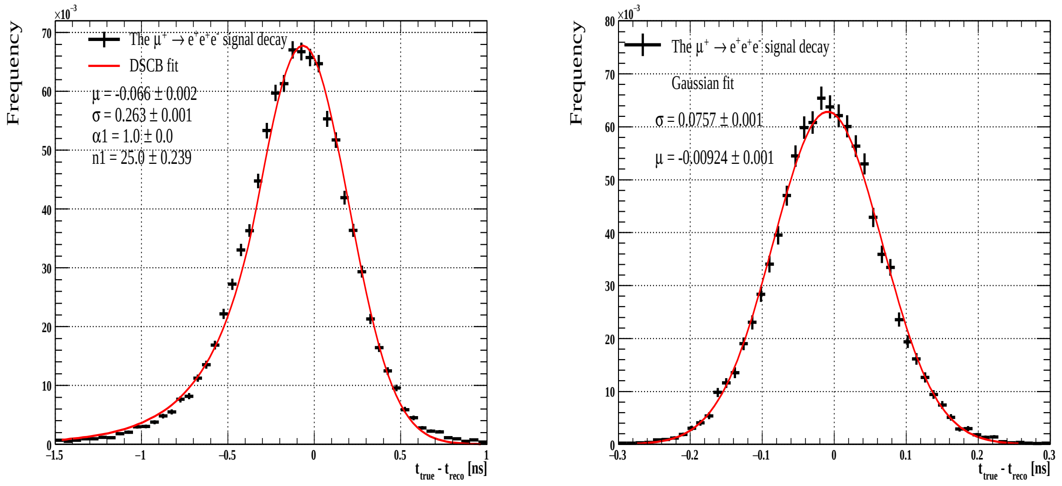

FIGURE 5.31: Left: Timing resolution for the fibre timing detector. Right: Timing resolution for the tile detector.

detector.

$$t^{(v)}_{track} = \frac{\sum_{i=1}^{hits} \frac{t_i^{(v)}}{\sigma_{t,i}^{(v)2}}}{\sum_{i=1}^{\text{hits}} \frac{1}{\sigma_{t,i}^{(v)2}}} \tag{7}$$

the timing χ^2 for each vertex was calculated using the following equation:

$$\chi^2_{\text{timing}}\left(\vec{v}\right) = \sum_{j=1}^{\text{tracks}} \frac{\left(t^{(v)}_{track,j} - \bar{t}^{(v)}_{track}\right)^2}{\sigma^{(v)}_{t,track,j}{}^{2}} \tag{8}$$

A constant time resolution σ_i layer is assumed for each sub detector layer. $\bar{t}^{(v)}_{track}$ is the weighted mean of the vertex timing of the three tracks in the decay. The fibre and tile time resolutions were estimated from the simulation by taking the difference between the true times and reconstructed times. The timing will have several components in simulation, more information was given in P. Eckert's thesis [22].

The fibre and tile time resolution, implemented in the simulation, seems to be well described by a single-sided crystal ball (function definition in appendix B.1) and a Gaussian function respectively (see figure 5.31). The time resolution for the fibres is about 263 ps and that for the tiles 75 ps. However, an extra cut was applied, as it was found that some vertices contain no reconstructed timing values, possibly due to detector imperfection as physically not all of the particle tracks are able to reach both timing detectors due to low transverse momentum or dark-rate. The two main mechanisms generating the dark-rate in the timing detectors are thermal excitation and quantum tunnelling. Thermal excitation is greatly enhanced by lattice defects, which introduce intermediate states between the band gaps, which are strongly dependent on silicon atom purity. Tunnelling assisted electron-hole pairings are generated when electrons in the p-layer tunnel across the junction into the n-layer's conduction band. When the over voltage is high, tunnelling becomes the dominant process because the tunnelling probability increases strongly with the electric field. In both processes, the temperature is not a factor, and therefore they cannot be suppressed by cooling. Figure 5.30 shows a bias in the mean of the timing resolution of > 3 sigma for the fibre detector. It is beyond the scope of this thesis to investigate further but it is proposed this should be a future area of study to improve the simulation of the track timing measurements. For this thesis, a cut on the chi2 of the timing of the vertex track is applied which should be less sensitive to this bias, as it should be dominated by the tile timing measurement.

[

This cut used ensured that every reconstructed signal decay contained complete timing information for all three tracks, and the vertex itself. This cut found that reconstructed vertices contained at least one track with no recorded timing information. Tracks get timing information from the fibre tracker and not all tracks have hits. The tile timing detector has more than no recorded timing values that are because of the acceptance region of the tile timing detector in the two recurl stations. Table 5.9 displays the amount of no recorded timing found in the data set with their error which is calculated from binomial errors per silicon, fibre, and tile detector, respectively.

The vertex timing resolution for vertices with three correctly reconstructed short tracks with 4-hits, long tracks with 6-hits, and long tracks with 8-hits, forward long tracks with 6-hits, central long tracks with 6-hits is shown in figure 5.32. The distributions seem to be well modelled by a double-sided crystal ball function only for long tracks with 6-hits and a Gaussian function for short tracks with 4-hits and long tracks with 8-hit. The vertex timing resolution is best for forward long tracks with 6-hits since these are the only tracks that reach the tile timing detector which has $\sigma = 0.038$ ns.

More information on timing propagation and suppression of background by using timing cuts to get the proper cut of χ_t^2 for vertex and check the combinatorial background suppression factor is given in appendix B (section B.1.1).

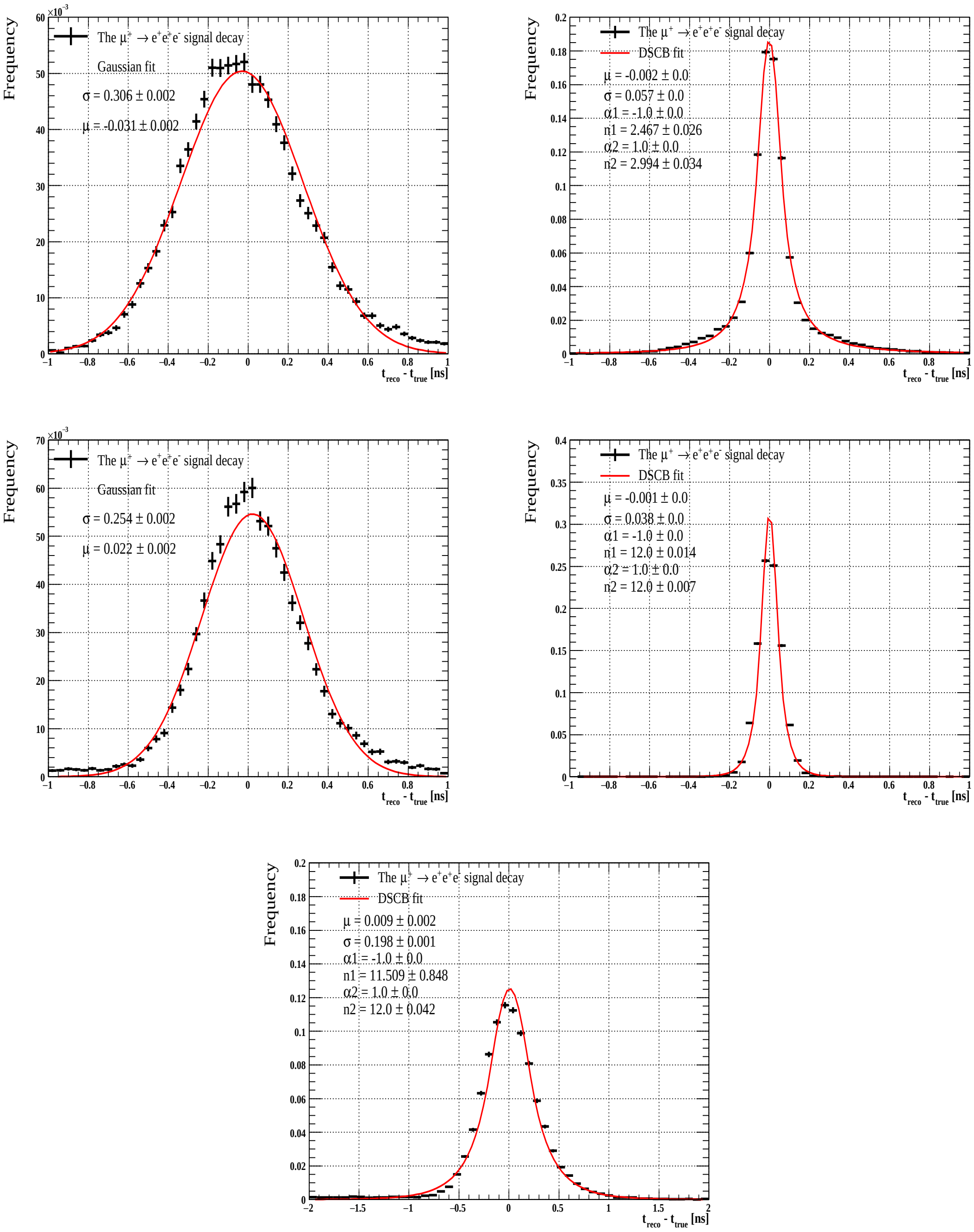

FIGURE 5.32: Vertex timing resolution for three correctly reconstructed short tracks with 4-hits, long tracks with 6-hits, and long tracks with 8-hits, forward long tracks with 6-hits, and central long tracks with 6-hits, respectively. The distributions are fitted by a double-sided crystal ball or a Gaussian function. Different fits were tested, these are the best fit have been found. The data is well modelled in clearly not consistent with the fit perfectly.

Track classification	MC [%]	Reconstructed [%]
A first silicon layer		
Short 4-hit	2.0±0.3	0
Long 6-hit	2.7±0.2	0
Long 8-hit	3.4±0.6	7.2±0.3
Fibre detector		
Short 4-hit	2.0±0.3	20.5±0.9
Long 6-hit	2.7±0.2	3.2±0.2
Long 8-hit	3.4±0.6	4.1±0.7
Tile detector		
Long 6-hit	2.7±0.2	36.7±0.6

TABLE 5.9: Extra cuts are also placed on the timing variables, as physically not all of the particle tracks are able to reach both detectors, so for fibre and tile measurements a certain percentage are removed from the selection as shown in this table.

5.5 Simulation of Signal and Background Events

5.5.1 Kinematics of the Signal Muon Decays in Phase Space

The kinematics, acceptance and efficiency of signal events passing the previously discussed event selection are discussed. In order to study the kinematics of signal muon decays, a signal sample of $\mu^+ \to e^- e^+ e^+$ events is generated. In general, one signal event is generated per frame. However, if a decay happens late in the frame no signal event is generated in the next frame since signal events are produced as special decays, which means there are no other decays involved. Non-signal muon decays are included in the simulation with the appropriate decay rate based on 10^8 μ/s on target. The number of generated signal decays is smaller than the number of frames because the generator level momentum cuts of track within (10 MeV < P < 65 MeV) are applied. Reconstructed events are used if they satisfy the selection cuts, previously described. When the number of decays on the target is N_t is known, the number of observed muon decays becomes:

$$N_{\mu\to eee} = N_t \cdot \epsilon \cdot BR_{\mu\to eee} \tag{9}$$

where $\mathrm{BR}_{\mu\to eee}$ is the assumed branching ratio of the signal decay. The signal selection efficiency is given as:

$$\epsilon = \frac{N_{\text{selected vertices}} \cdot \epsilon_t}{N_{\text{frames}}} \tag{10}$$

Events with decays in target region	163627
After simulation	
Events in acceptance	67529
Events in acceptance with 3-outgoing tracks	67002
Events in acceptance with 3-recurler tracks	43464
After reconstruction	
Events reconstructed with 3-outgoing tracks	60301
Events reconstructed with 3-recurler tracks	30371
After vertex fit	
Events reconstructed with 3-outgoing tracks	60203
Events reconstructed with 3-recurler tracks	30333
Events reconstructed with 3-outgoing tracks after cuts	46914
Events reconstructed with 3-recurler tracks after cuts	26365

TABLE 5.10: The number of the signal muon decay events in the acceptance after generated, reconstruction, vertex fit, and vertex fit after applying vertex selection cuts step.

where $N_{\text{selected vertices}}$ is the number of vertices passing all the selection requirements corrected for multiple reconstructions of the same vertex, and N_{frames} is the number of frames that corresponds to the number of generated signal events. The timing efficiency ϵ_t is taking as 98% [3]. The number of events left after each step in the simulation and reconstruction, vertex fit, and after applying the vertex selection cuts are listed in table 5.10 with about 2×10^5 signal events are simulated.

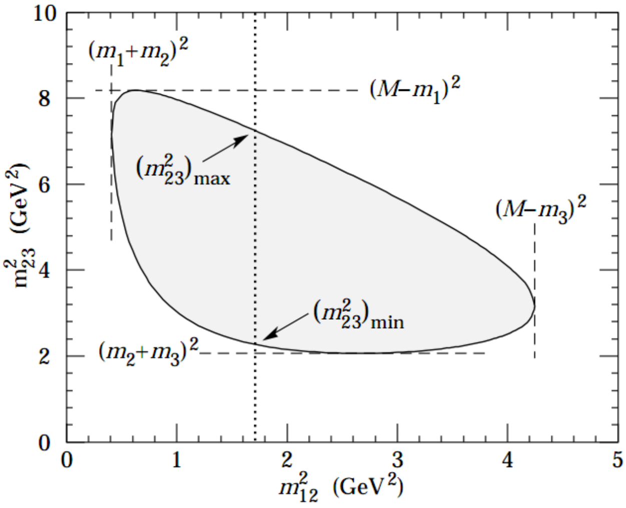

FIGURE 5.33: Schematic of a scatter plot in 2-dimensions of the m^2_{ee} in which the boundaries are limited by the masses of mother M and three daughter particles. This figure is adapted from [37].

Next, we compare the kinematic distribution at different stages of the signal selection. The phase space of a 3-body decay in the centre mass system of the muon decays can be displayed as scatter plots in 2-dimensions of the invariant masses squared of the 2 possible e^+e^- combinations in which the boundaries of the phase space of a 3-body decay

---

[3] It is estimated for $\chi^2_{timing} < 6$

are determined by the mother and daughter particle masses as shown in figure 5.33.

The orientation of the decay plane with respect to the spin of the muon is parameterized in $\cos(\tilde{\vartheta})$ and $\tilde{\boldsymbol{\varphi}}$ as shown in figure 5.34, where $\tilde{\boldsymbol{\varphi}}$ is the angle between the muon decay plane and the plane of the electron momentum and muon spin, and $\tilde{\vartheta}$ is the angle between the orientation of the muon spin and momentum of the electron. In the Mu3e experiment, the polarisation of the muon points in negative z-direction.

Kinematic distributions of the signal muon decays at generator level: The acceptance of all tracks and long tracks defines if a track has hit in each layer. A scatter plot of the invariant masses squared of the 2 possible e^+e^- combinations and the angular distribution based on the 4 momenta of: all $e^+e^+e^-$ combinations; $e^+e^+e^-$ combination in the "all tracks" acceptance and $e^+e^+e^-$ combinations in the "long tracks" acceptance are shown in figure 5.35. Signal decays can be missed in the detector if one of the decay particles has a p_T lower than 10 MeV or is emitted under a shallow angle with respect to the z-direction. In these situations, the particle will not cross all 4-pixel layers, preventing their trajectory from being reconstructed. Events are also missed if $|\cos(\tilde{\vartheta})| \approx 1$ since in this case the emitted electron is emitted under a small angle with respect to the beam direction. Events in the corners of the Dalitz plot do not survive since these correspond to cases where one decay particle has a momentum too low to be detected.

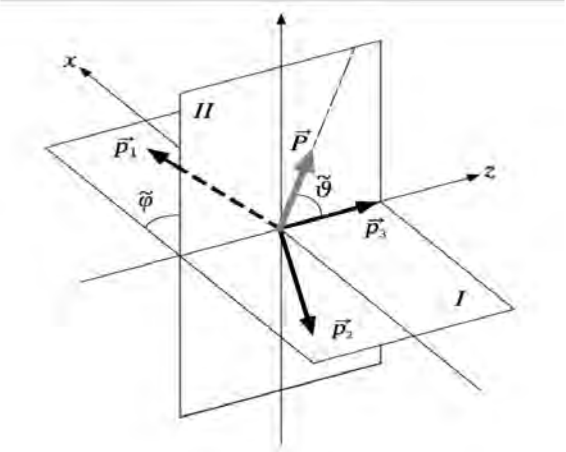

FIGURE 5.34: The orientation of the decay plane with respect to the spin of the muon is parameterized by in $\cos(\tilde{\vartheta})$ and $\tilde{\boldsymbol{\varphi}}$. The definition of angles $\tilde{\boldsymbol{\varphi}}$ and $\tilde{\vartheta}$ are between 0 to 2π and 0 to π, respectively. The decay positrons momenta $\vec{p}_1$ and $\vec{p}_2$ and the electron momentum $\vec{p}_3$ lie in plane I, while plane II is determined by the muon polarization vector $\vec{p}$ and electron momentum $\vec{p}_3$. This figure is taken from [31]

Kinematic distributions of the signal muon decay after the track reconstruction: The scatter plots, shown in figure 5.36, are based on all combinations of 2 positive and one

Phase space	$\epsilon_{\text{all 3 tracks (4, 6, 8 hits)}}$	$\epsilon_{\text{3 long tracks (6, 8 hits)}}$
events in acceptance	0.412(1)	0.265(1)
relative to all events in acceptance		0.643(3)
events after track reconstruction	0.368(1)	0.185(1)
relative to events in acceptance	0.892(5)	0.698(5)
events with reconstructed vertex	0.374(1)	0.188(1)
relative to events in acceptance	0.907(5)	0.708(5)
relative to events after track reconstruction	0.998(8)	0.998(8)
events with reconstructed vertex after cuts	0.290(1)	0.163(1)
relative to events with reconstructed vertex before cuts	0.776(4)	0.866(7)
relative to events in acceptance	0.704(4)	0.614(4)
relative to events after reconstruction	0.789(4)	0.879(7)

TABLE 5.11: Efficiency after track and vertex reconstruction and after vertex selection cuts for all combinations of three reconstructed tracks (all tracks) and long tracks only.

negative reconstructed tracks. These do not differ much from ones based on the generated momentum. In the angular distributions, an inefficiency at $\cos(\tilde{\vartheta})$ around zero is observed. Here, a decay particle is emitted perpendicular to the beam axis. Such particles perform multiple turns increasing the probability for wrong combinations of hits during the track reconstruction.

Kinematic distributions of the signal muon decay after the vertex reconstruction:

Figure 5.37 shows the angular distribution of the signal muon decays based on reconstructed track after vertex fitting. Inefficiencies of the vertex reconstruction stem from non-converging fits and configurations in which the reconstructed vertex position lies outside the target region.

The efficiency after the track and vertex reconstruction and after the vertex selection cuts for all combinations of three reconstructed short or long tracks are listed in table 5.11. The efficiency to select events within the acceptance is 70% and 61% for events with all tracks and 3 long tracks after track and vertex reconstruction and vertex selection, respectively. This efficiency will drop after the full selection cuts discussed later on.

Figure 5.38 illustrates signal efficiency as a function of the χ^2 of the vertex fit, the total reconstructed momentum p_{eee}, and the distance from the vertex to the target after applying vertex selection cuts. Figure B.20 shows signal efficiency and background suppression by cuts on the χ^2 of the vertex, the invariant mass m_{eee}, the total momentum p_{eee}, the target distance $|\mathrm{d}|$ of the two positrons and one electron for $\mu^+ \to e^+e^+e^-$ signal decays and radiative decays with internal conversion $\mu^+ \to e^+e^+e^-\nu\nu$ (IC).

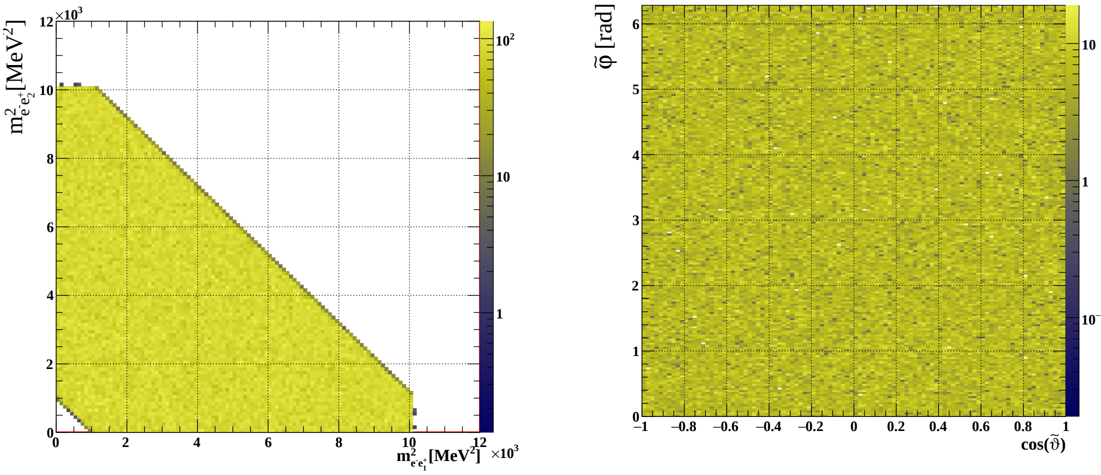

(A) Dalitz plot of all generated particles.

(B) Angular distribution of all generated particles.

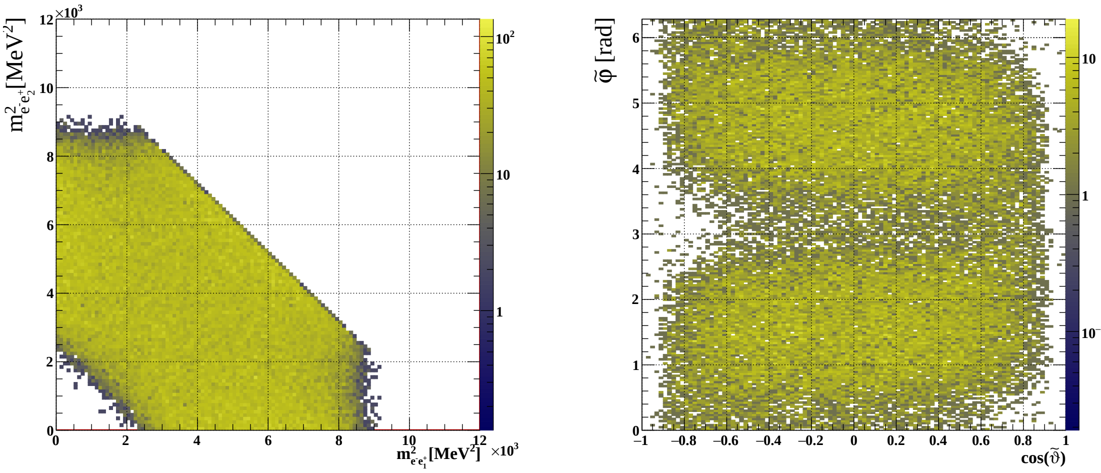

(C) Dalitz plot of generated particles passing acceptance cuts for all tracks.

(D) Angular distribution of generated particles passing acceptance cuts for all tracks.

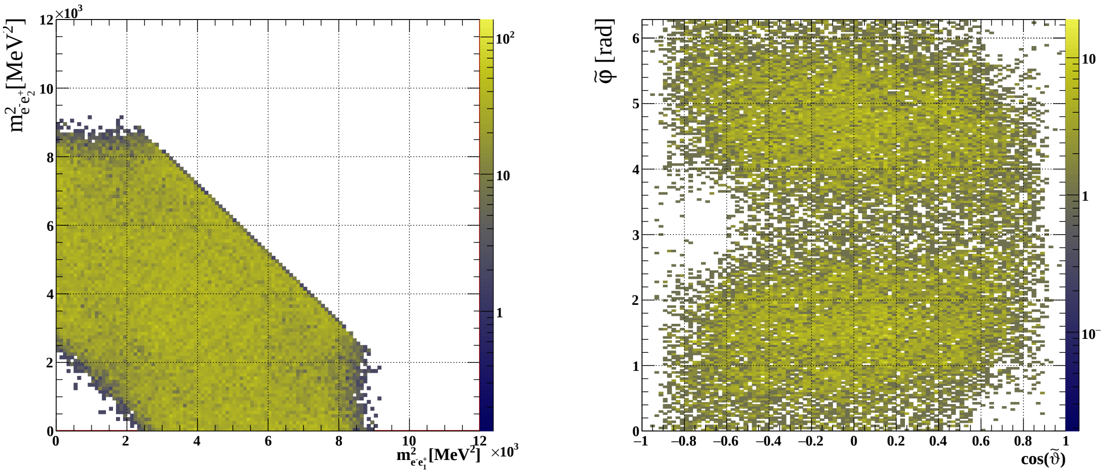

(E) Dalitz plot of generated particles passing acceptance cuts for only long tracks.

(F) Angular distribution of generated particles passing acceptance cuts for only long tracks.

FIGURE 5.35: Dalitz plots of the two body invariant masses of the e^+e^- system and the angular distribution of events at generator level, for all and long tracks. The plots are based on the true momenta at generator level.

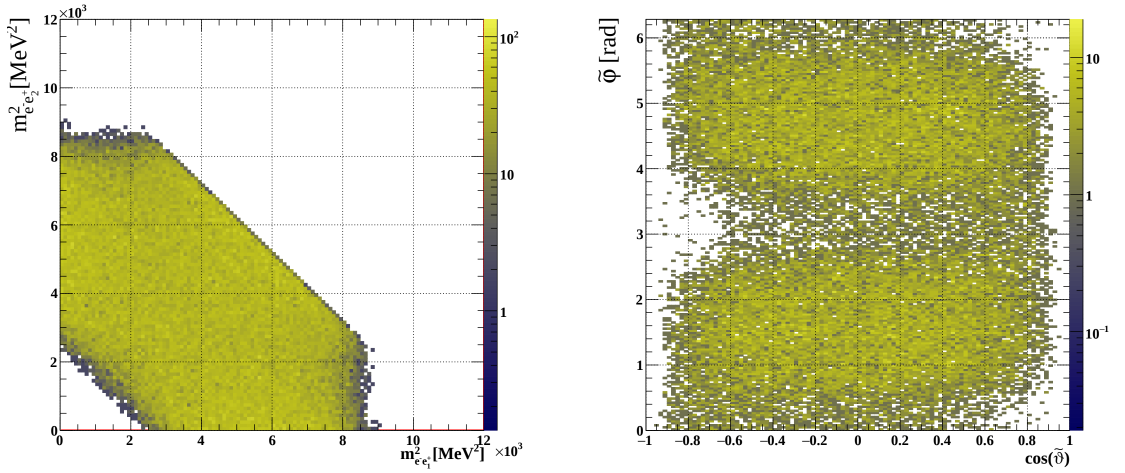

(A) Dalitz plot based on all reconstructed tracks.

(B) Angular distribution based on all reconstructed tracks

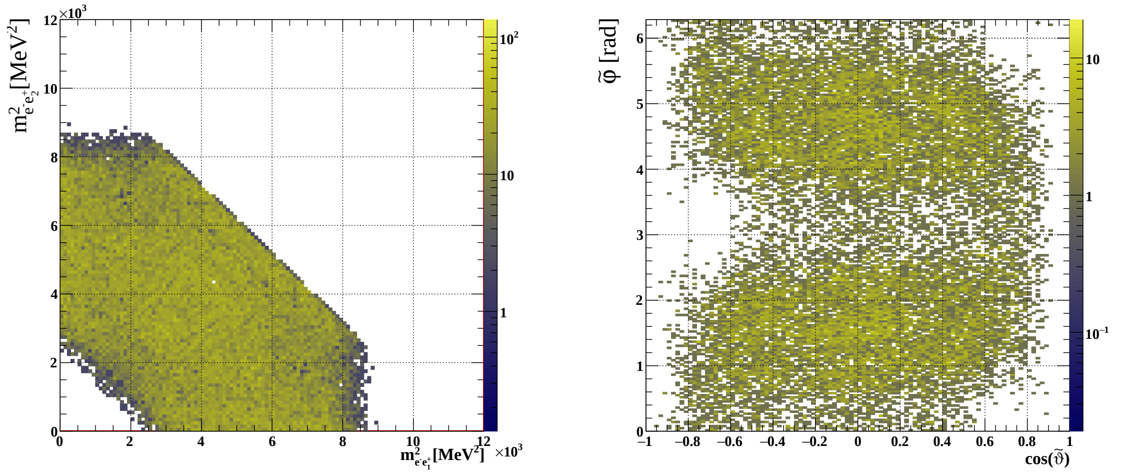

(C) Dalitz plot based on only long reconstructed tracks.

(D) Angular distribution based on only long reconstructed tracks.

FIGURE 5.36: Dalitz plots of the invariant masses of the e^+e^- system and the angular distribution of events based on all (top) and long (bottom) tracks at reconstruction step.

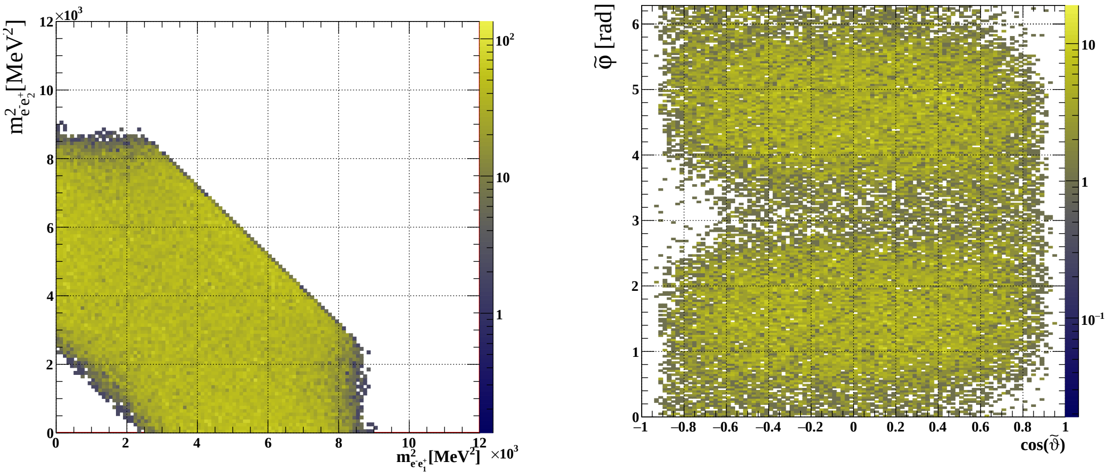

(A) Dalitz plot based on all reconstructed tracks in events with reconstructed vertex.

(B) Angular distribution based on all reconstructed tracks in events with reconstructed vertex.

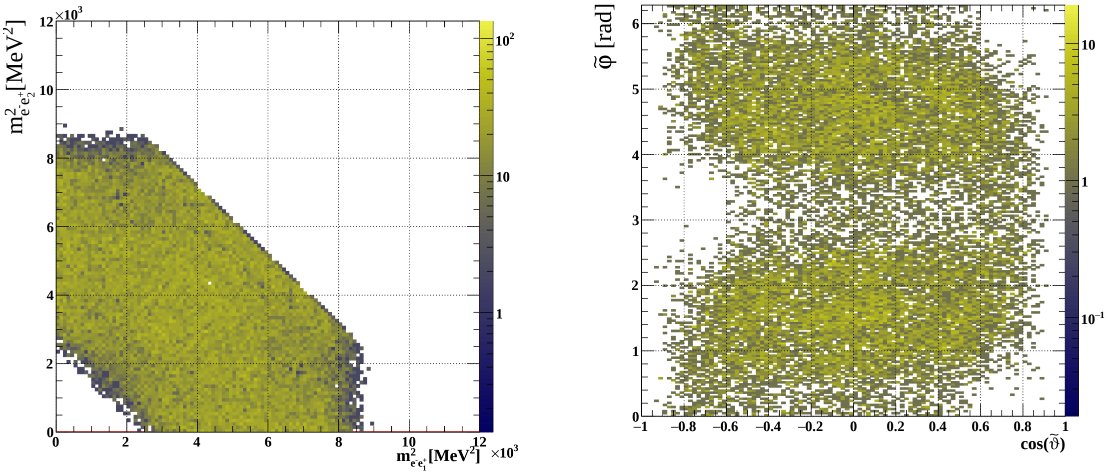

(C) Dalitz plot based on long reconstructed tracks in events with reconstructed vertex.

(D) Angular distribution based on only long reconstructed tracks in events with reconstructed vertex.

FIGURE 5.37: Dalitz plots of the invariant masses of the e^+e^- system and the angular distribution for all and reconstructed long tracks at vertex reconstruction step.

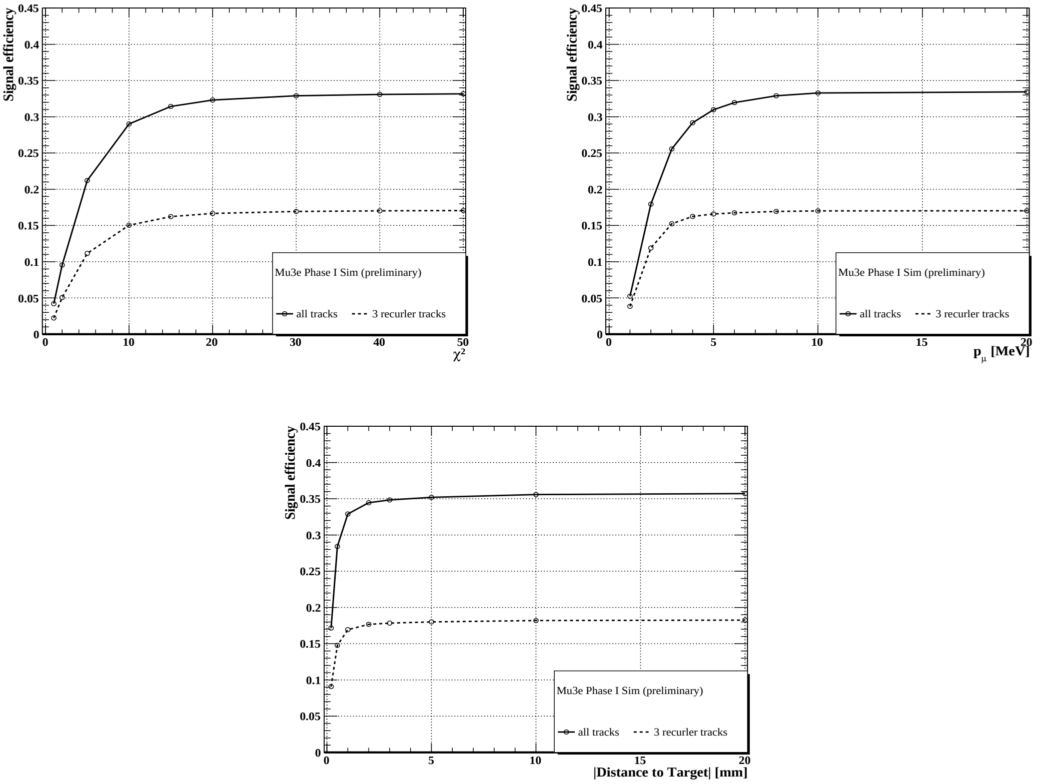

FIGURE 5.38: Signal efficiency as a function of the cut applied to χ^2 of the vertex fit, the reconstructed total momentum, and the target distance of the reconstructed vertex to the target, respectively from left to right for all and only long (recurler) reconstructed tracks.

Cut	Number of Frames	Efficiency
Frame Selection Cuts (See Section 5.1.4)		
$\geq$1 vertex	4.348795e+06	0.420
Recon vtx within acceptance	3.902449e+06	0.377
Duplicate removal (same tracks)	3.797798e+06	0.367
Duplicate removal (common tracks)	3.797798e+06	0.367
Duplicate removal (vtx-to-vtx distance)	3.673176e+06	0.355
Break-up in different vertex track quality	3 short	3 long
Efficiency	0.355	0.162
Vertex Selection Cuts (See Section 5.1.5)		
$\chi^2 < 30$	1.977392e+06	0.191
vertex target distance <3 mm	1.951384e+06	0.189
3-track system momentum <8 MeV	1.880665e+06	0.1817
103.5 MeV $\leq m_{eee} \leq$ 115 MeV	1.547917e+06	0.1496
Break-up in different vertex track quality	3 short	3 long
Efficiency	0.181	0.095

TABLE 5.12: Table showing the number of frames passing subsequent frame and vertex selection cuts for the scenario when signal muon decays are generated at one decay per frame in the nominal detector.

Table 5.12 shows the number of frames passing each frame and vertex selection cut for events with short and long tracks. Table 5.13 shows information on the origin of the selected vertices before and after the vertex cuts for the signal sample. Over 10M signal decays were reconstructed from the simulation. Table B.4 in appendix B shows the

Category	Number of vertices	Fraction
3 Signal:	2155642	0.567373
3 Michel:	5985	0.001575
3 Internal:	0	0.000000
3 Radiative:	0	0.000000
3 Phot:	0	0.000000
3 Bhabha:	0	0.000000
3 Brems:	0	0.000000
3 Pos Anni:	0	0.000000
3 Compton:	0	0.000000
1 int 2 Mic:	2	0.000001
2 int 1 Mic:	0	0.000000
>=1 pho:	3796	0.000999
>=1 brem:	0	0.000000
>=1 compton:	1583	0.000417
other:	1632328	0.429635
After applying vertex cuts:		
3 Signal:	1880581	1.0
3 Michel:	0	0.000000
3 Internal:	0	0.000000
3 Radiative:	0	0.000000
3 Phot:	0	0.000000
3 Bhabha:	0	0.000000
3 Brems:	0	0.000000
3 Pos Anni:	0	0.000000
3 Compton:	0	0.000000
1 int 2 Mic:	0	0.000000
2 int 1 Mic:	0	0.000000
>=1 pho:	0	0.000000
>=1 brem:	0	0.000000
>=1 compton:	0	0.000000
other:	0	0.000000

TABLE 5.13: Signal sample generation information per reconstructed vertex before and after applying vertex cuts. The classification shows the origin of the three tracks in the reconstructed vertices by applying all the signal properties. About 10 million decays were reconstructed from the simulation. Other is indicated for other types of backgrounds that are not in the same list. Before applying vertex selection cuts, 43% is indicated for other backgrounds that are not listed in this table, such as 1 Michel with 1 Radiative, 3 Bhabha with 2 Michel, 1 Internal with 1 Compton, etc.

number of frames passing the vertex selection criteria at the different vertex and track quality.

5.5.2 Simulation Background $\mu^+ \to e^- e^+ e^+ \nu_e \overline{\nu}_\mu$

The dominant background in the experiment results from the internal conversion process $\mu^+ \to e^- e^+ e^+ \nu_e \overline{\nu}_\mu$. As in the signal process, the three charged tracks originate from a single vertex. Therefore, the only distinguishing feature will be the total summed momenta of the electrons which for this process will be less than the muon mass.

Background from radiative $\mu^+ \rightarrow e^-e^+e^+\nu_e\overline{\nu}_\mu$ events is simulated. The internal conversion background is generated with weights, and phase space cuts are applied at the generator level. In particular, the following requirements are used: The minimum energy of each of the two positrons and the electron is 10 MeV, the invariant mass of the two positrons and the electron is at least 90 MeV, and the absolute value of the cosine of the polar angle of the decay positrons/electrons is less than 0.8.

Category	Number of vertices	Fraction
3 Michel:	19117	0.002436
3 Internal:	3319425	0.422896
3 Radiative:	1	0.000000
3 Phot:	0	0.000000
3 Bhabha:	0	0.000000
3 Brems:	0	0.000000
3 Pos Anni:	0	0.000000
3 Compton:	0	0.000000
1 int 2 Mic:	675219	0.086023
2 int 1 Mic:	3640731	0.463830
>=1 pho:	5760	0.000734
>=1 brem:	0	0.000000
>=1 compton:	2628	0.000335
other:	186393	0.023747
After applying vertex cuts:		
3 Michel:	0	0.000000
3 Internal:	122767	0.998455
3 Radiative:	0	0.000000
3 Phot:	0	0.000000
3 Bhabha:	0	0.000000
3 Brems:	0	0.000000
3 Pos Anni:	0	0.000000
3 Compton:	0	0.000000
1 int 2 Mic:	2	0.000016
2 int 1 Mic:	174	0.001415
>=1 pho:	0	0.000000
>=1 brem:	0	0.000000
>=1 compton:	0	0.000000
other:	14	0.000114

TABLE 5.14: Radiative with internal conversion sample information of the origin of the selected vertices after applying vertex cuts. The shows the origin of the three tracks in the reconstructed vertices. About 30 million decays were reconstructed from the simulation.

The weighted events are selected to the differential decay rate to correspond to the number of expected muon decays during phase I. They are weighted with corresponding value of the matrix elements based on the decay kinematics, it is needed with large background samples. The calculation of the matrix element stems from Signer et al. [43], where the polarization of the muon is taking into account. At the simulation level, the information about the weight is lost once the particle crosses a frame boundary. In these rare cases the weight is set to the mean weight of the whole sample. For the internal conversion events, large weights are observed which disturb the smoothness of

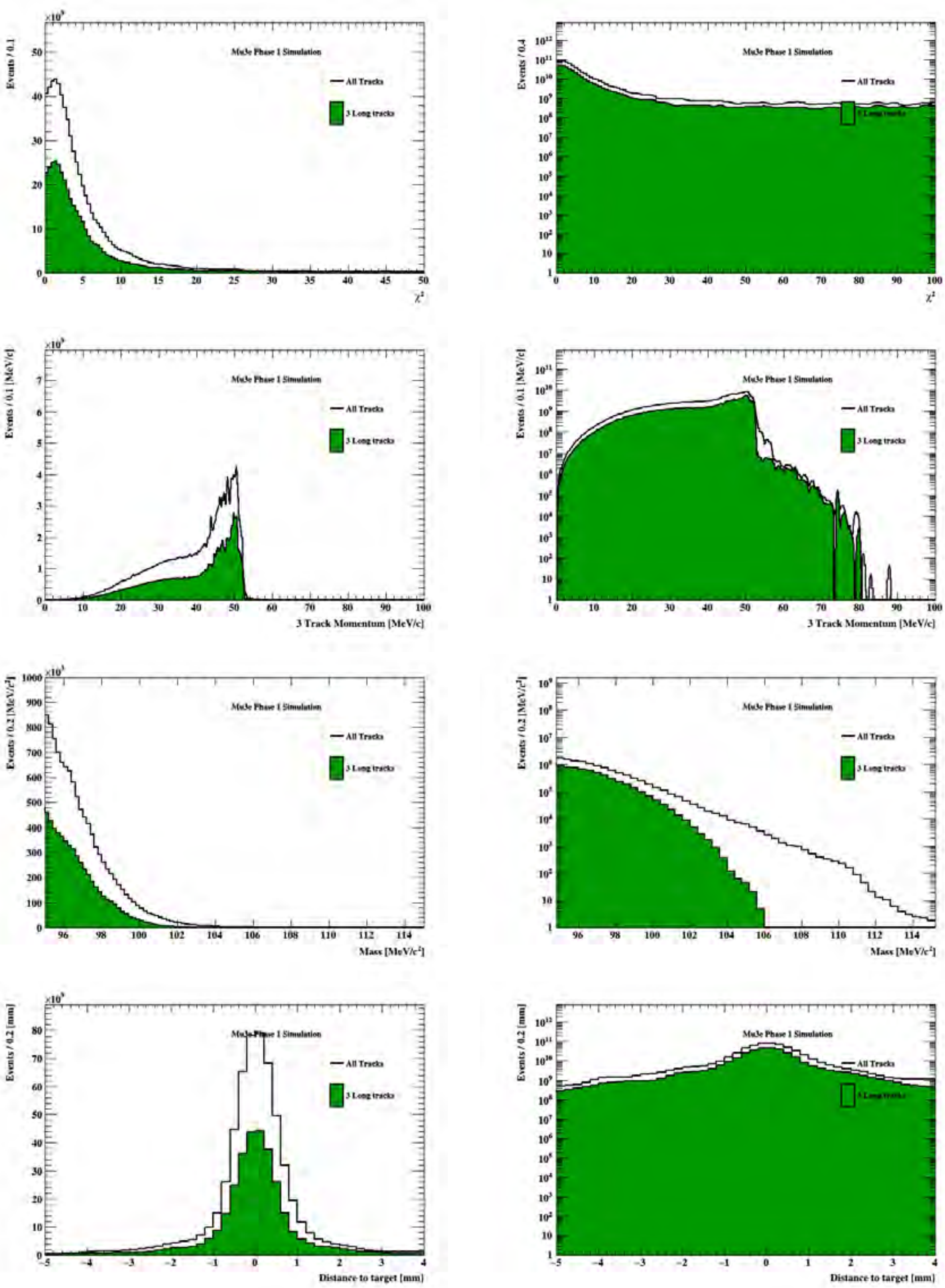

FIGURE 5.39: Distribution of the χ^2 of the vertex fit (top row), distance |d| to the target surface (second row), total momentum (third row), the invariant mass of the three electron system (bottom row) from radiative decays with internal conversion, $\mu \to eee\nu\nu$, after applying the selection cuts from table 5.4. On the right, the same distributions are shown on a log scale.

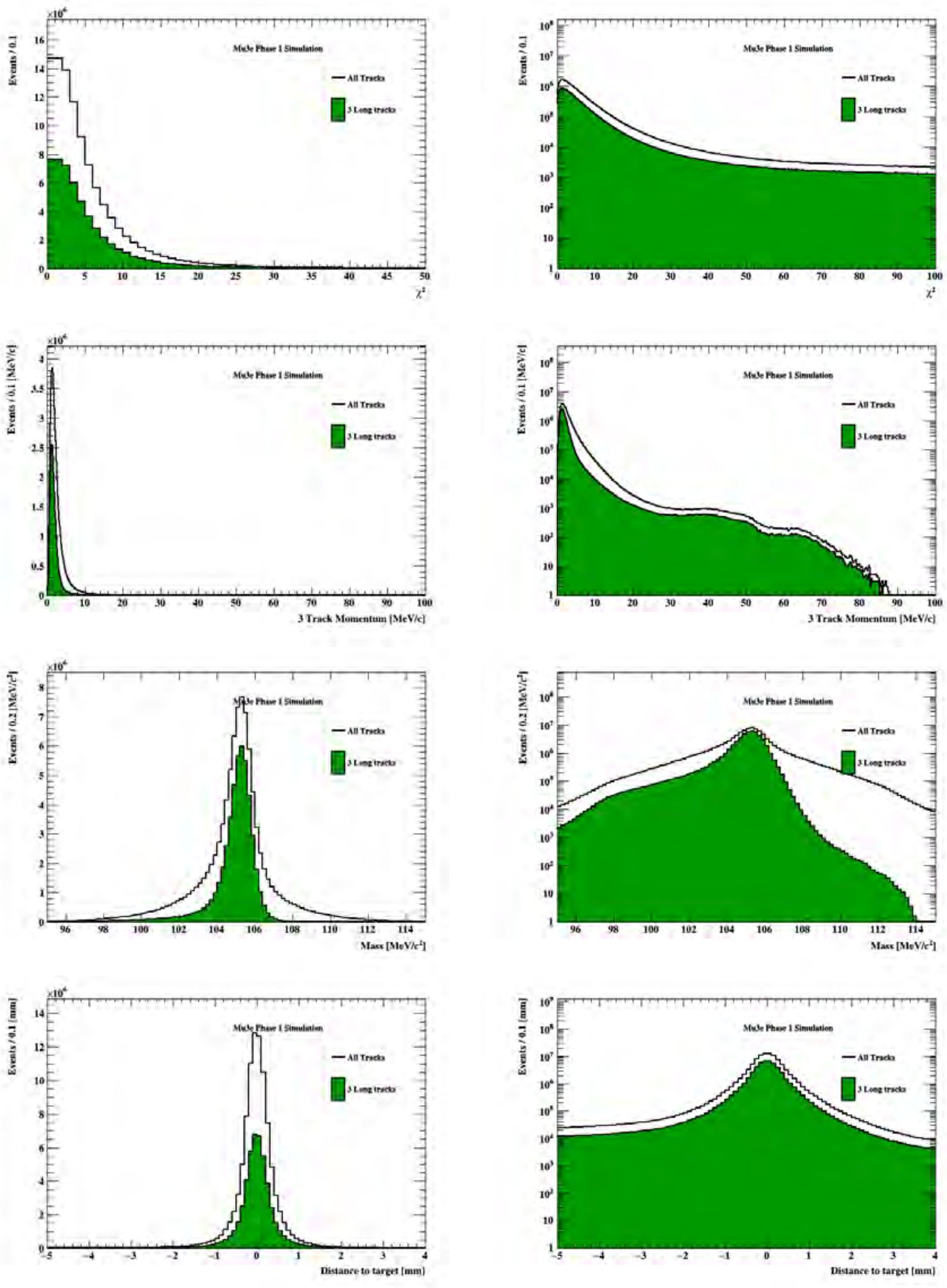

FIGURE 5.40: Distribution of the χ^2 of the vertex fit (top row), distance |d| to the target surface (second row), total momentum (third row) and the invariant mass of the three electron system (bottom row) for signal muon decays, $\mu \to$ eee, after applying the selection cuts in table 5.4. On the right, the same distributions are shown on a log scale.

the later p.d.f. so the weights larger than 1×10^7 are rejected when building the p.d.f. The mean weight for the internal conversion event is about 5000, and only a fraction of about 5×10^{-5} of the event are rejected with this selection. Due to the phase space cuts, the 30 million frames with one internal conversion decay per frame have a weight corresponding to $1.04227 \cdot 10^{13}$ decays [4].

Table B.1 in appendix B shows the number of weighted frames passing the selection cuts described in section 5.1.4. Table 5.14 shows the origin of the selected vertices before and after the vertex cuts, for the internal conversion sample. It can be seen that 99.8 % of accepted events from the sample to correctly reconstructed internal conversion decays and a small fraction are due to 2+1 combinatorial backgrounds.

The normalization of the internal conversion background has been performed as follows:

$$N_{(\mu\rightarrow eee\nu\nu)} = N_t \cdot \epsilon \cdot \mathrm{BR}(\mu \rightarrow eee\nu\nu) \quad \text{and} \quad \epsilon = \frac{N_{\text{weighted, pass selection}}}{N_{\text{initial sum of weights}} \cdot \epsilon_g} \tag{11}$$

where the branching ratio of the internal conversion is defined in Chapter 2 while ϵ_g is the timing efficiency of 98 %. The distributions of the χ^2 of the vertex fit, distance $|\mathrm{d}|$ to the target surface, total momentum, the invariant mass of the three electron systems for signal decays and background from radiative decays with internal conversion respectively after applying vertex selection cuts in table 5.5 are shown in figures 5.39 and 5.40. A plot showing both signal and main background distributions would be helpful for comparison.

The distribution of the invariant mass of the three electrons associated with the vertices, vertex cuts discussed in section 5.1, are shown, for signal and internal conversion events, in figure 5.41 (top) for vertices with both short and long tracks, and in figure 5.41 (bottom) for only long tracks. The normalization of the histograms follows equation 11 and assumes for muons 10^{15} muon decays in the target. The background is dramatically reduced in the background when only long tracks are used.

---

[4] The Kahan summation algorithm [29] in the mu3eAnaWeightSum executable is used to sum event weights in a sample.

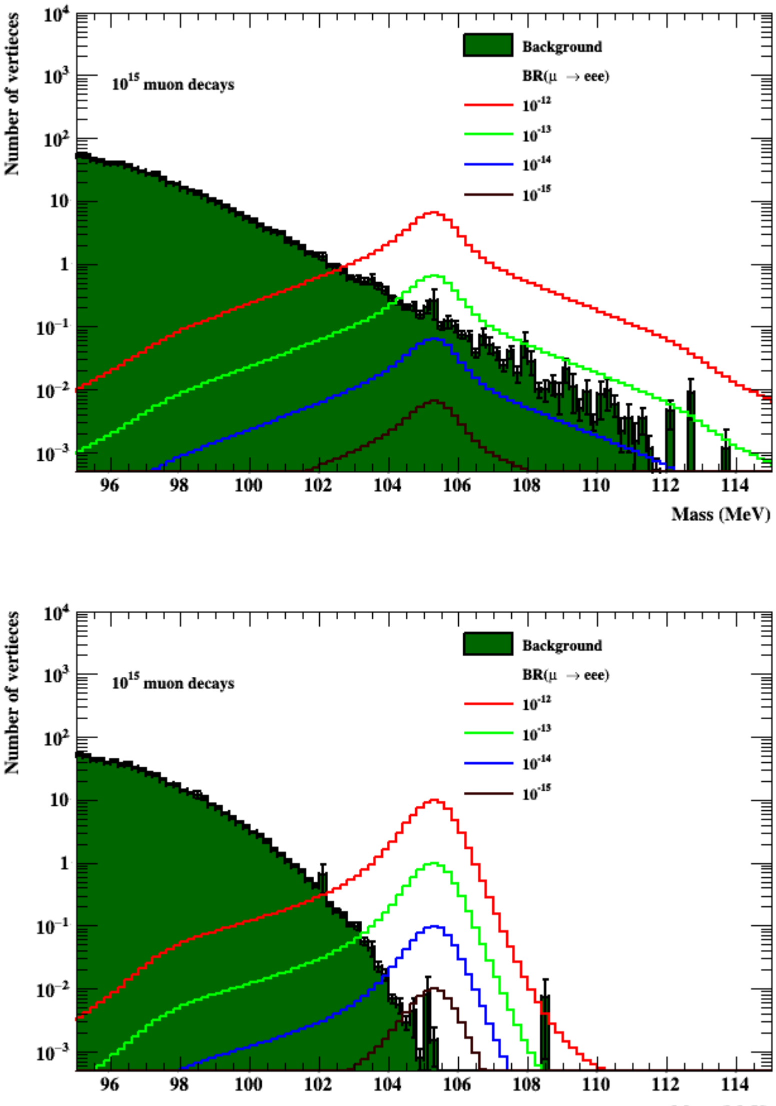

FIGURE 5.41: Spectra of the reconstructed invariant three-particle mass, after selection cuts, for signal decays for the background from radiative events with internal conversion expected for the full phase I run of the Mu3e experiment. Top: The invariant mass of the three tracks including all short and long tracks. Bottom: The invariant mass of the three tracks including only long tracks. The number of entries is 10 billion generated initially.

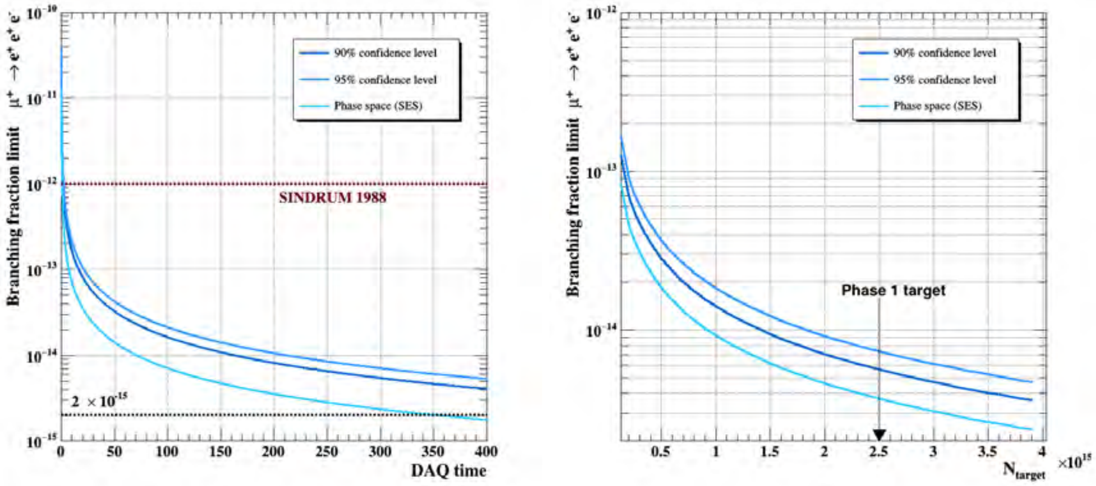

FIGURE 5.42: Single event sensitivity (SES) and the corresponding 90 % and 95 % C.L. upper limits as a function of the number of days of operation during phase-I (left) and the total number of muons on target (right).

5.5.3 Single Event Sensitivity

The sensitivity of the Mu3e experiment to a signal is estimated using the simulation and the determined selection efficiency. After applying selection cuts, it is assumed that all backgrounds will be suppressed well below the single event level.

The single-event sensitivity (SES) is defined as:

$$SES(\mu \to eee) \leq \frac{1}{\epsilon N_{\mu \to eee}} \tag{12}$$

where ϵ is the signal selection efficiency, calculated as defined in equation 1. N_μ is the expected number of muon signal decays in the target with the nominal Phase-I luminosity, $N_\mu = 1 \cdot 10^{15}$. In the absence of signal events, following Poisson statistics, an upper limit on the $\mu \to eee$ branching fraction of a rare decay can be derived:

$$B_{(1-\beta)CL} = -\ln\beta \cdot SES = \frac{-\ln\beta}{\epsilon N_{\mu \to eee}} \tag{13}$$

where $1 - \beta$ is the required confidence level. By using the signal efficiency after the selection that was described in table 5.7, the limits at 90 % and 95 % confidence level are shown in figure 5.42 as a function of days of data-taking during Mu3e Phase I. In the same figure, the single event sensitivity is also shown for comparison, as well as the

SINDRUM 90 % confidence level limit. Only long tracks have been used corresponding to a signal efficiency of $\epsilon = 0.163$.

6 Optimisation of Tracking with Holes on Track

The simulation of the Mu3e experiment in previous chapters assumed perfect performance of the detector. In reality, there will be alignment issues, and inefficient pixel sensors or modules. The impact of these effects is explored in this chapter. In the running experiment, known defects in the detector such as dead or noisy chips or modules will be recorded in a database. Improvements to the tracking reconstruction algorithms are discussed which are able to take into account these defects. This new algorithm can be used for data taking when the database is available. The optimisation of the tracking for inefficiencies on the inner and outer pixels layers are given in this chapter.

6.1 Optimisation of the Tracking Selection for Inefficient Pixel Layers

The track reconstruction for the Mu3e experiment is based on the multiple scattering triplet fit, outlined in Chapter 4. This section will outline the optimisation of tracking that can be used to exclude tracking layers when defects are known to be present. This is achieved using a sample of simulated muon decays. Figure 6.1 shows some event displays for reconstructed and true tracks for a perfect (left) and for an inefficient detector (right). In order to optimise the tracking for a track passing through an inefficient or masked layer, samples where a 100% inefficiency was introduced into a single layer were studied. For the purpose of the track optimisation it is assumed that inefficient layer is known to the tracking. A triplet of hits in the remaining 3 layers of the central station is reconstructed following the procedure described in section 4.1. A set of pre-selection cuts modified with respect to those described in section 5.1.1 are applied.

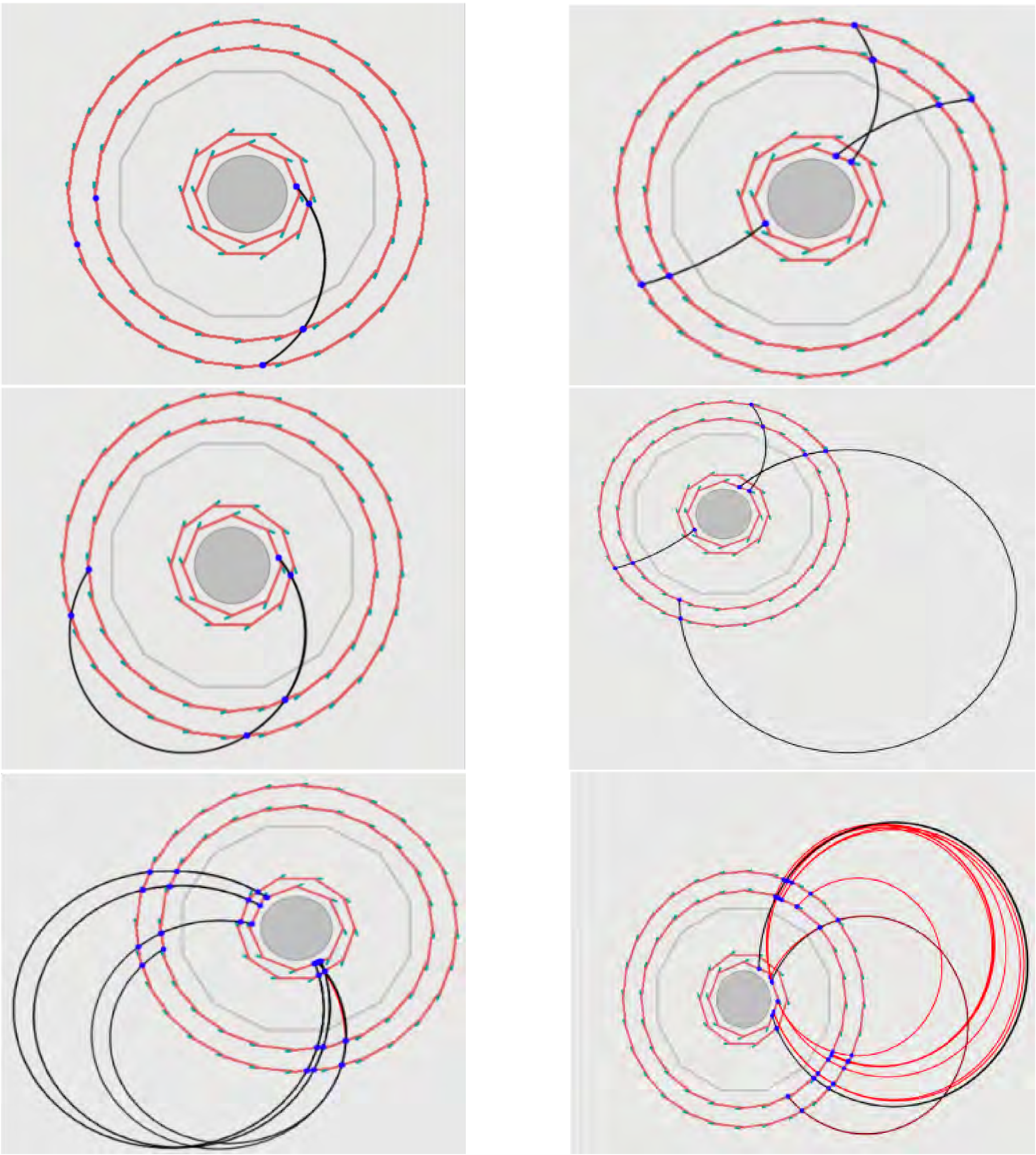

.

.

FIGURE 6.1: Examples of nominal tracks (left) and tracks with missing hits (right): standard short track with 4 pixel hits (top left), short track with missing pixel hits in 1-silicon layer (top right), standard long track with 6 pixel hits (middle left), long track with 5 hits with a missing pixel hit in one silicon layer (middle right), standard long track with 8 pixel hits (bottom left) and long track with 7-hits with a missing pixel hit in 1-silicon layer (bottom right).

.

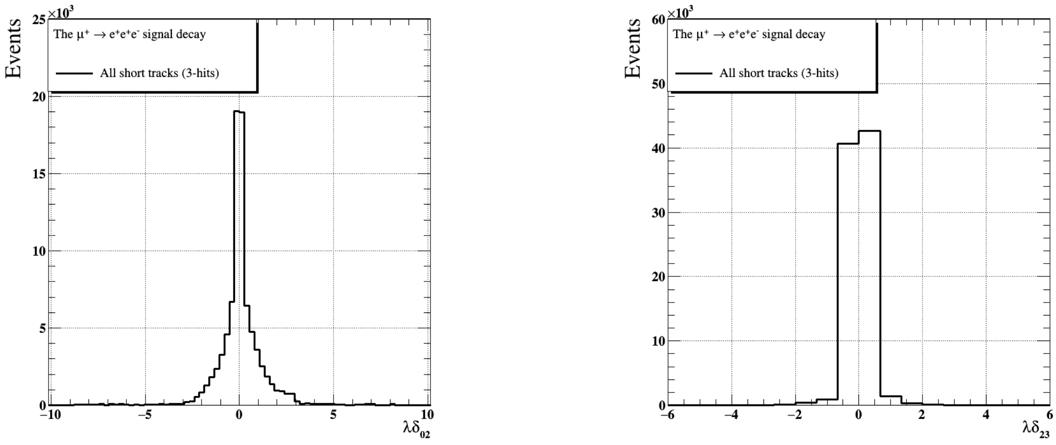

(A) z difference of hits between layers 0 and 2 in the central station of the detector.

(B) z difference of hits between layers 2 and 3 in the central station of the detector.

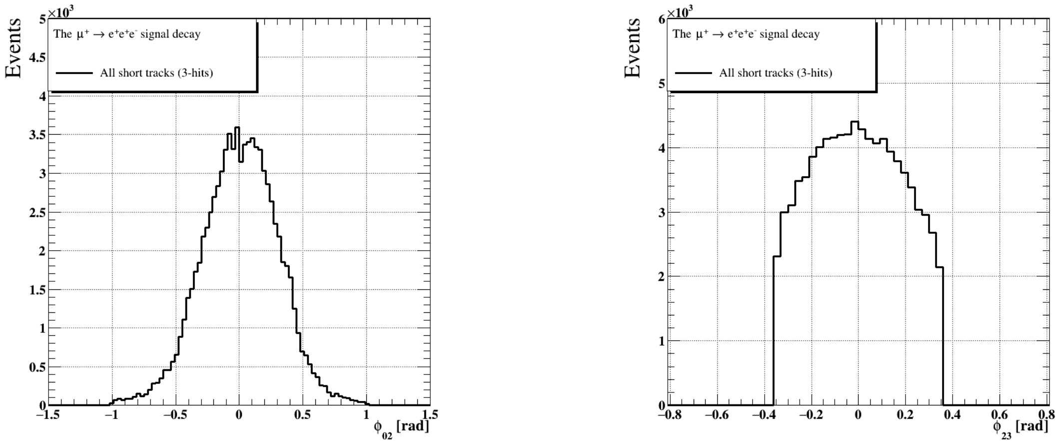

(C) $\Delta\phi$ distribution of hits between layers 0 and 2 in the central station of the detector.

(D) $\Delta\phi$ distribution of hits between layers 2 and 3 in the central station of the detector.

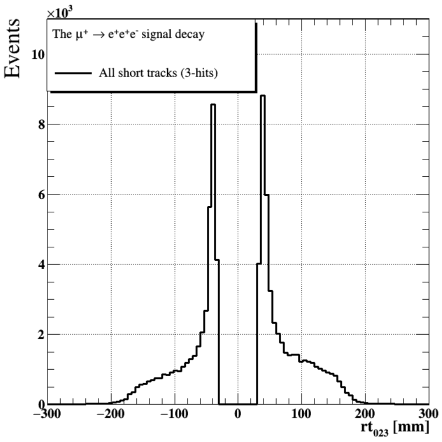

(E) Transverse radius distribution between layers 0, 2 and 3 in the central station of the detector.

FIGURE 6.2: Variables used in the optimized tracking cuts for short tracks with 3 pixel hits if layer 1 is 100% inefficient, for signal muon events.

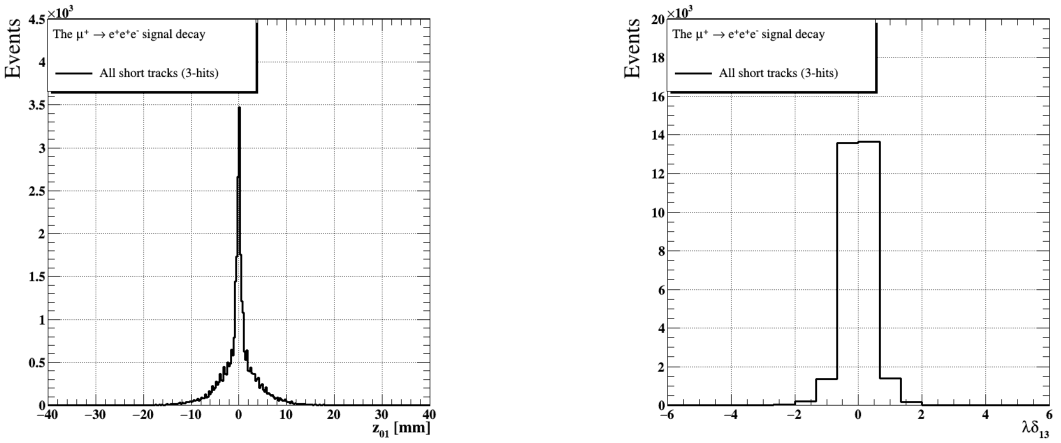

(A) z difference of hits between layers 0 and 1 in the central station of the detector.

(B) z difference of hits between layers 1 and 3 in the central station of the detector.

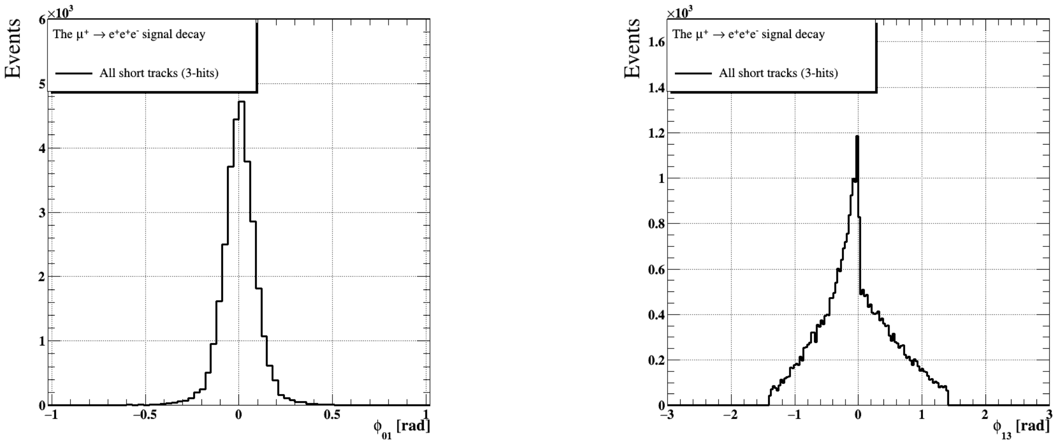

(C) $\Delta\phi$ distribution between layers 0 and 1 in the central station of the detector.

(D) $\Delta\phi$ distribution of hits between layers 1 and 3 in the central station of the detector.

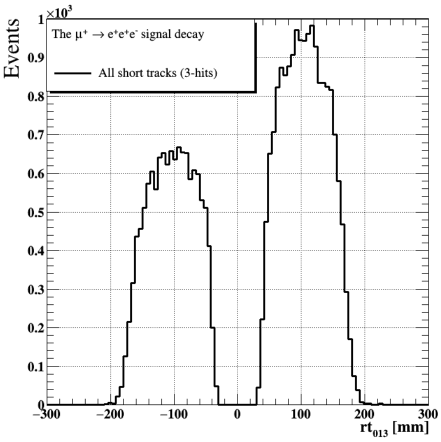

(E) Transverse radius distribution between layers 0, 1 and 3 in the central station of the detector.

FIGURE 6.3: Variables used in the optimized tracking cuts for short tracks with 3 pixel hits if layer 2 is 100% inefficient, for signal muon events.

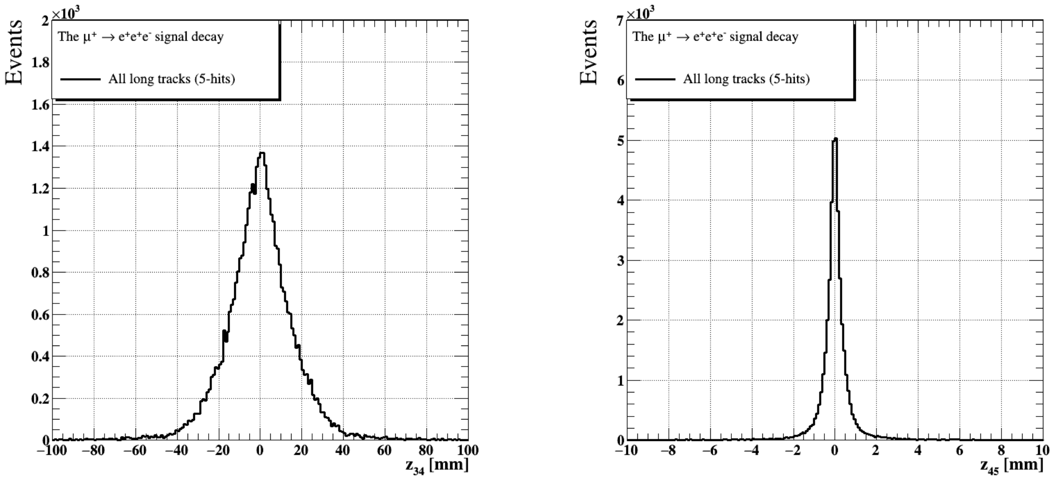

(A) z difference of hits between layers 3 and 4. (B) z difference of hits between layers 4 and 5.

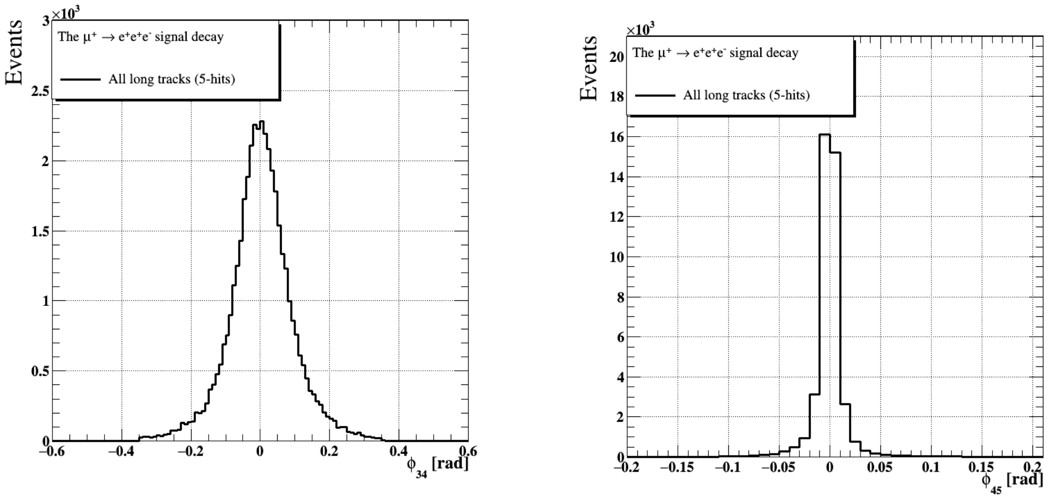

(C) $\Delta\phi$ distribution of hits between layers 3 and 4. (D) $\Delta\phi$ distribution between layers 4 and 5.

FIGURE 6.4: Variables used in the optimized cuts for long tracks with 5 pixel hits if layer 1 or 2 are 100% inefficient, for signal muon events.

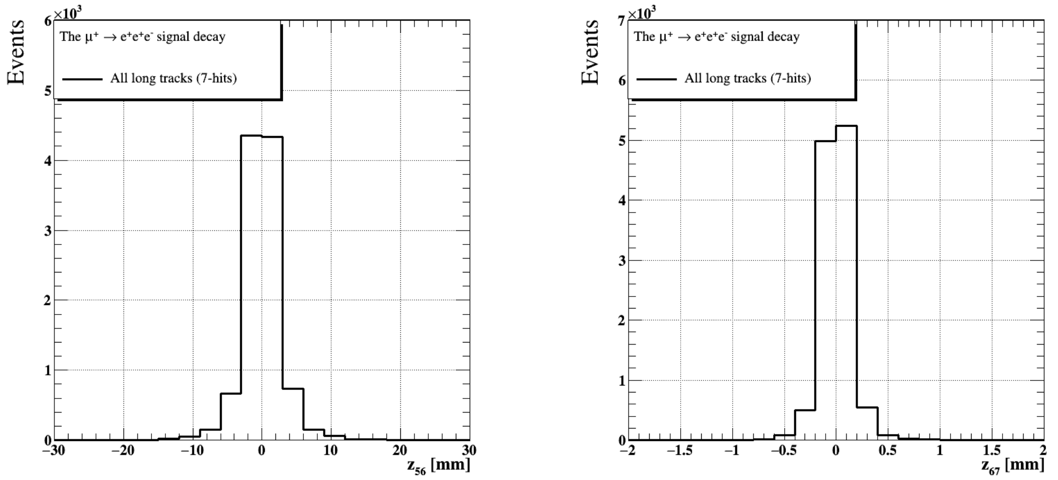

(A) z difference of hits between layers 5 and 6.

(B) z difference of hits between layers 6 and 7.

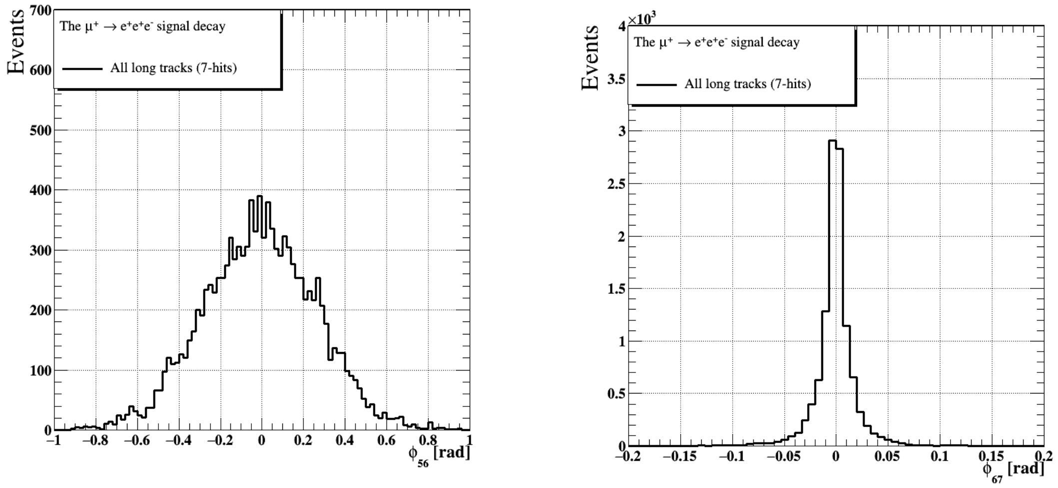

(C) $\Delta\phi$ distribution of hits between layers 5 and 6.

(D) $\Delta\phi$ distribution between layers 6 and 7.

FIGURE 6.5: Variables used in the optimized detector inefficient for the long tracks with 7 pixel hits if layer 1 or 2 are 100% inefficiency, for signal muon events.

In order to reduce the long computing time, some geometrical cuts need to be applied. These cuts include the constraints on variables such as Z, the ϕ angles and the transverse radius between layers.

The modified cuts are listed in tables 6.1 and 6.2 for short tracks with missing hits in layers 1 or 2, respectively. Tables 6.3 and 6.4 summarize the pre-selection cuts for 5-hit and 7-hit long tracks, respectively. Figures 6.2 to 6.5 show the distributions of the variables used in the pre-selection for each of these cases. The drift in the positive side in figure 6.3D is due to a constraint between the first two pixel layers and a large distance between layers 2 and 3, also the positrons are observed more than electron tracks.

variable	cut value
$\lvert\lambda\delta_{20}\rvert = \lvert z_{02}/r_{02}\rvert$	< 10 no unit
$\lvert\lambda\delta_{32}\rvert = \lvert z_{02}/r_{02} - z_{32}/r_{32}\rvert$	$<$ 4 no unit
$\lvert\phi_{20}\rvert$	$<$ 1.0 rad
$\lvert\phi_{32}\rvert$	$<$ 0.4 rad
$\lvert rt_{023}\rvert$	30 mm < $\text{rt}_{023} <$ 250 mm

TABLE 6.1: Summary of the optimized pre-selection cuts for short tracks with missing hits in layer 1 in which z_{ij} and ϕ_{ij} are the z-distance and azimuthal angle between hits on layers i and j, respectively.

variable	cut value
$\lvert z_{10}\rvert$	< 30 mm
$\lvert\lambda\delta_{31}\rvert = \lvert z_{10}/r_{10} - z_{31}/r_{31}\rvert$	$<$ 3 no unit
$\lvert\phi_{20}\rvert$	$<$ 0.5 rad
$\lvert\phi_{32}\rvert$	$<$ 1.5 rad
$\lvert \text{rt}_{013}\rvert$	30 mm < $\text{rt}_{013} <$ 250mm

TABLE 6.2: Summary of the maximized pre-selection cuts for short tracks with missing hits in layer 2 in which z_{ij} and ϕ_{ij} are the z-distance and azimuthal angle between hits on layers i and j, respectively.

variable	cut value
$\lvert z_{43}\rvert$	< 100 mm
$\lvert z_{54}\rvert$	< 8 mm
$\lvert \phi_{43}\rvert$	< 0.4 rad
$\lvert \phi_{54}\rvert$	< 0.1 rad

TABLE 6.3: Summary of the maximized pre-selection cuts for 5-hits long tracks in which z_{ij} and ϕ_{ij} are the z-distance and azimuthal angle between hits on layers i and j, respectively.

variable	cut value
$\lvert z_{54}\rvert$	< 20 mm
$\lvert z_{65}\rvert$	< 1 mm
$\lvert \phi_{54}\rvert$	< 1.0 rad
$\lvert \phi_{65}\rvert$	< 0.15 rad

TABLE 6.4: Summary of the maximized pre-selection cuts for 7-hits long tracks in which z_{ij} and ϕ_{ij} are the distance and azimuthal angle between hits on layers i and j, respectively.

Following the procedure presented in section 5.1.2, these track selection criteria have been optimised, based on the efficiency·purity. The variables used to separate correctly reconstructed tracks (truth-matched) of signal muon decays from fake tracks are: the χ^2 of the track fit, the dip angle λ_{01}, the intersection z_0 of the track with the target region, and the reconstructed momentum. These were discussed in the previous chapter.

Figure 6.6 shows the χ^2 of the track fit for all the types of tracks in the signal sample, with the corresponding efficiency, purity and their product. 7-hit long tracks have lower purity compared to nominal 8-hit tracks (see figure 5.8). The distributions for Z_0 and λ_{01} of the track for signal muon decays are shown in figures 6.7 and 6.8, respectively.

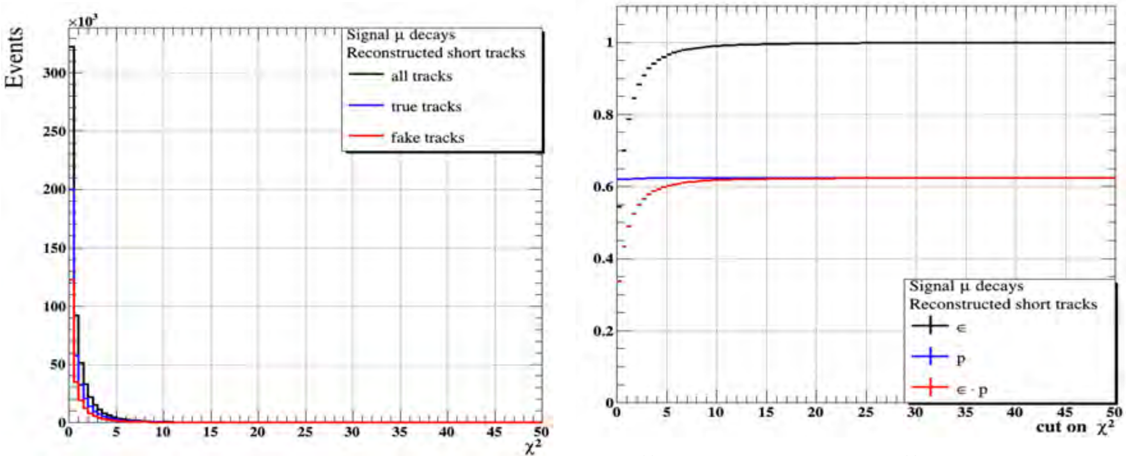

(A) χ^2 of the track fit for 3-hit short tracks for the signal muon decays.

(B) Efficiency, purity and efficiency×purity as a function of the applied χ^2 cut for 3-hit short tracks.

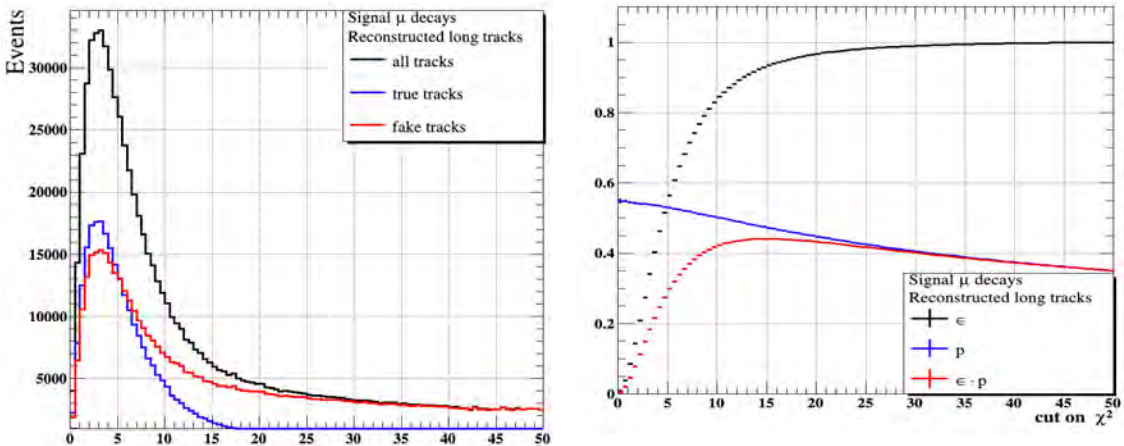

(C) χ^2 of the track fit for 5-hit long tracks for the signal muon decays.

(D) Efficiency, purity and efficiency×purity as a function of the applied χ^2 cut for 5-hit long tracks.

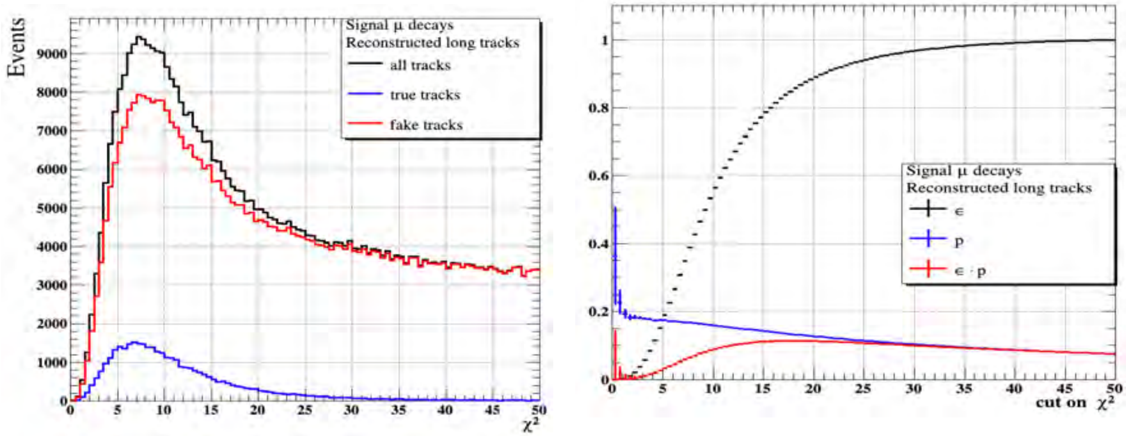

(E) χ^2 of the track fit for 7-hit long tracks for signal muon decays.

(F) Efficiency, purity and efficiency×purity as a function of the applied χ^2 cut for 7-hit long tracks.

FIGURE 6.6: χ^2 of the track fit for signal muon decays if layer 1 is inefficient.

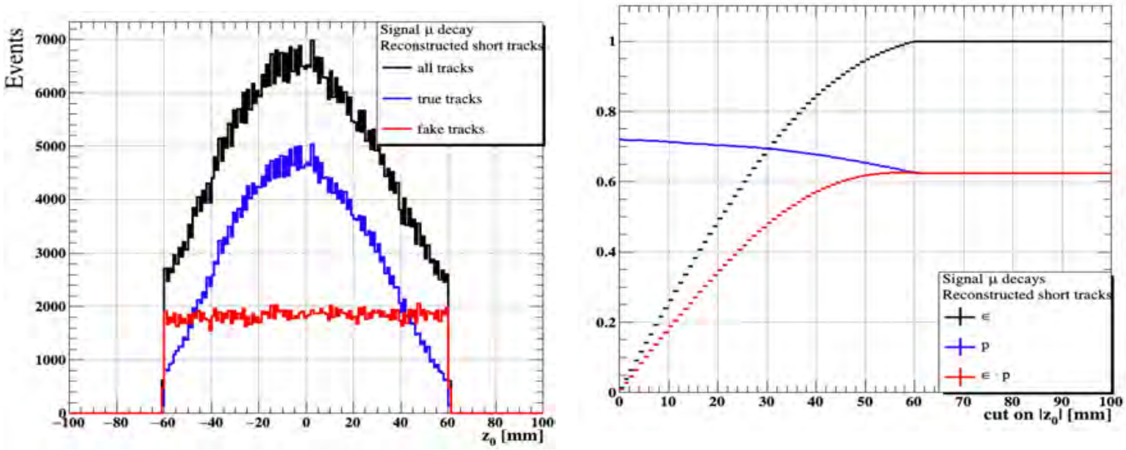

(A) Z_0 of the track for 3-hit short tracks for the signal muon decays.

(B) Efficiency, purity and efficiency×purity as function of the applied Z_0 cut for 3-hit short tracks.

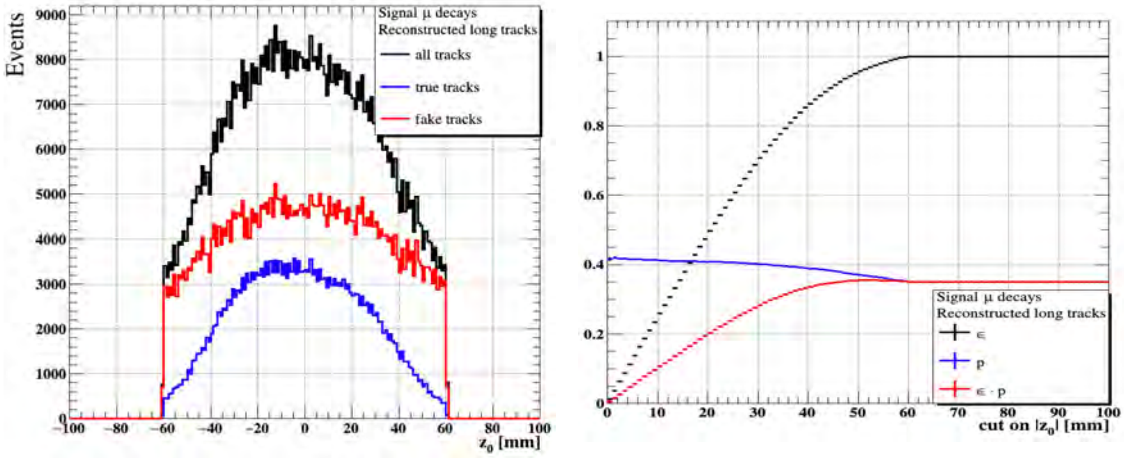

(C) Z_0 of the track for 5-hit long tracks for the signal muon decays.

(D) Efficiency, purity and efficiency×purity as a function of the Z_0 cut for 5-hit long tracks.

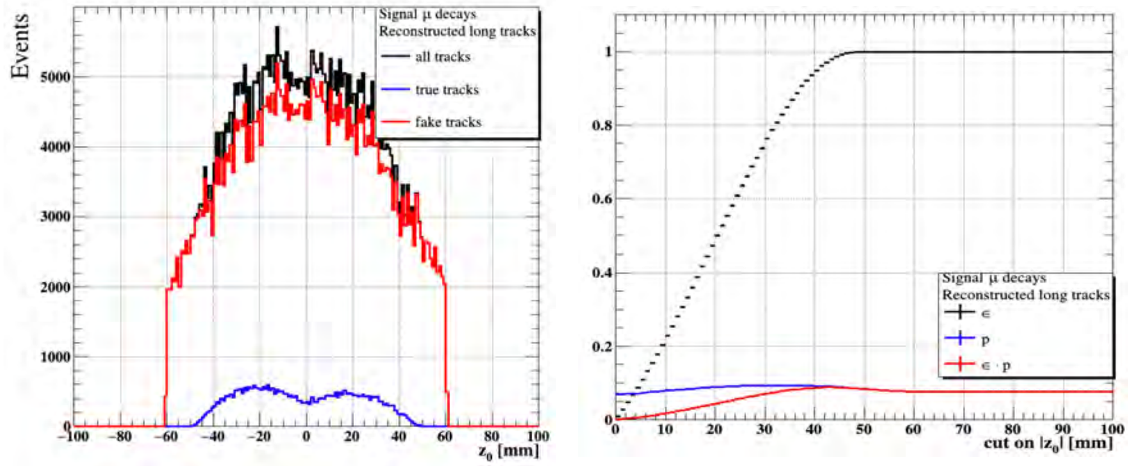

(E) Z_0 of the track for 7-hit long tracks for the signal muon decays.

(F) Efficiency, purity and efficiency×purity as a function of the Z_0 cut for 7-hit long tracks.

FIGURE 6.7: Z_0 of the track for signal muon decays if layer 1 is inefficient.

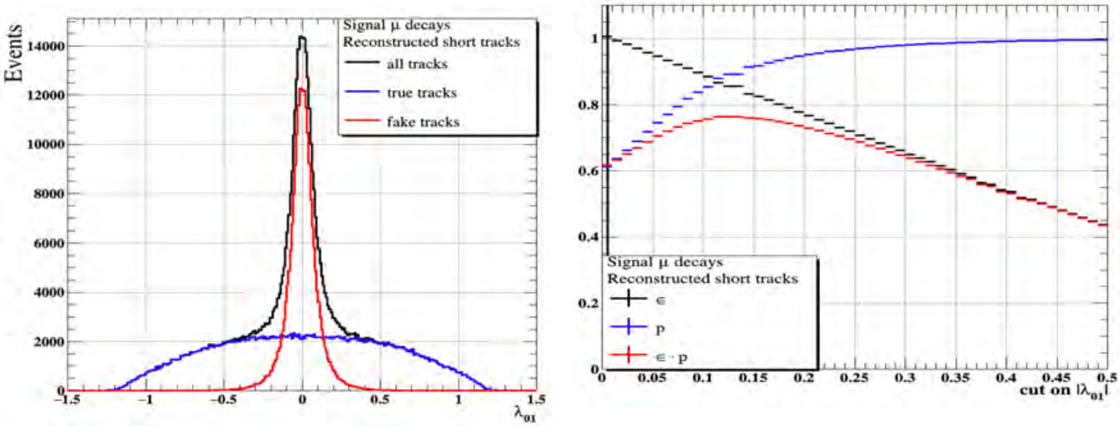

(A) λ_{01} of the track for 3-hit short tracks for the signal muon decays.

(B) Efficiency, purity and efficiency×purity as a function of the applied λ_{01} cut for 3-hit short tracks.

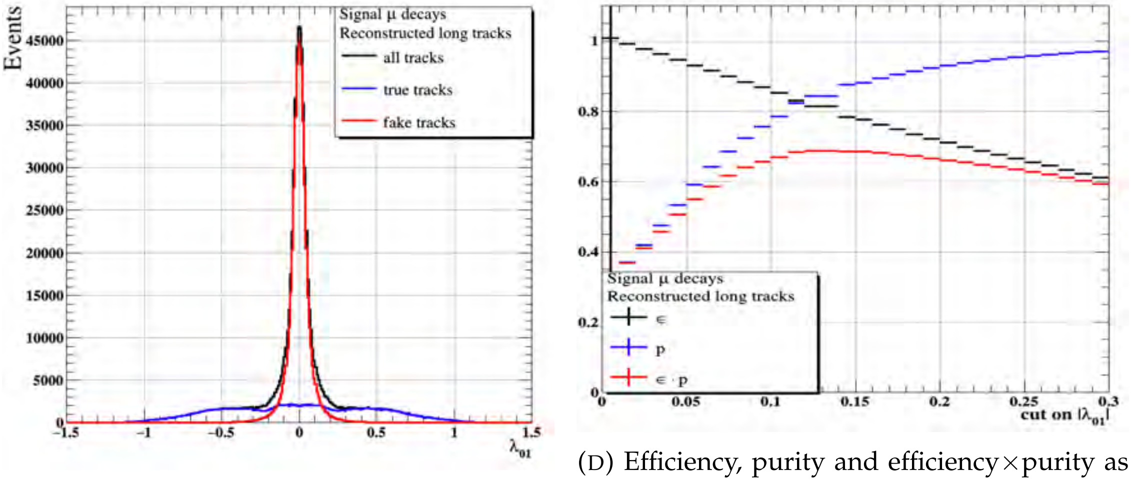

(C) λ_{01} of the track for 5-hit long tracks for the signal muon decays.

(D) Efficiency, purity and efficiency×purity as a function of the applied λ_{01} cut for 5-hit long tracks.

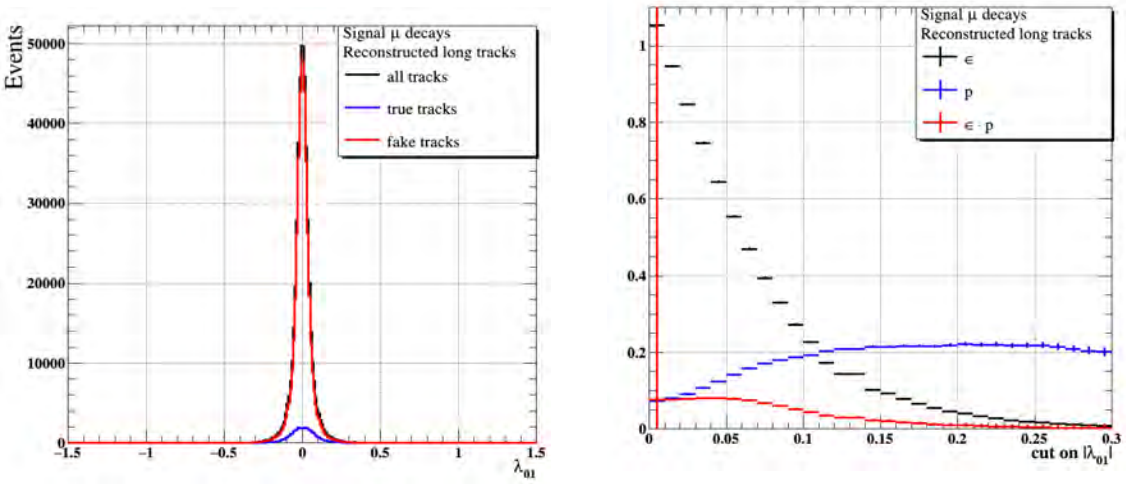

(E) λ_{01} of the track for 7-hit long tracks for the signal muon decays.

(F) Efficiency, purity and efficiency×purity as a function of the applied λ_{01} cut for 7-hit long tracks.

FIGURE 6.8: λ_{01} of the track for signal muon decays if layer 1 is inefficient.

There is a large distance between layer 1 and 2 in the central station of the detector as shown in figure 5.3. These means that if layer 2 has missing hits, more fake tracks will be observed and there is a smaller purity than the case of a missing inner layer hit. Figure 6.9 shows the χ^2 of the track fit for all types of tracks for signal decays and the corresponding efficiency, purity and the product between them. Further cuts are placed on Z_0 and λ_{01} of the track. These are listed in table 6.5 and are applied to tracks with missing hits in any of the layers. The distributions of Z_0 and λ_{01} for different track categories are shown in figures 6.10 and 6.11, respectively.

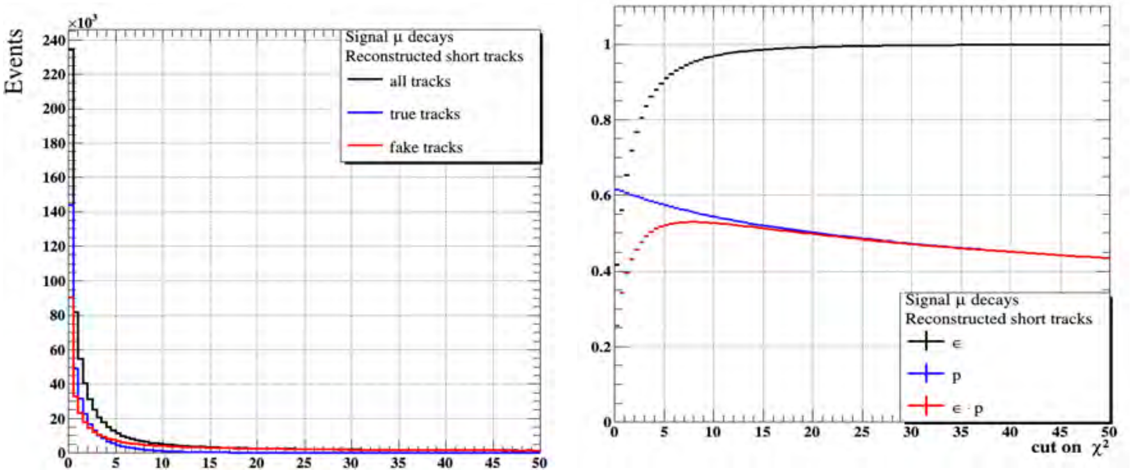

(A) χ^2 of the track for 3-hits short tracks for the signal muon decays.

(B) Efficiency, purity and efficiency×purity as a function of the applied χ^2 cut for 3-hits short tracks.

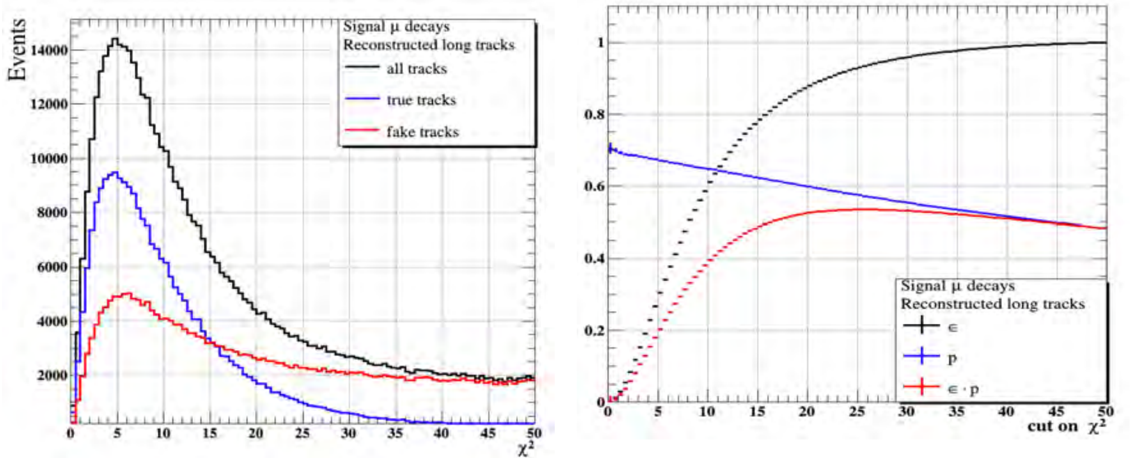

(C) χ^2 of the track fit for 5-hits long tracks for the signal muon decays.

(D) Efficiency, purity and efficiency×purity as a function of the applied χ^2 cut for 5-hits long tracks.

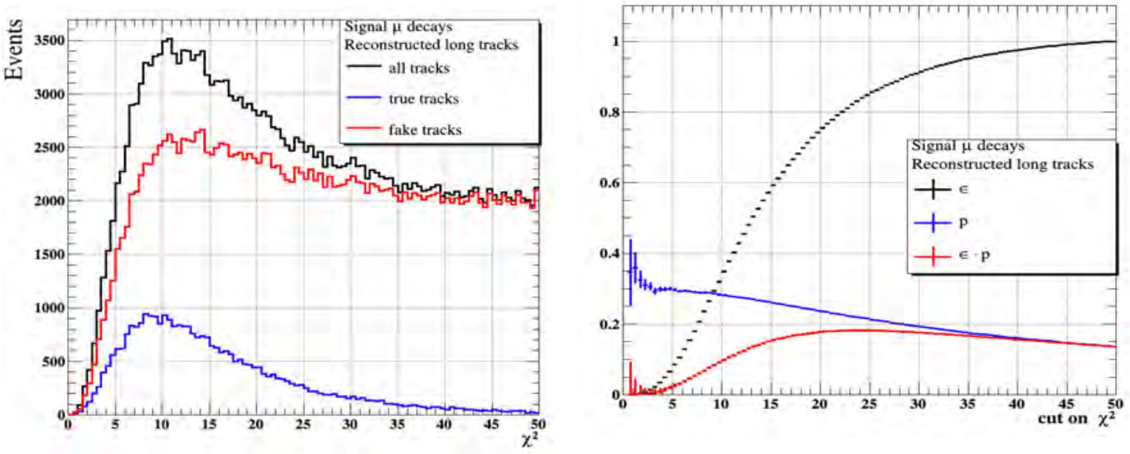

(E) χ^2 of the track fit for 7-hits long tracks for the signal muon decays.

(F) Efficiency, purity and efficiency×purity as a function of the applied χ^2 cut for 7-hits long tracks.

FIGURE 6.9: χ^2 of the track for signal muon decays if layer 2 is inefficient.

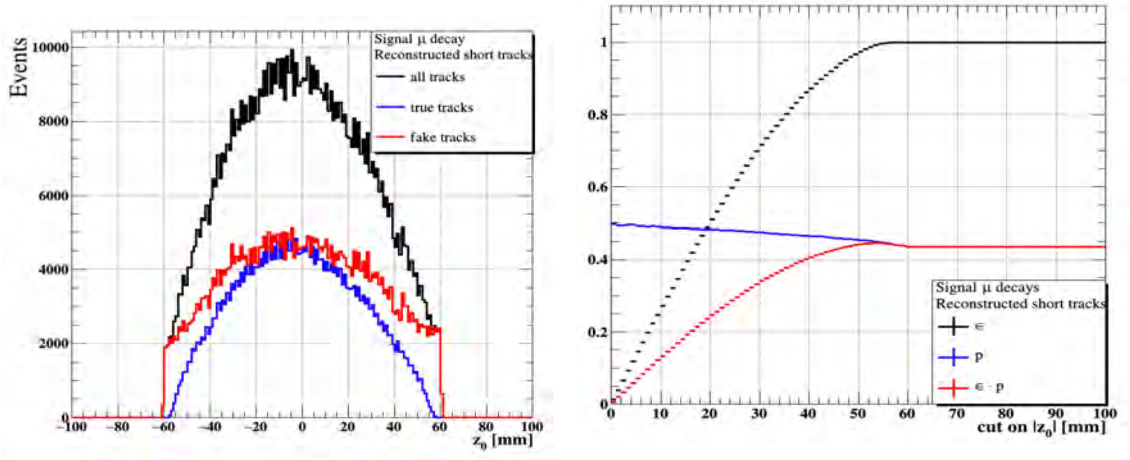

(A) Z_0 of the track for 3-hits short tracks for the signal muon decays.

(B) Efficiency, purity and efficiency×purity as a function of the applied Z_0 cut for 3-hits short tracks.

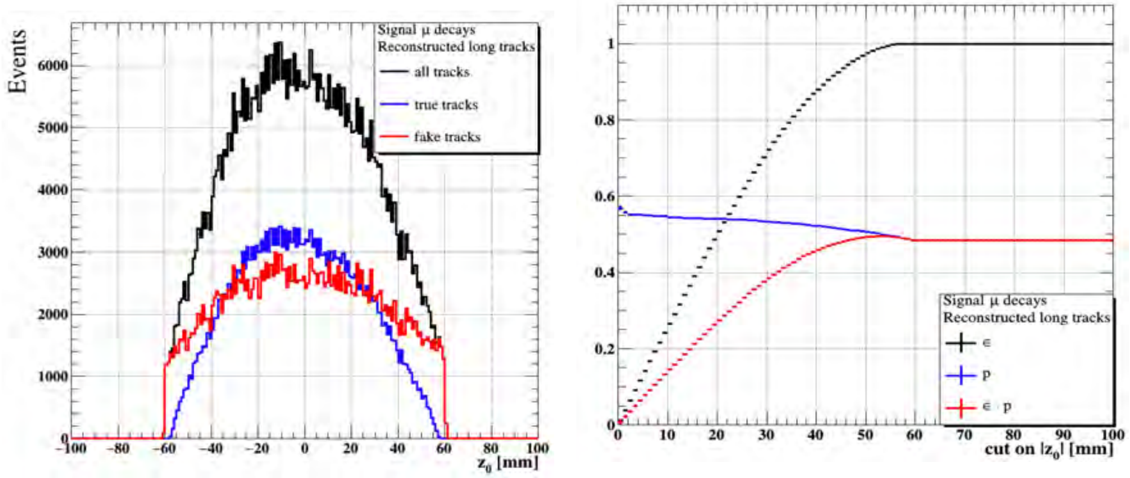

(C) Z_0 of the track for 5-hits long tracks for the signal muon decays.

(D) Efficiency, purity and efficiency×purity as a function of the applied Z_0 cut for 5-hits long tracks.

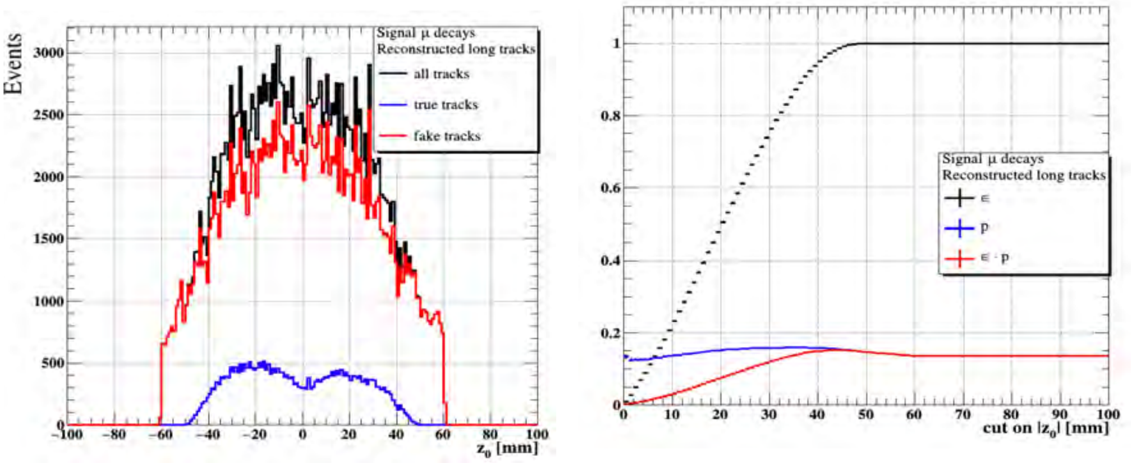

(E) Z_0 of the track for 7-hits long tracks for the signal muon decays.

(F) Efficiency, purity and efficiency×purity as a function of the applied Z_0 cut for 7-hits long tracks.

FIGURE 6.10: Z_0 of the track for signal muon decays if layer 2 is inefficient.

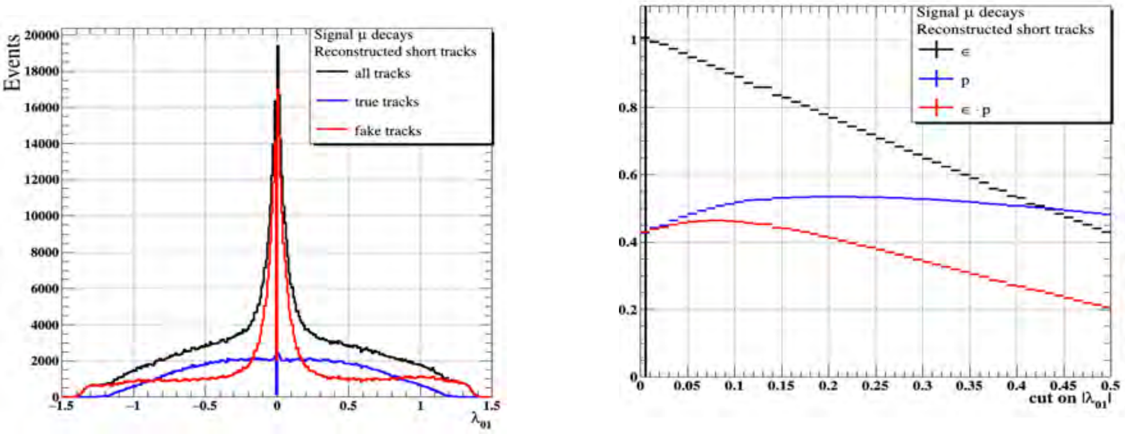

(A) λ_{01} of the track for 3-hits short tracks for the signal muon decays.

(B) Efficiency, purity and efficiency×purity as a function of the applied λ_{01} cut for 3-hits short tracks.

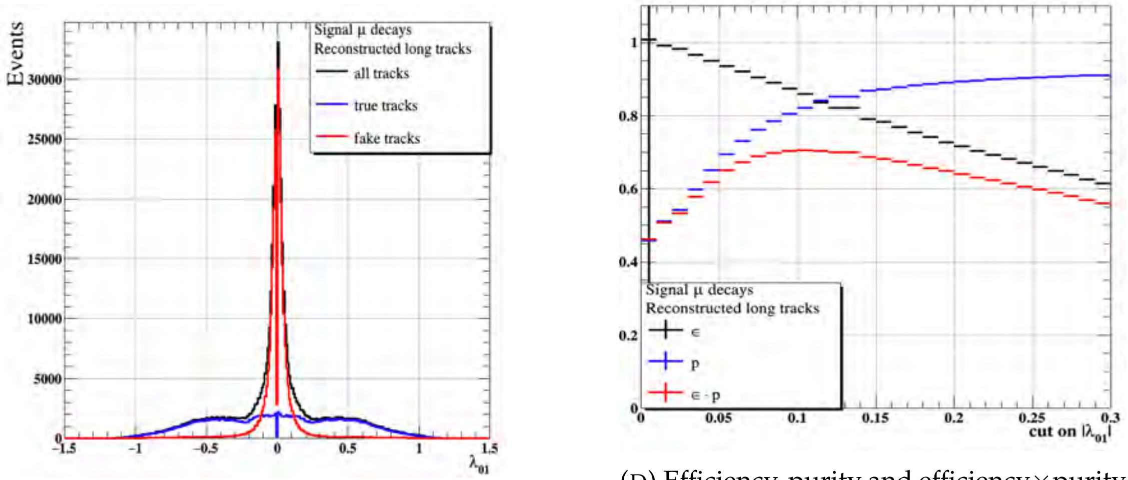

(C) λ_{01} of the track for 5-hits long tracks for the signal muon decays.

(D) Efficiency, purity and efficiency×purity as a function of the applied λ_{01} cut for 5-hits long tracks.

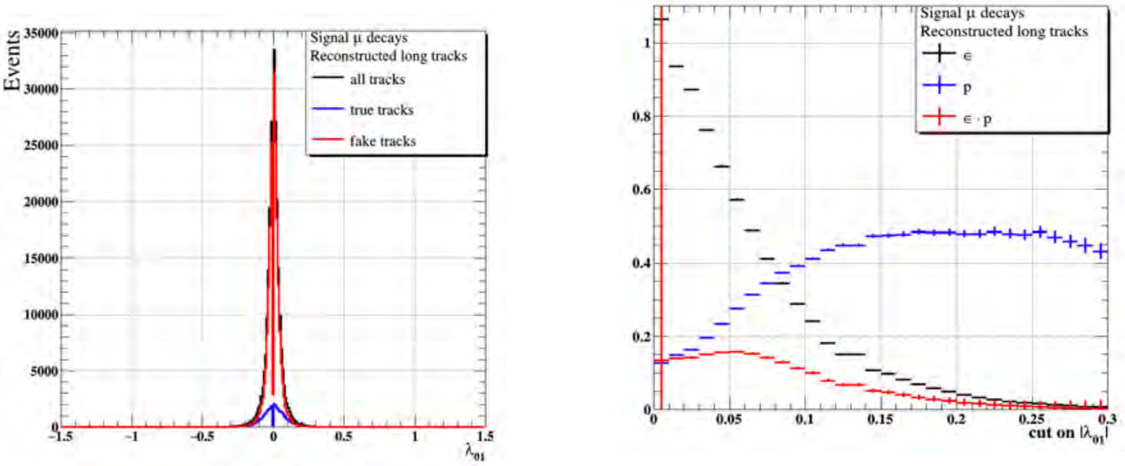

(E) λ_{01} of the track for 7-hits long tracks for the signal muon decays.

(F) Efficiency, purity and efficiency×purity as a function of the applied λ_{01} cut for 7-hits long tracks.

FIGURE 6.11: λ_{01} of the track for signal muon decays if layer 2 is inefficient.

The resultant overall track efficiency, purity and their product for the nominal tracking and for tracks with missing hits in layers 1 or 2 are shown in tables 6.6, 6.7 and 6.8. For

z0 (mm)	< 50
$\lambda 01(rad) : 3-, 5-, 7-hits$	> 0.1
$\chi^2 : 3-, 5-, 7-hits$	10, 20, 20

TABLE 6.5: Selection cuts for short and long tracks in the inefficient detector.

completeness, the results for tracks with missing hits in layers 0 and 3 are shown in the next chapter (figure 7.1). Figures 6.12 and 6.13 show the reconstructed momentum after applying the track selection cuts for the different categories of long tracks with missing hits to compare with nominal tracks in figures 5.12 (Chapter 5). Inefficiencies in the inner pixel layers have a greater impact on the performance of tracks than inefficiencies in the outer layers. Others decays are shown as well due to the composition, such as correctly reconstructed positron tracks.

6.1.1 Momentum, Vertex and Mass Resolution for Tracks with Missing hits

For the study of the momentum resolution, a signal sample was simulated and reconstructed to compare reconstructed and simulated momenta after applying the previously discussed cuts to select tracks with missing hits. The short and long tracks are split into different bins between 10 to 55 MeV/c, and the resolution is estimated in each bin by fitting the distribution of the difference between the true and reconstructed momentum to a double-sided crystal ball function. The fit results are summarised in figure 6.14 for nominal tracks and tracks with new tracking algorithm applied to the detector simulated with 100% inefficiencies in layers 1 and 2. In these plots, it can be seen that the resolution steadily deteriorates as the momentum of the tracks increases. In addition, it can be seen that the resolution for long tracks is much better than short tracks. Also, resolution for tracks with missing hits in inner layers are critical more than outer pixel layers.

The properties of the vertex fit are studied in simulated events to check how well the vertex fit performs with an inefficient detector. Figure 6.16 shows distance between the reconstructed and true vertex position in x, y, z and in 3 dimensions with 3 long tracks after applying the frame selection cuts described in section 5.1.3 for detector with 100% inefficiency for inner pixel layer 1.

The invariant mass resolution of the signal muon decays must be good in order to reject backgrounds that occur in the Mu3e experiment, but the detector could be inefficient, so the mass resolution will be worse compared with the nominal detector shown in the

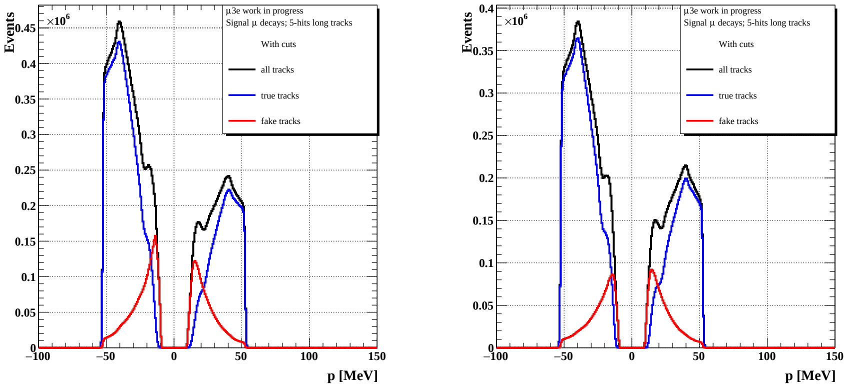

FIGURE 6.12: Reconstructed momentum for signal muon decays after applying the track reconstruction cuts for the long nominal and tracks with 5-pixel hits if layer 1 and 2 are inefficient, respectively from left to right.

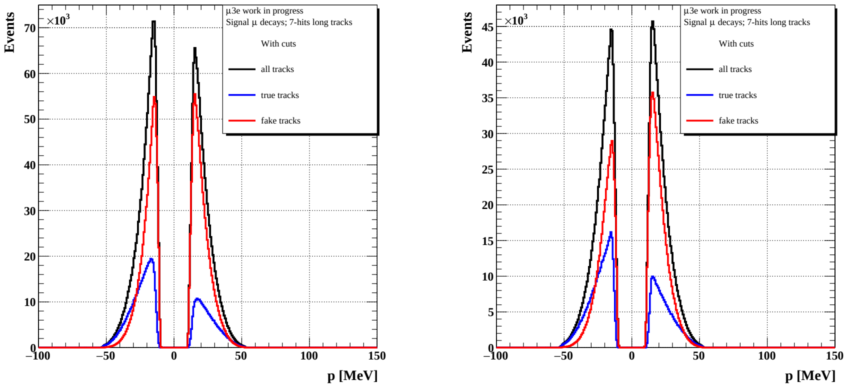

FIGURE 6.13: Reconstructed momentum for signal muon decays after applying the track reconstruction cuts for the long nominal and inefficient tracks with 7-pixel hits if layer 1 and 2 are inefficient, respectively from left to right.

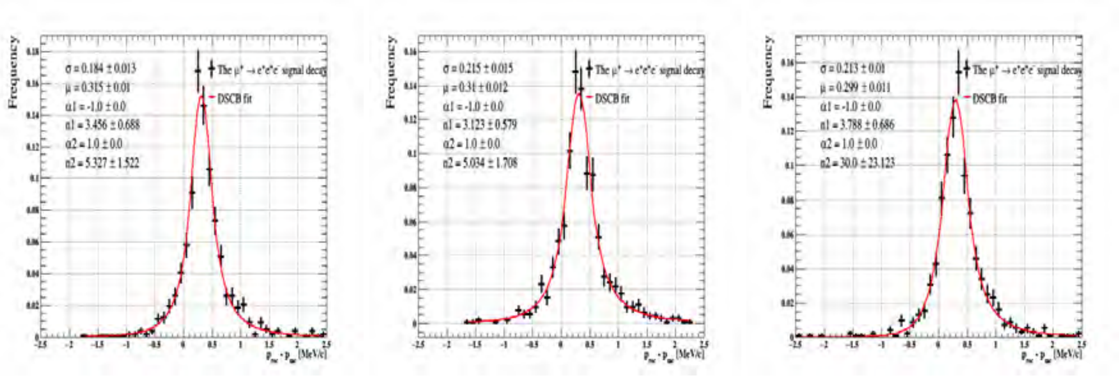

(A) 5-hits; 18-20 MeV (B) 5-hits; 20-22 MeV (C) 5-hits; 22-24 MeV

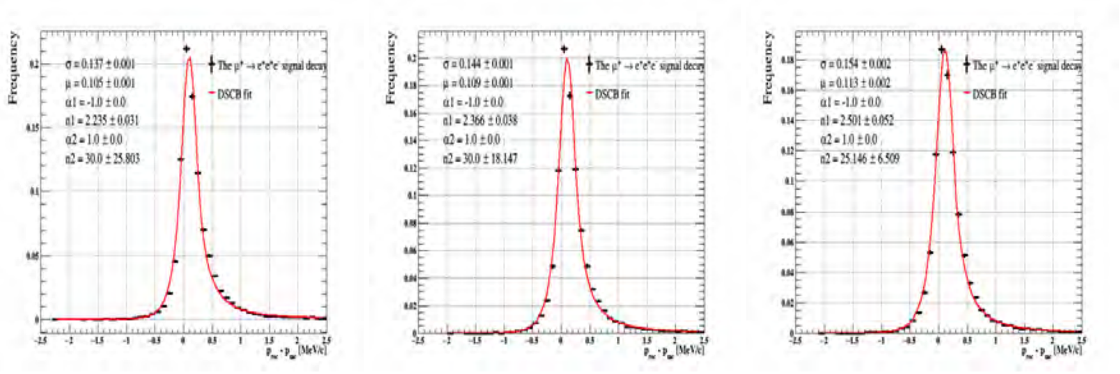

(D) 5-hits; 18-20 MeV (E) 5-hits; 20-22 MeV (F) 5-hits; 22-24 MeV

FIGURE 6.14: Momentum resolution (with track momenta 18-20, 20-22, 22-24 MeV) for long tracks with 5-hits 100% inefficiency in layer 1 and 2, respectively. The fitting function is a Double-sided crystal ball function.

Chapter 5. The reconstructed muon mass in Mu3e phase 1 simulation is shown in figure 6.17 for three long tracks for inefficient inner pixel layer 1 with 10% inefficiency. A double-sided crystal ball function is used to fit the distributions, the resolution around $\sigma = 0.401 \pm 0.006\ MeV/c^2$ is determined compared to a value of $0.391 \pm 0.002\ MeV/c^2$ for the nominal detector as presented in figure 5.27 (Chapter 5).

Also, it is important to check the signal efficiency for three tracks after the vertex fit for phase-space distribution for nominal and inefficient detector if layer 1 or 2 is inefficient. These are shown in table 6.10, 6.11 and 6.12, respectively. Inefficiencies in inner pixel layers have a greater impact on signal efficiency than inefficiencies in outer layers.

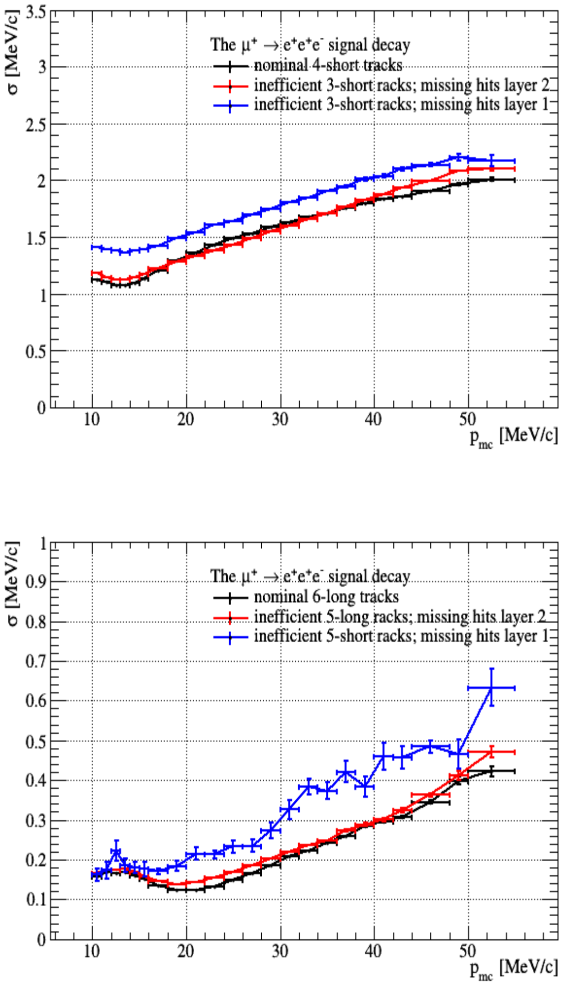

FIGURE 6.15: Summary plots for the variations of the momentum resolutions obtained via using Double-sided crystal ball fit as a function of the true track momentum for nominal tracks and tracks with missing hits in inner and outer pixel layers.

Reconstruction	Cuts applied	
Short 4-hit tracks	ϵ	0.904
	p	0.931
	$\epsilon \cdot p$	0.841
Long 6-hit tracks	ϵ	0.898
	p	0.907
	$\epsilon \cdot p$	0.814
Long 8-hit tracks	ϵ	0.945
	p	0.642
	$\epsilon \cdot p$	0.607

TABLE 6.6: Efficiency ϵ, purity p and $\epsilon \cdot p$ after applying selection cuts for signal muon decays in a perfect detector.

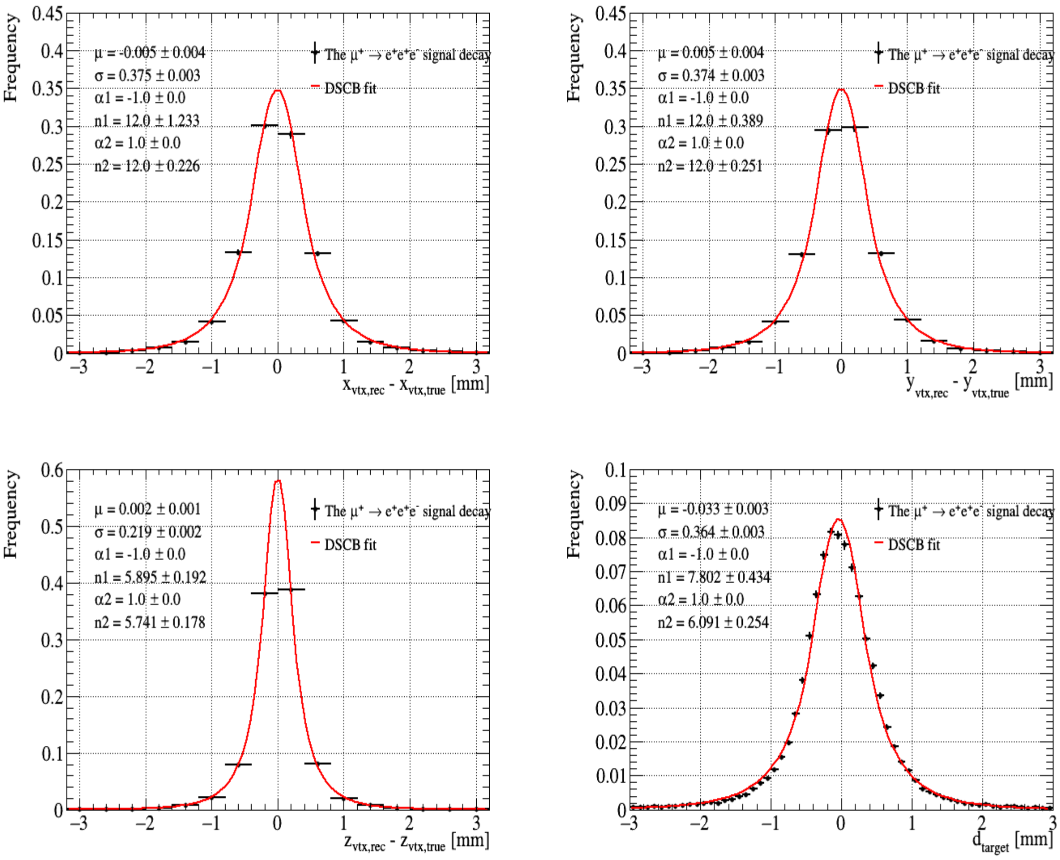

FIGURE 6.16: Vertex resolution of the signal muon decays in Mu3e phase 1 simulation in the case if inner layer 1 is inefficient with 100% inefficiency, and target distance which is a distance of the reconstructed vertex to the target region (negative if inside the target). The three long tracks with 5-pixel hits only are selected, top left in x position, top right in y position, bottom left in z position and bottom right in the distance to the target. The fits are double-sided crystal ball functions.

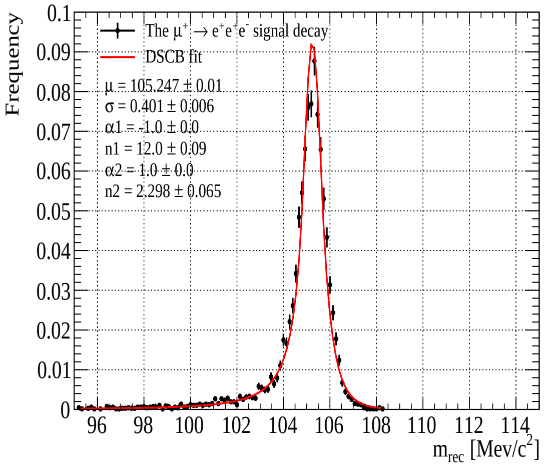

FIGURE 6.17: The reconstructed muon mass in Mu3e phase 1 simulation is shown in figure 6.17 for three long tracks in the scenario where pixel layer 1 has a 10% inefficiency. A double-sided crystal ball function is used to fit the distributions.

Reconstruction		Cuts applied
Short 3-hit tracks	ϵ	0.816
	p	0.884
	$\epsilon \cdot p$	0.722
Long 5-hit tracks	ϵ	0.743
	p	0.848
	$\epsilon \cdot p$	0.631
Long 7-hit tracks	ϵ	0.884
	p	0.142
	$\epsilon \cdot p$	0.126

TABLE 6.7: Efficiency ϵ, purity p and $\epsilon \cdot p$ after applying selection cuts for signal muon decays for an imperfect detector with layer 1 missing.

Reconstruction		Cuts applied
Short 3-hit tracks	ϵ	0.826
	p	0.671
	$\epsilon \cdot p$	0.554
Long 5-hit tracks	ϵ	0.79
	p	0.856
	$\epsilon \cdot p$	0.676
Long 7-hit tracks	ϵ	0.847
	p	0.23
	$\epsilon \cdot p$	0.195

TABLE 6.8: Efficiency ϵ, purity p and $\epsilon \cdot p$ after applying selection cuts for signal muon decays for an imperfect detector with layer 2 missing.

	$\epsilon_{\text{all tracks}}$	$\epsilon_{\text{3 recurler}}$
events with reconstructed vertex before cuts	0.776(4)	0.866(5)
events with reconstructed vertex after cuts	0.290(1)	0.163(1)

TABLE 6.9: Efficiency after the vertex fit for signal events for the perfect detector.

	$\epsilon_{\text{all tracks}}$	$\epsilon_{\text{3 recurler}}$
events with reconstructed vertex before cuts	0.555(3)	0.689(1)
events with reconstructed vertex after cuts	0.163(1)	0.071(1)

TABLE 6.10: Efficiency after the vertex fit for signal events if layer 1 is 100% inefficient.

	$\epsilon_{\text{all tracks}}$	$\epsilon_{\text{3 recurler}}$
events with reconstructed vertex before cuts	0.633(4)	0.790(2)
events with reconstructed vertex after cuts	0.192(4)	0.098(3)

TABLE 6.11: Efficiency after the vertex fit for signal events if layer 2 is 100% inefficient.

7 Expected Performance of the Mu3e Experiment in Different Detector Conditions

In this chapter, the results of studies of the Mu3e tracking performance in different scenarios are presented. Section 7.1 explores the impact of detector inefficiencies and how performance can be recovered using the tracking modifications discussed in Chapter 6. Section 7.2 explores the impact of noise, and 7.3 the impact of misalignment.

7.1 Detector Inefficiency Due to Missing Pixel Hits

Figure 7.1 shows how the efficiency of the nominal, long-6 and long-8 tracks and the recovered new holes on track algorithm of the long-5 and long-7 tracks, vary as a function of the detector inefficiency for the different central pixel layers. This plot was produced using the method introduced in Chapter 6, where a random number generator is used to remove the pixel from the reconstruction, for a given layer. In this plot, the modified tracking from Chapter 6 is only applied if the standard tracking fails once the MC truth information is missed. These plots demonstrate that long-5 and long-7 hit tracks could successfully recover tracks that would be lost if there are known detector inefficiencies.

To understand how this tracking performance corresponds to the resultant impact on the physics performance of the Mu3e experiment, the effect on the single event sensitivity (SES) is estimated for inefficiencies introduced into the individual layers separately. The assumption is made that after the tracking and vertex selection cuts are applied that all types of background are still suppressed and free. The validity of this assumption is discussed in section 7.1.1 and the impact of the detector inefficiencies on the (SES) is presented in section 7.1.2.

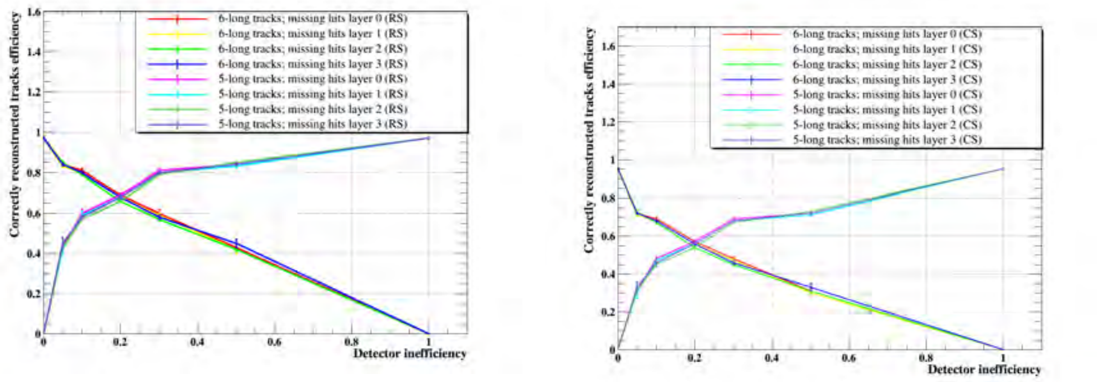

(A) Long tracks with 5 and 6-pixel hits are extrapolated into the recurl stations of the detector.

(B) Long tracks with 5 and 6 pixel hits that recurl back into the central station of the detector.

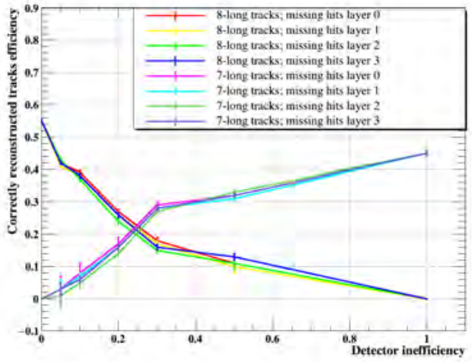

(C) Long tracks with 7 and 8 pixel hits that recurl back into the central station of the detector

FIGURE 7.1: Track efficiency for different categories of long-8 and long-7 tracks as a function of the hit efficiency in the pixel layers 0, 1, 2 or 3.

7.1.1 Background Estimate with New Tracking Selection

In this section, the efficiency of the new tracking for the long track selection of Chapter 5 is studied for a detector with a 10% inefficiency applied to layer 1. For comparison, results of the new tracking for all tracks (short and long) is presented in appendix B.18. Figure 7.2 shows the invariant mass distribution of the three electron candidates passing the vertex and frame selection of 5.14 and 5.15 for the new tracking.

The normalization of the histograms follows equation 11 in Chapter 5 and assumes for muons decaying with the phase-I target $N = 1 \cdot 10^{15}$. For this inefficient detector scenario considered, the nominal track selection yields a background estimate in the signal region, of 103.5 to 115 MeV of 0.121±0.017 and 3.84±0.21 for long and all tracks respectively. For the new tracking selection a higher estimate of 0.228±0.019 and 14.7±0.2 is obtained.

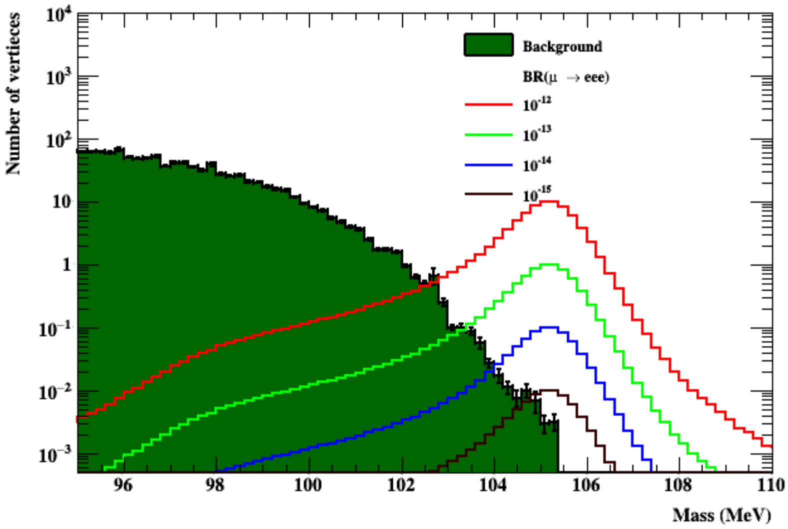

FIGURE 7.2: Spectra of the reconstructed invariant three-particle mass of signal decays and background from radiative events with internal conversion in phase I of the Mu3e experiment after the vertex selection cuts. The plot is on a logarithmic y-axis scale. The invariant mass of the three tracks includes only long tracks with 5-, 6-, 7-, and 8-hits. It is applied when the layer 1 inefficiency is encountered with 10% inefficiency as inefficient tracks with missing hits in layer 1 for both reconstructed and truth (MC) tracks.

Cut	Number of Frames	Efficiency
Frame Selection Cuts (See Section 5.3)		
$\geq$1 vertex	2.521900e+07	0.569
Recon vtx within acceptance	2.393432e+07	0.540
Duplicate removal (same tracks)	1.820622e+07	0.411
Duplicate removal (common tracks)	1.820622e+07	0.411
Duplicate removal (vtx-to-vtx distance)	1.404000e+07	0.317
Break-up in different vertex track quality	Short	3 long
Efficiency	0.317	0.092
Vertex Selection Cuts (See section 5.3.1)		
$\chi^2 < 30$	1.082111e+07	0.244
vertex target distance <3 mm	1.069821e+07	0.242
3-track system momentum <8 MeV	6.130030e+06	0.1384
103.5 MeV $\leq m_{eee} \leq$ 115 MeV	1.0698e+06	0.241
Break-up in different vertex track quality	Short	3 long
Efficiency	0.141	0.0089

TABLE 7.1: Table showing the number of frames passing subsequent frame and vertex selection cuts for the scenario of nominal and inefficient tracks with 10% inefficiency. The nominal tracks are tracks with single hit in each pixel layer, but ineffecienct tracks have missing hit in a layer.

Table 7.1 presents the number of frames passing subsequent frame and vertex selection cuts, while table 7.2 is listed the number of events passing signal selection created from in the simulation for nominal and inefficient three tracks with 10% inefficiency in layer 1.

Cut flows for studies of radiative with internal conversion muon decays generated at one

Category	Number of vertices	Fraction
3 Signal:	10697247	0.999910
3 Michel:	0	0.000000
3 Internal:	0	0.000000
3 Radiative:	0	0.000000
3 Phot:	0	0.000000
3 Bhabha:	0	0.000000
3 Brems:	0	0.000000
3 Pos Anni:	0	0.000000
3 Compton:	0	0.000000
1 int 2 Mic:	0	0.000000
2 int 1 Mic:	0	0.000000
>=1 pho:	26	0.000002
>=1 brem:	0	0.000000
>=1 compton:	11	0.000001
other:	922	0.000086

TABLE 7.2: Table showing the number of signal vertices created from the simulation for nominal and inefficient tracks with 10% inefficiency.

Cut	Number of Frames	Efficiency
Frame Selection: Cuts (See Section 5.3)		
$\geq$1 vertex	4.161e+11	0.327
Recon vtx within acceptance	3.732e+11	0.294
Duplicate removal (vtx-to-vtx distance)	3.732e+11	0.294
Duplicate removal (same tracks)	3.552e+11	0.279
Duplicate removal (common tracks)	3.552e+11	0.279
Vertex Selection Cuts (See Section 5.3.1)		
$\chi^2 < 30$	1.680e+11	0.1322
vertex target distance <3 mm	1.035e+11	0.08
3-track system momentum <8 MeV	1.117e+09	0.000879
103.5 MeV $\leq m_{eee} \leq$ 115 MeV	2.07e+05	1.62e-07

TABLE 7.3: Table showing the number of frames passing subsequent frame and vertex selection cuts for the scenario when radiative with internal conversion muon decay generated at one decay per frame for nominal and new tracks with 10% inefficiency.

decay per frame for nominal and inefficient tracks with 10% inefficiency are presented in table 7.3 and table 7.4 is for radiative with internal conversion sample information of the origin of the selected vertices after applying vertex cuts. Based on this study, the assumption is made that the signal selection is "background free", for new tracking for inefficiencies of up to approximately 10%.

7.1.2 Single Event Sensitivity (SES) with New Tracking Selection

Figure 7.3 shows the single event sensitivity (SES) versus data taking days for the nominal tracking when inefficiencies of up to 20% are introduced into pixel layers 1 and 2, respectively. Figure 7.4 shows the corresponding SES for new tracking. It can be seen from these plots the improvements in SES obtained.

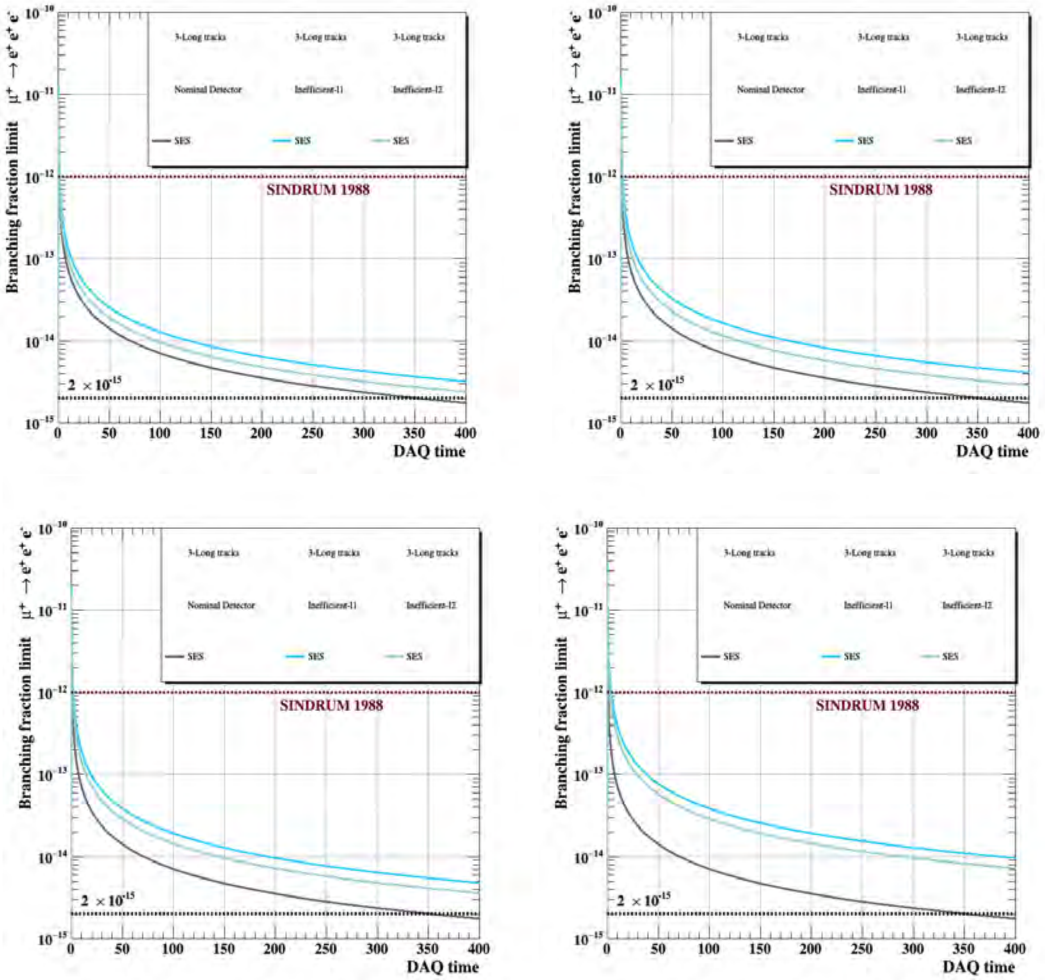

FIGURE 7.3: Single event sensitivity SES and the corresponding 90% and 95% C.L. upper limits versus data taking days for the phase I Mu3e detector only for nominal long tracks with inefficiency 5%, 10%, 15% and 20%, respectively. The unit of DAQ time (x-axis) is days.

Category	Number of vertices	Fraction
3 Signal:	0	0.00
3 Michel:	0	0.00
3 Internal:	1116567931.705	1.00
3 Radiative:	0	0.00
3 Phot:	0	0.00
3 Bhabha:	0	0.00
3 Brems:	0	0.00
3 Pos Anni:	0	0.00
3 Compton:	0	0.00
1 int 2 Mic:	0	0.00
2 int 1 Mic:	0	0.00
>=1 pho:	0	0.00
>=1 brem:	0	0.00
>=1 compton:	0	0.00
2 rad 1 pho:	0	0.00
2 rad 1 brem:	0	0.00
2 rad 1 comp:	0	0.00
1 rad 2 pho:	0	0.00
1 rad 2 brem:	0	0.00
1 rad 2 comp:	0	0.00
other:	0	0.00

TABLE 7.4: Radiative with internal conversion sample information of the origin of the selected vertices after applying vertex cuts. This shows the origin of the three tracks in the reconstructed vertices for nominal and new tracks with 10% inefficiency. A floating point number is due to weighting. A complete simulation is challenging since the branching ration for this decay is 3.4×10^{-5}, the high mass tail is better populated using weighted events. When three recurling tracks are required, migrations from lower masses than 90 MeV are strongly suppressed. Our interest lies in the region of phase space where neutrinos carry the least momentum, particularly the branching fraction in the region of high visible mass (we used a lower cutoff of 90 MeV).

Studies when 100% inefficiency applied to a layer show an understanding of the importance of existing all inner or outer pixel layers. Figure B.11 in appendix B shows how SES with 0, 5, 10, 15, 20, 100 % inefficiency new tracking if layers 0 and 3 are inefficient. They are shown to be very similar to layer 1 and 2 due to the relative distance between them.

To summarise figures 7.3 and 7.4, tables 7.5 and 7.6 list the SES and the corresponding 90% and 95% upper limits versus data taking days for the phase I Mu3e detector for signal muon decays in the different scenarios. It presents nominal detector, 5, 10, 15 and 20 % detector inefficiency at 300 data taking days if layer 1 or 2 is inefficient, respectively. It can be seen that inefficiencies in inner pixel layers have a greater impact on SES than inefficiencies in outer layers, so layer 1 is a more critical one than layer 2.

Table 7.7 is a summary table for vertex resolution, momentum resolution and signal efficiency for signal muon decays for the nominal detector, and when a random 30% inefficiency is included in layers 1 or 2. For comparison with the results given in Chapter 5, the vertex resolution and efficiency are given for all long tracks, whilst the momentum

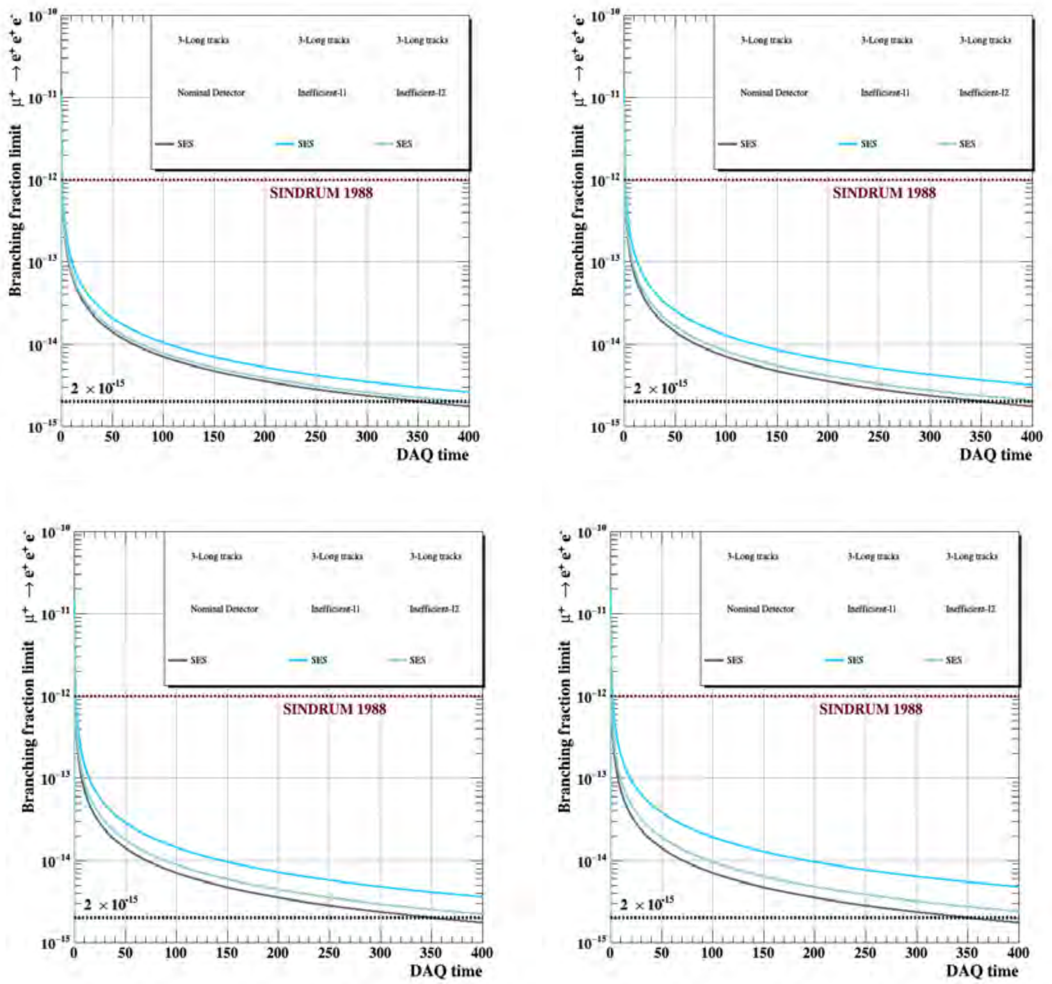

FIGURE 7.4: Single event sensitivity SES and the corresponding 90% and 95% C.L. upper limits versus data taking days for the phase I Mu3e perfect and imperfect detector only for long tracks with inefficiency 5%, 10%, 15% and 20%, respectively. The unit of DAQ time (x-axis) is days.

Detector Scenario	SES	90%CL	95%CL
Nominal detector	$2.5{\cdot}10^{-15}$	$5.5{\cdot}10^{-15}$	$6.7{\cdot}10^{-15}$
5% inefficient detector	$4.1{\cdot}10^{-15}$	$9.1{\cdot}10^{-15}$	$1.1{\cdot}10^{-14}$
10% inefficient detector	$4.5{\cdot}10^{-15}$	$9.9{\cdot}10^{-15}$	$1.3{\cdot}10^{-14}$
15% inefficient detector	$4.9{\cdot}10^{-15}$	$1.2{\cdot}10^{-14}$	$1.5{\cdot}10^{-14}$
20% inefficient detector	$5.2{\cdot}10^{-15}$	$1.4{\cdot}10^{-14}$	$1.7{\cdot}10^{-14}$

TABLE 7.5: Summary table for some physical studies studied in this thesis to highlight single event sensitivity (SES) and the corresponding 90% C.L. and 95% C.L. upper limits versus data taking days for the phase I Mu3e detector for signal muon decays for the nominal detector, 5, 10, 15 and 20 % detector inefficiency at 300 data taking days if layer 1 is inefficient.

Detector Scenario	SES	90%CL	95%CL
Nominal detector	$2.5{\cdot}10^{-15}$	$5.5{\cdot}10^{-15}$	$6.7{\cdot}10^{-15}$
5% inefficient detector	$2.8{\cdot}10^{-15}$	$6.1{\cdot}10^{-15}$	$8.1{\cdot}10^{-15}$
10% inefficient detector	$3.1{\cdot}10^{-15}$	$6.3{\cdot}10^{-15}$	$8.5{\cdot}10^{-15}$
15% inefficient detector	$3.3{\cdot}10^{-15}$	$7.2{\cdot}10^{-15}$	$9.1{\cdot}10^{-15}$
20% inefficient detector	$4.1{\cdot}10^{-15}$	$8.0{\cdot}10^{-15}$	$1.0{\cdot}10^{-14}$

TABLE 7.6: Summary table for some physical studies studied in this thesis to highlight single event sensitivity (SES) and the corresponding 90% C.L. and 95% C.L. upper limits versus data taking days for the phase I Mu3e detector for signal muon decays for the perfect detector, 5, 10, 15 and 20 % detector inefficiency at 300 data taking days if layer 2 is inefficient.

resolution is presented only for 5(6) hit tracks for the new(nominal) tracking selection. It can be seen that inefficiencies in inner layers have a greater impact on SES and resolution than inefficiencies in outer layers. The same table is shown in appendix B.13 to check the compatible results if layer 3 or 0 is inefficient.

7.2 Extended Studies on the Noise in the Mu3e Pixel Detector

The noise of a sensor is defined as pixels firing producing hits that are not correlated to a passing particle. Noise can be due to leakage currents in the sensing diode or noise in the circuitry. Multiple noise hits can create ambiguities for the tracking algorithm, which can result in fake tracks and an incorrect reconstruction of vertices or particle momenta. The probability to reconstruct fake tracks, as defined in Chapter 5, depends on the number of tracks per event and the number of noise hits per layer. The Monte-Carlo truth information is used to separate the candidates with correctly assigned hits from track candidates with noise hits.

Parameter	Nominal	Inefficient (I1)	Inefficient (I2)
$x_{rec} - x_{true}$ [mm]	0.212 ± 0.002	0.809 ± 0.006	0.726 ± 0.004
$y_{rec} - y_{true}$ [mm]	0.214 ± 0.002	0.812 ± 0.006	0.704 ± 0.004
$z_{rec} - z_{true}$ [mm]	0.115 ± 0.001	0.631 ± 0.005	0.605 ± 0.001
momentum resolution [MeV/c]	0.148 ± 0.001	0.512 ± 0.003	0.316 ± 0.002
signal efficiency	0.163 ± 0.001	0.100 ± 0.004	0.130 ± 0.002

TABLE 7.7: Summary table for some physical studies studied in this thesis to highlight vertex resolution is for nominal tracks with 6-long or 8-long tracks and inefficient tracks with 5-long or 7-long tracks, momentum resolution for long tracks with 6 and 5-pixel hits and signal efficiency for long tracks only with 6-, 5-, 7- and 8-hits. The inefficiencies studies are with recovering nominal tracks due to the loose cut with 30% inefficiency and the rest are nominal tracks.

Detector Scenario	SES	90%CL	95%CL
Nominal detector	$2.5{\cdot}10^{-15}$	$5.5{\cdot}10^{-15}$	$6.7{\cdot}10^{-15}$
5 Hz noise	$2.6{\cdot}10^{-15}$	$5.8{\cdot}10^{-15}$	$6.9{\cdot}10^{-15}$
10 Hz noise	$2.69{\cdot}10^{-15}$	$6.4{\cdot}10^{-15}$	$7.2{\cdot}10^{-15}$
15 Hz noise	$2.7{\cdot}10^{-15}$	$6.6{\cdot}10^{-15}$	$7.8{\cdot}10^{-15}$
20 Hz noise	$2.73{\cdot}10^{-15}$	$6.9{\cdot}10^{-15}$	$8.1{\cdot}10^{-15}$

TABLE 7.8: Summary table for some physical studies studied in this thesis to highlight single event sensitivity (SES) and the corresponding 90% C.L. and 95% C.L. upper limits for the phase I Mu3e detector for signal muon decays for nominal detector and [0 to 20] Hz noise after 400 data taking days.

The tracking efficiency, purity and their product for different simulated noise values are shown in figure 7.5. It shows that the purity is relatively stable up to approximately 20 Hz, which is much larger than the highest noise rate seen for the MuPix prototypes in which the measured noise rate is less than 1 Hz at DESY but around 19 Hz at PSI lab due to the beam environment. A slight drop in signal efficiency is observed as the noise rate per pixel increases as shown in figure 7.6. Tables B.3, B.4, B.5 and B.6 list the signal efficiency after reconstruction and vertex fit step for phase-space distributed events for different simulated noise values from 0 (nominal detector) to 20 Hz per pixel. After checking the signal efficiency, figure 7.7 shows the single event sensitivity (SES) and the corresponding 90% and 95% C.L. upper limits versus data taking days for the phase I Mu3e detector for 0 (nominal detector) and [5 to 20, inefficient detector] Hz noise rate per pixel only for long tracks, respectively. The noise has only a small impact on single event sensitivity (SES) as listed in table 7.8.

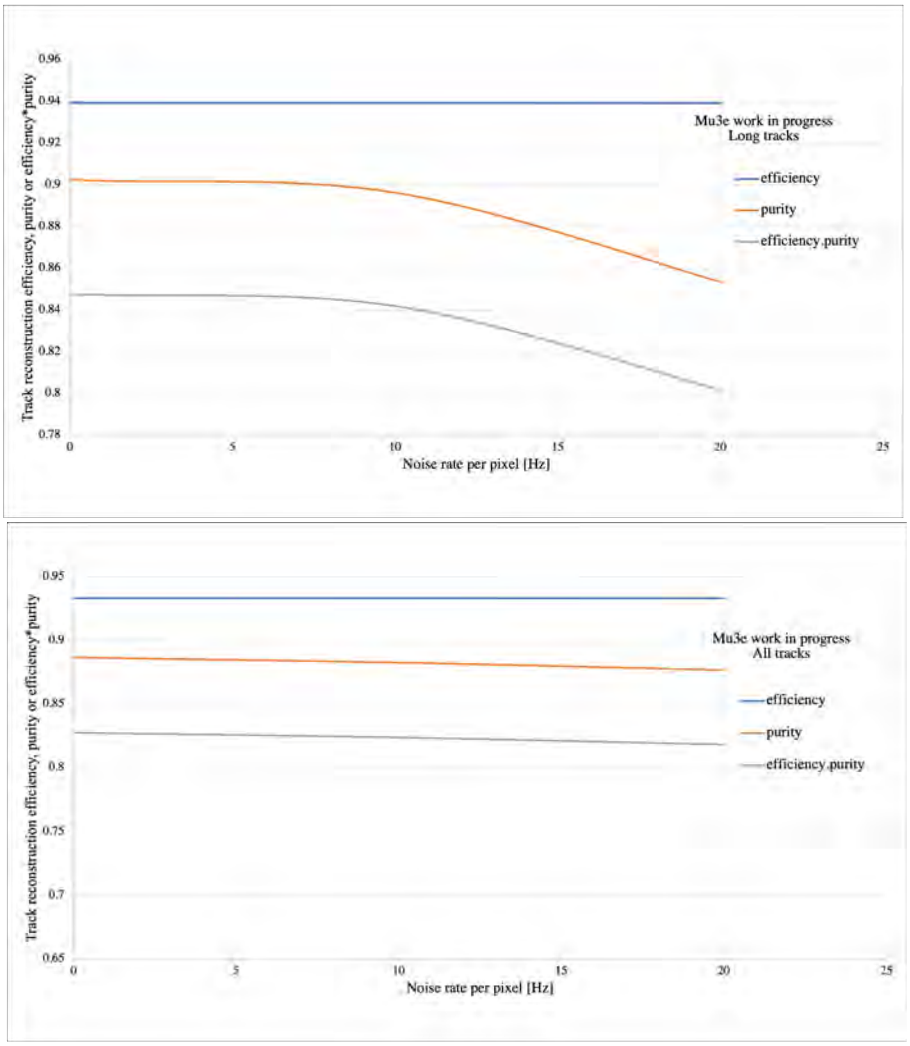

FIGURE 7.5: Summary plot for different detector noise rates per pixel go from 0 to larger than 20 Hz for tracking efficiency and purity of different track candidates in which highest noise rate per pixel for MuPix prototype is less than 20 Hz for long and all tracks, respectively.

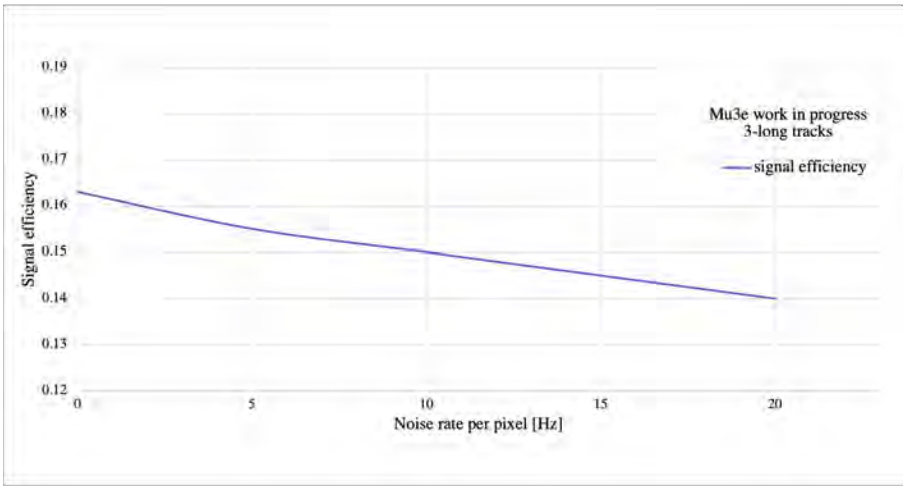

FIGURE 7.6: Summary plot for different detector noise rates per pixel go from 0 to larger than 20 Hz for signal efficiency of three long tracks of signal events in which highest noise rate per pixel for MuPix prototype is less than 20 Hz.

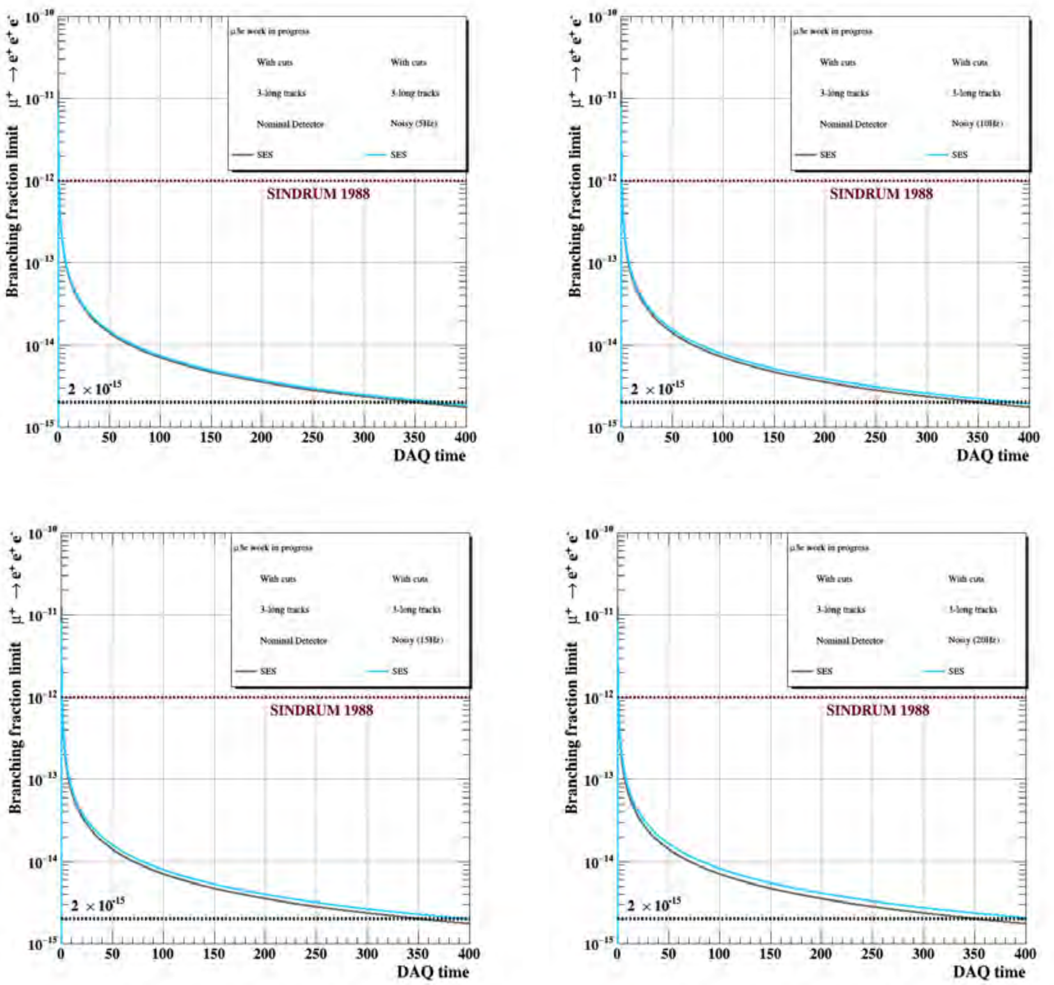

FIGURE 7.7: Single event sensitivity (SES) versus data taking days for the phase I Mu3e detector for only reconstructed three long tracks for a different levels of noise in the pixel sensors as 0 (nominal detector), 5, 10, 15 and 20 Hz noise rate per pixel, respectively. The unit of DAQ time (x-axis) is days.

Parameter	Nominal	5 Hz	10 Hz	15 Hz	20 Hz
$x_{\text{rec}} - x_{\text{true}}$ [mm]	0.212 ± 0.002	0.233 ± 0.003	0.241 ± 0.006	0.250 ± 0.004	0.260 ± 0.003
$y_{\text{rec}} - y_{\text{true}}$ [mm]	0.214 ± 0.002	0.243 ± 0.006	0.256 ± 0.004	0.261 ± 0.003	0.264 ± 0.003
$z_{\text{rec}} - z_{\text{true}}$ [mm]	0.115 ± 0.001	0.125 ± 0.005	0.130 ± 0.001	0.137 ± 0.001	0.141 ± 0.001
momentum resolution [MeV/c]	0.148 ± 0.001	0.158 ± 0.003	0.170 ± 0.002	0.189 ± 0.001	0.229 ± 0.002
signal efficiency	0.163 ± 0.001	0.155 ± 0.004	0.151 ± 0.004	0.145 ± 0.004	0.140 ± 0.004

TABLE 7.9: Summary table of some physical studies studied in this thesis to highlight vertex resolution, momentum resolution and signal efficiency for signal muon decays for different levels of simulated noise per pixel rate [5 to 20] Hz. The vertex resolution is for sets of three long tracks, the momentum resolution for long tracks with 6-pixel hits and the signal efficiency for three long tracks.

Table 7.9 is a summary table showing the effect of noise on the vertex resolution, the momentum resolution and the signal efficiency for signal muon decays for different levels of simulated noise per pixel. The vertex resolution is for sets of three long tracks, the momentum resolution for long tracks with 6-pixel hits and the signal efficiency for three long tracks. It is observed that the resolutions and signal efficiency deteriorate as the noise per pixel increases.

7.3 Expanded Studies to Understand Increased Misalignment of the Mu3e Pixel Detector

In tracking detectors, it is vital to know accurately in space where the detector elements are located. Any misalignment can reduce the position and moment resolution of the detector. Alignment software is used to align the detector before track reconstruction occurs. Figure 7.8 shows a schematic view of the hierarchical structure of the Mu3e tracking detector for alignment purposes. In any real experiment, there will be small deviations from the ideal design geometry due to limits on the mechanical assembly precision. There are also environmental factors that can affect the detector geometry over time such as thermal expansion. These can result in offsets or rotations of composite parts or individual sensors of the detector from their nominal positions. In this section, the alignment software of Mu3e is described and a study of the effects of possible misalignment modes is performed. The impact on the performance of the track reconstruction is evaluated.

Two different types of misalignment are applied and evaluated in this chapter. These are

Relative misalignment	$\sigma_{\mathrm{off,x,y}}$ μm	$\sigma_{\mathrm{rot,x,y}}$ mrad	$\sigma_{\mathrm{off,z}}$ μm	$\sigma_{\mathrm{rot,z}}$ mrad
sensors vs. ladders	50(100)	5(10)	5(100)	5(10)
ladders vs. modules	150(300)	1(2)	150(300)	1(2)
modules vs. layers.	150(300)	1(2)	150(300)	1(2)
layers vs. layer pairs	25(50)	0.2(0.2)	50(50)	0.2(0.2)
layer pairs globally	150(300)	1(2)	250(300)	1(2)

TABLE 7.10: Expected misalignment scenario after detector construction. The depicted values represent realistic estimates for the standard deviation of the Gaussian distribution used for misalignment. In parentheses, the expected worst case is given. It is used to truncate the Gaussian. Offsets are given in μm and rotations in mrad.

hierarchy and sensor-level, the two types are considered and described in more detail later in this chapter. As a previous study was performed [9] in 2018, the updates in this analysis take into consideration the latest Mu3e software (v4.5), the optimised tracking selection given in Chapter 4, and the latest detector design as presented in Chapter 3.

7.3.1 The Mu3e Misalignment and Alignment Tools

The Mu3e software is used to both artificially introduce misalignment and to evaluate the effect of misalignment either from the real or simulated detector. The Mu3e alignment software, MU3EPIXAL [9], uses the track fitting library WATSON [28] and the Milleped-II algorithm to align the misaligned detector. It incorporates a General Broken Lines (GBL) [9] track fitter optimised for thin sensors and provides a very useful interface to PEDE [9] which calculates the alignment corrections. The misalignment tool MU3EMISAL [9] has been created, to apply possible misalignment modes to the pixel detector, as well as apply misalignment separately at the individual sensors level. It was decided to perform the misalignment at the reconstruction level rather than simulation level to save computation time. In comparison to reconstruction, simulation would take approximately a factor of 12 longer to process. Geometrical movements of detector parts are only able to move hits, but not to remove hits that should not have been detected to begin with. After simulation, misalignment is applied to prevent GEANT4 volume overlap by applying misalignment. A conservative estimate of the magnitude of possible misalignment of sensors and sub-assemblies is summarized in table 7.10. The nominal (simulated) geometry is modified with random Gaussian distributed values that reflect these error estimates. A track-based alignment is used to align the detector. For individual sensors, local coordinate systems are defined, for composite parts, the global coordinate system is used.

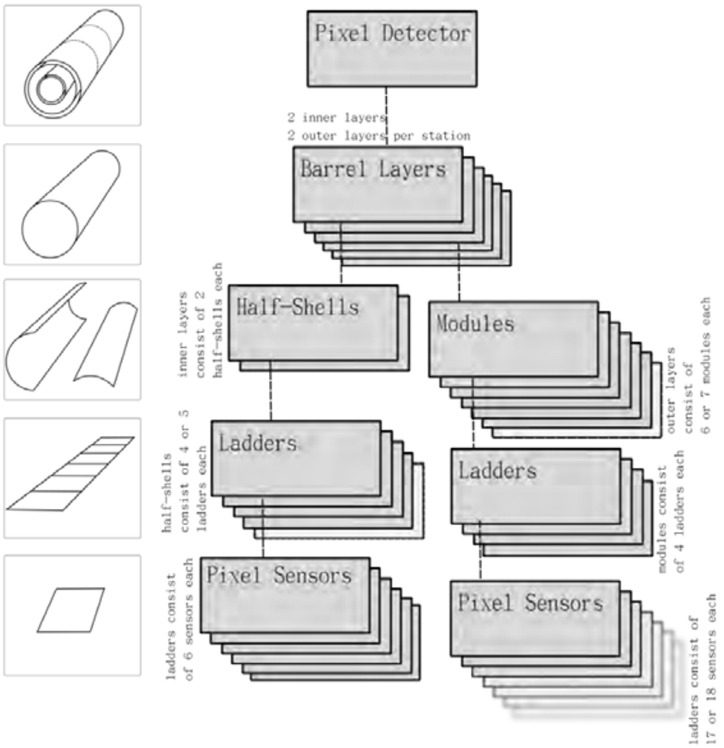

FIGURE 7.8: Schematic depiction of the hierarchical structure of the Mu3e tracking detector.

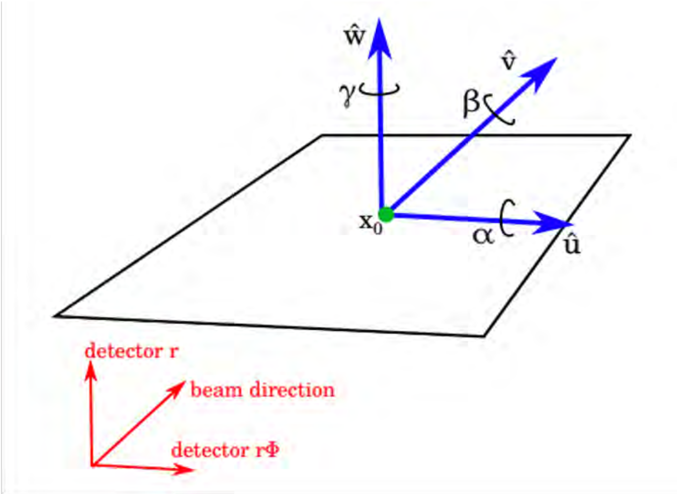

FIGURE 7.9: Rigid body parameters, the basic alignment parameters are offsets and rotations relative to their nominal position and orientation. The unit vectors $\hat{\mathbf{u}}$, $\hat{\mathbf{v}}$, and $\widehat{\mathbf{w}}$ define a right-handed local coordinate system for individual sensors. $\hat{\mathbf{u}}$ and $\hat{\mathbf{v}}$ are parallel to the sensor edges and span the nominal plane in which the sensor lies. The green dot, marked with a x_0, labels the centre and represents a reference point. The red coordinate system is a reference to the global coordinates. Hence, $\hat{\mathbf{u}}$ points in $r\phi$-direction, $\widehat{\mathbf{w}}$ points in radial-direction (away from the centre) of the barrel and in beam direction.

For alignment parametrisation: the parameters used to describe the corrections to the detector geometry are alignment Jacobians. To describe the detector geometry, the sensors are assumed to be rigid bodies, and a reference point x_0 and a rotation matrix R [1] are defined as shown in figure 7.9. Transformations from a local into the global coordinate system can therefore be defined as:

$$\boldsymbol{x} = \boldsymbol{R}\boldsymbol{q} + \boldsymbol{x}_0 \tag{1}$$

Here, $\mathbf{q} = (\widehat{\mathbf{u}},\widehat{\mathbf{v}},\widehat{\mathbf{w}})^T$ describes a local point on a sensor with reference point x_0 that is transformed into the global point $\mathbf{x} = (\widehat{\mathbf{x}},\widehat{\mathbf{y}},\widehat{\mathbf{z}})^T$. For composite detector parts, the reference points are the centre of mass of the active surfaces of all included sensors. The unit vectors $\widehat{\mathbf{u}}$, $\widehat{\mathbf{v}}$, and $\widehat{\mathbf{w}}$ define a right-handed local coordinate system for individual sensors. $\widehat{\mathbf{u}}$ and $\widehat{\mathbf{v}}$ are parallel to the sensor edges and span the nominal plane in which the sensor lies. Further description of the rigid body parameters is given in figure 7.9.

Offset corrections for sensors are given in the local coordinate system with respect to the nominal position,

$$\Delta \boldsymbol{q} = (\Delta u, \Delta v, \Delta w)^\top$$

Rotations are defined by the small angles α, β and γ and can be expressed in the form of three rotation matrices for rotations around the respective axes:

$$\Delta \boldsymbol{R}_\alpha = \begin{pmatrix} 1 & 0 & 0 \\ 0 & \cos\alpha & \sin\alpha \\ 0 & -\sin\alpha & \cos\alpha \end{pmatrix} \tag{2}$$

$$\Delta \boldsymbol{R}_\beta = \begin{pmatrix} \cos\beta & 0 & -\sin\beta \\ 0 & 1 & 0 \\ \sin\beta & 0 & \cos\beta \end{pmatrix} \tag{3}$$

---

[1] Rotations are defined by the small angles α, β and γ

$$\Delta \boldsymbol{R}_{\gamma} = \begin{pmatrix} \cos\gamma & \sin\gamma & 0 \\ -\sin\gamma & \cos\gamma & 0 \\ 0 & 0 & 1 \end{pmatrix} \tag{4}$$

Combining these matrices for rotations around all three axes in a given order yields

$$\Delta R = \begin{pmatrix} \cos\beta\cos\gamma & \cos\alpha\sin\gamma + \sin\alpha\sin\beta\cos\gamma & \sin\alpha\sin\gamma - \cos\alpha\sin\beta\cos\gamma \\ -\cos\beta\sin\gamma & \cos\alpha\cos\gamma - \sin\alpha\sin\beta\sin\gamma & \sin\alpha\cos\gamma + \cos\alpha\sin\beta\sin\gamma \\ \sin\beta & -\sin\alpha\cos\beta & \cos\alpha\cos\beta \end{pmatrix} \tag{5}$$

The corrected global position of a rigid body can therefore be determined as:

$$\boldsymbol{x}_{\text{corr}} = \boldsymbol{R}\Delta\boldsymbol{R}(\boldsymbol{q} + \Delta\boldsymbol{q}) + \boldsymbol{x}_0 \tag{6}$$

In addition to random sensor-level and hierarchical misalignments, possible weak mode misalignments need to be considered. Weak modes are global deformations that may not affect the χ^2 of the track and therefore can not easily be aligned using only track-based software alignment. Figure 7.10 shows an overview of possible misalignment modes that are expected to represent alignment weak modes for the Mu3e detector, some of these will be discussed in this section.

7.3.2 Results for a Full Pixel Detector Alignment at the Hierarchy Level

To study the tracking performance of the detector with misalignment, misalignment are applied in the simulation at each level of the hierarchy following the values quoted in table 7.10. The sample used for the subsequent alignment includes tracks from muon decays, cosmic muons [2] and Mott scattering electrons and positrons. Cosmic muons have trajectories that connect detector parts that are not usually connected by particles coming from the muon decay in the target. This has the advantage to reduce weak modes in the detector alignment when included in the track-based alignment algorithm.

---

[2] a cosmic muon generator based on the spectrum and angle parametrisation was implemented.

(A) Torsion

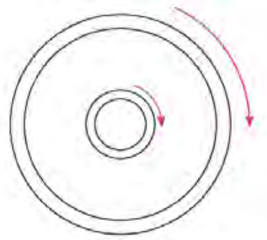

(B) Curling

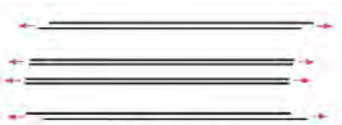

(C) Shearing

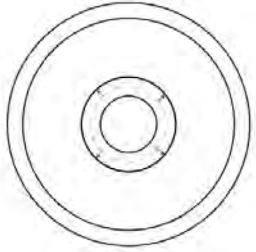

(D) Radial

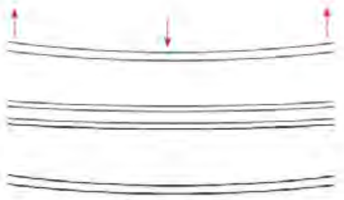

(E) Bowing

(G) Stretching

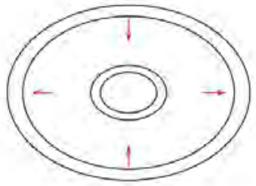

(F) Elliptical

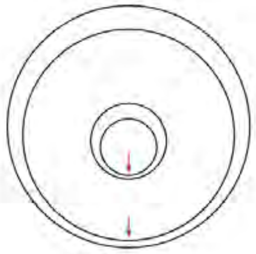

(H) Sagitta

FIGURE 7.10: Schematical depiction of expected possible weak modes for the Mu3e detector. Left side figures are in rz-view and right side figures are in xy-view of the detector.

Having very high forward momenta is also valuable for the track based alignment. In general, using different types of tracks will help reduce weak modes. When there is a weak misalignment mode, the data cannot clearly show you the alignment. There are many distortions that have similar data results. Therefore, it needs to be fixed during construction. In order to suppress these weak modes, MU3EPIXAL was designed to include external measurements. Although the results have improved, there is still a residual misalignment that is not satisfactory. Due to the current weak mode, further improvement of the alignment did not yield a better result. Further investigation is needed to recover results that go beyond the scope of this work.

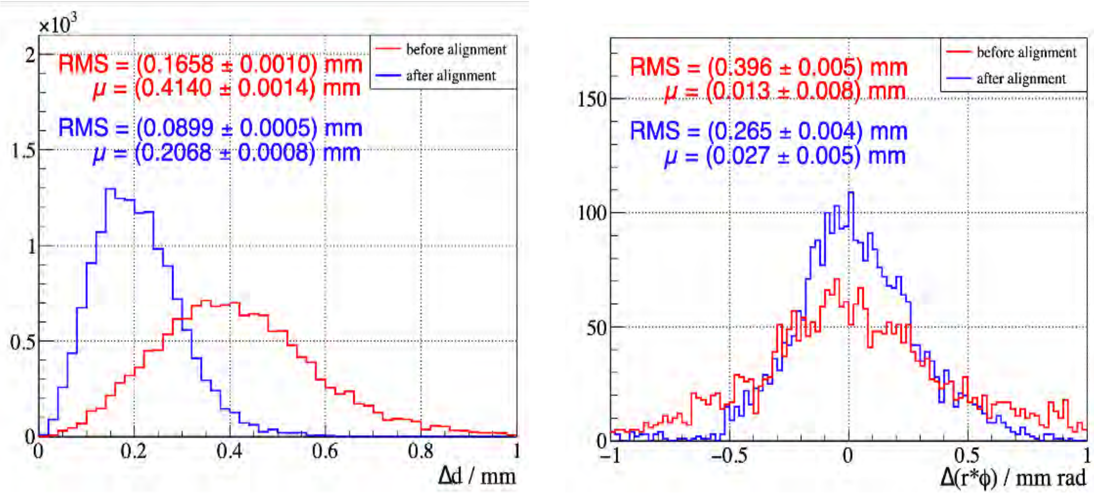

FIGURE 7.11: Geometry comparison between misaligned and aligned detector. Absolute offset; measured at the corners and the centres of all sensors (left) and $\Delta(r\phi)$ before and after the alignment.

Figure 7.11 shows the absolute offset and offset in rϕ of each sensor for the mis- and re-aligned rigid body parameters for the central detector station. It shows that the absolute offset Δd [3] can be reduced by MU3EPIXAL, while $\Delta(r\phi)$ gets a smaller improvement. The leftover misalignment is connected to the weak mode of bowing of sensor layers since longer ladders will sag due to gravitational force. Although the outcomes could be improved, these results are already quite good and do certainly serve as a proof of principle.

Figure 7.12 shows the offset in x and y of each sensor as a function of the position in z, before (left) and after (right) alignment of the complete pixel detector. Also shown is the absolute offset as a function of radius before and after alignment. There is a worsening of the alignment precision for sensors at the end of all stations. This is due to the lower statistics available for the outer sensors. It can be seen that the alignment precision is

---

[3] $\Delta d = \sqrt{\Delta x^2 + \Delta y^2 + \Delta z^2}$

worse for the outer detector layers than the inner layers (r). This is mostly due to the weakly constrained alignment of the z-position for the recurl stations (z).

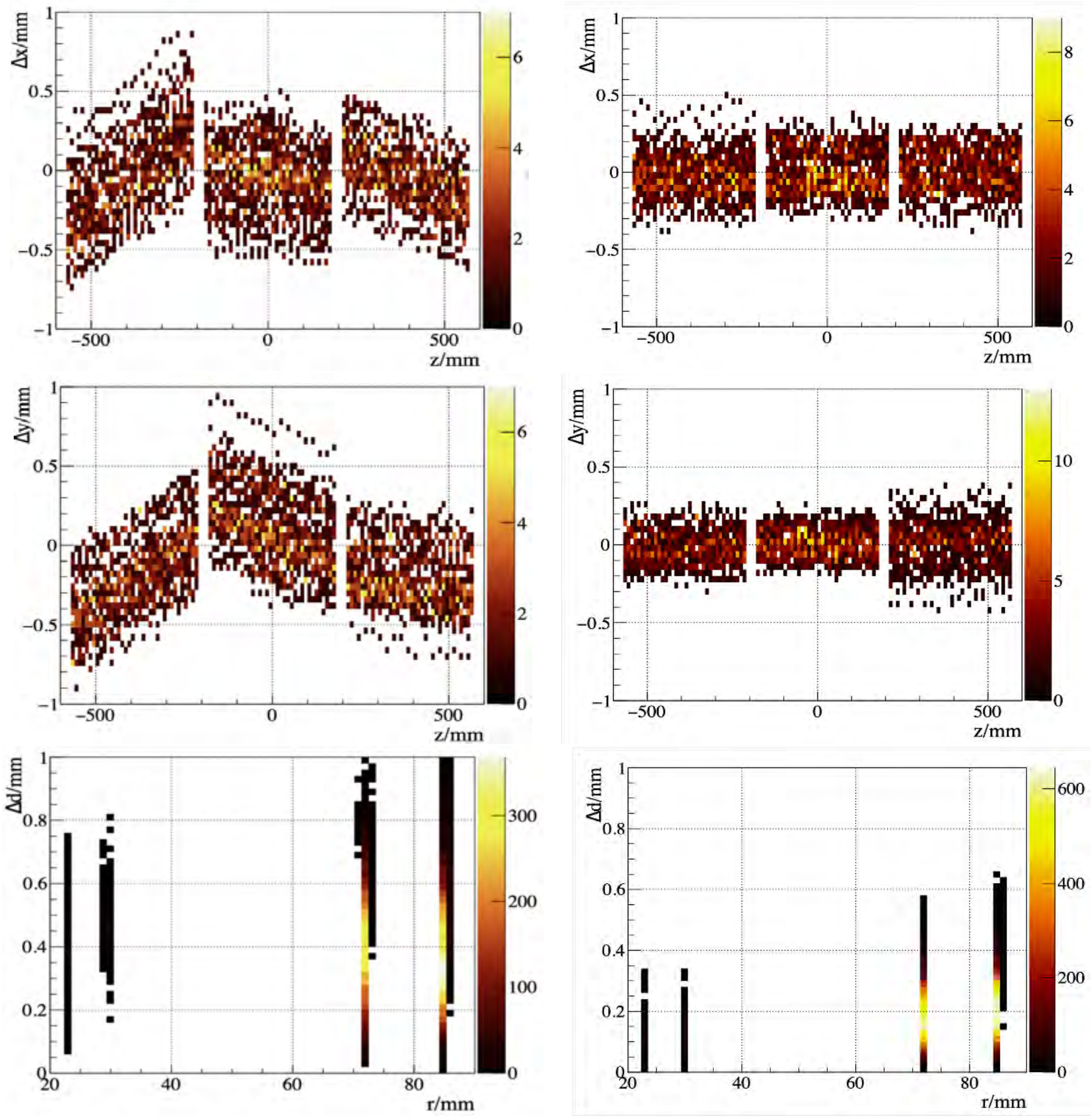

FIGURE 7.12: Offset in x and y as a function of position in z before (left) and after (right) alignment of the complete pixel detector. Also, Absolute offset as a function of radius is shown. The color scale is indicated to the tracks intensity.

Figure 7.13 shows some large structural deformations that include global misalignment and weak modes. These are an offset in z as a function of position in z (Stretching), elliptical, bowing and Sagitta. The resulting Δz and Δd distributions are shown before (left) and after (right) alignment. It can be seen how much the alignments improve these distributions.

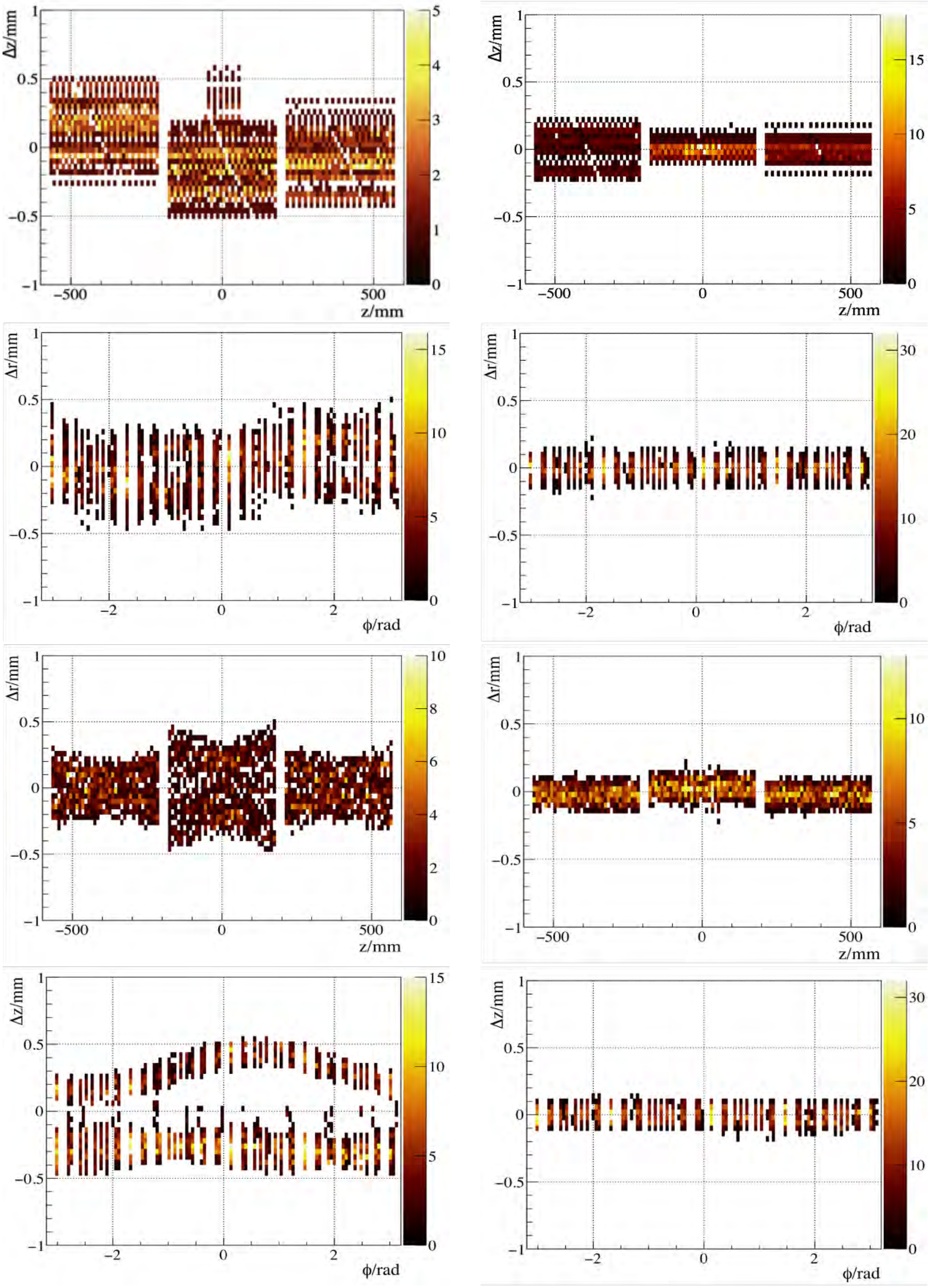

FIGURE 7.13: Weak modes presented, offset in z as a function of position in z (Stretching), elliptical, bowing and Sagitta, respectively before (left) and after (right) alignment of the pixel detector.

To further investigate the impact on the performance of the tracking detector before and after alignment, a sample of Michel positrons is produced for a detector where only the sensors are individually misaligned according to the sensor vs. layer values given in table 7.10.

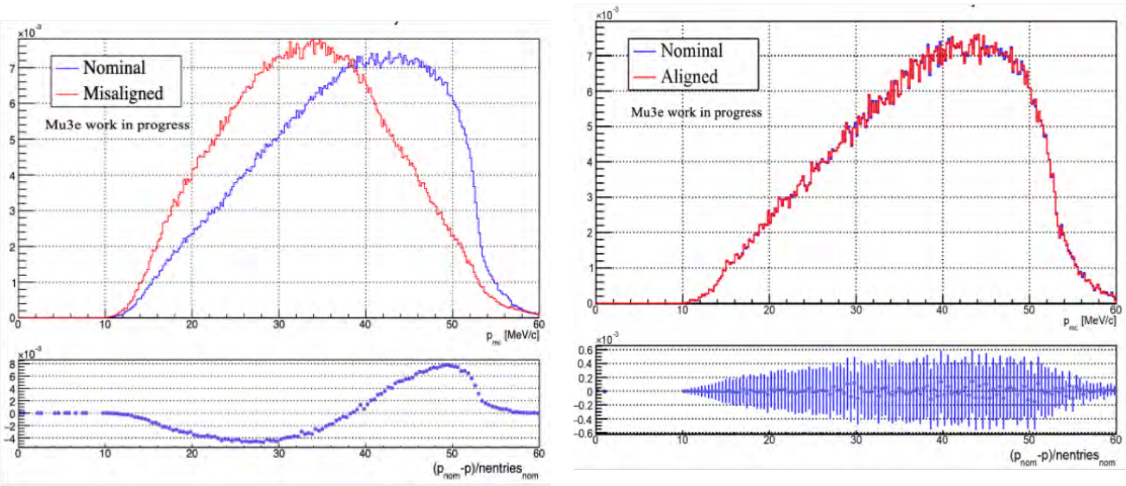

(A) Reconstructed momentum of Michel positrons for the nominal detector versus the (misaligned) detector. The lower graph shows the relative difference between the two.

(B) Reconstructed momentum of Michel positrons for the nominal detector versus the detector after sensor alignment. The lower graph shows the relative difference between the two.

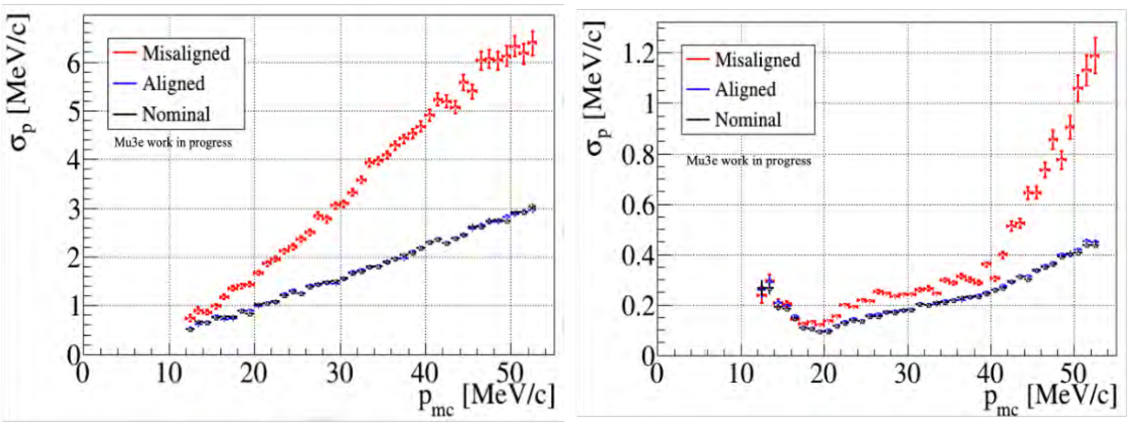

(C) Momentum resolution as a function of true momentum. The error bars correspond to the width of a Gaussian fit to the difference between true and measured momenta for only short tracks.

(D) Momentum resolution as a function of true momentum. The error bars correspond to the width of a Gaussian fit to the difference between true and measured momenta for only long tracks.

FIGURE 7.14: Reconstructed momentum of Michel positrons for the nominal detector versus the detector before and after sensor alignment. The lower graph shows the relative difference between the two. Momentum resolution as a function of true momentum. The error bars correspond to the width of a Gaussian fit to the difference between true and measured momenta.

Figure 7.14 shows the reconstructed momentum of Michel positrons for the nominal detector versus the detector after applying misalignments to layer 1. The lower graph shows the relative difference between the two. Also, shown is the momentum resolution as a function of true momentum. It can be seen that the distribution is clearly heavily affected by misplaced sensors in layer 1, with a systematic effect of lowering the reconstructed momentum as well as producing a deterioration in the momentum resolution. After alignment, the distribution matches the one for the nominal geometry.

Parameter	Nominal	misaligned	aligned
$x_{\text{rec}} - x_{\text{true}}$ [mm]	0.212 ± 0.002	0.601 ± 0.010	0.213 ± 0.002
$y_{\text{rec}} - y_{\text{true}}$ [mm]	0.214 ± 0.002	0.510 ± 0.060	0.215 ± 0.002
$z_{\text{rec}} - z_{\text{true}}$ [mm]	0.115 ± 0.001	0.720 ± 0.050	0.116 ± 0.001
momentum resolution [MeV/c]	0.148 ± 0.002	0.983 ± 0.003	0.141 ± 0.002
signal efficiency	0.163 ± 0.001	0.100 ± 0.004	0.159 ± 0.002

TABLE 7.11: Vertex and momentum resolution and signal efficiency is showing for nominal tracks with 6-long or 8-long tracks. Misalignments are applied only for one inner pixel layer based on the values in table 7.10.

Mis-alignment of the Mu3e tracker at the layer level and beyond can negatively affect the geometrical acceptance of the detector for signal events which could limit the sensitivity of the Mu3e experiment. The impact of larger structural misalignments on the performance of the detector, such as displacements of the inner vertex and recurl layers are investigated in both directions, parallel and perpendicular to the beam direction. Also, the impact of noise is studied for the same misalignments by using signal muon events. Figures on each case are shown in appendix B.6.2 independently.

Table 7.11 shows the vertex and momentum resolution as well as the signal efficiency for 6-long or 8-long tracks where the misalignments are applied only for one inner pixel layer 1 with the values that are mentioned in table 7.10. It can be seen that the alignment procedure successfully regains the vertex and momentum resolution of the long-6 or long-8 tracks for the nominal detector within statistical uncertainties. The signal efficiency is also largely recovered.

8 Readout Hardware for the MuPix Pixel Sensor Prototypes

The performance of the pixel detector is evaluated through a series of prototype sensors. In this chapter, MuPix pixel sensor prototypes will be described in detail. The analogue pixel electronics will be presented as well as the digital periphery and the readout state machine. The chapter also presents the various hardware components that are required to operate the MuPix prototypes along with the readout firmware and software. The temperature is a very important issue in the Mu3e experiment to study cooling performance, so the setup is shown with the results.

8.1 Semiconductors Pixel Detector

Particles in physics experiments are typically identified by the characteristic signature they leave in the detector. The identification of charged particles typically is via charge and mass. We can reconstruct the mass of the decaying particle by measuring the momenta of the decay products. When interacting with the material, many particles lose a part or all of their energy by ionisation processes. The energy loss releases charge carriers that can be exploited to obtain information about the particles.

Semi-conductor sensors are based on the production of e^- hole pairs by electromagnetic interactions of the incident particles with the silicon. The relevant particles in the Mu3e experiment are electrons and positrons with energies in the range of $(10 - 53)$ MeV. They will lose energy via Coulomb collisions. When a fast charged particle passes through matter, it undergoes a series of Coulomb collisions with the atomic electrons of the material. As a result, the atoms end up in excited or ionised states, while the particle loses small fractions of its kinetic energy, but the trajectory of the charged particle is mostly unaffected.

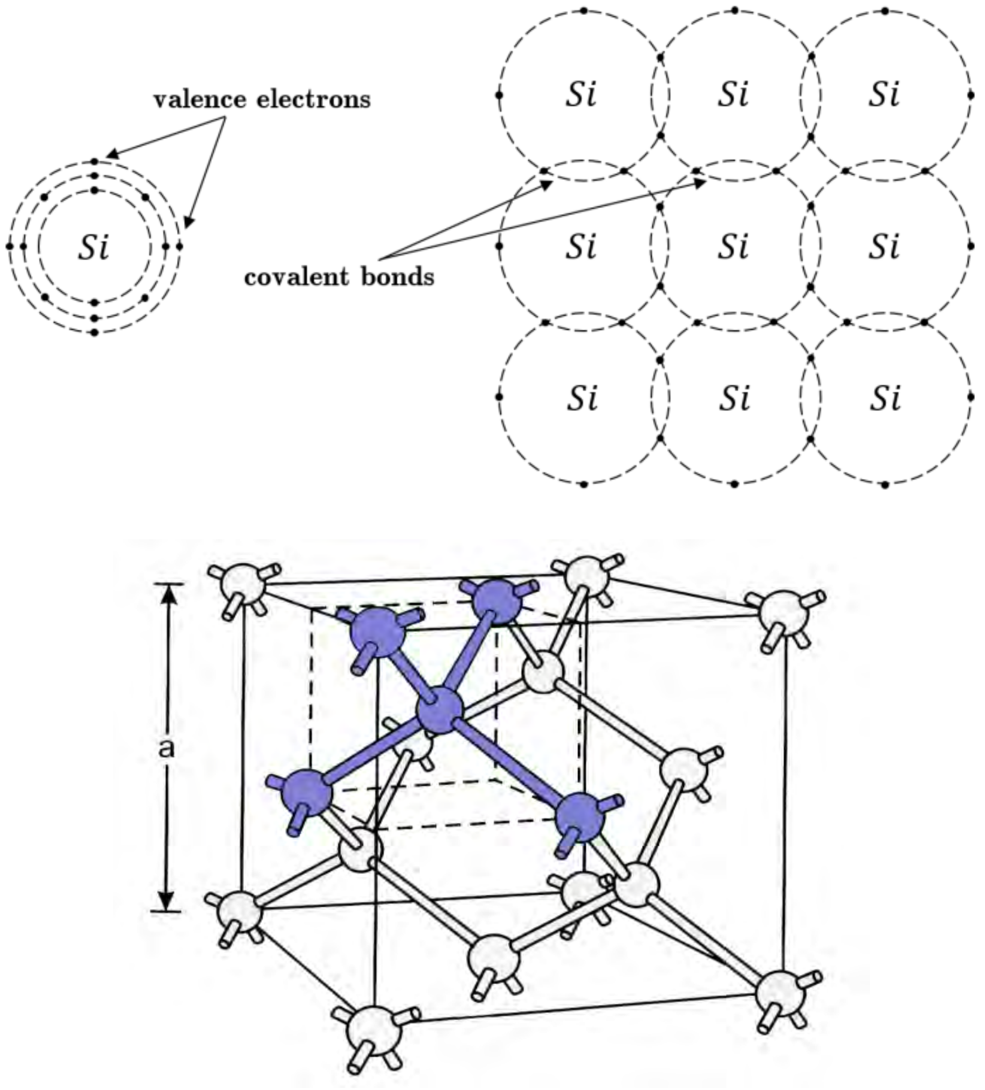

FIGURE 8.1: Left: Atom of silicon. There are four electrons in the valence shell. Right: Pure silicon crystal lattice. Each atom of silicon shares one of its valence electrons with each of its four neighbours[42].

Semiconductor detectors are often made of silicon or germanium. In the Mu3e experiment, the tracker detector is made of silicon. Basic silicon properties are listed in the appendix in Tab. A.1. A silicon atom belongs to group IV elements. It has 14 electrons of which 2 electrons are in the first atomic shell, 8 electrons in the second atomic shell, and 4 electrons in the third outermost atomic shell. The latter 4 valence electrons form a covalent bonds with neighbouring atoms which results in a diamond lattice as shown in figure 8.1. At low temperatures, all electrons are bound, but at higher temperatures, thermal vibrations break some of the bonds. Free electrons cause conductivity, while the remaining open bonds attract other electrons. In semiconductors, the conduction and valence bands are separated by an energy gap. The band gap in semiconductors is small and electrons already occupy the conduction band at room temperature. Electrons from the conduction band may recombine with holes in the valence band.

To increase the conductivity of a semiconductor, impurity atoms from group III or group IV are introduced into the crystal lattice. This process is known as doping. Doping with group V elements like phosphorous (P) with 5 valence electrons is known as doping with donor atoms. These release one of their electrons into the conduction band, leaving a positively charged ion (see figure 8.2, right). Acceptors like the group III element boron (B) capture one of the valence electrons of a neighbouring silicon atom creating a hole (see figure 8.2, left). Implanting acceptor elements which release positive charge carriers results in p-type semiconductors while adding donor elements that contribute negative charge carriers as doping produces n-type semiconductors.

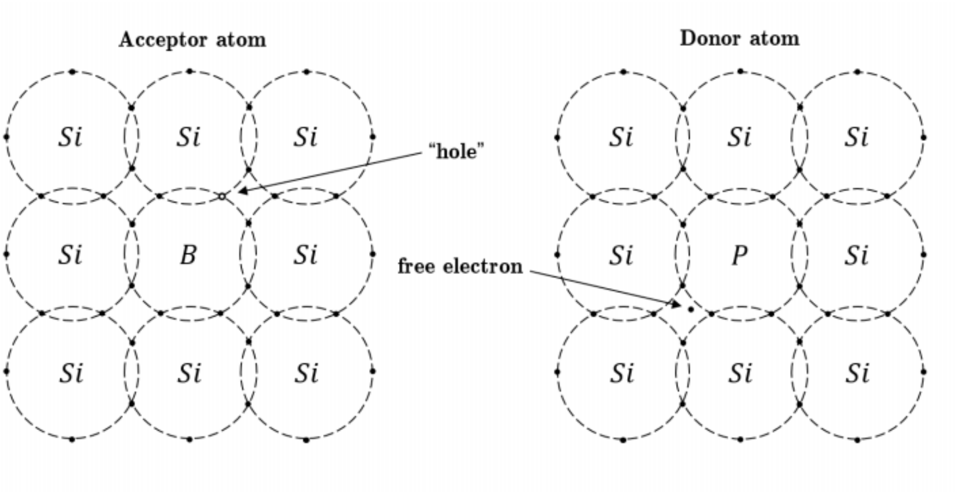

FIGURE 8.2: Left: P-type semiconductor. With boron as a dopant, one bond is left open for electrons from the lattice to occupy. This "hole" can move through the lattice by continually being filled, increasing the conductivity of the crystal. Right: N-type semiconductor. With the additional electron from the valence shell of phosphorus, the conductivity of the crystal is increased[42].

Semiconductor detectors are normally based on diodes formed by a PN junction. If p-doped and n-doped materials are brought into contact, the junction acts as a diode. Holes diffuse into the n-doped region, while electrons diffuse into the p-doped material until thermal equilibrium is reached.

The remaining ions create a space charge region and an electric field stopping further diffusion. The space charge region is also known as the depletion region and is empty of free charge carriers. An external voltage between the different doping regions allows to manipulate the width of this region due to the change in the drift field. By applying V_+ to the p-type semiconductor (anode) and V_- to the n-type semiconductor (cathode), the depletion region becomes narrower. This is known as a forward bias. If the polarity of the terminals is reversed, free electrons and holes are pulled away from the junction increasing the size of the depletion region. This is known as a reverse-bias. To calculate the width of the depletion region W_D as a function of bias voltage V_b [3]:

$$W_D = W_{D0} + \sqrt{\frac{2\epsilon_0 \epsilon_{Si}}{qN_{eff}} V_b} \tag{1}$$

where W_{D0} is the width at 0V bias voltage, ϵ_0 is the permittivity of free space, ϵ_{Si} is the relative permittivity of silicon, q is the elementary charge, and N_{eff} is the space charge.

8.2 Pixel Sensor Prototype

The three most recent MuPix sensor prototypes are discussed in this chapter.

8.2.1 MuPix8 Chip

For the pixel tracker in the Mu3e experiment, HV-MAPS have been adopted as the sensor technology of choice. The first large-scale prototype in the MuPix group was the MuPix8 chip. Figure 8.3 shows a picture of a MuPix8 chip with a total active area of 2cm×1cm. The pixel size is 80μm $\times 80\mu$m. HV-MAPS present many advantages as they integrate the sensing element, readout electronics in a single layer of silicon, offering high granularity, high speed, excellent radiation tolerance, and low power consumption. High signal and fast charge collection, combining compactness of CMOS with performance of hybrid planar silicon sensors. Critical properties for Mu3e experiment, sensors can be thinned to 50 μm without signal loss and sensors can operate in a high rate environment $(\sigma(\text{t}) < 25\text{ ns})$. Mu3e is the first high energy particle physics experiment to employ HV-MAPS in a tracker Mu3e would not be possible without this new technology.

The pixel matrix in MuPix8 has 128 columns and 200 rows with a total of 25,600 pixels. The matrix is divided into three submatrices (A, B, and C) with different signal transmission modes from the pixel to readout. They contain 48, 48, and 32 columns respectively. The chip includes a readout periphery which houses the bias block, digital readout and bonding pads at the bottom of the chip.

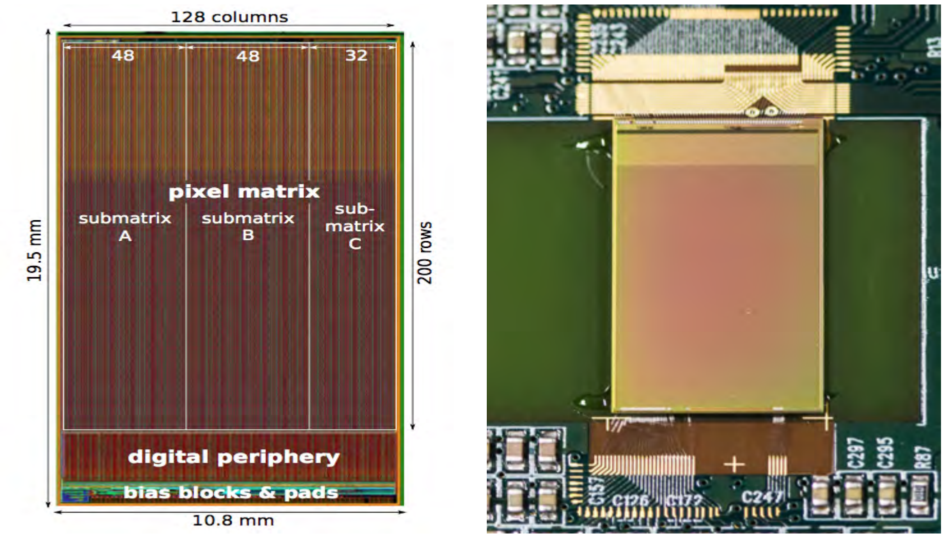

FIGURE 8.3: Left: design view of the MuPix8 prototype. The pixel matrix takes up most of the space, while the digital periphery part is located at the bottom of the sensor, and the bias blocks and pads are visible. Right: Photograph showing the MuPix8 chip glued and bonded to an insert PCB.

8.2.2 MuPix9 Chip

The MuPix9 is a small scale prototype made with an area of 8.7 mm × 3.6 mm, and it is arranged in 48 columns each with 20 pixels. Despite its small size, it contains new features including a new slow control to manage the chip configuration. The two power regulators are designed for voltage, current and temperature stability. It host a condensed MuPix8 Matrix A in which the pixels are in a (n) substrate instead of (p) substrate, pixel readout electronics and digital part with slow control. The layout of MuPix9 is shown in figure 8.8.

One of the critical aspects of experiments in high energy physics is the power supply of tracking modules in the detector. That is especially true for big experiments that need as low power as possible and minimized cables. Therefore, power regulators to allow for serial powering are explored. It has the advantage of a lower current flow through the cables, reducing power losses in the cables allowing the use of thinner cables and thus less material.

8.2.3 MuPix10 Chip

The MuPix10 chip is the first full size prototype chip for the Mu3e tracker. The pixel size of MuPix10 is 80 μm × 80 μm. It comprises a matrix of 256 × 250 pixels with an active area of 20.48 mm × 20.00 mm, and the size of the die is 20.66 mm × 23.14 mm as shown

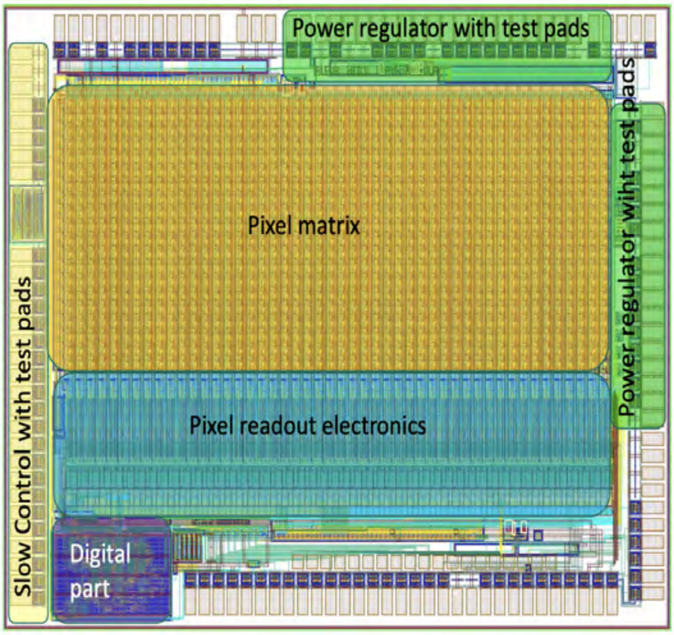

FIGURE 8.4: The layout of the MuPix9 with the main concepts of the sensor

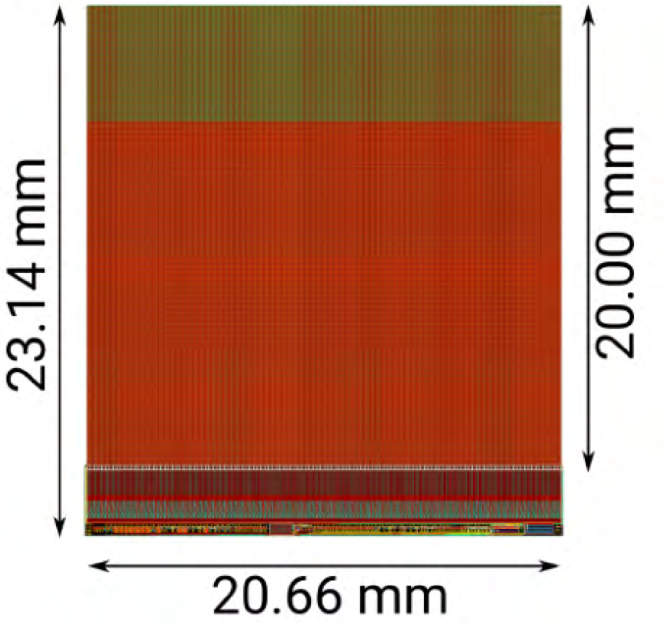

FIGURE 8.5: The layout of the MuPix10 with the main concepts The pixel matrix at the top and the readout cell, end of the column, state machine and periphery blocks at the bottom.

in figure 8.5. There is a deep n-well used as the charge collection electrode, electronics in shallow n-and p-wells and charge sensitive PMOS amplifier feedback circuit and output driver (source follower) are included in each pixel. Also, an improved routing of analogue signals from the pixels to the periphery is implemented to avoid capacitive coupling between the signal lines of neighbouring pixels.

8.2.4 MuPix8 Setups in the Liverpool

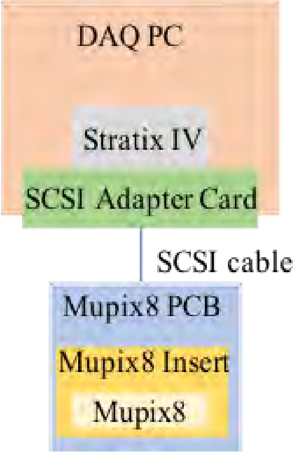

FIGURE 8.6: Schematic of the setup of the single MuPix8 chip onto the MuPix8 insert.

Figure 8.4 shows a schematic diagram of the MuPix8 setup. Photographs for the setup in Liverpool are shown in figure 8.5. The MuPix8 sensor is glued to a small PCB (called insert), which can be easily plugged into the bigger PCB. The MuPix8 PCB provides the interface for the readout of one MuPix8 chip. The PCB is connected to an adapter card via a SCSI cable. The adapter card is needed for connection between the Stratix IV (FPGA) and the data acquisition PC. A schematic view and photographs for Stratix IV and SCSI adapter cared are shown in the appendix in figure A.1. Hit map of MuPix8 for individual links on the PCB for port A, B and C are shown in the figure 8.8.

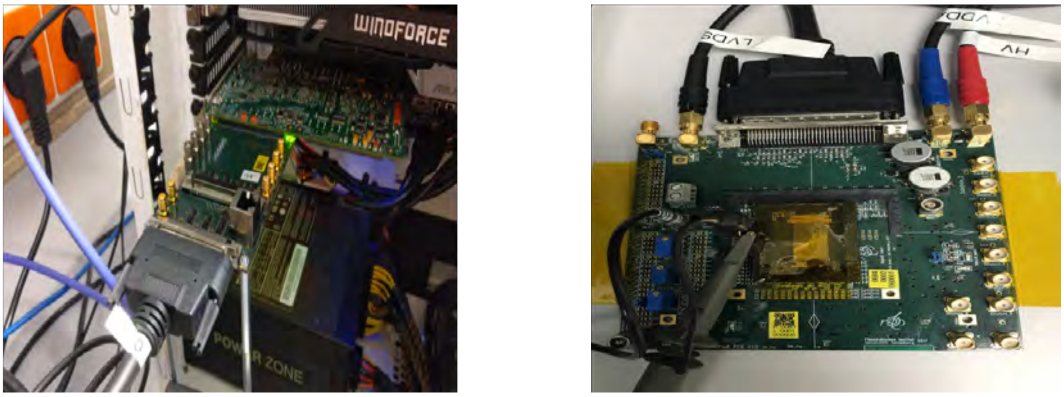

FIGURE 8.7: Left: FPGA and GPU. Right: The Mupix8 on the PCB

8.2.5 Calibration of Temperature MuPix8 Sensor

The ability to monitor the temperature is important in the Mu3e experiment to verify the cooling performance of the detector since thermal runaway is most often caused by failure of the cooling system. Must life with relatively high thermal gradient $(0°C - 55°C)$

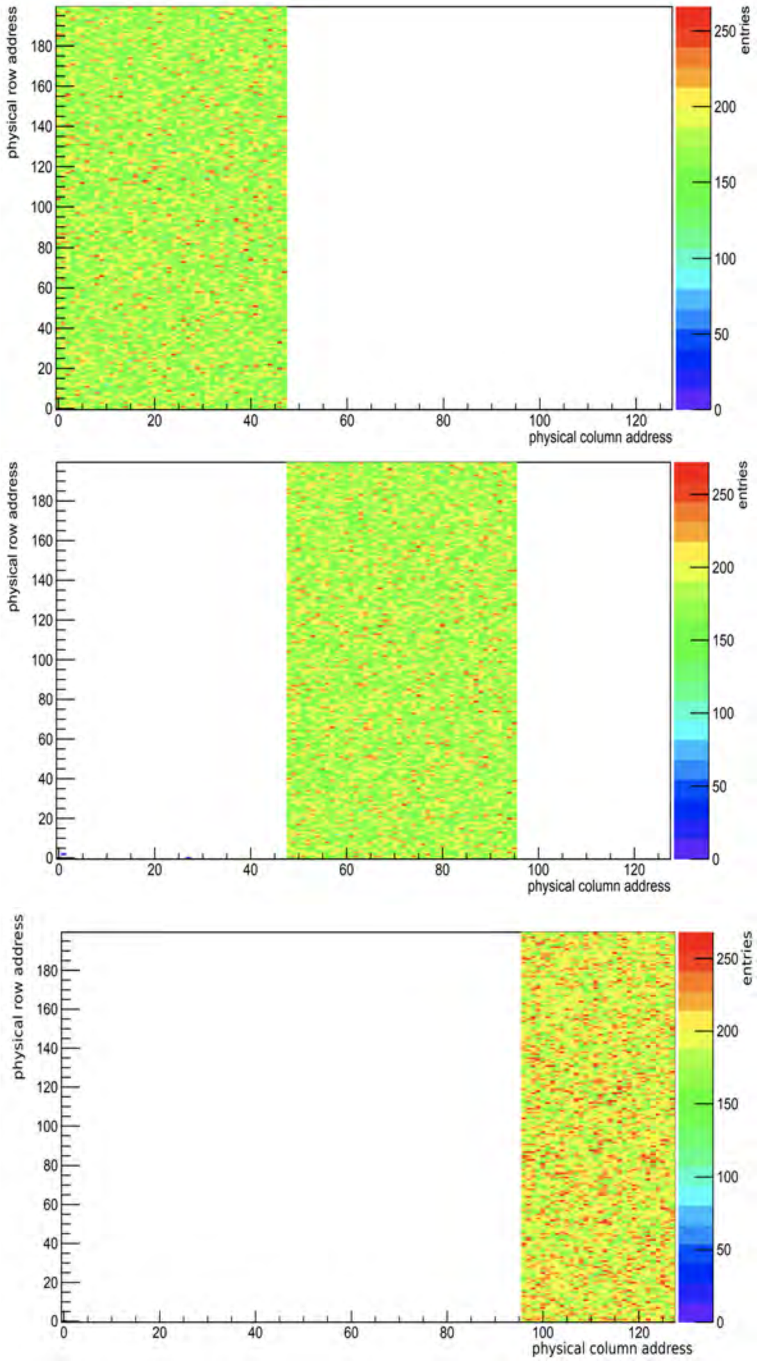

FIGURE 8.8: Hit map of MuPix8 on the PCB for port A, B and C.

due to 4.5 kW power dissipation in very low mass structure. To monitor the temperature, MuPix8 has a temperature sensor on-chip based on a diode. A current injected into the diode results in a voltage drop. This voltage drop is proportional to the temperature. To validate its functionality, the temperature sensor has been calibrated.

In this work, the calibration has been implemented as a two steps technique. First, we calibrate an IR camera with a PT1000 resistance glued to a broken MuPix8 chip which is mounted to a spare PCB since PCB will allow reading PT1000 resistance[1] easily. The temperature of the chip is controlled with a Peltier of the TCT set-up to cooler. The setup is shown in the appendix in figure A.3. The second step of the calibration is the calibration of the MuPix8 temperature sensor with the calibrated IR camera. The setup for this is shown in appendix figure A.8. All measurements were done using software described in the appendix A.3.

Its setup is as shown in the appendix in figure A.3. Second step calibration, we calibrate the MuPix8 temperature sensor with the calibrated IR camera, its setup is shown in appendix figure A.8. All measurements were done using software, more description on this software is in the appendix A.3.

8.2.6 Results on Calibration of Temperature

Calibration of the IR camera is required because temperature measurements with the camera are material dependent due to different surface emissivities. Therefore, a broken MuPix8 chip has been brought into thermal contact with a resistor PT1000 in a temperature-controlled environment. The temperature of the MuPix8 is read from the IR camera and simultaneously the temperature of the PT1000 was measured. Figure 8.9 shows calibration curves between an IR camera and a PT1000 element for the MuPix8 chip, the PCB, and the Mupix8 chip with the Typpex[2] added. Figures from 8.10, 8.11 and 8.12 show the measurement yields a calibration curve with a linear behaviour for the MuPix8 chip, the PCB, and the MuPix8 with Typpex, independently.

The calibration curve can be used to correct the temperatures measured with the IR camera. These corrected temperatures against the voltage measured across the diode integrated on the MuPix8 chip for a constant temperature DAC setting, i.e. for a constant injected current via using equation 2 in which $T_{IR_{Mupix8}}$ as a function of $V_{diode,95mA}$. The working point has been chosen at a current of 95 mA where the voltage spread for different temperatures is good as shown in figure 8.13 (Left), IV curves for the MuPix8

---

[1] The sensors used in the setup are PT1000 resistance thermometers. The temperature of MuPix could be read off from the IR camera. Simultaneously, the temperature of the resistor was measured using a PT1000 element in contact with the resistor.

[2] A white paint.

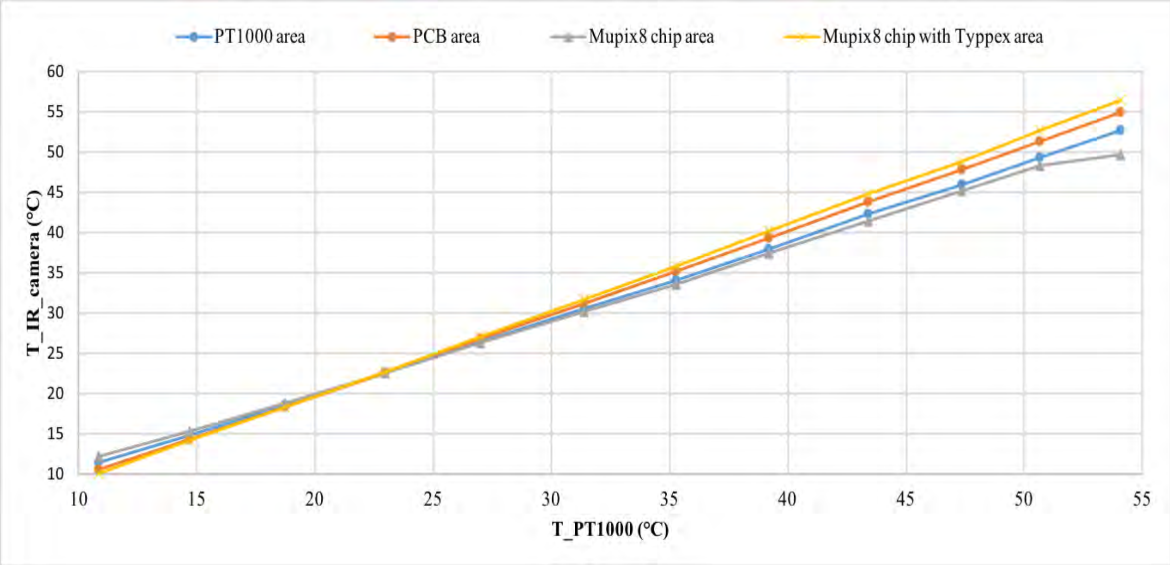

FIGURE 8.9: Calibration curve between an IR camera and a PT1000 element for the MuPix8 chip, the PCB, and the MuPix8 with Typpex.

temperature diode at different temperatures.

$$T_{IR_{Mupix8}} = a \times V_{diode,95mA} + b \qquad (2)$$

where a and b are defined in the same linear equation of MuPix8, so calibration of MuPix8 temperature sensor via using equation 2 is shown in figure 8.10 (Right) in which calibration curve of the MuPix8 temperature from the calibrated IR camera readings against V$_{diode}$.

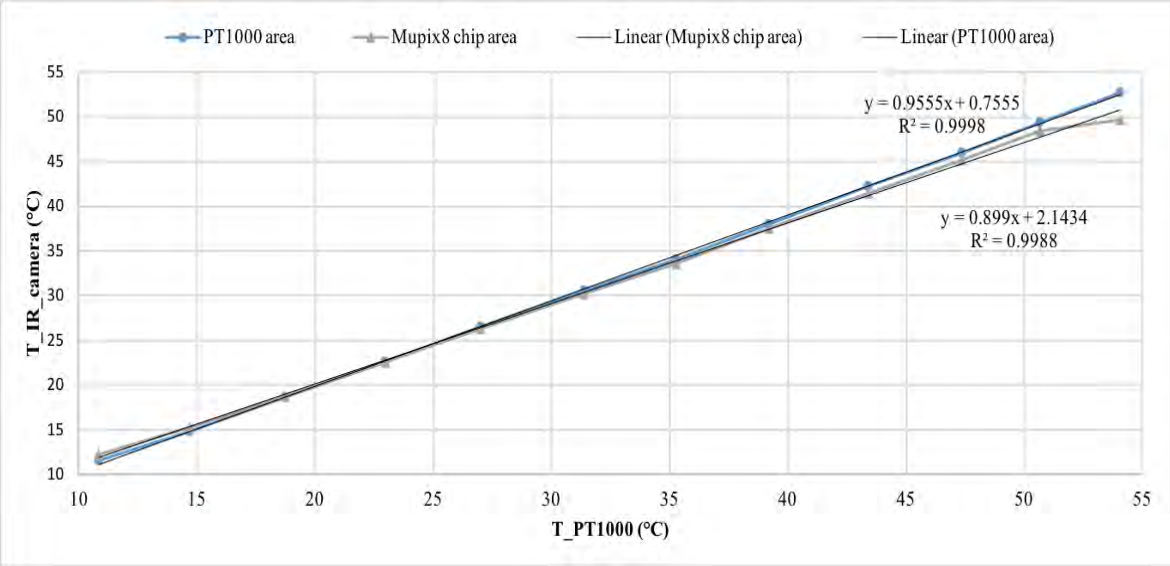

FIGURE 8.10: Calibration curve between an IR camera of a PT1000 element, MuPix8 chip, and temperature of the PT1000 with a linear fit.

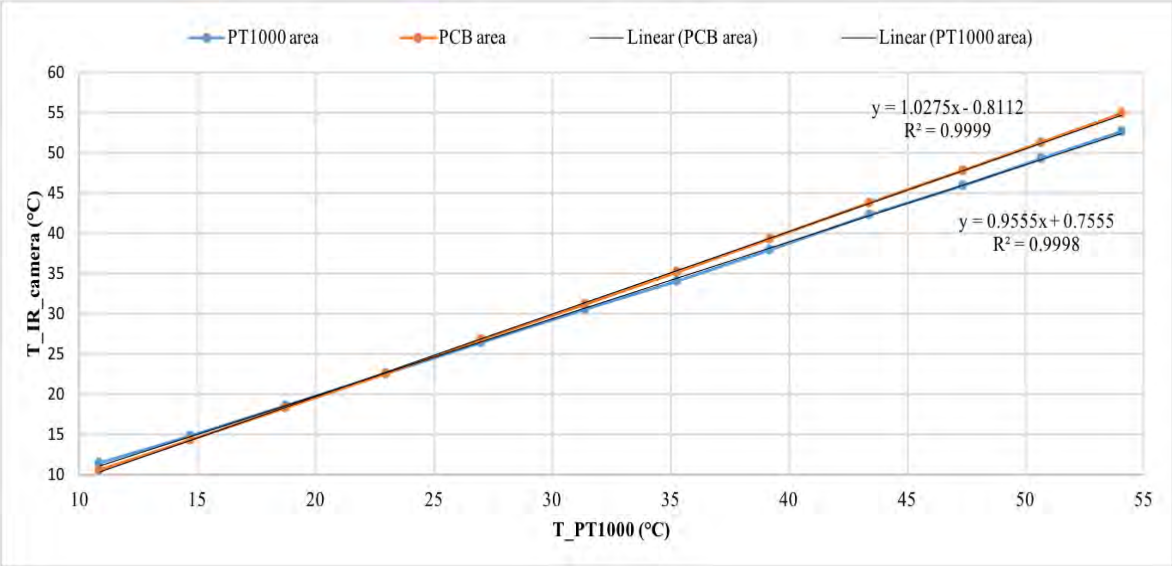

FIGURE 8.11: Calibration curve between an IR camera of a PT1000 element, PCB area, and temperature of the PT1000 with a linear fit.

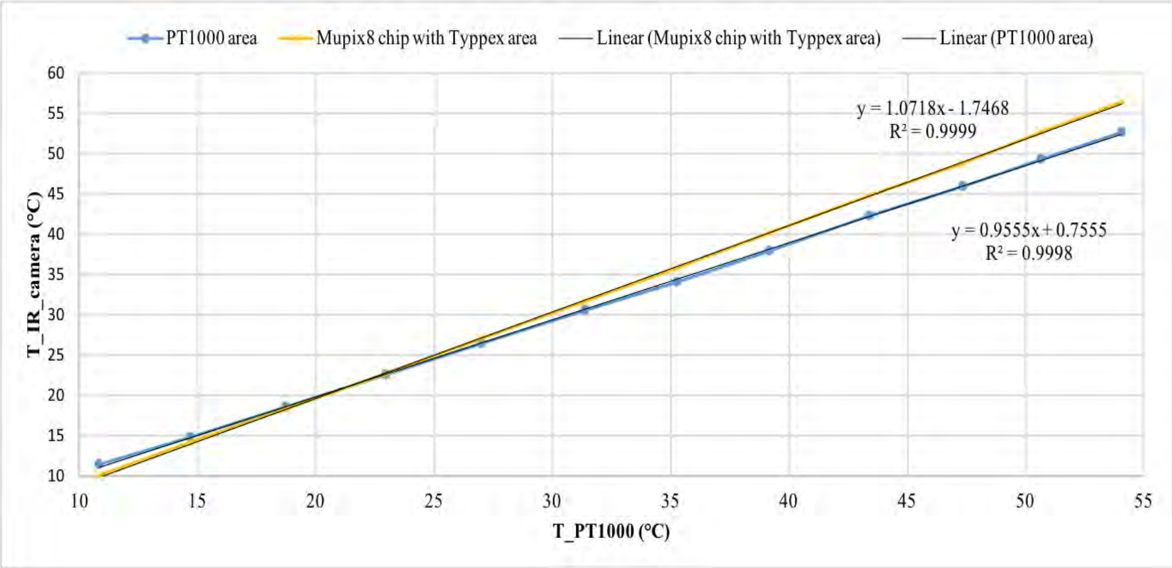

FIGURE 8.12: Calibration curve between an IR camera of a PT1000 element, MuPix8 chip with typpex, and temperature of the PT1000 with a linear fit.

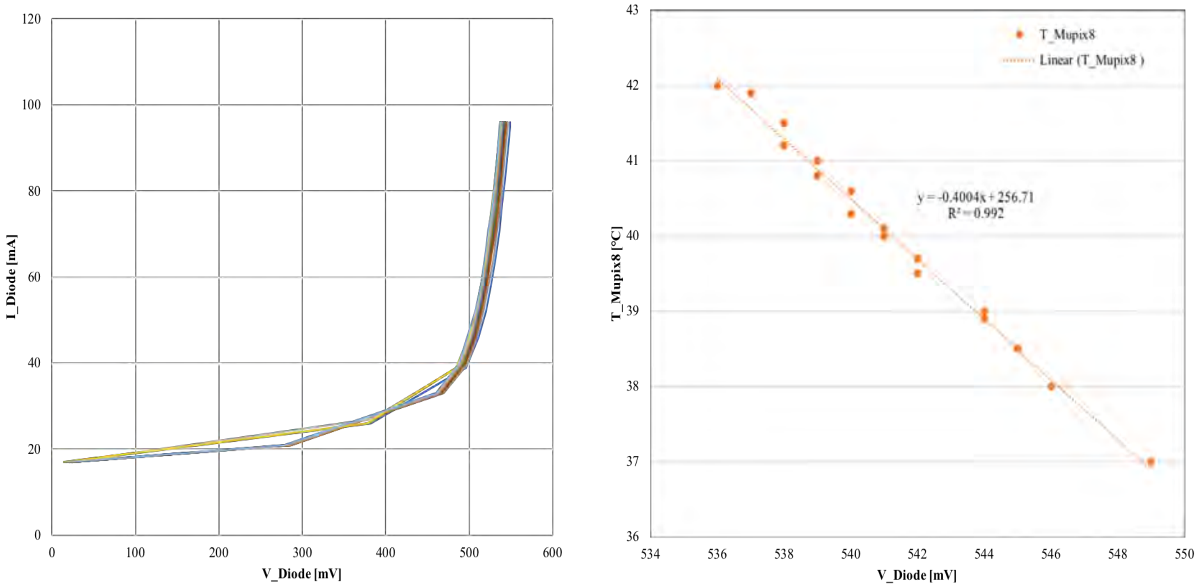

FIGURE 8.13: Left: IV curves for the MuPix8 temperature diode at different temperatures. Different curves are indicated to that the working point has been chosen at a current of 95 mA for all different colors where the voltage spread for different temperatures is good separation. Right: Calibration curve of the MuPix8 temperature from the calibrated IR camera readings against V_{diode} in which x in the slope equation is indicated to V_{diode}.

9 Track Reconstruction and Analysis with Pixel Telescope Data

This particle tracking telescope uses four or eight planes of MuPix sensors for tracking, in addition to two scintillating tiles in front and back for precise timing. A telescope is used to measure the efficiency and noise of sensor prototypes, as well as their spatial and time resolution. In this chapter, the analysis of test-beam data takes with the MuPix telescope is presented. Test-beam data were collected in the πM1 beam line at PSI on 14/10/2019.

9.1 Geometry and Coordinate Systems

In high energy particle physics experiments, tracking detectors are often used to reconstruct the momentum, charge, and direction of charged particles in the presence of a magnetic field $\vec{B}$. Since the high hit multiplicities from multiple tracking layers produce a combinatorial problem that can introduce fake tracks, a track model is required to describe the particle trajectory between tracking layers. As a result of fitting the track model to observed hits, a set of hits can be assigned to a single track. The number of high hit multiplicities n_i depend upon the number of planes i, so the total number of possible track candidates n_{tc} is given via:

$$n_{tc} = \sum_{i=0}^{n} n_i \tag{1}$$

Fitting a track trajectory requires knowledge of the measurement uncertainties. First, each pixel position has an uncertainty σ_m which in the case of the MuPix pixel detector can be induced by a pixel pitch $p_{x/y} : \sigma_m = p_{x/y}/\sqrt{12}$, assuming no charge sharing between pixels. Multiple scattering in a tracking layer can distort the particle trajectory adding an uncertainty to the scattering angle σ_{MS}. Finally, energy losses in the tracking layers could change the curvature of the particles. The main uncertainties in this model are from the intrinsic detector resolution from the pixel pitch. All of these measurement uncertainties are neglected in the straight line model (SLM) used in test-beam analysis. To calculate χ^2, there is assumed some error due to a bit of misalignment of planes.

A particle track is propagated from layer to layer, assuming that the particle leaves a hit in all individual planes within a search window. The best-reconstructed tracks are selected based on a smallest value of χ^2 cut in a given frame. If any two tracks share the same hit, both tracks will be rejected.

In the scope of this thesis, the track reconstruction method used for the test-beam analysis is SLM ignoring multiple scattering, as opposed to the broken line model (BLM, which considers the scattering of tracks [25]. In the case of a missing hit in a layer, the track is still accepted. The SLM has the advantage that it is a very fast model compared to BLM.

Two coordinate systems are considered by the tracking algorithm. In the following, the coordinate systems and track fit model are discussed. Subsequently, the principle of the device under test (DUT) is described. Two coordinate systems are considered by the tracking algorithm for the test-beam analysis. These are the global and local Cartesian coordinate systems. The global coordinate system is defined on the first-pixel sensor plane, where the z-axis is the beam direction and the x and y axes are defined to be parallel to the columns and rows of the pixel matrix in which telescope layers are not rotated to each other. In general, hits in the global coordinate system are denoted as $\mathbf{x} = (x, y, z)^T$ in which the origin is set to the centre of pixel (0,0) in the first pixel layer.

The local coordinate system is chosen for the other planes (1,2,3). They are given in unit of pixels and denoted as $\mathbf{x} = (c, r, 0)^T$, in which c is the column and r is the row along the x and y-direction, respectively. The z-axis is the normal vector to the plane. Figure 9.1 shows a sketch of the coordinate systems.

9.2 Coordinate Transformation

Shifts and rotations of the local coordinate system compared to the global system are needed to move between these two coordinate systems. The transformation is defined

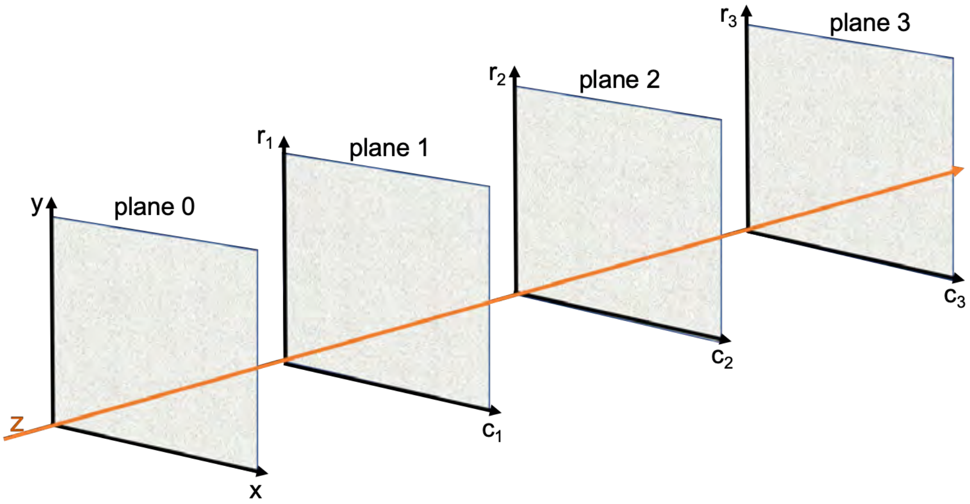

FIGURE 9.1: Sketch of the coordinate systems. (x,y,z) is the global coordinate system defined by the column and row axes of layer 0. The z-axis is the beam direction which is drawn with orange colour. The local coordinate system (c,r,0) is defined for the other planes.

as:

$$\mathbf{x} = \mathbf{Q}\mathbf{u} + \mathbf{t} \tag{2}$$

where t is the shift between planes and Q is a 3x3 transformation matrix with two parts. The first term is a 3x3 rotation matrix R, and the second term is a diagonal 3x3 matrix P that in which matrix P converts column and row numbers to the distances on the plane. Q and t are given as:

$$\mathbf{Q} = \mathbf{R}.\mathbf{P}; \qquad \mathbf{t} = \begin{pmatrix} \text{offset}_x \\ \text{offset}_y \\ \text{offset}_z \end{pmatrix} \tag{3}$$

The pitch pixel matrix P is defined as:

$$\boldsymbol{P} = \begin{pmatrix} p_x & 0 & 0 \\ 0 & p_y & 0 \\ 0 & 0 & 1 \end{pmatrix} \tag{4}$$

For a 3x3 rotation matrix R, Euler Angles are used:

$$\boldsymbol{R}=\boldsymbol{R}_x\boldsymbol{R}_y\boldsymbol{R}_z \tag{5}$$

A rotation around z-axis is performed first as:

$$\boldsymbol{R}_z = \begin{pmatrix} \cos\psi & \sin\psi & 0 \\ -\sin\psi & \cos\psi & 0 \\ 0 & 0 & 1 \end{pmatrix} \tag{6}$$

The coordinate transformations are implemented in the Transform3D class of ROOT package [17].

9.3 Track Model Reconstruction Without Multiple Scattering

A straight line model (SLM) describes a particle trajectory through tracking layers without a magnetic field. The suitability of using this model depends on the particle momentum, the pixel pitch, the number of layers and the thickness of the material. With a low material budget and high momentum particles, the multiple scattering (MS) can be ignored.

A particle track without MS in the absence of a magnetic field $\vec{B}$ is described by a simple straight track as:

$$\mathbf{f}(z) = \mathbf{a} + \mathbf{s} \cdot z \tag{7}$$

where z is the z-position in the global coordinate system, a is an initial x and y position in the global coordinate system at z=0, and s is a constant two dimensional slope. In the case of straight line reconstruction without MS, and tracks that are assumed to be perpendicular to the planes, a χ^2 definition can be formulated as:

$$\chi^2 = \sum_{i=0}^{n_{\text{planes}}} \left(\frac{(P_{x,i} - (a_x + s_x \cdot z_i))^2}{\sigma_{i,x}^2} + \frac{\left(P_{y,i} - \left(a_y + s_y \cdot z_i\right)\right)^2}{\sigma_{i,y}^2} \right) \tag{8}$$

where i is the number of reference planes, n_{planes} is the number of reference planes in which $P_i = (x_i, \mathrm{y}_i, \mathrm{z}_i)^T$ being the pixel centers in the global coordinates, while the measurement uncertainties are $\sigma_{x,i} = P_x/\sqrt{12}$ and $\sigma_{y,i} = P_y/\sqrt{12}$ for each plane i. In order to get the best estimator of χ^2, one can calculate the derivatives of χ^2 with respect to the track parameters and setting them equal zero to find the minimum χ^2, the set of derivatives can be rearranged in lead to the following matrix form:

$$\begin{pmatrix} \sum_{i=1}^{n} x_i \\ \sum_{i=1}^{n} (x_i \cdot z_i) \\ \sum_{i=1}^{n} y_i \\ \sum_{i=1}^{n} (y_i \cdot z_i) \end{pmatrix} = \begin{pmatrix} \sum_{i=1}^{n} z_i & \sum_{i=1}^{n} 1 & 0 & 0 \\ \sum_{i=1}^{n} z_i^2 & \sum_{i=1}^{n} z_i & 0 & 0 \\ 0 & 0 & \sum_{i=1}^{n} z_i & \sum_{i=1}^{n} 1 \\ 0 & 0 & \sum_{i=1}^{n} z_i^2 & \sum_{i=1}^{n} z_i \end{pmatrix} \cdot \begin{pmatrix} s_x \\ a_x \\ s_y \\ a_y \end{pmatrix} \tag{9}$$

Uncertainties on the parameters s$_{x,y}$ and a$_{x,y}$ can be derived from the second derivative of χ^2. These derivatives can be calculated as:

$$\begin{aligned} \sigma_{a_x}^{-2} &= \frac{1}{2}\frac{\partial^2 \mathcal{X}^2}{\partial a_{x^2}} = \sum_{i=1}^{n} \frac{z_i^2}{\sigma_{x_i}^2} \\ \sigma_{x_0}^{-2} &= \frac{1}{2}\frac{\partial^2 \mathcal{X}^2}{\partial x_0^2} = \sum_{i=1}^{n} \frac{1}{\sigma_{x_i}^2} \\ \sigma_{a_y}^{-2} &= \frac{1}{2}\frac{\partial^2 \mathcal{X}^2}{\partial a_y^2} = \sum_{i=1}^{n} \frac{z_i^2}{\sigma_{y_i}^2} \\ \sigma_{y_0}^{-2} &= \frac{1}{2}\frac{\partial^2 \mathcal{X}^2}{\partial y_0^2} = \sum_{i=1}^{n} \frac{1}{\sigma_{y_i}^2} \end{aligned} \tag{10}$$

9.4 Device Under Test Studies Using Tracking information

One of the layers of the telescope is considered to be the device-under-test (DUT) and is studied in order to characterise the properties of the MuPix prototypes. A track is extrapolated to a DUT layer in order to determine an efficiency and noise rate per pixel or per layer of the detector, as well as the spatial resolution of hits. The DUT layer can be placed in the middle of the tracking telescope.

9.5 Hit Matching Method

One of the layers of the telescope is considered to be the device-under-test DUT, and is studied in order to characterize the properties of the MuPix prototypes. After definition of the DUT layer and the global and local coordinate systems, an extrapolated track with intersections $t_{inter,i}$ is matched to hits $h_{pos,i}$ on the DUT layer. A region of interest ROI is defined to remove edge effects and some selection cuts are applied, including a time window cut and a matching radius cut (see figure 9.2), defined using the equation:

$$\left(t_{\text{inters },x} - h_{\text{pos },x}\right)^2 + \left(t_{\text{inters, }y} - h_{\text{pos, },y}\right)^2 \leq r_{\text{cut}}^2 \tag{11}$$

If there are more than one hit within the radius cut, the closest hit will be assigned to the track. The distribution of matching distances is shown in figure 9.3. The matching radius cut is set at 400 μm.

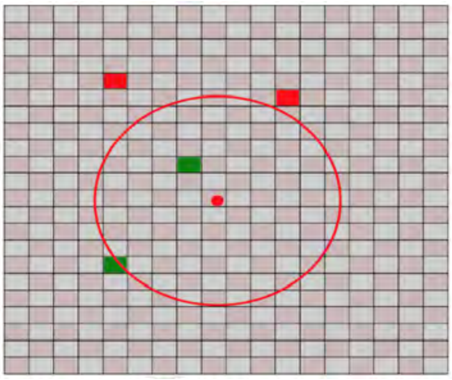

FIGURE 9.2: Searching window to match a hit in each layer

The matching algorithm considers the extrapolation of all tracks to the DUT layer. In the case of a missing hit in a layer, this track will be rejected. Figure 9.4 displays the multiplicity of hits per frame [1] after applying cuts, the maximum number of hits depending on the higher number of layers. The efficiency for the matched tracks is 0.998 in which the total number of tracks for the DUT layer is 1258818 for run 1429 and matched tracks extrapolated into the DUT layer in ROI is 1256610.

9.6 Efficiency Calculation

The sensor efficiency ϵ is the ratio between the number of matched tracks with a hit m and a total number of matched and unmatched tracks extrapolated into the DUT ROI N:

---

[1] When the particle hits the chips, the hit is saved in the pixel with its timestamp, but then it awaits the DAQ to take it out, and this loops over column and rows, so it happens that the hits are not sent out in time sequence. The firs thing then is to align them in time, a procedure called sorting. After sorted, the hits are aligned and one can "create" the time frames by basically dividing the hit stream in chunks, such as time windows. The idea is that then you correlate all the hits within a time window to reconstruct tracks. (the sorting is done with the timestamp information).

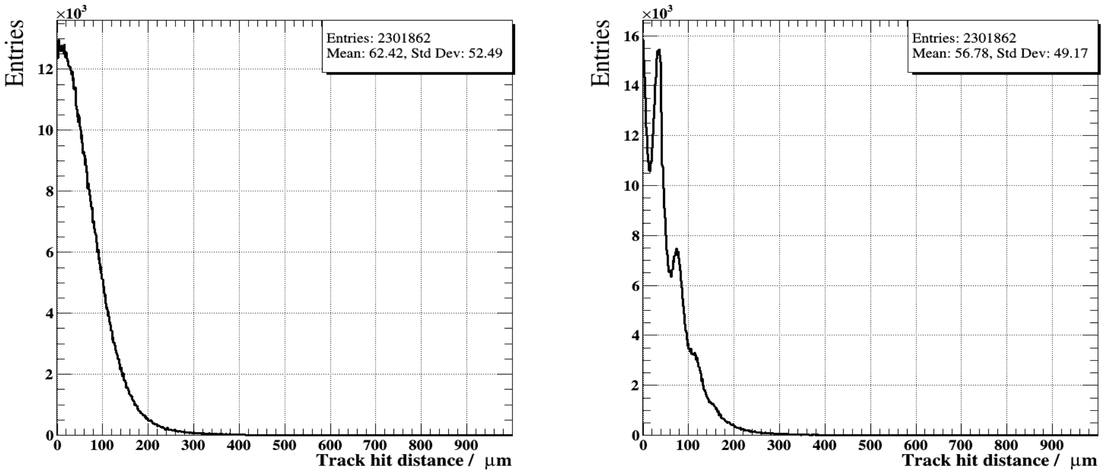

FIGURE 9.3: Searching for a window within 400 μm along the horizontal and vertical direction, respectively.

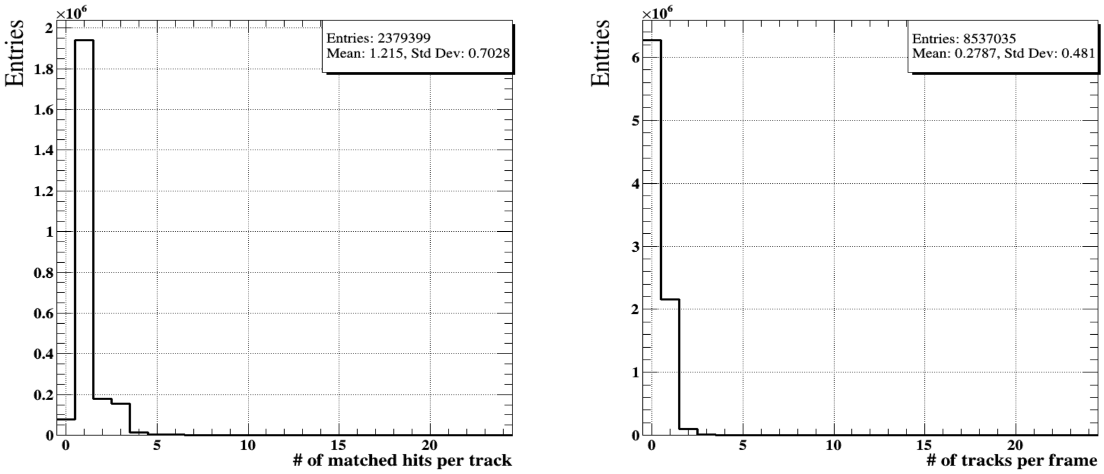

FIGURE 9.4: Multiplicity of matched hits (DUT) per track (left) and tracks with matched DUT hit per frame (right).

$$\epsilon = \frac{m}{N} \tag{12}$$

The uncertainty on the efficiency is given by binomial statistics:

$$P(m, N, \epsilon) = \frac{N!}{m!(N-m)!}\epsilon^m (1-\epsilon)^{N-m} \tag{13}$$

and the standard deviation on a binomial distribution is:

$$\sigma = \frac{\sqrt{m\left(1-\frac{m}{N}\right)}}{N} \tag{14}$$

During test-beam, hits that are not assigned to a track are referred to as unmatched hits. There are two contributions to the unmatched hits in test-beam measurements. The real noise is of the sensor diode (It is created either by leakage currents in the sensing diode or noise in the circuity), and accidentals which means actual particles are crossing the sensor which are not correlated with any track that the telescope observed.

In general, accidental hits occur at a low rate where tracks are missing due to tracking inefficiencies on the layers or geometrical mis-alignment of the telescope. The πM1 beam line [1] at PSI provides a mixed particle beam consisting of pions, muons, electrons, and protons, with pions being the dominant component. The sensor noise rate can be measured without particle source injection. However, during beam operation, the sensor noise rate can change because of increasing the activity. The average pixel noise rate can be estimated as follow:

$$\overline{n_p} = \frac{n_{hits} - m}{N_p \Delta t} \tag{15}$$

n_{hits} is all total number of hits, m is the number of hits matched to tracks, N_p is the number of pixels, and Δt is the runtime. This calculated noise rate is an estimation as it includes unmatched hits due to inefficiencies and misalignment of layers.

9.7 Clustering Algorithm

The resolution of the pixel measurement is dependent on the size of the hit clusters. A clustering algorithm associates hits in pixels to form single clusters. Figure 9.5 shows locations cluster of different sizes. The largest cluster size is four if the a particles hits the corner between 4 pixels.

The cluster size depends on three parameters: the charge is required to trigger a pixel hit, the total deposited charge, and the width of the ionization. The charge deposition can be estimated with a landau distribution, and the ionization width is estimated by a Gaussian intensity distribution.

The charge deposited in an individual pixel cell can be calculated as:

$$Q_{\text{cell}} = Q_p A \int_{x_{\min}}^{x_{\max}} \int_{y_{\min}}^{y_{\max}} e^{0.5\left(\frac{x-\mu x}{\sigma}\right)^2} e^{0.5\left(\frac{y-\mu y}{\sigma}\right)^2} dxdy \tag{16}$$

where Q_p is the total charge, $x_{min,max}$ to $y_{min,max}$ represent the pixel boundaries and σ_{ion} is the ionization width which defines by the Gaussian width $\sigma = \sigma_{ion}/\sqrt{2}$. A is a normalization factor which normalizes the two dimensional Gaussian:

$$\frac{1}{A} = \int_{-\infty}^{\infty} \int_{-\infty}^{\infty} e^{0.5\left(\frac{x-\mu x}{\sigma}\right)^2} e^{0.5\left(\frac{y-\mu y}{\sigma}\right)^2} dxdy \tag{17}$$

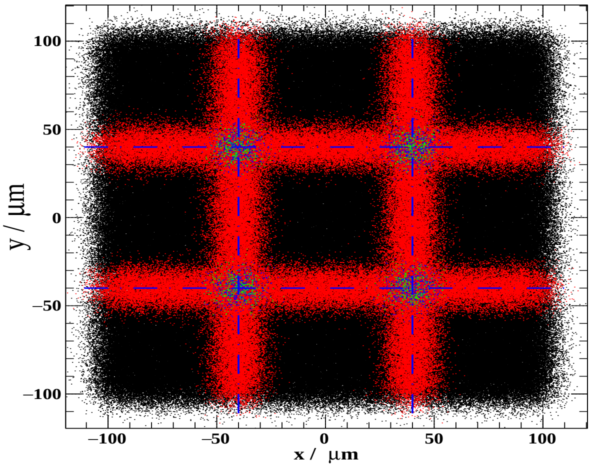

FIGURE 9.5: Simulated positions of the cluster with different sizes. Single clusters are drawn as black dots, the double cluster in red, the triple cluster in blue and the quadruple in green. The dashed blue lines mark the pixel edges. A detection threshold of 10 % and a charge cone σ of 3 μm is assumed.

The probability to create a cluster of a particular size is related to the probability of charge sharing which depends on the charge deposition and ionization width. For a simulated sample of hits, sizes as function of position are shown in figure 9.5. In the central region of the pixel cells, single clusters are produced while the two-pixel cluster sizes are created along the edges of pixel cells. In the corner of the pixel cells, 4-hit cluster sizes are observed, surrounded by small regions with 3-hit clusters.

In addition to charge sharing, cluster sizes can also be affected by cross-talk. Cross-talk occurs due to the capacitive coupling of signals between neighbouring transmission lines for analogue signals from the pixels to the periphery. While pixel clusters caused by charging sharing alone consist of 1, 2, 3 or 4 directly neighbouring pixels, clusters due to cross talk can extend over 3 more pixels along the column direction (since the transmission lines run along the column direction) as shown in figure 9.6.

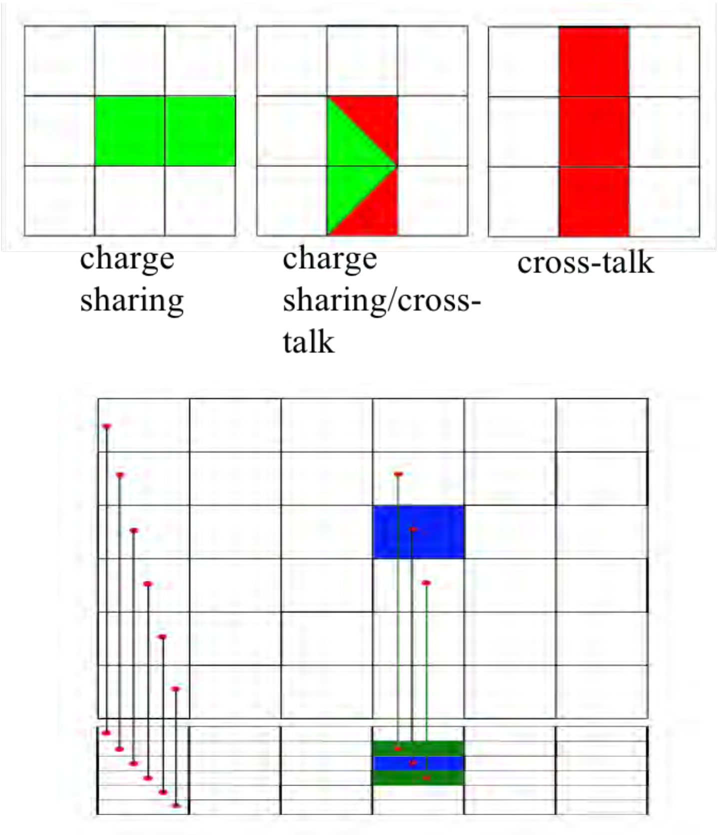

FIGURE 9.6: Sketch of one dimensional double, triplet cluster sizes is originated via charge sharing. Single cluster sizes are created by cross-talk while the transmission lines run along the column direction is shown in the bottom.

9.7.1 Analysis Procedure

The analysis procedure for the data recorded during the test-beam and sorted as a file on the data collector is presented in figure 9.8. For each frame, the data is sorted and converted into a ROOT ntuple. Hot pixels are removed, and the clustering is performed. From this, the hit positions are extracted and an alignment procedure is performed. The figure for the data collector is shown in the appendix A.3. The timing and TOT information is also stored.

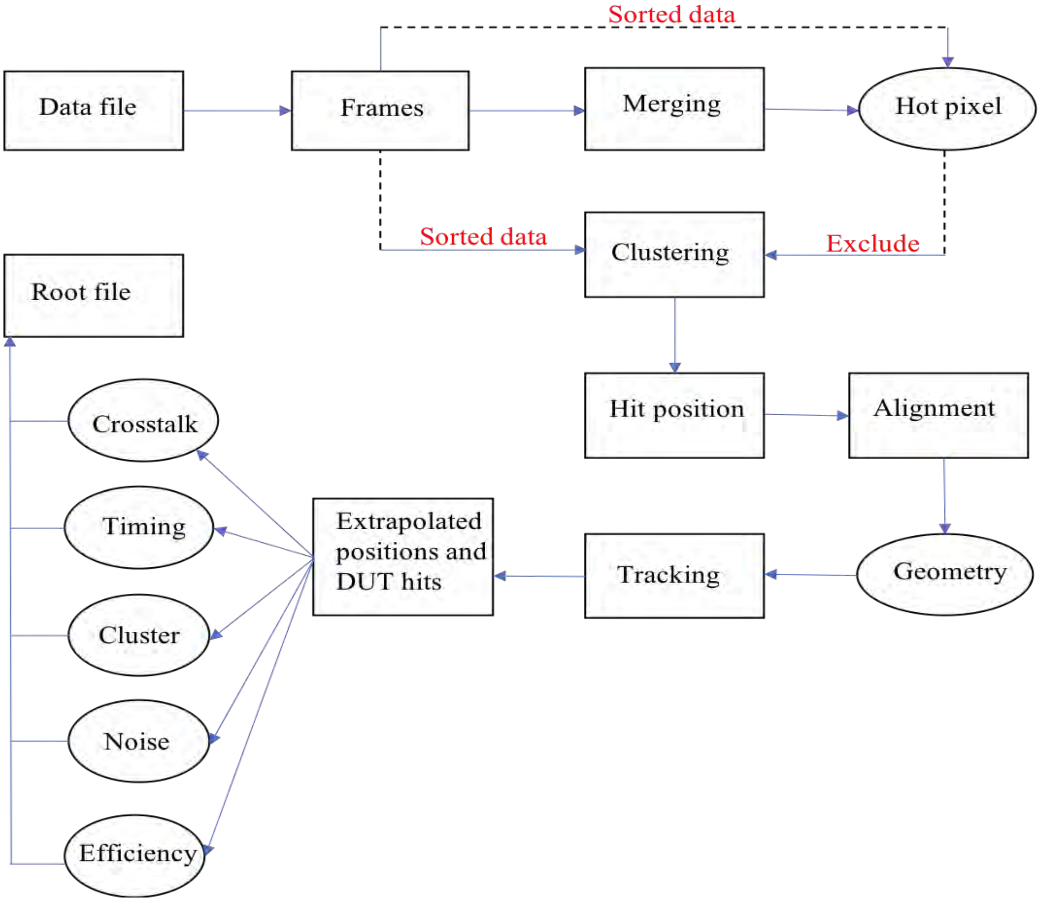

FIGURE 9.7: Analysis procedure for data obtained with the MuPix telescope.

The software readout chain consists of a GUI and an online monitoring tool, figures are shown in the Appendix A. It is implemented in C++ and uses Qt libraries, boost library, and the JSON library. The readout software copies the data provided via the two FPGAs to local memory, then as a final data stream to disk. For analysis, the data file is opened and frames are extracted. The frames contain individual sensor information, and they are merged according to their timestamps. Hot pixels are defined as those pixels which contain at least 5% of the total number of hits on the sensor. These are removed as they can be a source of fake tracks. For example, run 1409. Removing 251 noisy/hot pixels out of 589824 pixels reduces the total hit amount by a factor five.

Clusters are defined as sets of neighboring hits. Extracting hit positions is done next. Next, the frames are ready for telescope alignment, the alignment results are stored in a geometry file. The tracks are reconstructed and hits are used for DUT studies. In addition, cross-talk, timing resolution, cluster size, efficiency and noise rate can be studied using the matched and unmatched hits on the DUT. All results are stored as histograms in a root file.

10 Test-beam Data Acquisition System and Characterization of HV-MAPS

The test-beam telescope (Chapter 9) was used to investigate two HV-MAPS prototypes for the Mu3e detector, MuPix8 and MuPix9 (Chapter 8). The telescope setup, the readout design, DAQ concept, monitoring, and online efficiency calculation are presented. In addition, results from alignment stability, efficiency, noise cross-talk and time resolution studies of both prototypes are summarized in this chapter.

10.1 Telescope Setup and Configuration

The MuPix tracking telescope is optimized for high particle rates with low momentum tracks in which multiple scattering (MS) is the dominating effect for the track resolution. The planes are chosen to be thin as possible and only the central region of pixels is used to allow for miss-alignment of layers and MS.

10.1.1 Setup of Telescope Planes

The MuPix Telescope was operated at PSI, using the πM1 beam, from 13 to 22 Oct 2019. The πM1 beam is injected along the z-axis of the telescope, with momentum 270 MeV (pion, electrons, and muons), and a current of 1860.10 μA. It consists of four layers of MuPix8 sensors that are connected via SCSI cables to an FPGA inside the DAQ computer. Two trigger scintillators are mounted before the pixel layers and serve as an additional precise time reference for the study of the timing performance of pixel sensors with the

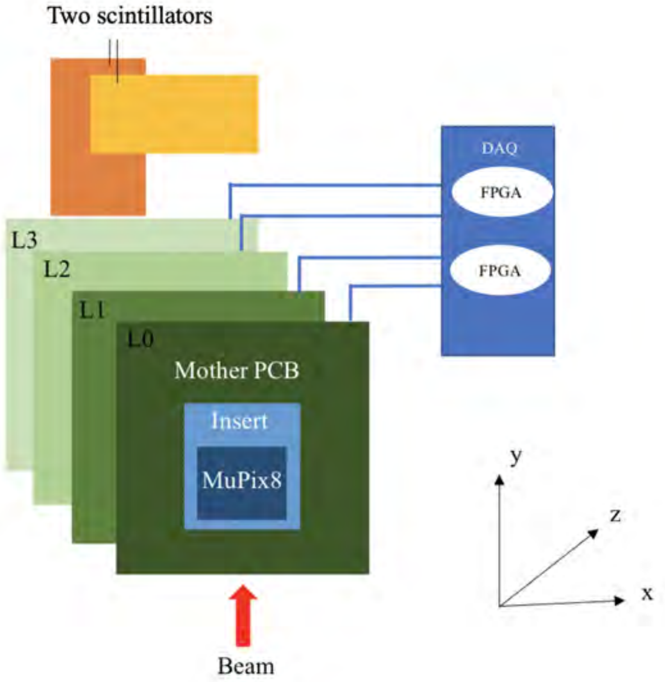

FIGURE 10.1: Sketch of the MuPix8 Telescope layout. Four sensors are mounted on PCBs board and framed by two trigger scintillators.

MuPix telescope, see figure 10.1. The timing scintillator detector has a good timing resolution of 10 ps. The MuPix sensors are mounted on insert-PCBs and insert in mother-PCBs. To operate, a GUI is included in the telescope DAQ and a four-plane telescope using the same software DAQ with the Mu3e front-end board (More discussion of DAQ and software in the previous chapter).

FIGURE 10.2: Picture of the MuPix8 Telescope layout. Four sensors are mounted on PCB boards.

The MuPix8 telescope is shown in figure 10.2, with the configuration given for the data analysed in table 10.1. The connection to the PC was done via 8 flat ribbon cables surrounded by aluminium to protect them against external electric fields. All PCBs were connected to a separate low voltage power supply, while the high voltage was connected to a shared high voltage supply and set to 60 V for the MuPix8 sensors, and 40 V for MuPix9. For testing the MuPix8 prototype, layer 2 is chosen to be the DUT. For testing MuPix9, layer 2 is substituted with a MuPix9 prototype.

Layer	Sensor ID	Board ID	Distance [mm]	Resistivity (Ωcm), Thickness(μm)
1	265-3-9	242-3-19	0	200,100
2	265-3-1	242-3-33	68.4	80,100
3	265-3-16	242-3-13	138	200,100
4	265-2-16	242-3-16	211	200,100

TABLE 10.1: MuPix Telescope configurations on all the sets of runs.

10.1.2 Cluster Size and Cross-talk Studies

As mentioned in the previous chapter, understanding the cluster size is critical to achieving the best hit position resolution on the reference planes of the telescope. Figure 10.3 shows the total number of hits after removing hot pixels for the MuPix8 and MuPix9 DUTs, respectively. The difference in the number of hot pixels is due in part to the value of the amplification used for the DUTs. The total number of particle hits are 29M for MuPix8 while 24M for MuPix9. Figure 10.4 shows that MuPix8 has an average cluster size of 1.29 compared to a value of 1.13 for MuPix9. This difference is due to cross-talk. Only matrix A is shown.

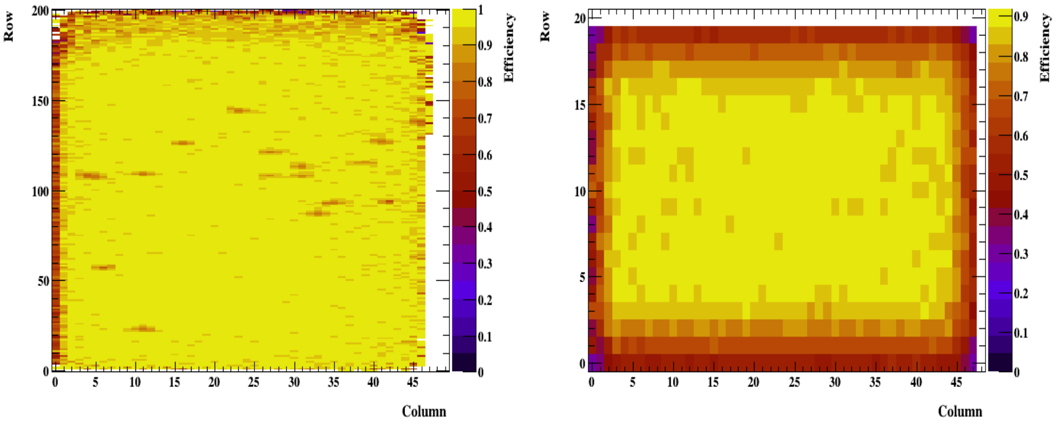

FIGURE 10.3: Efficiency map for reference layer 1 for MuPix8 of run 1429 with threshold 545 mV and for MuPix9 of run 2178 with threshold 610 mV, respectively.

Figure 10.5 shows vertical and horizontal cluster size distributions for matched clusters for data for MuPix8, operated at -60 V bias and a threshold of 545 mV (Left), and for

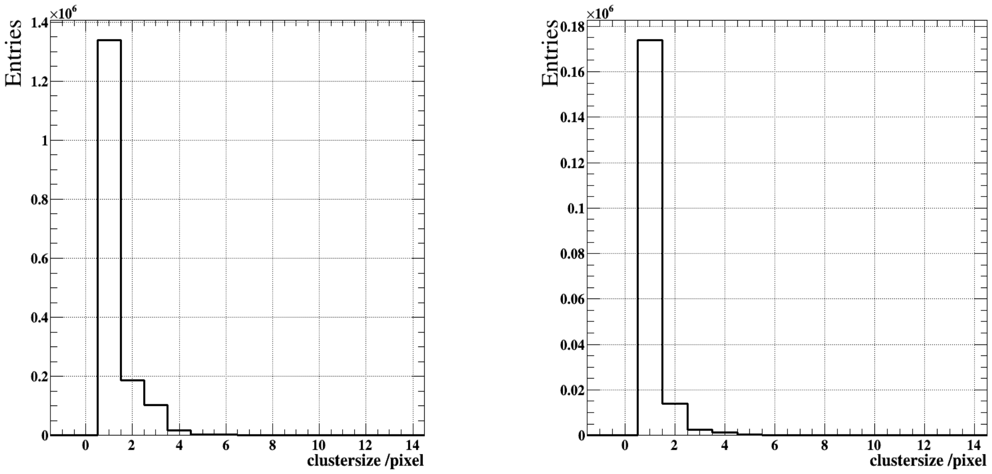

FIGURE 10.4: Cluster size for MuPix8 (left) and MuPix9 (right) DUT layer.

MuPix9 operated at -40 V bias (Right). In MuPix8 a substantial increase in the number of 2- and 3-hits cluster is observed along the vertical (column) direction, consistent with cross-talk. This is not observed in MuPix9 where the signal lines are much shorter, the fact that it is smaller is also the reason why it has less cross-talk.

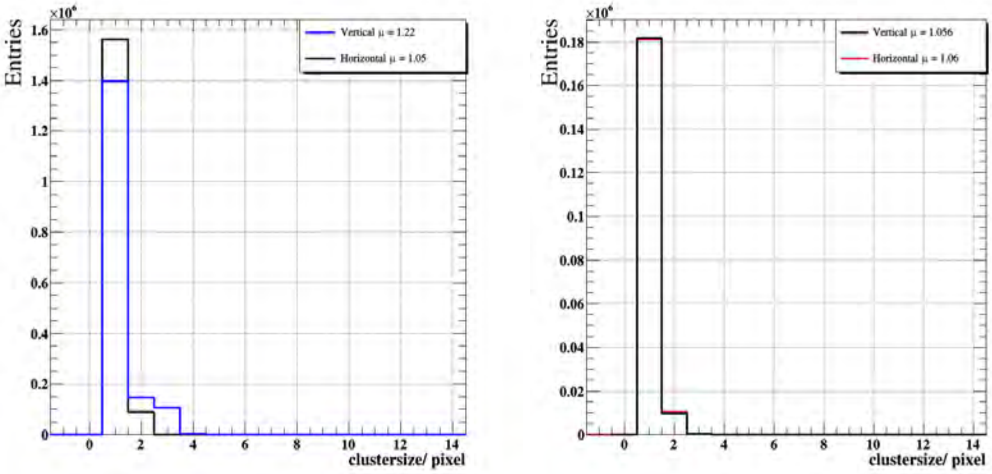

FIGURE 10.5: Vertical and horizontal cluster size distribution for matched clusters for data taking for MuPix8, at -60 V bias and a threshold of 545 mV (Left), and for MuPix9 at -40 V bias (Right).

In addition, to understand the cluster positions for all single, double, triplet matched clusters, figure 10.6 shows the distribution of clusters across the surface area of MuPix8 are observed more frequently at the top end of the matrix, corresponding to longer routing lines. MuPix9 is shown in figure 10.7.

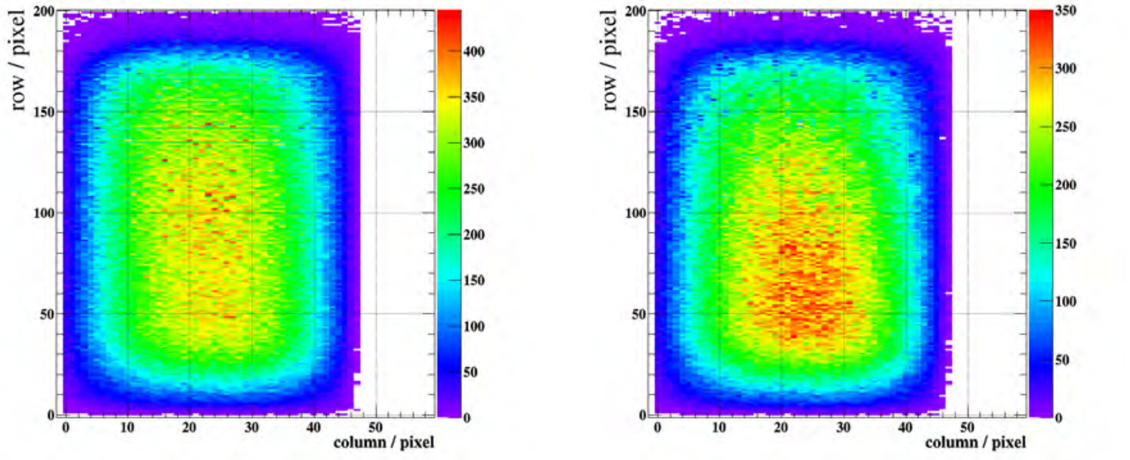

(A) All.

(B) 1-pixel.

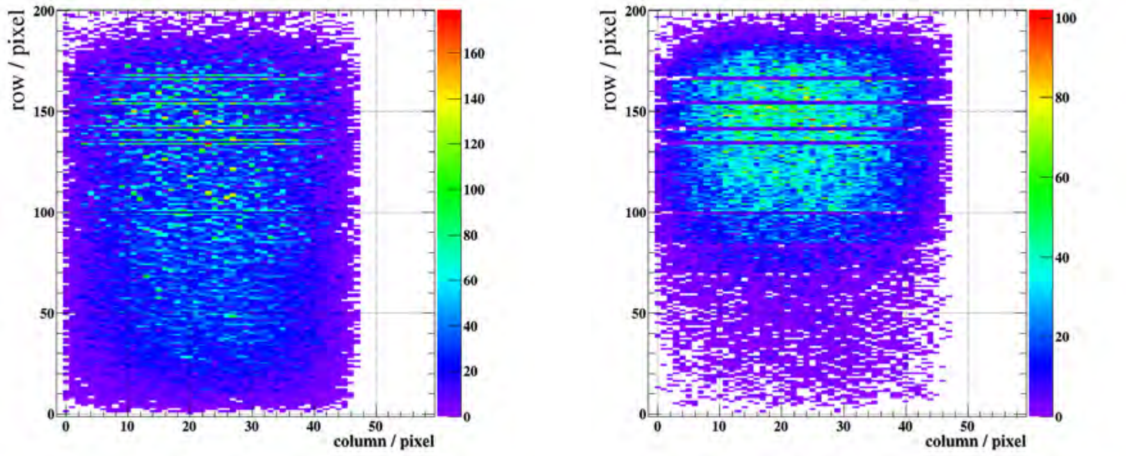

(C) 2-pixels

(D) 3-pixels

FIGURE 10.6: Cluster position for all matched clusters, and with a multiplicity of 1, 2, and 3 matched clusters, respectively. A threshold of 545 mV and a bais of -60 V is used on MuPix8.

10.1.3 Alignment

Before reconstructing particle trajectories, the software alignment (see Chapter 7) has to be applied to account for mis-alignment of the sensor planes if the planes are not perfectly aligned mechanically. The correlations between row and row addresses of different sensor layers are expected to show a diagonal line as well as the column address correlations to study the shift of the sensors. However, no lines are expected for the correlations between rows and columns, if there is a line, it is a clear hint for a relative rotation of layers. The geometry alignment parameters of each plane should be known, such as ID plane, MuPix type, number of columns, number of rows, pitch column, pitch row, and offset between layers.

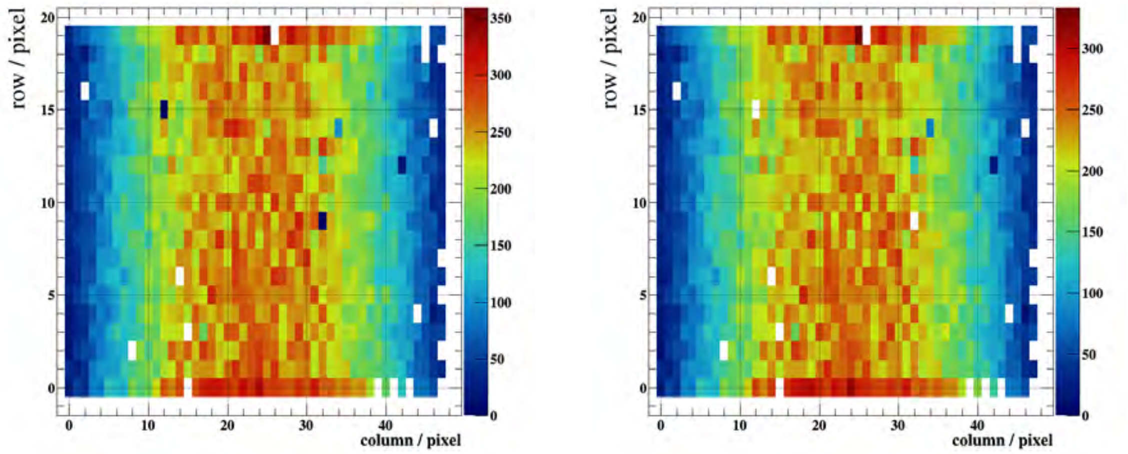

(A) All.

(B) 1-pixel.

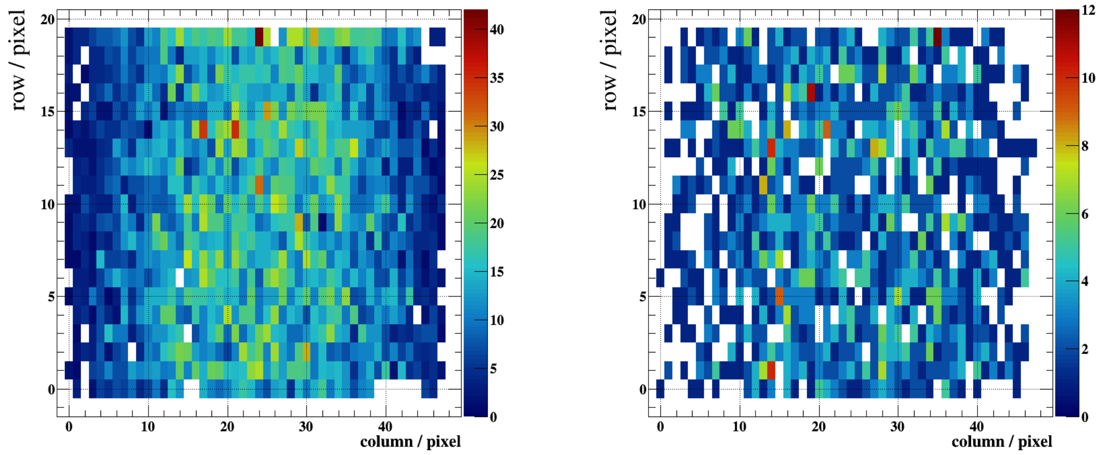

(C) 2-pixels

(D) 3-pixels

FIGURE 10.7: Cluster position for all matched clusters, and with a multiplicity of 1, 2, and 3 matched clusters, respectively. A threshold of 620 mV and a bais of -40 V is used on MuPix9.

There are pixel layers mis-alignments, that need to be corrected using millipede, same method that is discussed in the Chapter 7. Alignment parameters x, y positions and rotations are calculated step by step. The shift in the x-y axis is allowed first then only rotations around the z-axis which is beam direction. Finally, shifts in the x-y axis and z-axis are applied at the same time. After the alignment, tracks can be reconstructed by using SLM. Events with a single cluster on each layer are selected to avoid confusion and a straight line fit to the central region is applied to the hits in all layers excluding the DUT layer. The resultant χ^2 distribution for MuPix8 and MuPix9 is shown in figure 10.8, and a cut is applied at χ^2= 100.

The resulting residuals for the DUT are shown in figure 10.9, the x and y residuals are 72.93 μm and 72 μm, respectively. This is larger than the expected pixel resolution of

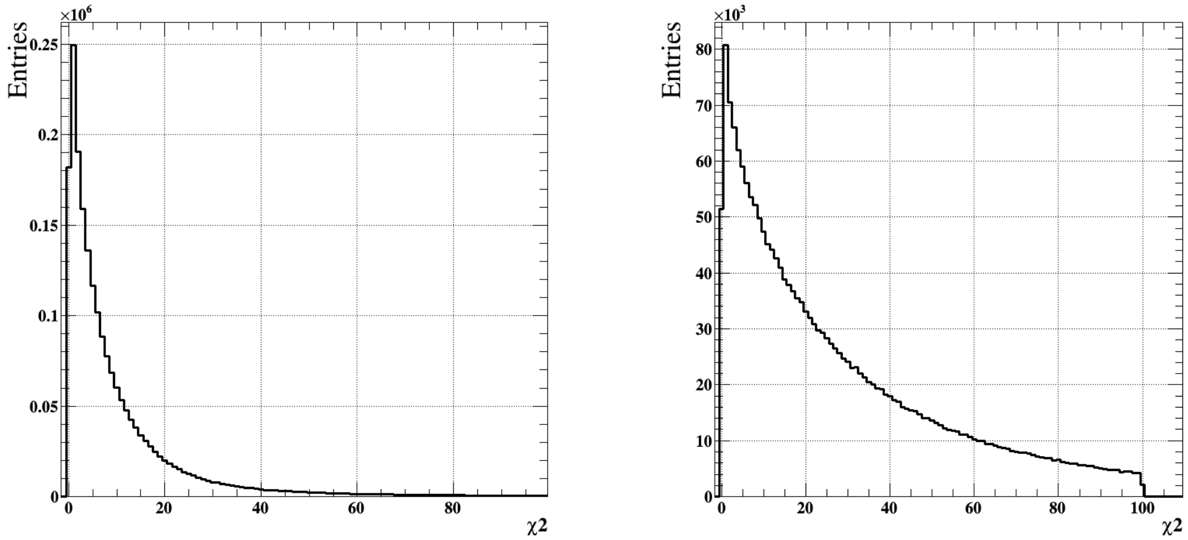

FIGURE 10.8: The χ^2 distribution obtained with DUT excluded with a single run with MuPix8 (Left) and MuPix9 (Right).

23.4 μm, which can be due to scattering or the residual mis-alignments of layers. The average direction of beam particles is not perfectly align to the planes at all position as expected at PSI (see figures in the Appendix A), away from the beam spot particles move away from the beam. There is no effect on the column plots as the beam spot is made larger in the x-direction.

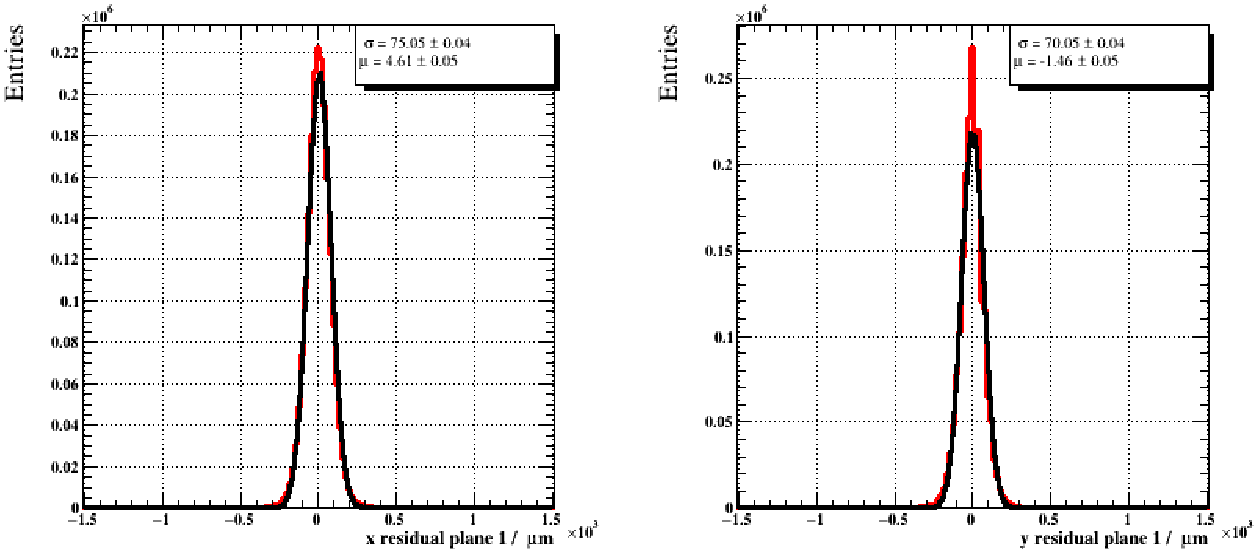

FIGURE 10.9: Unbiased DUT residuals and a reference track cut of $\chi^2 = 100$ for MuPix8. Black line is indicated to fit function and red line is for data.

To check for possible rotations of the DUT with respect to the other planes x- and y-residuals can be studied as function of the row or column position, see figure 10.9. Based on this, any correlations would be an indication of a rotation.

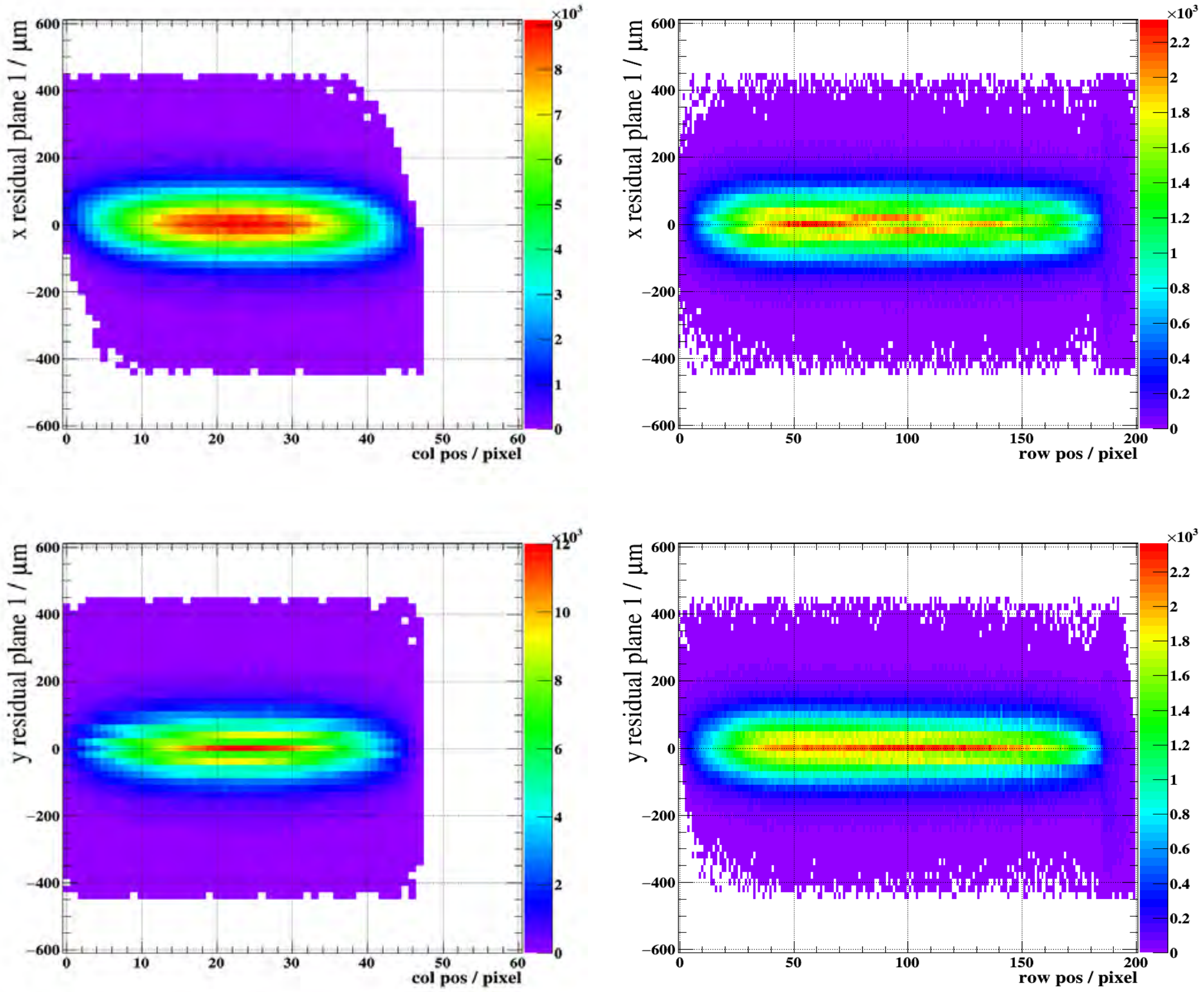

FIGURE 10.10: Column and row residuals against the column and row positions for DUT layer..

10.1.4 Alignment Stability

The alignment stability is very important to study the spatial resolution of DUT layer because small movements of the telescope layers can spoil the pointing resolution. Therefore, the x and y residuals are checked over a set of runs. Figure 10.11 shows the residuals of each plane of MuPix8 telescope and their RMS using SLM fit. The mean x and y residuals are stable between -1 to 1 μm over a complete set of runs. A bit large x or y residuals or values of residual grow or fall smoothly with increasing time can be explained as a bit of miss-alignment and scattering due to the limited number of layers.

More mis-alignments are expected with MuPix9 Telescope due to its small size compared with rest of MuPix8 layers and the nature of the test beam which constitutes a mixture of soft particles which allows significant multiple scattering. The rest of the three layers are MuPix8 sensors and beam alignment as shown in figure 9.12. It shows that X and

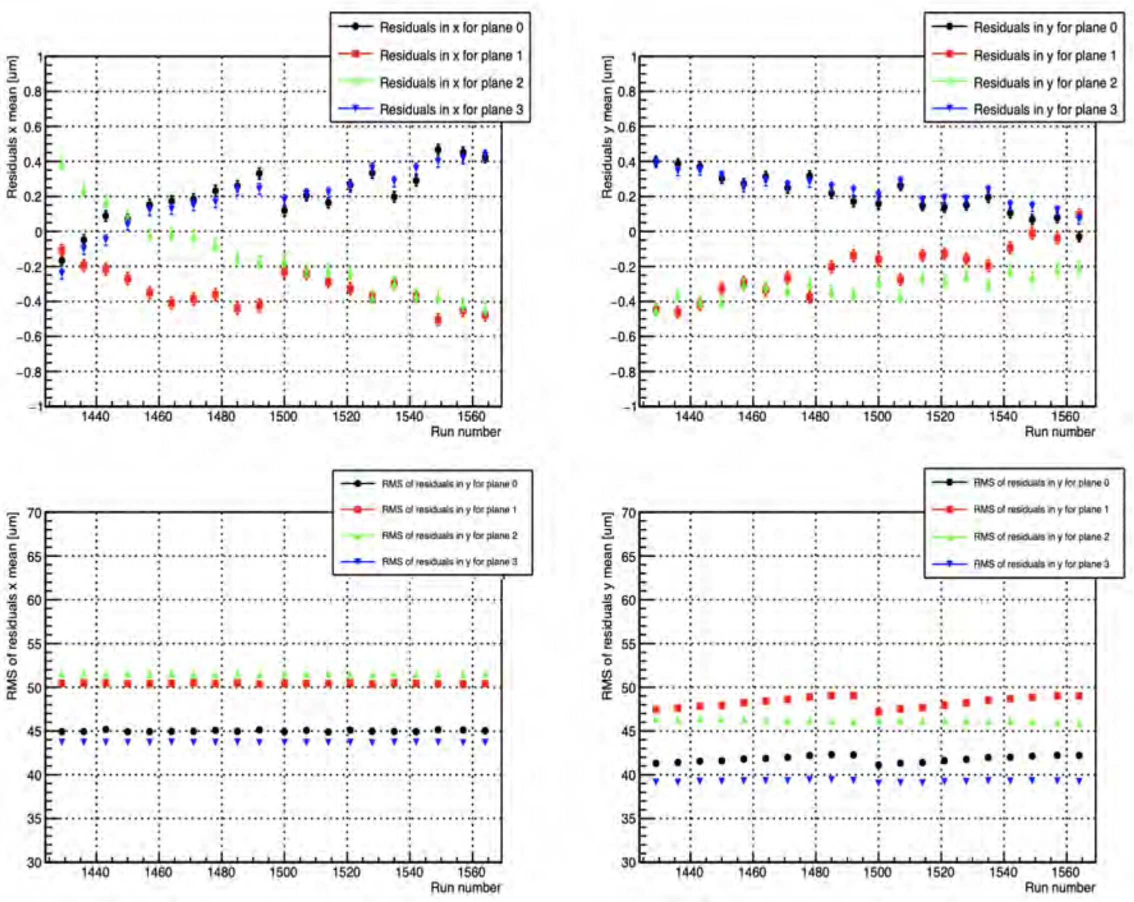

FIGURE 10.11: X and Y residuals of MuPix8 telescope layers and their RMS width as a function of the run number from 1429 to 1570, respectively. The residuals are stable on the 1 μm level over the complete run set.

Y residuals of MuPix9 DUT layer and their RMS width as a function of the run number from 2164 to 2220, respectively. The residuals are stable mostly between -5 to 5 μm level over the complete run set.

10.1.5 Pointing Resolution of Telescope

The telescope resolution is required to resolve effects on inefficiencies at certain positions of DUT layer. The normal Gaussian fit distribution is sufficient for studying the alignment stability, but it can be used to study the pointing resolution of the telescope. The pointing resolution of DUT layer can be checked via the distance between the measured and predicted hit along x and y which is called residuals. The Gaussian smeared box fit is used to check the pointing resolution of the telescope, the theoretical model of this fit is shown in figure 10.13 in which a worse resolution can spoil the edges. It can be

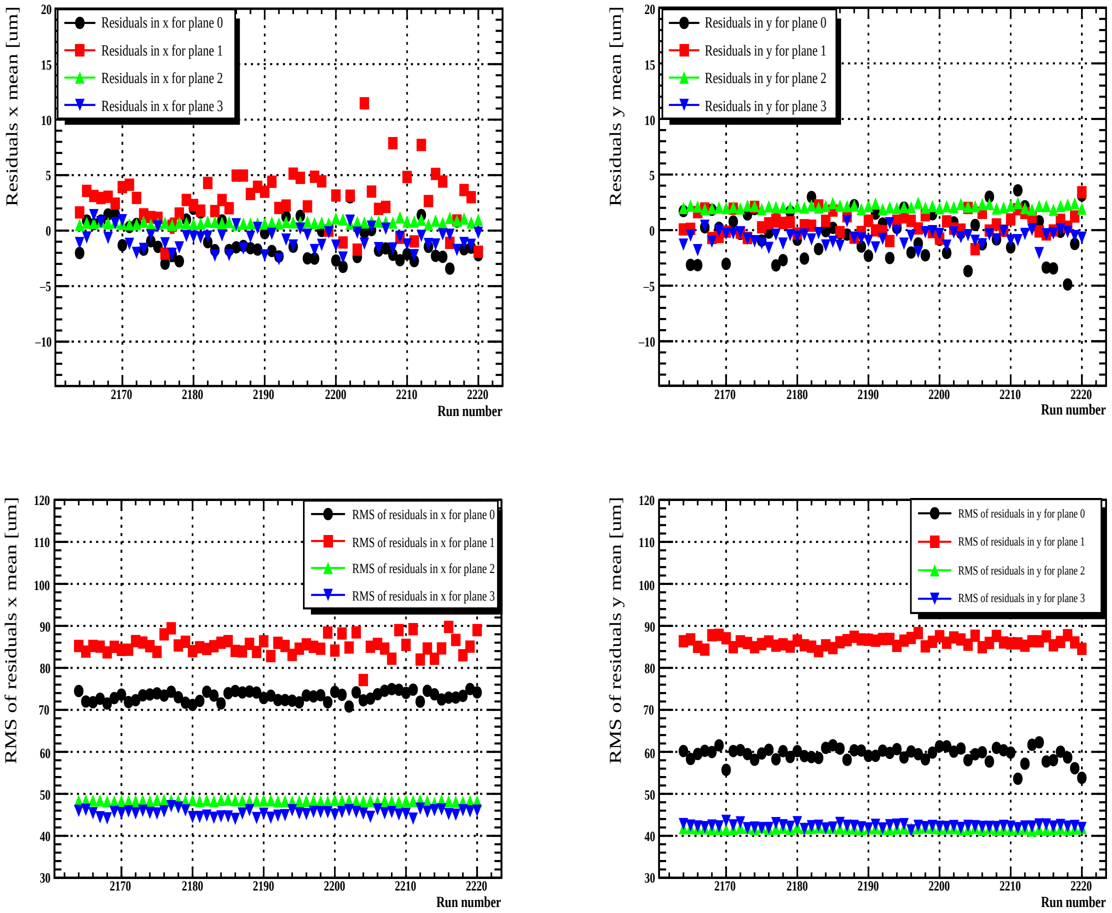

FIGURE 10.12: X and Y residuals of MuPix9 DUT layer and their RMS width as a function of the run number from 2164 to 2220, respectively. The residuals are stable nearly between -5 to 5 μm level over the complete run set These sets are within default MuPix8 DACs for DUT.

described as an error function which is indicated as s-curve:

$$\operatorname{erf}(x) = \frac{2}{\sqrt{\pi}} \cdot \int_0^x e^{-y^2} dy \tag{1}$$

This is an error function that can be described only for a one-pixel edge located at position x = 0, in order to fit both edges with one fit, the following function is used:

$$f(x) \approx A \left[\operatorname{erf}\left(\frac{w/2 - |x - c|}{\sigma\sqrt{2}} \right) + 0.5 \right] ; (w >> \sigma) \tag{2}$$

where the w is being the width of the box which is referred to as pixel pitch, c is the pixel centre position, A is the scaling factor, and σ is the resolution. The resolution of a straight line fit through three layers strongly depends on the $\chi 2$ cuts. Tighter cuts

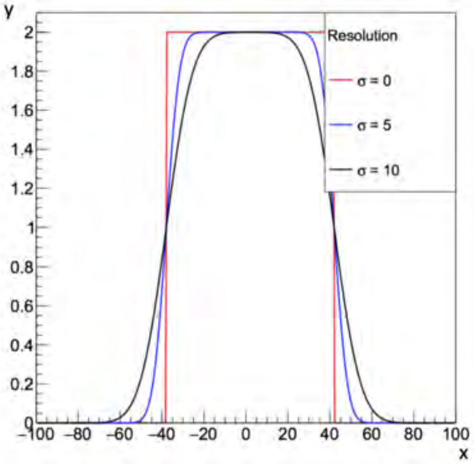

FIGURE 10.13: Gaussian smeared box fit for two edges with different resolutions.

lead to a smaller average of residuals and less scattering. For a $\chi 2$-cut of 10, the spatial resolution for the DUT layer is shown in figure 10.14 via using the Gaussian smeared box fit, under two different assumptions. Firstly, the top two figures show the fit allowing the pixel pitch (w in equation 2) to be a free parameter of the fit. Secondly the two bottom plots are fitting by assuming the pixel pitch is 81×80 μm^2 for run 1429 to 1491. The resolution is worse compared with the expected pixel resolution which should be around 23 μm assuming a single cluster size. This is due to the nature of the test beam which constitutes a mixture of soft particles which allows significant multiple scattering and more spikes on the peaks are due to cross-talk.

Two factors that can effect the measured pointing resolution of the telescope are the χ^2 cut on the track and the matching radius used (as discussed in Chapter 9). The effect of the χ^2 cut is shown in figure 7.15. According to the interpretation, the resolution drops with looser cuts, consistent with allowing larger scattering angles and the observed increase in track reconstruction. By analyzing the resolution power $\sigma/\sqrt{(N)}$ where N is the number of reconstructed tracks, we can determine the optimal compromise between the resolution and the available statistics. The effect of the $\chi 2$ cuts on the spatial resolution for both axes is shown in figure 10.16.

The spatial resolution can also be affected by the choice of matching radius. The pointing resolution of DUT layer is shown in figure 10.17 with a matching radius of 100 μm. The difference between a measured hit and predicated along x and y axes are shown. The radial cut is 100 μm. The resolution is 41 μm × 47 μm. More spikes on the peaks are due to cross-talk, better spatial resolution vertically has compared with the horizontal

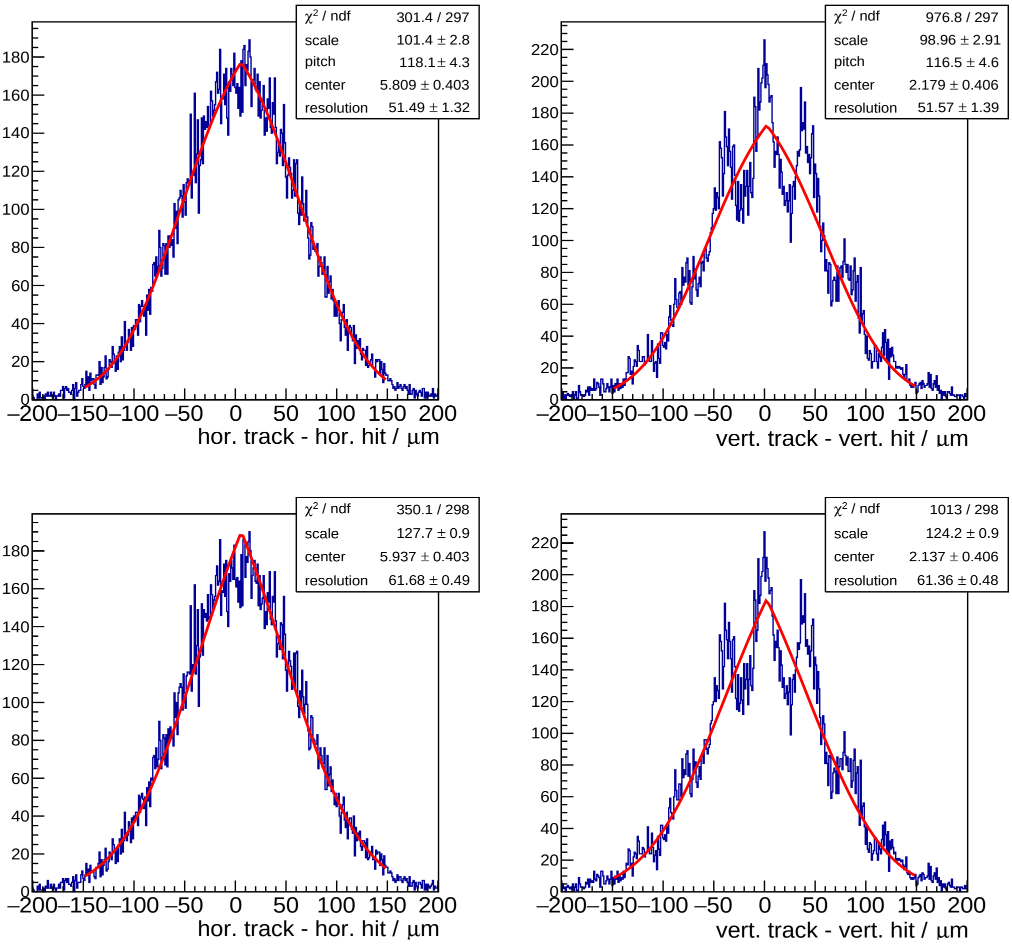

FIGURE 10.14: Pointing resolution on the DUT for a straight line fit through all three layers with a $\chi 2$ of 10. The two top plots are with free pixel pitch parameter while the two bottom plots are fitting by assuming the pixel pitch is $81 \times 80 \mu m^2$ for run 1270 to 1277.

direction. In the principle, higher double clusters have better spatial resolution due to cross-talk as shown in figure 10.5 that double clusters vertically more than horizontally.

10.1.6 Efficiency and Noise Studies

Cluster size of hits is homogeneously distributed over the sensor, the position of the all matched clusters next to single, double and the MuPix8. The single clusters are located mainly on the bottom half of the sensor, while the double and triple clusters are located in the top part of the sensor. These observations are explained by the increasing connection line length and so larger interline capacities and a stronger coupling. For the triple clusters, an extra column dependence becomes visible.

To study the efficiency, it is best to check matched and unmatched tracks that must be known. Figure 10.18 shows matched tracks and unmatched tracks for only one single

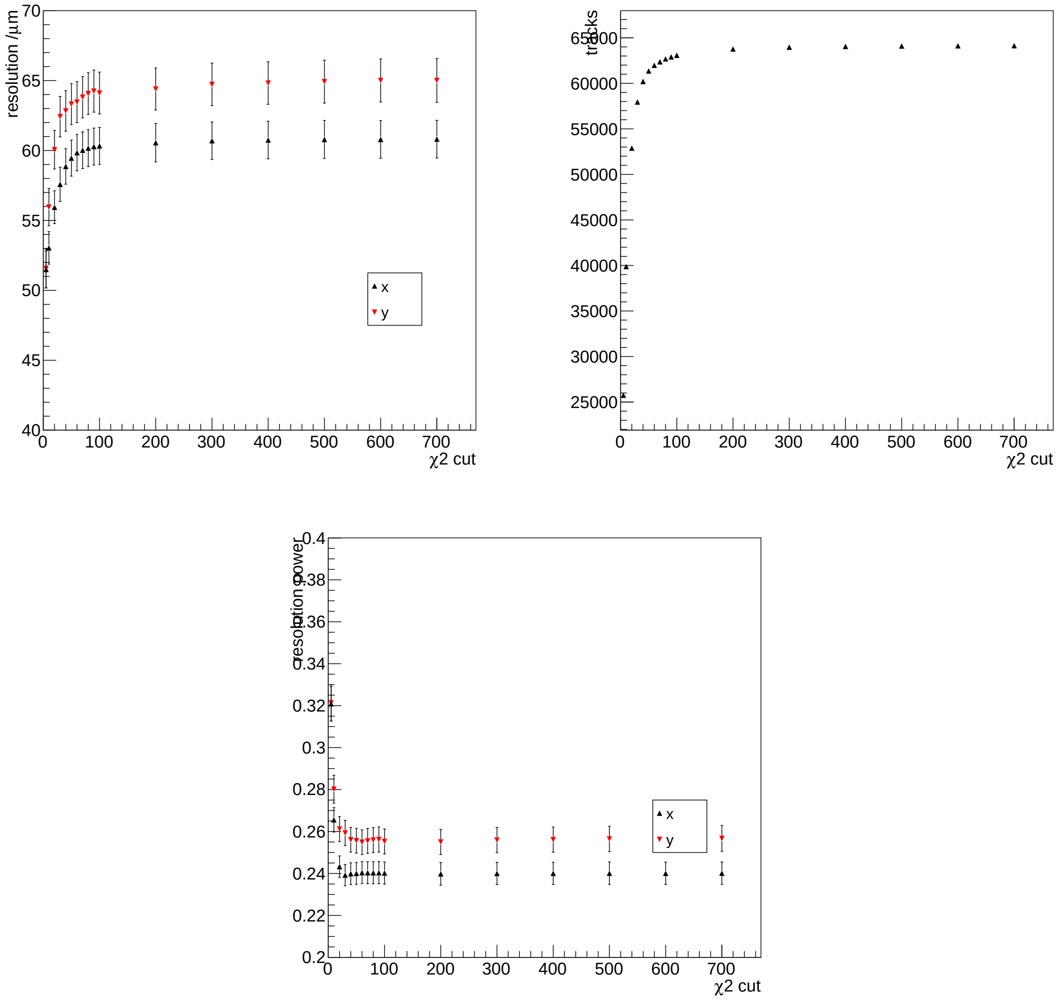

FIGURE 10.15: Influence of the χ^2 cut on the resolution, number of reconstructed tracks, and resolution power for run 1270 to 1277, respectively.

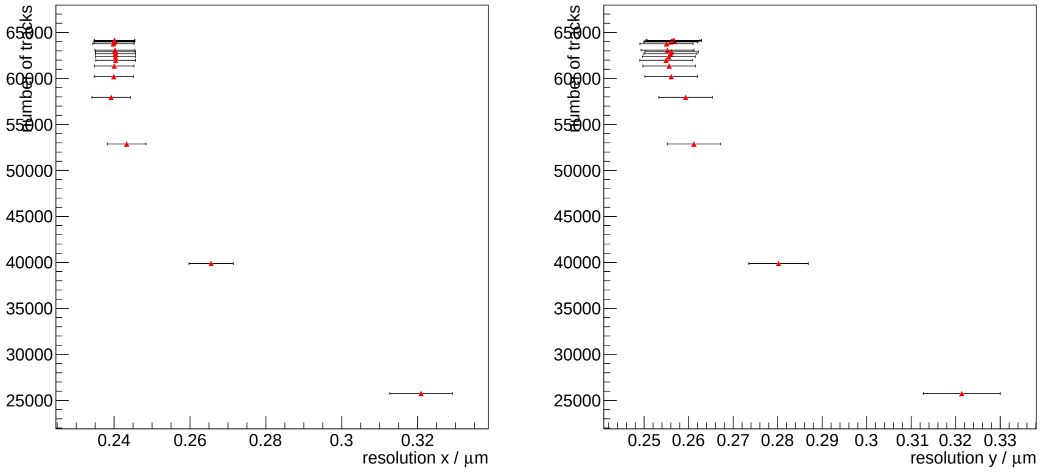

FIGURE 10.16: Resolution x and y with the number of reconstructed tracks, for run 1270 to 1277, respectively.

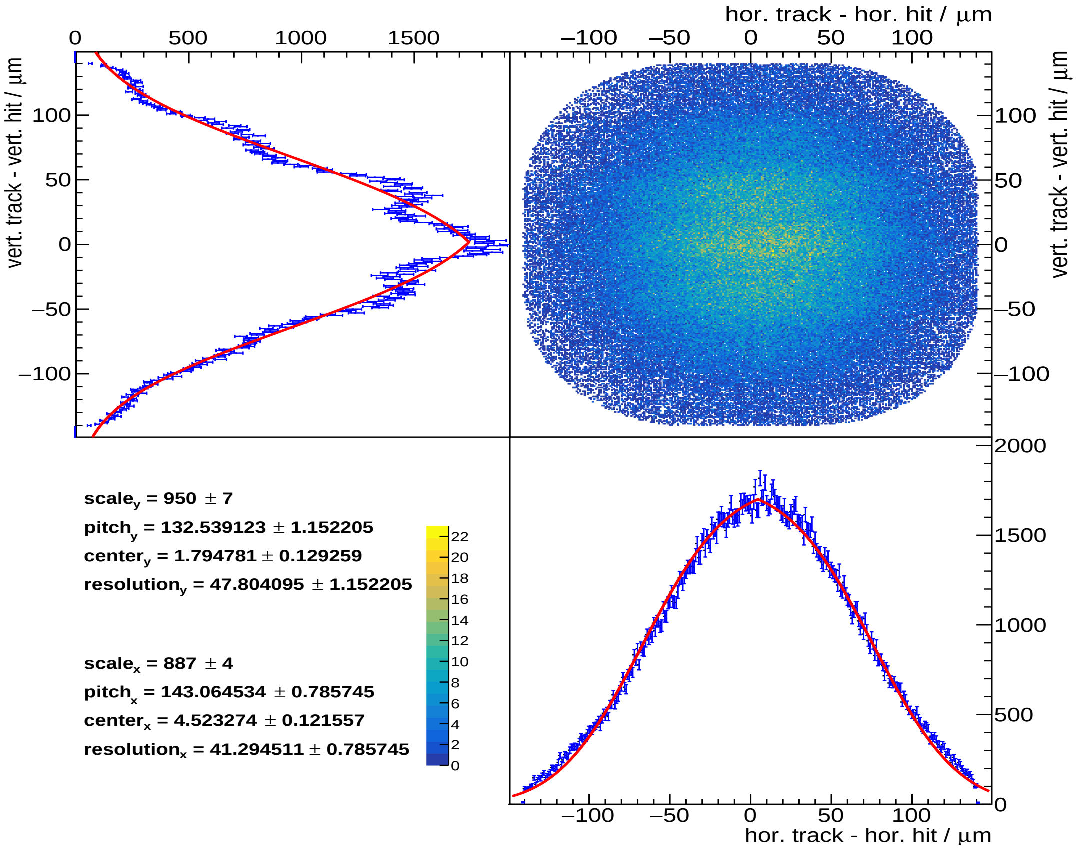

FIGURE 10.17: Difference between measured hit and predicated along x and y axes are shown. The radial cut is 100 μm. The resolution is 41 μm × 47 μm. More spikes on the peaks are due to cross-talk, better spatial resolution vertically has compared with the horizontal direction. In the principle, higher double clusters have better spatial resolution due to cross-talk.

run 1429 with threshold 545 mV for MuPix8, respectively. Inefficiency at the edges of sensors because the analysis was done with excluding the 3 columns and row. Noise rate per pixel depends on the total number of tracks and matched tracks, figure 10.19 shows noise map for same prototype with same matched and total tracks in figure 10.18 in which total number of tracks is 1235869 while matched number of tracks is 1234423 given efficiency in the region of interest 0.998±0.001. In summary, efficiency and noise rate per pixel for different DAQ, MuPix8 is shown in figure 10.20. Also, efficiency and noise studies for the MuPix9 are shown in figures 10.21 and 10.22.

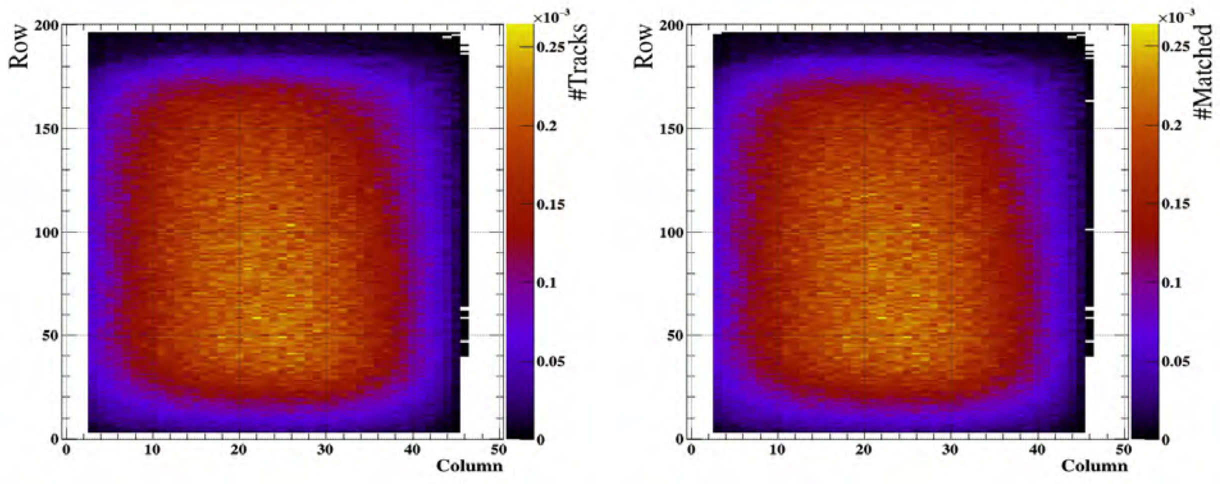

FIGURE 10.18: Matched tracks and unmatched tracks for only one single run 1429 with threshold 545 mV for MuPix8, respectively. Inefficiency at the edges of sensors because the analysis was done with excluding the 3 columns and rows.

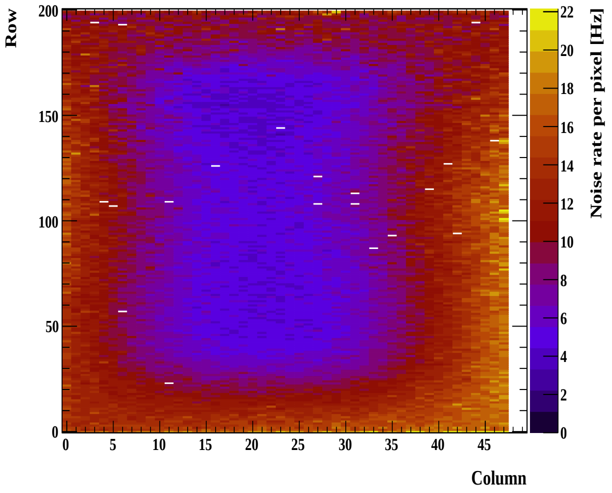

FIGURE 10.19: Noise map for only one single run 1429 with threshold 545 mV for MuPix8 calculating form number of tracks and matched tracks in figure 10.18. Inefficiency at the edges of sensors because the analysis was done with excluding the 3 columns and rows.

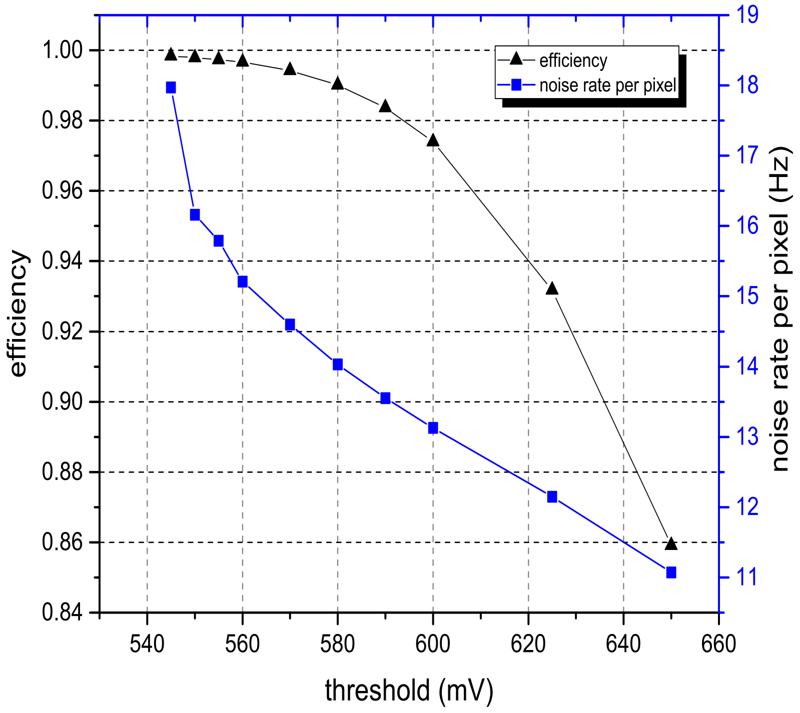

FIGURE 10.20: Efficiency and noise rate per pixel are shown for different DAQ runs for the MuPix8 after masking noisy pixels.

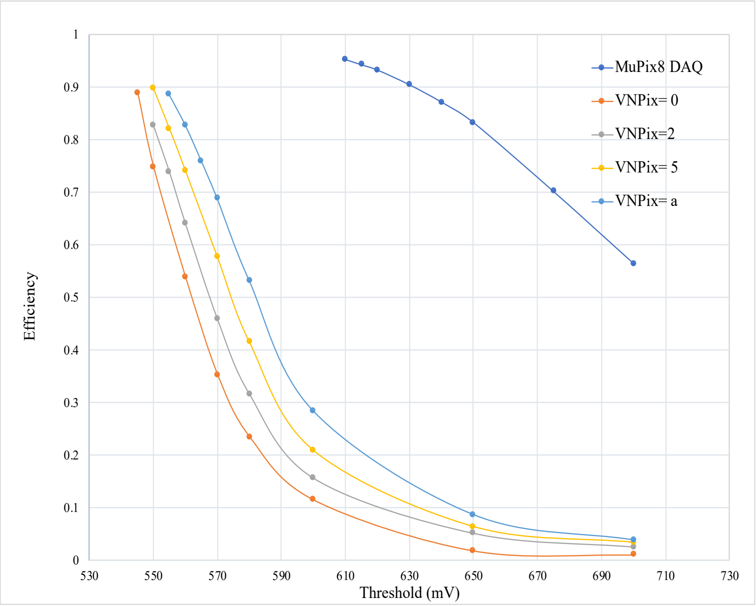

FIGURE 10.21: Efficiency is shown for different analog pixel DAC runs as shown in the legend for the MuPix9 after masking noisy pixels.

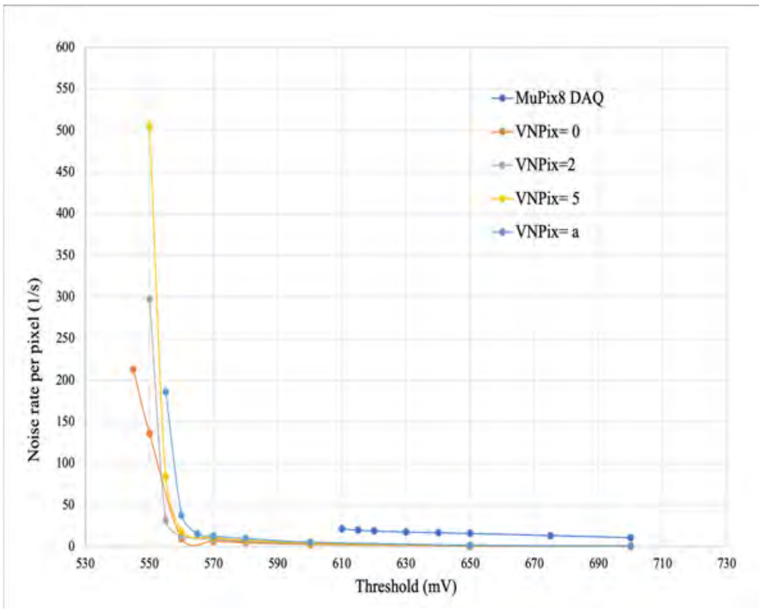

FIGURE 10.22: Noise rate per pixel is shown for different analog pixel DAC runs as shown the legend for the MuPix9 after masking noisy pixels.

11 Conclusion

The Mu3e experiment is a new search for the lepton-flavour violating decay of a positive muon into two positrons and one electron. The Mu3e experiment's purpose is to investigate lepton flavour violating decay, with the design goal a sensitivity to a branching ratio of one in 2×10^{15} in phase-I and one in 10^{16} muon decays for phase-II, improving upon previous experiments, such as SINDRUM and MEG.

Various properties of the Mu3e software have been tested. Currently, the results seem to agree with the expected behaviour. Physical studies on the reconstruction and simulation for track and vertex with results have been discussed for signal and internal conversion background. Track candidate classification in the Mu3e experiment with events display have been shown and discussed for short and long tracks, and problem with low linear momenta for tracks. Vertex fits are performed with all possible combinations of one electron and two positron track candidates. A few selections on the tracks are applied on the vertex, kinematic, and timing for signal decay in order to distinguish signal and suppress background categories. The Single Event Sensitivity (SES) is defined and used to assess the performance of the experiment for a signal selection using 3 long-tracks.

In this thesis, the track reconstruction and event selection have been optimised in the case of the nominal designed detector, and imperfect scenarios where pixel detector inefficiencies exist in the central station. It has been shown, in the case of "known inefficiencies" that the SES can be partially recovered by using new tracking selection which takes these known defects into account. Inefficiencies have been artificially introduced into the pixel layers in the central station and a new tracking selection has been developed to allow some track reconstruction efficiency to be recovered. The ultimate goal is to allow the tracking algorithm to access dead sensor information in a conditions database, and apply the modified selection when the track is extrapolated to known defects.

In the real experiment, correctly reconstructed tracks could have a missing hit in a layer.

Therefore, there are different categories of tracks that have been established which are short 3, long 5, and 7 hits tracks. The new tracks reconstruction is performed in several steps. In a first step, each triplet is used as a seed for finding and reconstructing tracks that consist of at least 3 hits with a hole. After that, short tracks are used for the reconstruction of recurling particles that form long tracks. There are two categories of long tracks: 5- and 7- hits tracks with a hole. Long 7-hit tracks are reconstructed by using long 5-hits tracks corresponding to one full turn in the central station. Long 5-hit tracks are reconstructed from a short track and a pair of hits in two outer layers, either in the central or recurl stations of the detector. As a future step, more studies can be conducted to check tracking performance if there are more than one missing hit in a track. Alternatively, the imperfect track can be extrapolated to two recurl stations rather than being treated as the only imperfect track in the central station as in this thesis. A different reconstruction method can improve purity on long tracks with 7-pixel hits than using long tracks with 5-hits as seeds, as demonstrated in this thesis. By using short tracks with 3-hits, it might be possible to create some new tracks with 7-pixel hits.

In addition, a study of the origin of fake tracks has been performed. A fake track can have various sources. For instance, a track is reconstructed of a positron that is mistaken for an electron, and particles that perform many turns in the central station of the detector are produced fake tracks because an emitted particle is emitted perpendicular to the beam axis. The track selection criteria, for the different categories of tracks, have been optimised by understanding the efficiency, purity, and fake rates.

Three cuts are applied on the tracks during the reconstruction step: the χ^2 of the track fit, the dip angle and the intersection z_0 of the track with the target region. The final step of the reconstruction is the vertex fit: three tracks from the signal decay should originate from a common point, and there is a couple of variables that can be used to separate signal events from background, such as χ^2 of the vertex fit, the distance of the reconstructed vertex to the target region, the total momentum and invariant mass of the three-particle system. In addition, timing information is provided by the fibre and tile timing detectors and is used to reduce fake tracks due to random combinations of hits and to check the correct direction of travel. Also, timing in the reconstruction and analysis framework has been studied for suppression of combinatorial background candidates. For timing layer resolution, fibre and tile time resolution in the simulation is implemented. The timing information from fibre can use it to resolve the charge id ambiguity for central reconstructed long tracks with 8-hit. Because the certain timing and tracking resolution for the fibre, tile timing detector is placed in the two recurl station to increase the acceptance and efficiency with better timing resolution.

The performance of the alignment software for Mu3e has been evaluated. Further work is needed to refine the performance further in the presence of realistic detector conditions. The track based alignment for the Mu3e pixel detector is set on a great path to deliver excellent and reliable results which can be achieved after some fine tuning and an efficient suppression of the occurring weak mode. In addition, multiple noise hits can create ambiguities, which can result in an wrong assignment and an incorrectly reconstruction of verticies or particle momenta. Fake tracks, due to mis-reconstruction of an event, are not always match-able and will therefore decrease the measured sensor efficiency. With the future development of a conditions database, very noisy modules could be masked, and the tracking efficiency recovered by the use of the new tracking discussed in this the thesis.

The development and implementation of the detector conditions database for the Mu3e experiment is beyond the scope of this thesis, but is the next step. The software will need methods to allow the tracking algorithms access to the database to ensure the appropriate tracking selection is used for a given track since in the real experiment there will be inefficiency for performance of tracks.

The temperature of the pixel detector is a very important issue in the Mu3e experiment (cooling). To monitor the temperature, MuPix has a temperature sensor on-chip. The calibration of temperature of final HV-MAPS prototypes for the Mu3e experiment were successfully tested as a two step technique. A number of hardware components have been designed to complete the data acquisition chain of the MuPix chip. Their functionality has been proven successfully and a calibration for the on-chip temperature diode has been performed. For the current default settings, the MuPix reaches a temperature of $\sim 42°\text{C}$. This study on the calibration temperature measurements is still under ongoing development, new infrared thermal IR camera will be used to test chips more precisely, so similar studies in the future could yield different results than those presented here.

The MuPix telescope has been adapted for two MuPix prototype generations – MUPIX8 and MUPIX9 – and improved significantly in the scope of this thesis. In the scope of this thesis, the fits are evaluated and compared and the use of a fast straight line fit for the MuPix telescope is validated. The MuPix telescope will be an excellent test bench for the next prototypes and is expected to be heavily used in upcoming beam times. Two prototypes have been studied: The small-scale MUPIX9 and its successor, the large-scale MUPIX8. Both sensors show an excellent performance. Efficiencies above 99 % at noise rates below 20 Hz per pixel are observed, fulfilling the Mu3e requirements

The first mu3e integration run was in May/Jun 2021, during an extensive campaign at PSI. This is the first time parts of the detector were operated together inside the experiment magnet and with a muon beam stopping on a target in the centre of the experiment. Pixel ladders were successfully operated with high-flow gaseous helium cooling. A slice of the final data acquisition system was employed, allowing for thorough tests of firmware and software. The large data set taken is being analyzed in preparation for another integration run soon. The work in this thesis on the tracking software is being developed for these runs to study the tracking performance for inefficient tracks due to missing hit or noisy hit.

Part I

Appendix

A Hardware

A.1 Silicon Properties

Property	Value	Unit
Atomic number (Z)	14	
Nucleon number	28.09	
Density (ρ)	2.33	g/cm^3
Crystal Structure	Diamond	
Atom density	5.02×10^{22}	$1/\mathrm{cm}^3$
Intrinsic charge density (n)	1.5×10^{10}	$1/\mathrm{cm}^3$
Dielectric constant (ϵ)	11.9	
Band gap at 300K	indirect, direct band gap = 1.12 , 3.4	eV
Average creation energy for an electron-hole pair (ω)	3.66	eV
Fano Factor (F)	0.115	
Mobility (μ)	$\mu_n = 1450, \mu_p = 500$	cm^2/sV

TABLE A.1: Silicon properties [6, 23, 33, 39, 42]

A.2 The Chip Electronics Implemented on the MuPix8 prototype

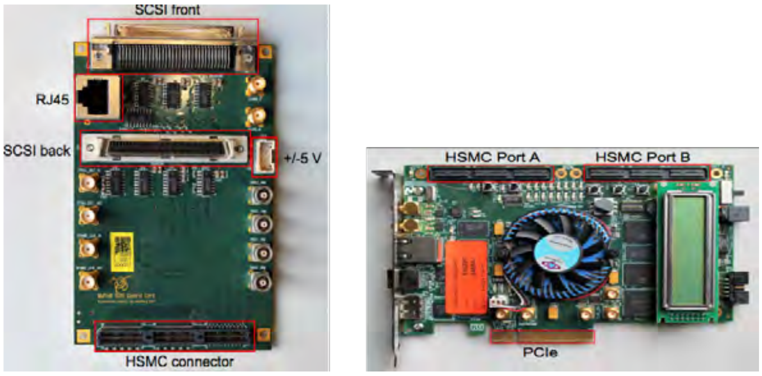

FIGURE A.1: Schematic of the **Stratix IV** and **SCSI Adapter Card** of the MuPix8. Left: photograph of the **Stratix IV** dev board in which the **FPGA** is hidden behind the fan in the centre. Right: Schematic and photographs of the **MuPix8 SCSI Adapter Card**.

A.3 The Single MainWindow

Throughout this project, all measurements were done using a piece of software in hardware. The DAQ software is implemented in some libraries, such as C++ based on Qt, Eigen, and boost library. It comprises the readout software, and an online monitoring feature and a GUI for a user-friendly control. GUI is built in a way such that multiple dialog windows can be accessed from a MainWindow. In this report, it has used the **Single MainWindow** (As can be seen in appendix in figure B.2). The Single MainWindow is dedicated to the single setup such that a large spectrum of functions is provided to operate the single setup and easy adjustments to chips settings quickly.

FIGURE A.2: Left: Full setup to display the Single MainWindow. Right: Screenshot of the MainWindow of the single software.

A.4 Figures of the setup of the calibration Temperature MuPix8 sensor

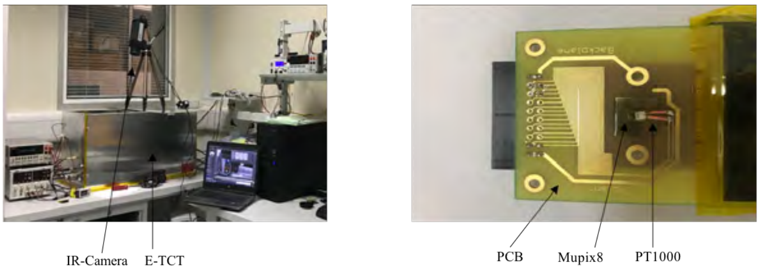

FIGURE A.3: Left: Full setup to calibrate an IR camera with a PT1000 glued to a piece of MuPix8 with PCB. Right: Screenshot of the full setup with IR camera and Edge-TCT.

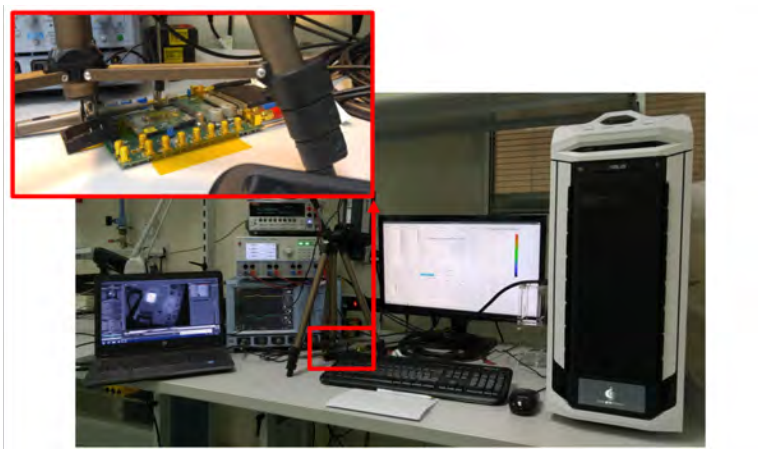

FIGURE A.4: Full setup for calibration MuPix8 temperature sensor.

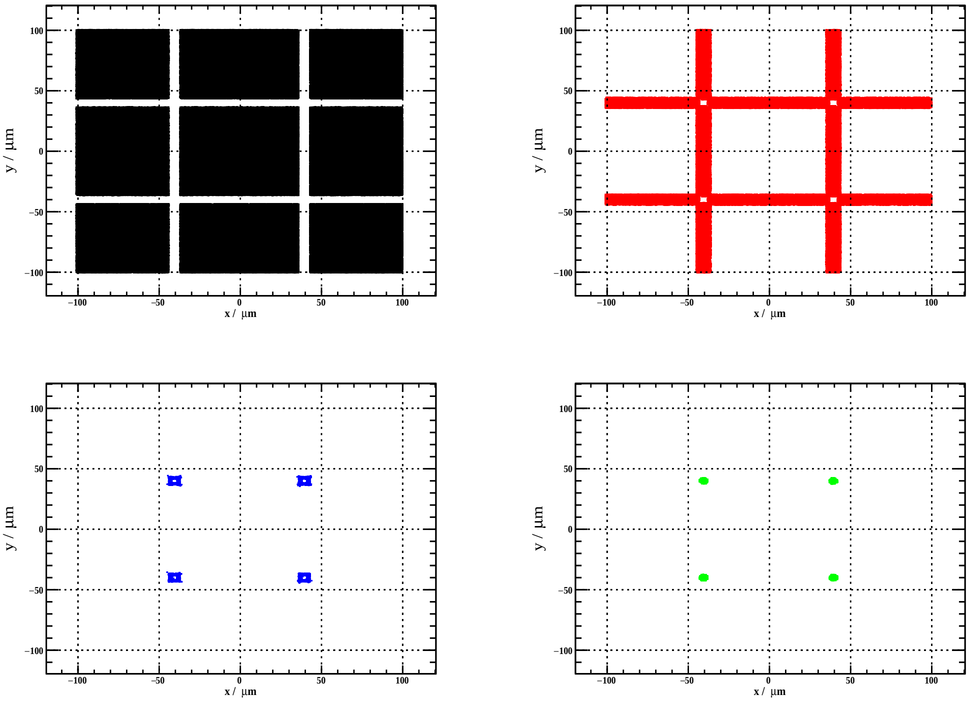

FIGURE A.5: Single, doublet, triplet, and quadruple cluster size, respectively.

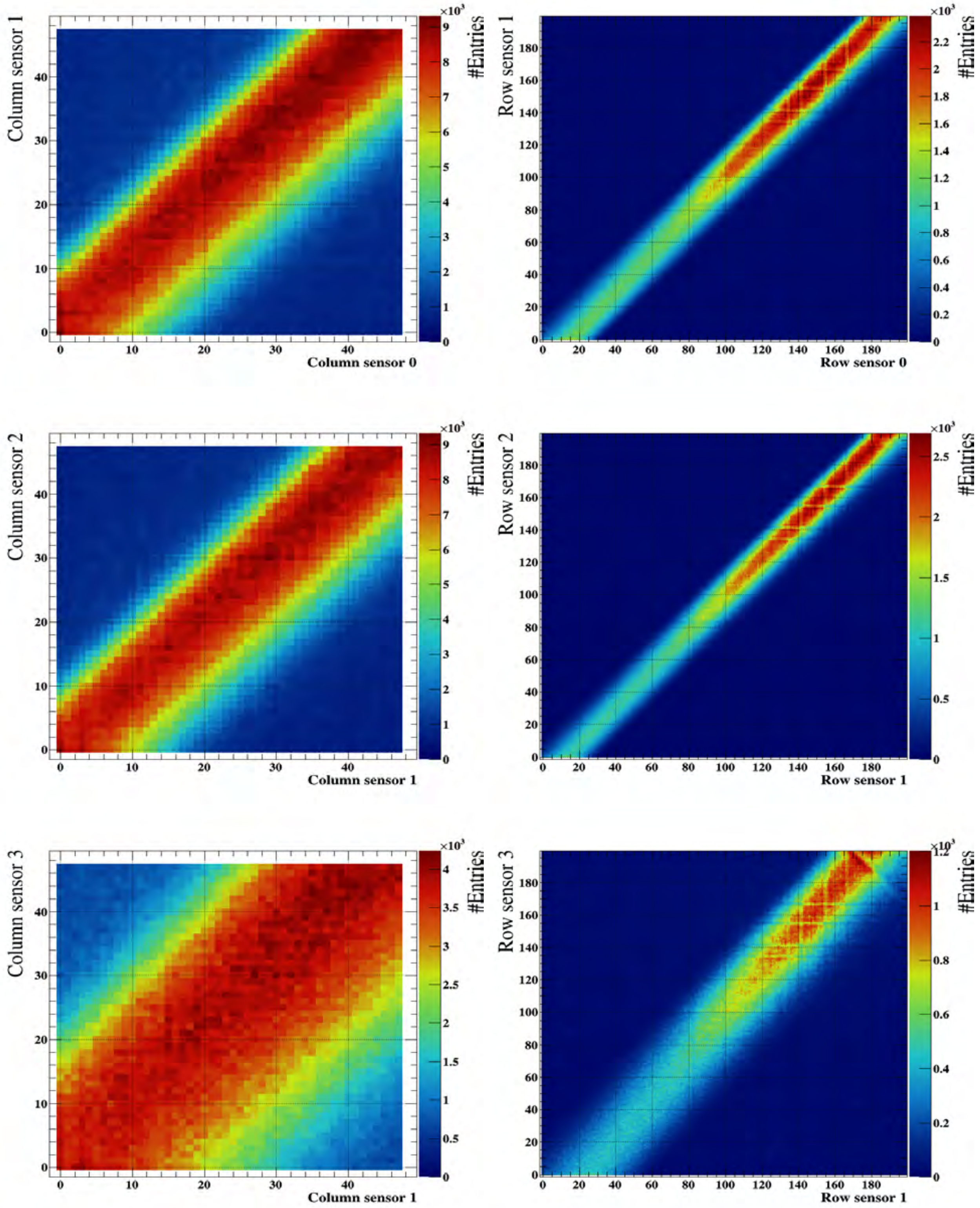

FIGURE A.6: Correlation between DUT layer and layers 2 and 3. Slight misalignment is between layer 1 and 2 on the y-direction more than x, also the beam is more spreading due to the mixed beam at PSI.

B Software

B.1 Simulation and Reconstruction Study

Cut		Efficiency		
Generated Number of muon decays	3.000000e+07	-		
Sum of Weights	1.04227×10^{13}			
Number of frames passing the following cuts:				
(Cut #1) ≥1 vertex	9.682639e+06	0.323		
(Cut #2) Recon vtx within acceptance	8.480103e+06	0.283		
(Cut #3) Duplicate removal (same tracks)	8.303653e+06	0.277		
(Cut #4) Duplicate removal (common tracks)	8.303653e+06	0.277		
(Cut #5) Duplicate removal (vtx-to-vtx distance)	7.439840e+06	0.248		
Break-up in different vertex track quality	Short or better	≥1 long	≥2 long	3 long
frames with 1 vertex	7.069005e+06	6.930015e+06	6.130114e+06	3.470133e+06
frames with 2 vertex	3.518930e+05	3.433240e+05	2.873700e+05	1.394790e+05
frames ≥ 3 vertex	1.894200e+04	1.841600e+04	1.538300e+04	7.595000e+03
Total number of frames	7.439840e+06			
Efficiency	0.248	0.243	0.214	0.121
Number of vertices per frame classification	1 vertex	2 vertices	≥3 vertices	
Number of frames	7.069005e+06	3.518930e+05	1.894200e+04	
Cut # 6 details	No of Frames	Efficiency		
$\chi^2 < 30$	2.679664e+06	0.089		
vertex target distance <3 mm	2.634049e+06	0.088		
3-track system momentum <8 MeV	1.229570e+05	4.098567e-03		
Break-up in different vertex track quality	Short or better	≥1 long	≥2 long	3 long
frames with 1 vertex	1.229490e+05	1.198240e+05	1.100580e+05	6.924900e+04
frames with 2 vertex	4.000000	4.000000	4.000000	3.000000
frames ≥ 3 vertex	0.000000	0.000000	0.000000	0.000000
Total number of frames	1.229530e+05			
Efficiency	4.098433e-03	3.994267e-03	3.668733e-03	2.308400e-03
Number of vertices per frame classification	1 vertex	2 vertices	≥3 vertices	
Number of frames	1.229490e+05	4.000000	0.000000	
Cut # 7 details	3 Short or better	≥1 long	≥2 long	3 long
frames with 1 vertex	254.000000	226.000000	154.000000	28.000000
frames with 2 vertex	0.000000	0.000000	0.000000	0.000000
frames ≥ 3 vertex	0.000000	0.000000	0.000000	0.000000
Total number of frames	254.000000			
Efficiency	8.466667e-06			

TABLE B.1: Cut flows for studies of radiative with internal conversion muon decays generated at one decay per frame with using weights.

TABLE B.2: Cut flows for studies of signal muon decays generated at one decay per frame.

Cut		Efficiency		
Generated Number of muon decays	1.034481e+07	-		
Number of frames passing the following cuts:				
(Cut #1) $\geq$1 vertex	4.348795e+06	0.420		
(Cut #2) Recon vtx within acceptance	3.902449e+06	0.377		
(Cut #3) Duplicate removal (same tracks)	3.797798e+06	0.367		
(Cut #4) Duplicate removal (common tracks)	3.797798e+06	0.367		
(Cut #5) Duplicate removal (vtx-to-vtx distance)	3.673176e+06	0.355		
Break-up in different vertex track quality	Short or better	$\geq$1 long	$\geq$2 long	3 long
frames with 1 vertex	3.555810e+06	3.435818e+06	2.933218e+06	1.628102e+06
frames with 2 vertex	1.130340e+05	1.090000e+05	8.940200e+04	4.213300e+04
frames $\geq$ 3 vertex	4.332000e+03	4.197000e+03	3.398000e+03	1.554000e+03
Total number of frames	3.673176e+06			
Efficiency	0.355	0.343	0.293	0.162
Number of vertices per frame classification	1 vertex	2 vertices	$\geq$3 vertices	
Number of frames	3.555810e+06	1.130340e+05	4.332000e+03	
Cut # 6 details	No of Frames	Efficiency		
$\chi^2 < 30$	1.977392e+06	0.191		
vertex target distance <3 mm	1.951384e+06	0.189		
3-track system momentum <8 MeV	1.880665e+06	1.817979e-01		
Break-up in different vertex track quality	Short or better	$\geq$1 long	$\geq$2 long	3 long
frames with 1 vertex	1.880575e+06	1.817306e+06	1.617055e+06	9.848480e+05
frames with 2 vertex	45.000000	45.000000	43.000000	36.000000
frames $\geq$ 3 vertex	0.000000	0.000000	0.000000	0.000000
Total number of frames	1.880620e+06			
Efficiency	1.817936e-01	1.756776e-01	1.563197e-01	9.520562e-02
Number of vertices per frame classification	1 vertex	2 vertices	$\geq$3 vertices	
Number of frames	1.880575e+06	45.000000	0.000000	
Cut # 7 details	3 Short or better	$\geq$1 long	$\geq$2 long	3 long
frames with 1 vertex	1547878.000000	1505152.000000	1368260.000000	892752.000000
frames with 2 vertex	39.000000	39.000000	37.000000	30.000000
frames $\geq$ 3 vertex	0.000000	0.000000	0.000000	0.000000
Total number of frames	1547917.000000			
Efficiency	1.496322e-01			

B.1.1 Timing propagation and suppression of background

The insufficiency in the reconstruction algorithm's error propagation that should be improved. In order to study this failure in timing detector, the BLUE is used to propagate the track timing errors manually [32]. The BLUE combines the timing information generated from all timing detectors and propagates this to the innermost silicon layer to estimate the combined error of this measurement is estimated. The purpose of using this method is to figure out the errors happening during the reconstruction algorithm such as long tail of $\chi^2_{\text{timing}}(\vec{v})$. The equation is used to combine the separate resolutions for timing detectors:

$$\delta t_{\text{ combined }} = \sqrt{\frac{\delta t_1^2 \cdot \delta t_2^2}{\delta t_1^2 + \delta t_2^2}} \tag{1}$$

where $\delta t_{\text{ combined }}$ is the combined resolution, δt_1, and δt_1 are the resolutions of two separate measurements. The error on efficiency of $\chi^2_{\text{timing}}(\vec{v})$ is important to know the suppression factor that it is used as a cut. The corresponding errors were assumed to be binomial in which binomial distribution is defined:

$$P(m, N, \epsilon) = \frac{N!}{m!(N-m)!}\epsilon^m(1-\epsilon)^{N-m} \tag{2}$$

Where N is the total number of events, ϵ is the probability of events passing a selection, and m is the number of events that pass selection. Also, the standard deviation on a binomial distribution is:

$$\sigma = \frac{\sqrt{m\left(1-\frac{m}{N}\right)}}{N} \quad \text{and} \quad \sigma_{\text{ suppression }} = \frac{\sigma_\epsilon}{\epsilon^2} \tag{3}$$

where m is the number of events that pass selection and N is the total number of events. The suppression is the inverse of efficiency, so the error in the suppression is estimation via differentiation of the suppression with respect to the efficiency of the selection cut. Where ϵ is the efficiency, and σ_ϵ is the error on the efficiency of the selection cut. The errors on the $\chi^2_{\text{timing}}(\vec{v})$ are given by the width of the histogram bins.

In addition, tracks with one hit in tile detector is supposed because with more than one hit will give higher timing errors and with two hit in tile detector the particle will need high energy to reach the tile layer again within 65 ns frame length. Hence, the vertex timing was calculated by using these new timing resolution of three tracks. Using a Gaussian number generator with the standard deviation are equalling the new estimated resolutions by using TRandom3 class, so new track times randomised, their $\chi^2_{\text{timing}}(\vec{v})$ were

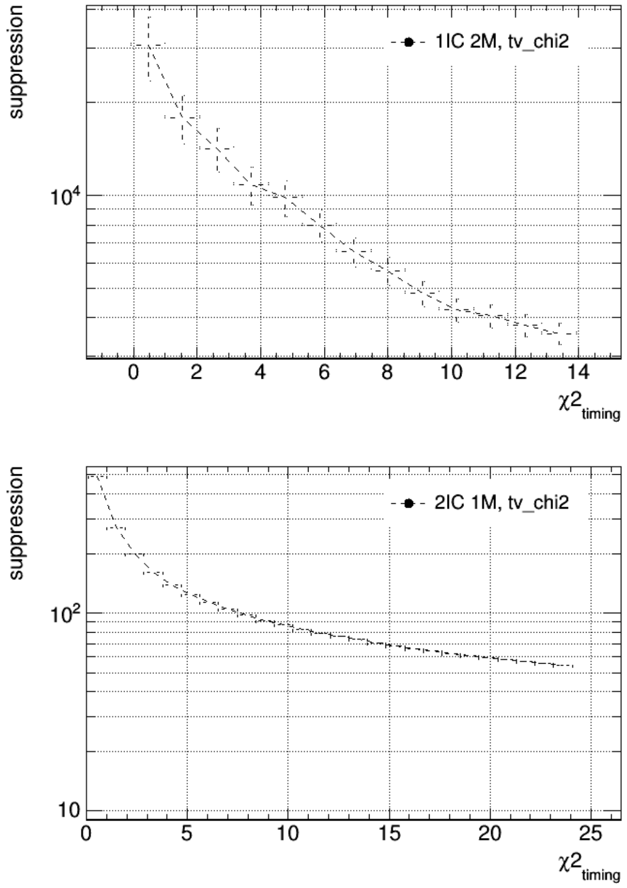

FIGURE B.1: New suppression factors for the 2+1 background with two and three uncorrelated vertices of signal timing efficiency.

calculated. As a result, it is obvious that from figure B.1 and B.2, cuts 7 for $\chi^2_{\text{timing}}\,(\vec{v})$ and 6 for $\chi^2_{\text{timing, Bhabha}}\,(\vec{v})$. The cut on $\chi^2_{\text{timing}}\,(\vec{v})$ give a suppression of factor 105 for 2+1 background consisting of 2 internal conversion and 1 Michel background (two vertices are timing independently), and 6500 suppression for 1 internal conversion and 2 Michel background (3 uncorrelated vertices are not coincidence in time) in which logarithmic scale for the suppression axis is used.

B.1.2 Improving Background Suppression

In order to enhance the suppression factor of combinatorial background, the timing resolution of timing detector must be improved. Reconstructing the timing errors of the tracks manually, the new timing resolution of tile timing detector is 30 ps which is better than previous timing resolution. As a result, the long tail of $\chi^2_{\text{timing}}\,(\vec{v})$ is hidden when timing resolution is calculated manually with new signal timing efficiency as shown in figure B.3 (First) with new signal timing efficiency (Second).

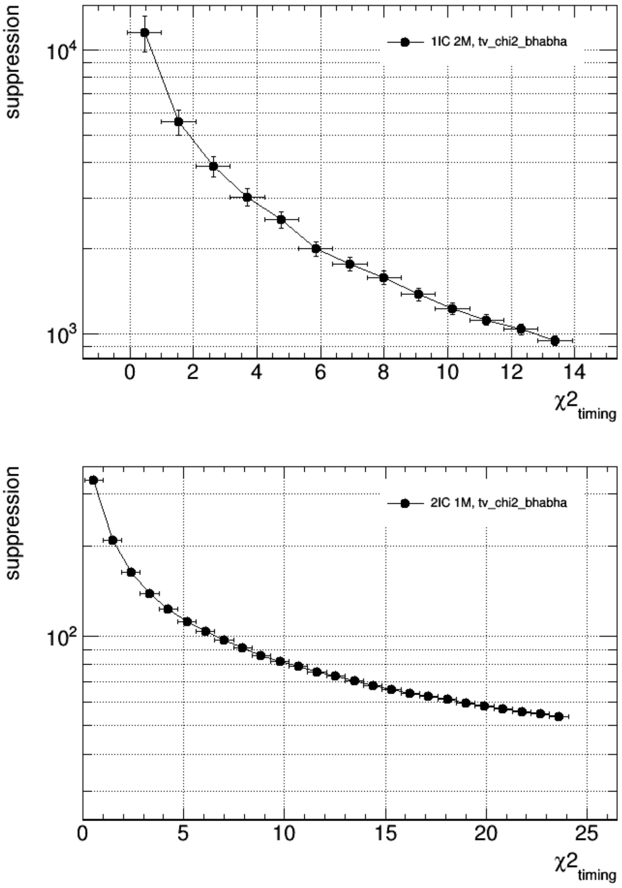

FIGURE B.2: New suppression factors for the 2+1 background with two and three uncorrelated vertices of Bhabha timing efficiency.

Also, figure B.4 and B.5 display the somewhat improvement in the suppression for a $\chi^2_{\text{timing}}\,(\vec{v})$ and $\chi^2_{\text{timing, Bhabha}}\,(\vec{v})$ where cuts of 6 and 7 when compared with previous figures. For the 2+1 case of 2 internal conversion and 1 Michel decay, the suppression increases to 115. For the 2+1 case of 2 Michel and 1 internal conversion decay, the suppression increases to 7500.

B.2 Resolution Study (Double sided crystal ball function)

where $A_i = \left(\frac{n_i}{|\alpha_i|}\right)^{n_i} \cdot e^{-\frac{\alpha_i^2}{2}}$ and $B_i = \frac{n_i}{|\alpha_i|} - |\alpha_i|$ and i = 1,2 for the power-law either side of the Gaussian centre. The Crystal Ball function is also defined, as it can be used for distributions which have a Gaussian centre with a side that has a long, power-law tail. The single sided crystal ball function is defined, with a power-law long tail on the left

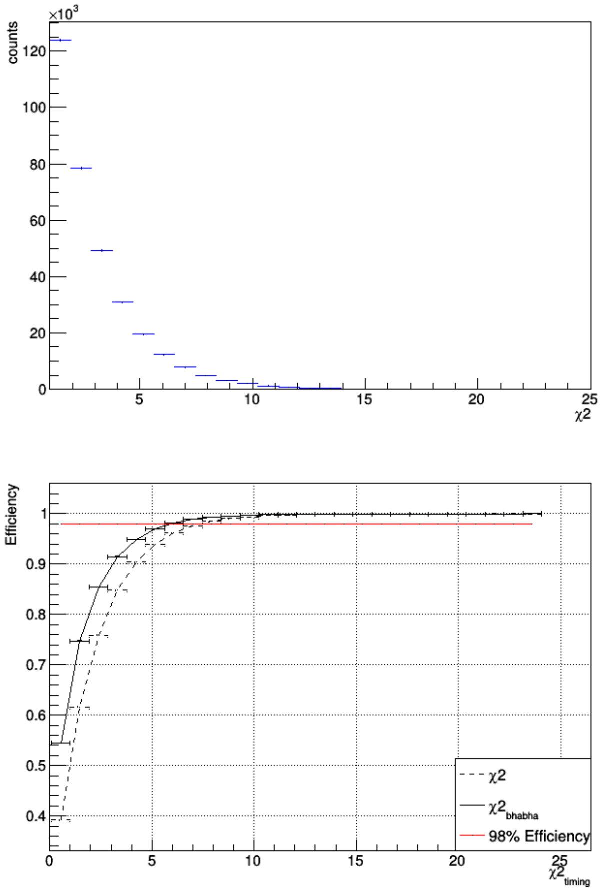

FIGURE B.3: Top: The χ^2_{timing} distributions for signal created using the signal vertex information. Long tail of the distribution is disappeared with an improved timing resolution of tile detector. Bottom : Signal timing efficiency for a selection of cuts on χ^2_{timing}.

hand side of the Gaussian peak:

$$\text{CB}\ \ (x_o|\mu,\sigma,\alpha,n) = N \cdot \begin{cases} e^{-\frac{(x_o-\mu)^2}{2\sigma^2}}, & \text{for } -\alpha > \frac{x_o-\mu}{\sigma} \\ A \cdot \left(B - \frac{x_o-\mu}{\sigma}\right)^{-n}, & \text{for } \frac{x_o-\mu}{\sigma} \leq -\alpha \end{cases} \tag{5}$$

Where $A = \left(\frac{n}{|\alpha|}\right)^n \cdot e^{-\frac{\alpha_l^2}{2}}, B = \frac{n}{|\alpha|} - |\alpha|, N = \frac{1}{\sigma(C+D)}, C = \frac{n}{|\alpha|} \cdot \frac{1}{n-1} \cdot \exp\left(-\frac{|\alpha|^2}{2}\right)$, and $D = \sqrt{\frac{\pi}{2}}\left(1 + \text{erf}\left(\frac{|\alpha|}{\sqrt{2}}\right)\right)$, and where $\text{erf}\left(\frac{|\alpha|}{\sqrt{2}}\right)$ is the error function.

$$\text{erf}(x) = \int_{-x}^{x} e^{-t^2} dt \tag{6}$$

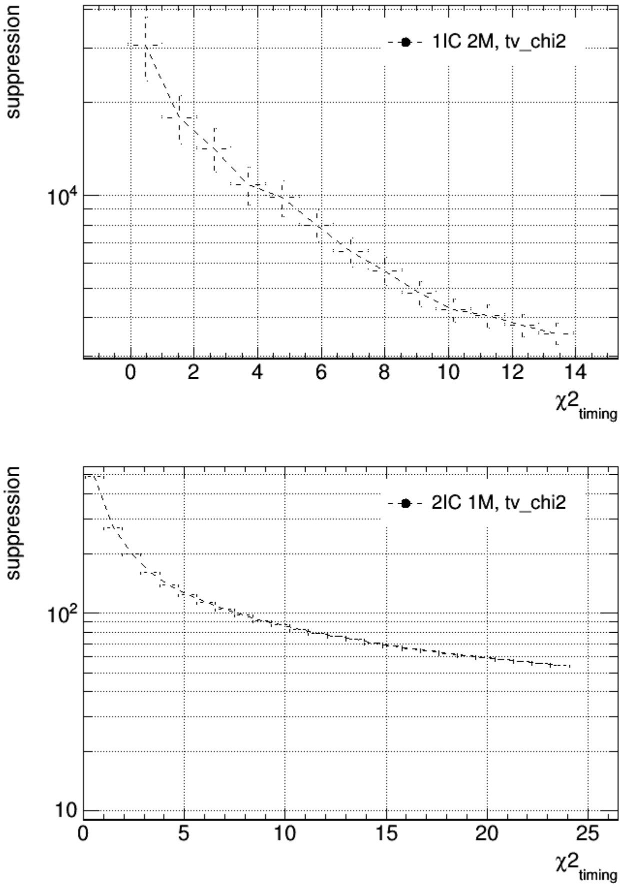

FIGURE B.4: New suppression factors for the 2+1 background with two and three uncorrelated vertices of signal timing efficiency.

B.3 Sources of Fake Tracks (Mis-Reconstruction Identification) by Reconstructed Variables

In order to understand the sources of fake tracks in the signal sample. A background sample of Michel decays is chosen because it is best to check the sources of fake tracks for a single track to avoid fake tracks due to the hit multiplicity. For this analysis, cuts on three spatial variables are applied: the χ^2 of the track fit, the dip angle λ_{01} and the intersection z_0 of the positron track with the target region. Figure B.7 is shown selection cuts on λ_{01} for reconstructed as short with 4-pixel hits and long tracks with 8-pixel hits. On the left-hand side, the λ_{01} distribution is shown, and on the right-hand side the yielded efficiency, purity, and the product between them for cuts of λ_{01}. The sample contains positrons from muon decays. Also, distribution of the reconstructed momentum of positron candidates before and after applying cuts of λ_{01}. Reconstructed true tracks are shown in blue, fake tracks in red and the total reconstructed tracks in black. A dashed line indicates the distribution before applying cuts, and a solid line after applying cuts.

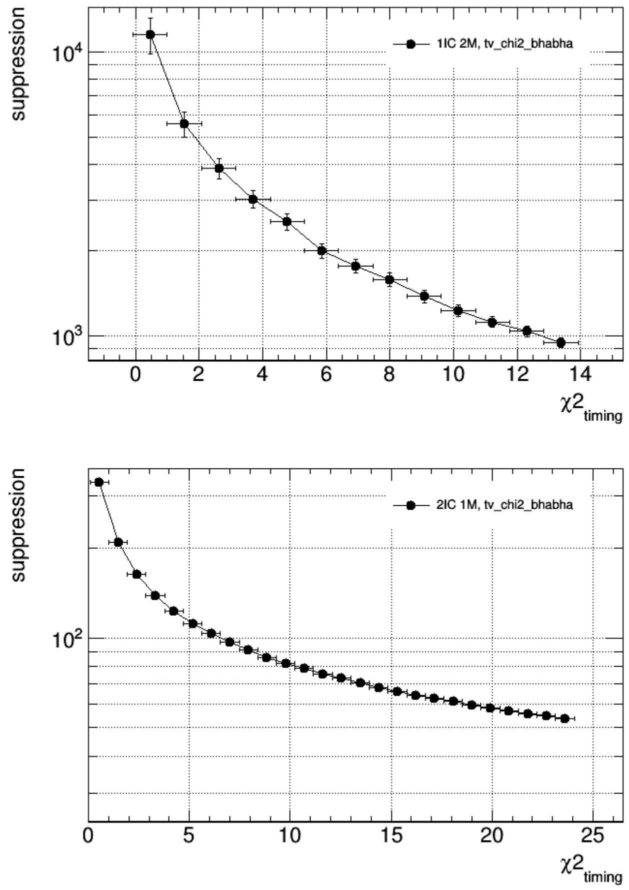

FIGURE B.5: New suppression factors for the 2+1 background with two and three uncorrelated vertices of Bhabha timing efficiency.

The same variable is shown in figure B.8 for long tracks with 6-pixel hits either in the central station or in the two recurl stations of the detector.

Figure B.9 is shown selection cuts on χ^2 for reconstructed as short with 4-pixel hits and long tracks with 8-pixel hits. On the left-hand side, the χ^2 distribution is shown, and on the right-hand side the yielded efficiency, purity, and the product between them for cuts of χ^2. The sample contains positrons from muon decays. Also, distribution of the reconstructed momentum of positron candidates before and after applying cuts of χ^2. Reconstructed true tracks are shown in blue, fake tracks in red and the total reconstructed tracks in black. A dashed line indicates the distribution before applying cuts, and a solid line after applying cuts. The same variable is shown in figure B.10 for long tracks with 6-pixel hits either in the central station or in the two recurl stations of the detector.

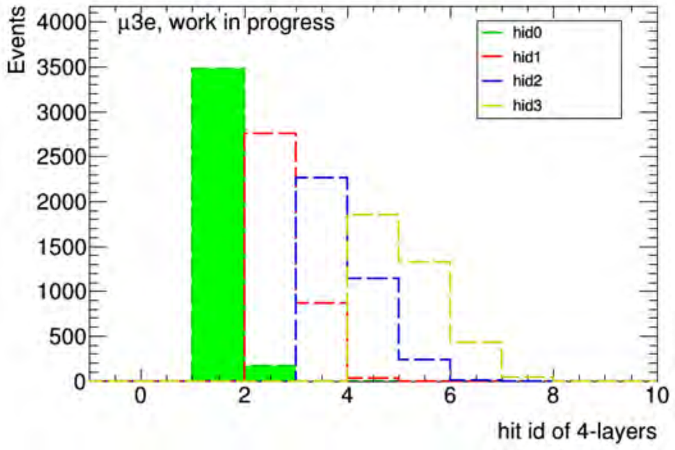

FIGURE B.6: Hit id of four layers in the central station of the detector.

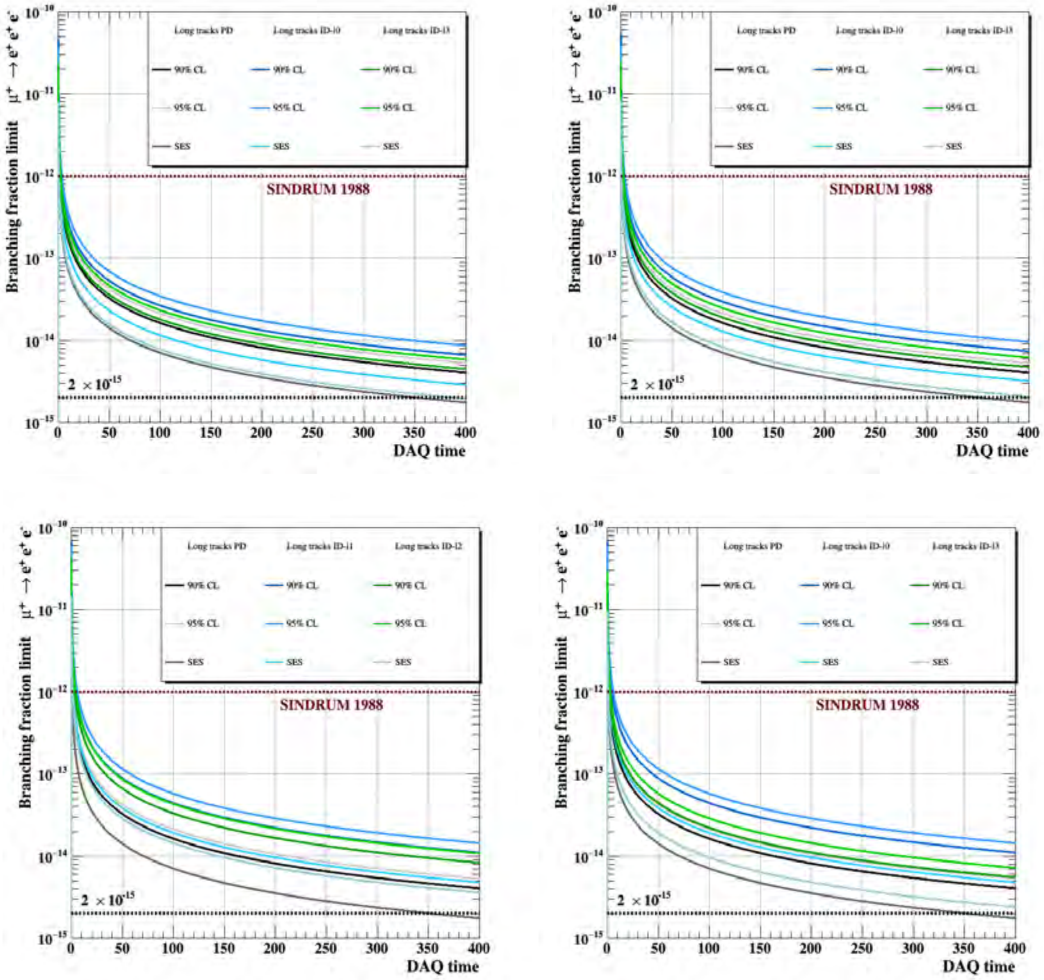

FIGURE B.7: Single event sensitivity SES and the corresponding 90% and 95% C.L. upper limits versus data taking days for the phase I Mu3e detector only for long tracks with inefficiency 5%, 10%, 15% and 20% if layer 0 and 3 are inefficient.

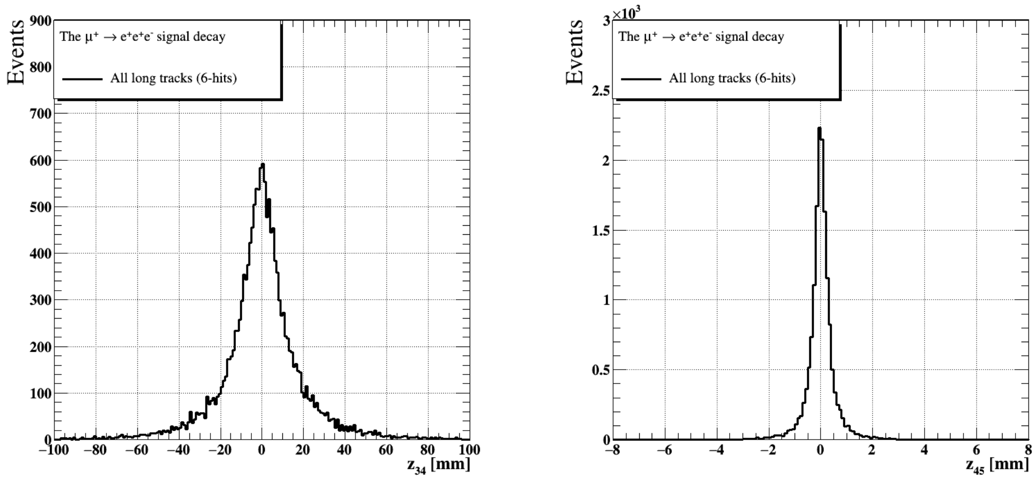

(A) Z distribution between layer 3 and 4.

(B) Z distribution between layer 4 and 5.

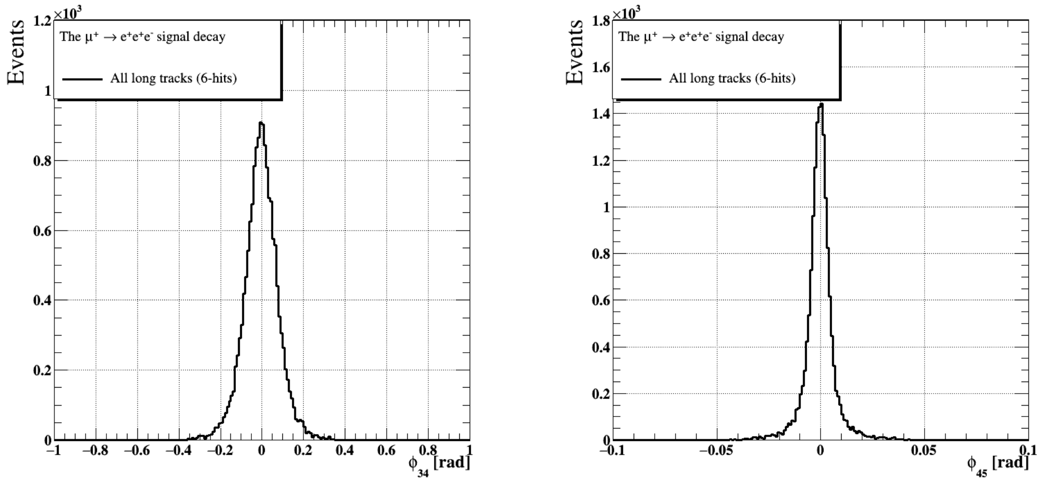

(C) ϕ distribution between layer 3 and 4.

(D) ϕ distribution between layer 4 and 5.

FIGURE B.8: Z and ϕ distribution for long tracks with 6-hits of the signal muon decays.

B.4 Detector Inefficiency; Extended Studies on the Inefficient Pixel Detector with Missing Hits in 0 and 3 Layer

B.5 Pre-Selection cuts for long tracks

In this section, the effect on the efficiency and purity of the track reconstruction as the noise rate per pixel goes from 0 to 20 Hz (the highest noise rate per pixel seen for the MuPix prototypes test-beam measurements (see next two chapters), is presented. Tables B.3, B.4, B.5 and B.6 list the signal efficiency after reconstruction and vertex fit step for phase space distributed events for different simulated noise values from 0 (nominal detector) to 20 Hz per pixel. A slight drop of signal efficiency is observed as the noise rate

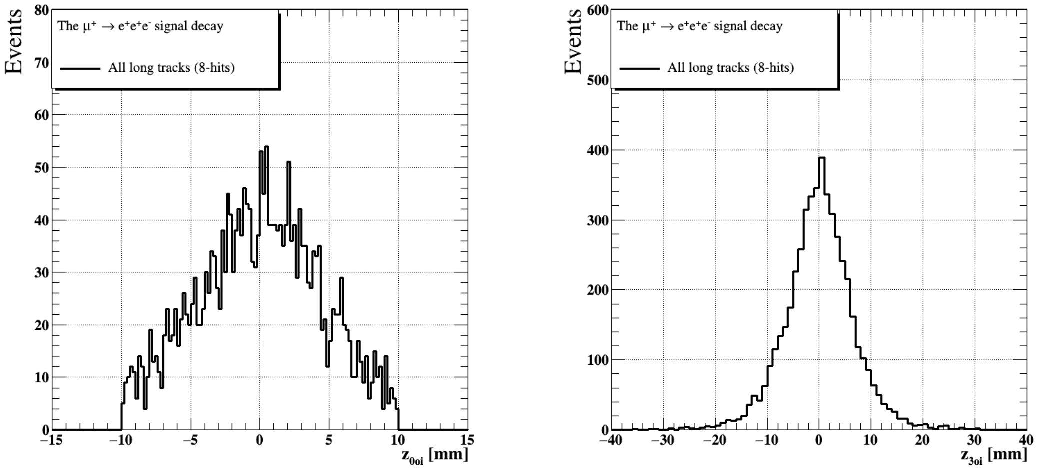

(A) Z distribution between layer 0 (out-going) and (in-going) in the central station of the detector.

(B) Z distribution between layer 3 (out-going) and (in-going) in the central station of the detector.

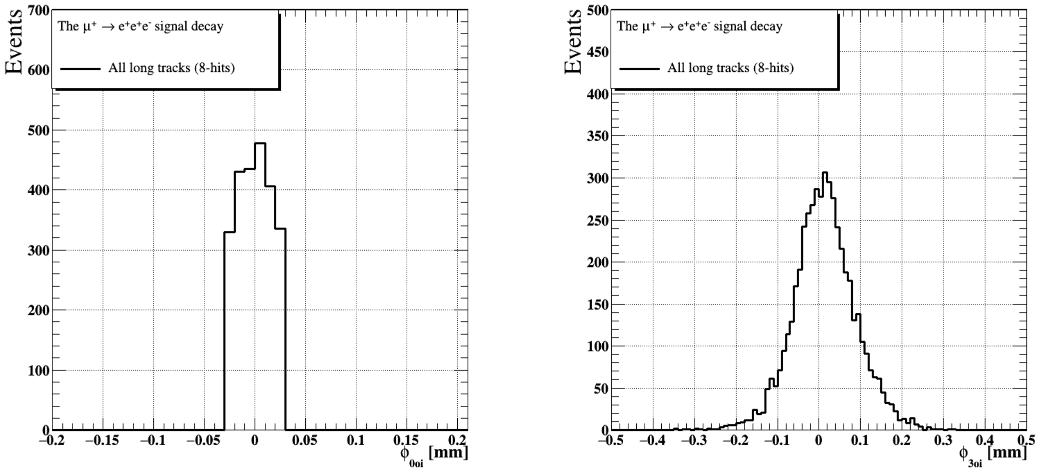

(C) ϕ distribution between between layer 0 (out-going) and (in-going) in the central station of the detector.

(D) ϕ distribution between between layer 3 (out-going) and (in-going) in the central station of the detector.

FIGURE B.9: Z and ϕ distribution in the central station of the detector for long tracks with 8 pixel hits of the signal muon decays.

per pixel increases.

B.6 Additional Results on the Mis-alignments of the Mu3e Pixel Detector

B.6.1 Momentum Resolution for Long Tracks Corresponding to the RMS of the Difference Between True and Reconstructed Momentum (Alignment at Sensor Level)

Individual sensor misplacement: Effects of positrons and orientation misalignment of individual sensors may affect the momentum resolution of the reconstructed tracks. In order to investigate, a sample of signal muon events was simulated with a sensor-level misalignment. The track resolution and efficiency are investigated as a function of the local coordinate system on the sensor. Figure 7.13 shows the standard deviations of the random shifts and rotations are depicted on the x- and y-axis, respectively. It can be seen the momentum resolution and efficiency can negatively affect as misalignment of individual sensors is applied.

Phase space	$\epsilon_{\text{all tracks (4, 6, 8 hits)}}$	$\epsilon_{\text{3 long tracks (6, 8 hits)}}$
events in acceptance	0.412(1)	0.265(1)
relative to events in acceptance		0.643(3)
Nominal detector with 0 Hz noise rate per pixel		
events after track reconstruction	0.368(1)	0.185(1)
relative to events in acceptance	0.892(5)	0.698(5)
events with reconstructed vertex	0.374(1)	0.188(1)
relative to events in acceptance	0.907(5)	0.708(5)
relative to events after track reconstruction	0.998(8)	0.998(8)
relative to events with reconstructed vertex before cuts	0.776(4)	0.866(7)
events with reconstructed vertex after cuts	0.290(1)	0.163(1)
relative to events in acceptance	0.704(4)	0.614(4)
relative to events after reconstruction	0.789(4)	0.879(7)
Noise in the pixel sensors as 20 Hz noise rate per pixel		
events after track reconstruction	0.367(7)	0.179(4)
relative to events in acceptance	0.910(2)	0.684(2)
events with reconstructed vertex	0.354(6)	0.173(4)
relative to events in acceptance	0.878(2)	0.658(2)
relative to events after track reconstruction	0.964(2)	0.962(3)
relative to events with reconstructed vertex before cuts	0.735(1)	0.812(2)
events with reconstructed vertex after cuts	0.274(5)	0.148(4)
relative to events in acceptance	0.680(1)	0.563(1)
relative to events after track reconstruction	0.747(1)	0.823(2)

TABLE B.3: Signal efficiency after reconstruction and vertex fit step for phase space distributed events for perfect detector and noise in the pixel sensors as 20 Hz noise rate per pixel.

Phase space	$\epsilon_{\text{all tracks}}$	$\epsilon_{\text{3 recurler}}$
events in acceptance	0.412(1)	0.265(1)
relative to events in acceptance		0.643(3)
events after reconstruction	0.368(1)	0.185(1)
relative to events in acceptance	0.892(5)	0.698(5)
events with reconstructed vertex	0.355(1)	0.178(1)
relative to events in acceptance	0.862(4)	0.673(5)
relative to events after reconstruction	0.965(5)	0.963(7)
relative to events with reconstructed vertex before cuts	0.737(4)	0.823(6)
events with reconstructed vertex after cuts	0.276(1)	0.155(1)
relative to events in acceptance	0.669(4)	0.583(4)
relative to events after reconstruction	0.749(4)	0.835(7)

TABLE B.4: Efficiency after reconstruction and vertex fit for phase space distributed events as 5 Hz noise rate per pixel.

Phase space	$\epsilon_{\text{all tracks}}$	$\epsilon_{\text{3 recurler}}$
events in acceptance	0.403(7)	0.262(5)
relative to events in acceptance		0.650(1)
events after reconstruction	0.368(7)	0.180(4)
relative to events in acceptance	0.912(2)	0.687(2)
events with reconstructed vertex	0.355(6)	0.173(4)
relative to events in acceptance	0.880(2)	0.661(2)
relative to events after reconstruction	0.964(2)	0.962(3)
relative to events with reconstructed vertex before cuts	0.736(1)	0.813(2)
events with reconstructed vertex after cuts	0.275(5)	0.149(4)
relative to events in acceptance	0.682(1)	0.566(1)
relative to events after reconstruction	0.748(1)	0.824(2)

TABLE B.5: Efficiency after reconstruction and vertex fit for phase space distributed events as 10 Hz noise rate per pixel.

Phase space	$\epsilon_{\text{all tracks}}$	$\epsilon_{\text{3 recurler}}$
events in acceptance	0.403(7)	0.262(5)
relative to events in acceptance		0.650(1)
events after reconstruction	0.368(7)	0.179(4)
relative to events in acceptance	0.911(2)	0.684(2)
events with reconstructed vertex	0.355(6)	0.173(4)
relative to events in acceptance	0.879(2)	0.659(2)
relative to events after reconstruction	0.964(2)	0.963(3)
relative to events with reconstructed vertex before cuts	0.736(1)	0.813(2)
events with reconstructed vertex after cuts	0.275(5)	0.1489(4)
relative to events in acceptance	0.682(1)	0.564(1)
relative to events after reconstruction	0.748(1)	0.813(2)

TABLE B.6: Efficiency after reconstruction and vertex fit for phase space distributed events as 15 Hz noise rate per pixel.

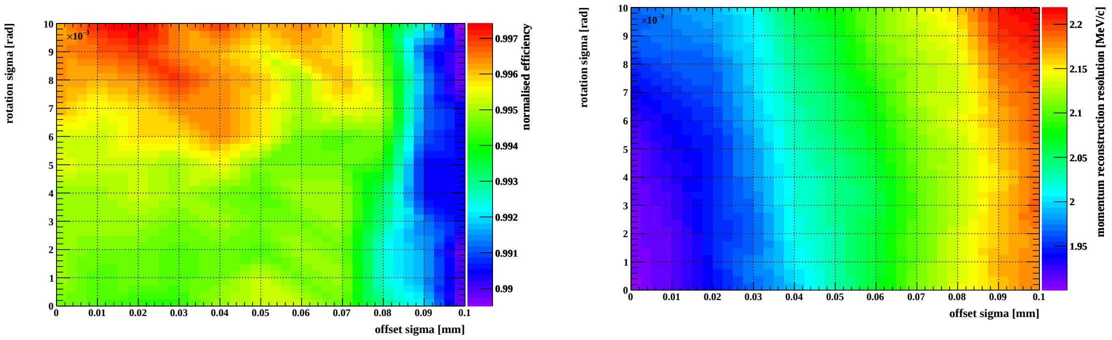

(A) Track reconstruction efficiency normalised to a perfectly aligned detector (short tracks with 4-pixel hits).

(B) Momentum resolution for long tracks corresponding to the RMS of the difference between true momentum and reconstructed momentum (short tracks with 4-pixel hits).

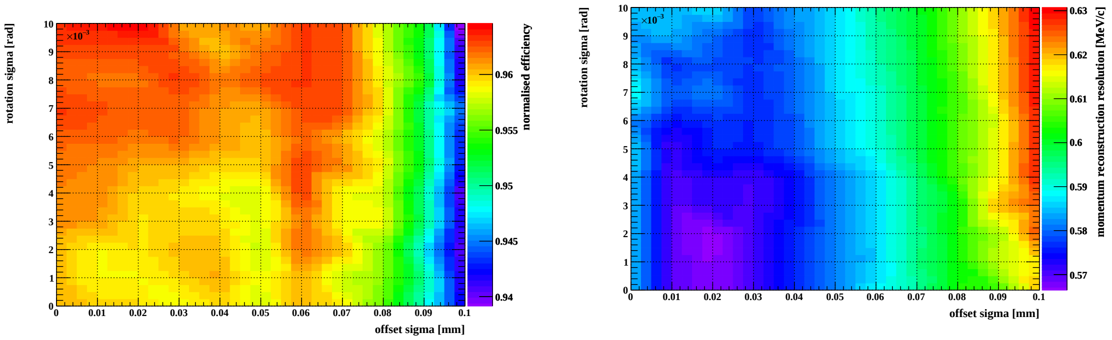

(C) Track reconstruction efficiency normalised to a perfectly aligned detector (long tracks with 6-pixel hits).

(D) Momentum resolution for long tracks corresponding to the RMS of the difference between true momentum and reconstructed momentum (long tracks with 6-pixel hits).

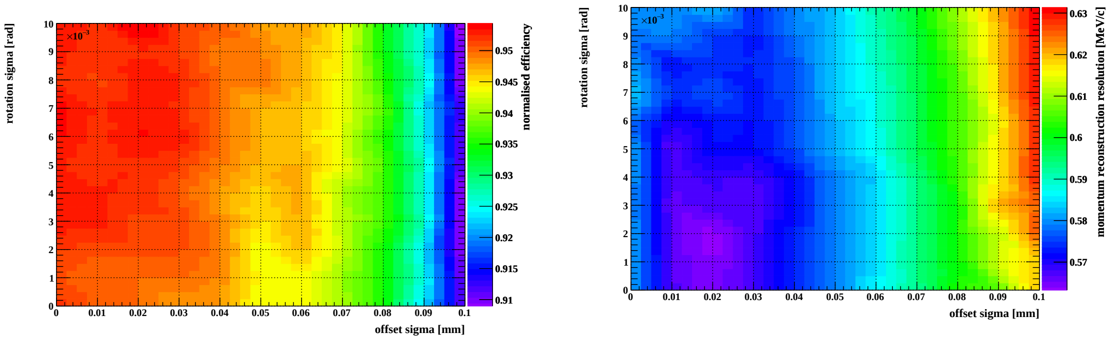

(E) Track reconstruction efficiency normalised to a perfectly aligned detector (all long tracks with more than 4-pixel hits).

(F) Momentum resolution for long tracks corresponding to the RMS of the difference between true momentum and reconstructed momentum (all long tracks with more than 4-pixel hits).

FIGURE B.10: Individual sensor misplacement: Effects of position and orientation misalignment of individual sensors on momentum resolution. The standard deviations of the random shifts and rotations are depicted on the x- and y-axis, respectively.

B.6.2 Results of the Vertex Reconstruction of Signal Events for a Nominal and Misaligned detector

Misalignment of the Mu3e at the layer level and beyond can negatively affect the geometrical acceptance of the detector for signal events which would be a huge drawback for the success of the Mu3e experiment. In this section, the impact of larger structural misalignments on the performance of the detector is investigated. In particular, displacements of the inner vertex and recurl layers are investigated in both directions of parallel and perpendicular to the beam direction. Also, the impact of noise will be studied for the same misalignments by using signal muon events, such as if vertex layers are perpendicular to the beam direction.

Vertex layers are perpendicular to the beam direction: The misalignment is applied on the inner layers with the same values as mentioned in table 7.10, vertex layers are translated perpendicular to the beam direction. Figure 7.14 shows the stated offsets which correspond to the systematic misplacement of the first and second vertex layers (inner-pixel layers) perpendicular to the z-direction. The calculation of the vertex resolution in the x-direction is compromised due to the large offset of the reconstructed vertex from its nominal position.

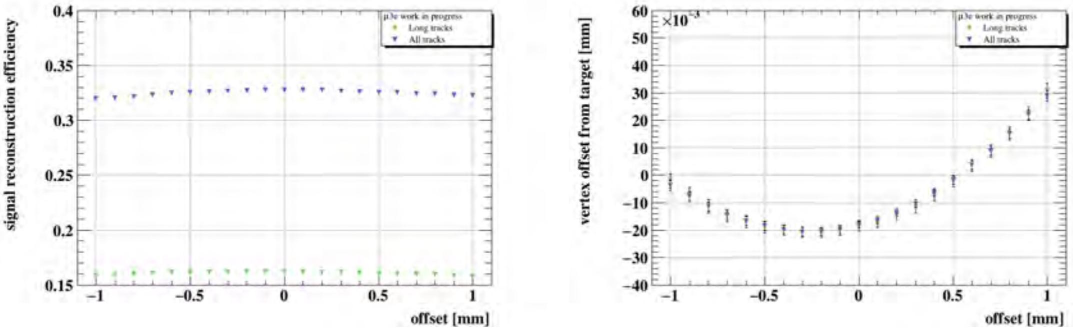

(A) Signal reconstruction efficiency for the signal muon decays.

(B) Absolute offset from reconstructed vertex to target surface.

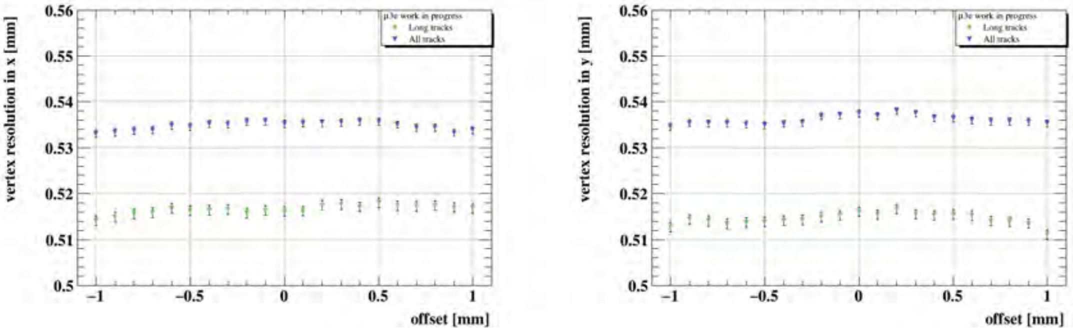

(C) Vertex resolution in x.

(D) Vertex resolution in y.

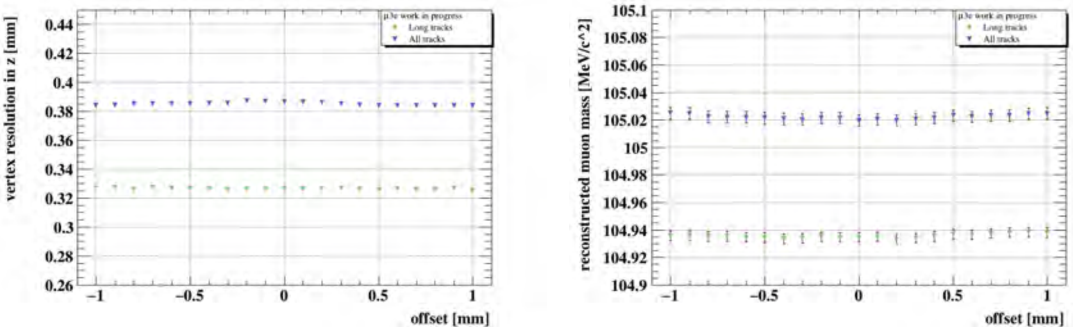

(E) Vertex resolution in z.

(F)) Reconstructed mass of the decayed muon.

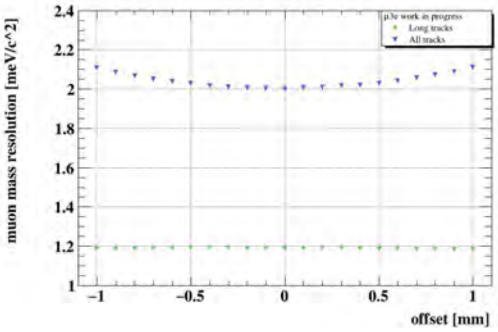

(G) Mass resolution for the decayed muon.

FIGURE B.11: Vertex layers perpendicular to beam direction: Effects on the reconstruction performance for signal decays. Each plot hosts results for utilising only long tracks (green) and for all possible tracks (blue) for reconstruction. The stated offsets correspond to the systematic misplacement of the vertex layers (inner two layers) perpendicular to the beam direction. The calculation of the vertex resolution in x is compromised due to the large offset of the reconstructed vertex from its nominal position.

Vertex layers are parallel to the beam direction: Mis-alignments on the inner pixel layers are applied, translating the vertex layers parallel to the beam direction. Figure 7.15 shows the stated offsets have corresponded to the systematic misplacement of the first and second vertex layers (inner-pixel layers) parallel to the z-direction. Negative offsets are indicated to upstream and positive offsets to downstream misplacements. The calculation of the vertex resolution in the z-direction is compromised due to the large offset of the reconstructed vertex from its nominal position[1].

---

[1] in this section, nominal position in refereed to offset = 0 mm

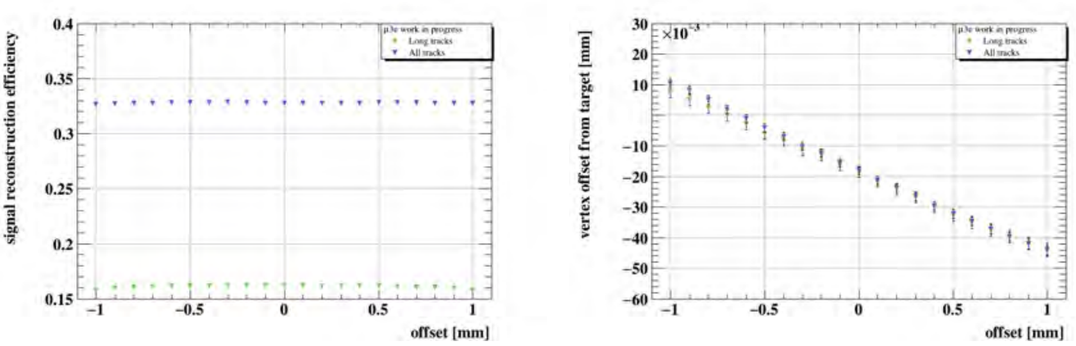

(A) Signal reconstruction efficiency for the signal muon decays.

(B) Absolute offset from reconstructed vertex to target surface.

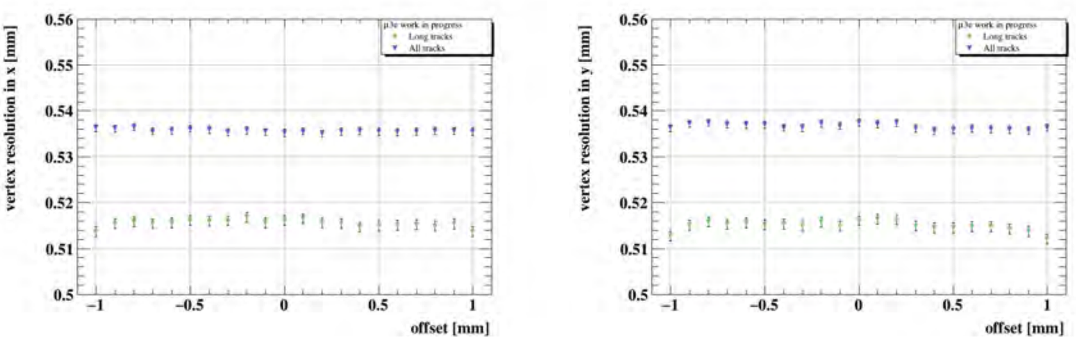

(C) Vertex resolution in x.

(D) Vertex resolution in y.

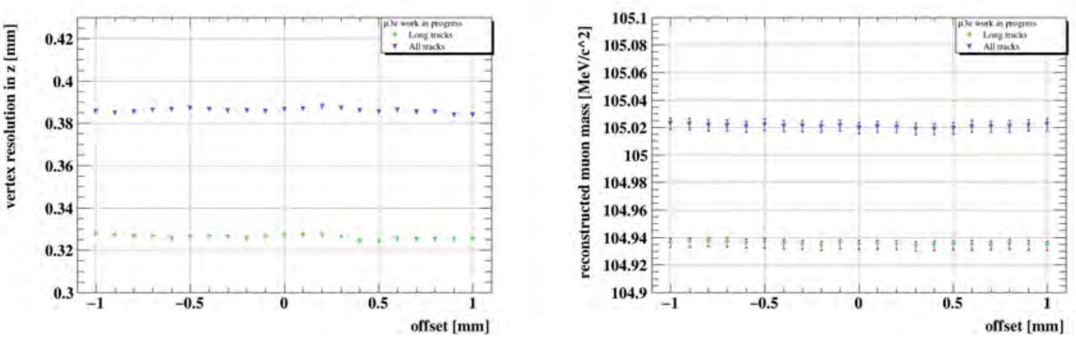

(E) Vertex resolution in z.

(F)) Reconstructed mass of the decayed muon.

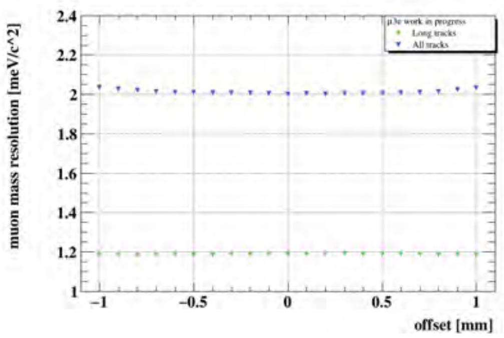

(G) Mass resolution for the decayed muon.

FIGURE B.12: Vertex layers parallel to beam direction: Effects on the reconstruction performance for signal decays. Each plot hosts results for utilising only long tracks (green) and for all possible tracks (blue) for reconstruction. The stated offsets correspond to the systematic misplacement of the vertex layers parallel to the beam direction, where negative offsets correspond to upstream and positive offsets to downstream misplacements. The calculation of the vertex resolution in z is compromised due to the large offset of the reconstructed vertex from its nominal position.

Recurl stations are parallel to the beam direction: Mis-alignments can be applied to the recurl stations to make them parallel to the beam direction. Figure 7.16 shows the stated offsets are indicated to the systematic misplacement of both recurl stations of the detector simultaneously parallel toward each other in the same direction of the beam. Negative offsets are corresponding to a stretching of the detector and a positive offset to a squeezing.

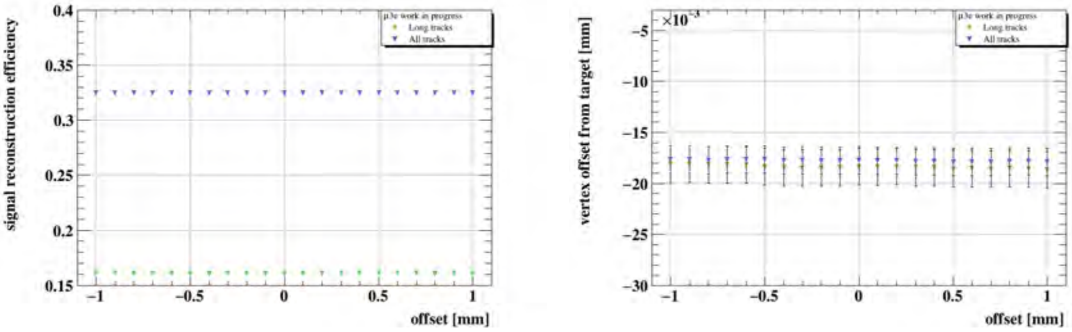

(A) Signal reconstruction efficiency for the signal muon decays.

(B) Absolute offset from reconstructed vertex to target surface.

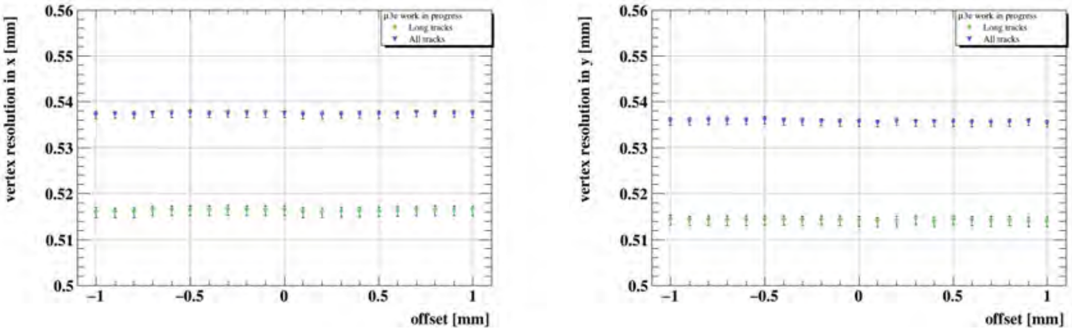

(C) Vertex resolution in x.

(D) Vertex resolution in y.

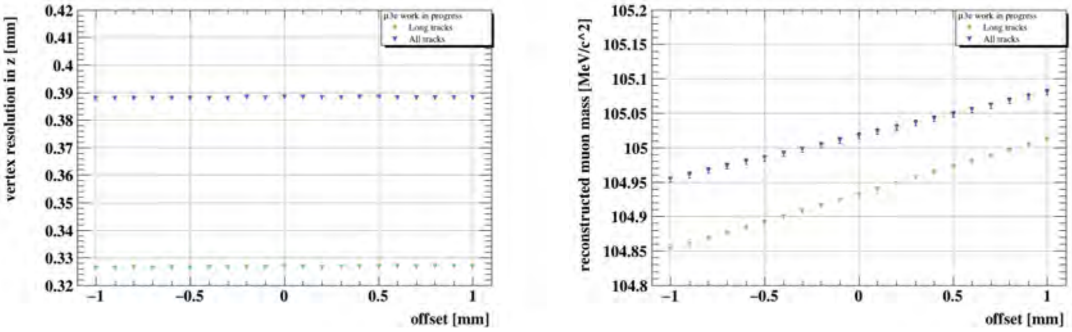

(E) Vertex resolution in z.

(F)) Reconstructed mass of the decayed muon.

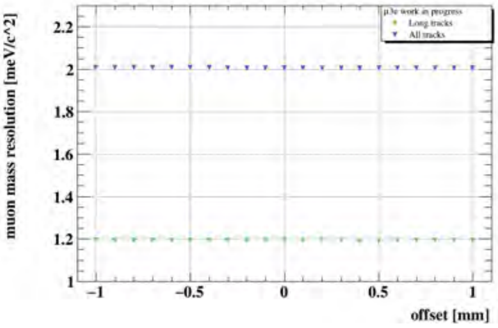

(G) Mass resolution for the decayed muon.

FIGURE B.13: Recurl stations parallel to beam direction: Effects on the reconstruction performance for signal decays. Each figure hosts results for utilising only long tracks (green) and for all possible tracks (blue) for reconstruction. The stated offsets correspond to the systematic misplacement of both recurl stations simultaneously towards each other (along beam direction). Hence, a negative offset corresponds to a "stretching" of the detector and a positive offset to a "squeezing".

Recurl stations are perpendicular to beam direction: If the recurl stations are perpendicular to the beam direction after applying the misalignments, different tracking performance is observed. Figure 7.17 shows the stated offsets are indicated to the systematic misplacement of both recurl stations of the detector simultaneously perpendicular toward each other in the opposite direction of the beam.

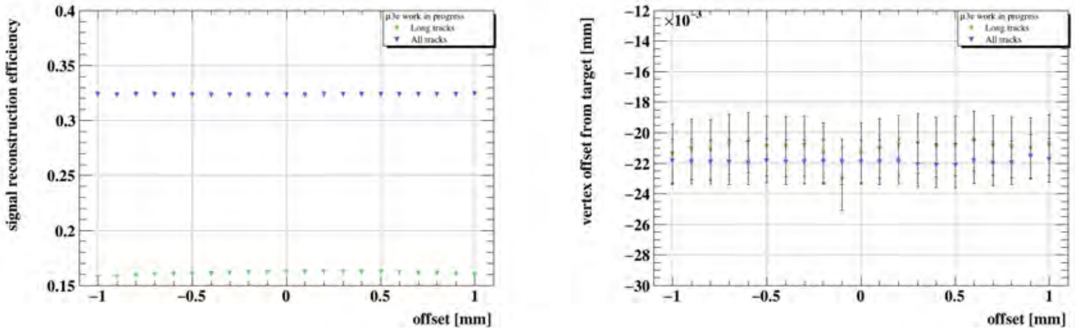

(A) Signal reconstruction efficiency for the signal muon decays.

(B) Absolute offset from reconstructed vertex to target surface.

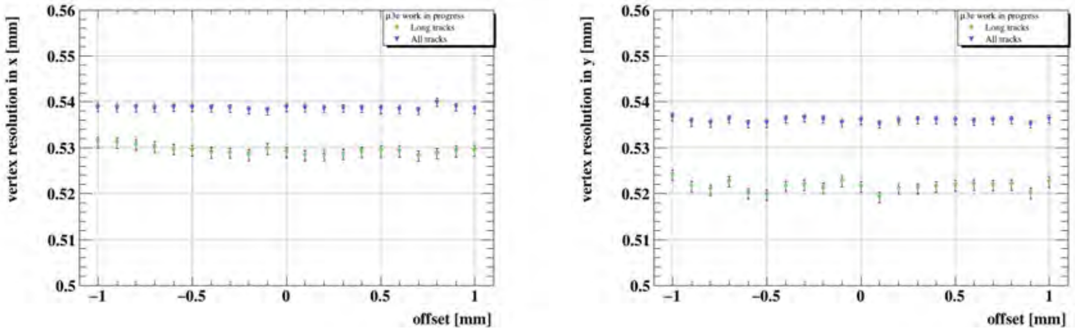

(C) Vertex resolution in x.

(D) Vertex resolution in y.

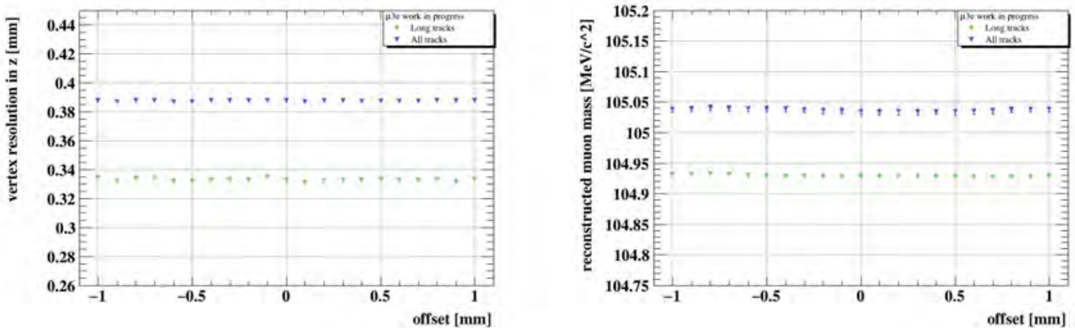

(E) Vertex resolution in z.

(F)) Reconstructed mass of the decayed muon.

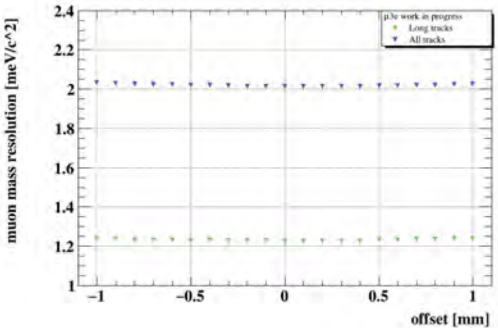

(G) Mass resolution for the decayed muon.

FIGURE B.14: Recurl stations perpendicular to beam direction: Effects on the reconstruction performance for signal decays. Each plot hosts results for utilising only long tracks (green) and for all possible tracks (blue) for reconstruction. The stated offsets correspond to the systematic misplacement of both recurl stations simultaneously perpendicular to the beam direction.

Further results, combine between the misaligned detector and noisy detector in the pixel sensors as 20 Hz noise rate per pixel as shown in figure 7.18. Efficiency is less and that is expected in the case if vertex layers perpendicular to the beam direction with injecting noise rate per pixel.

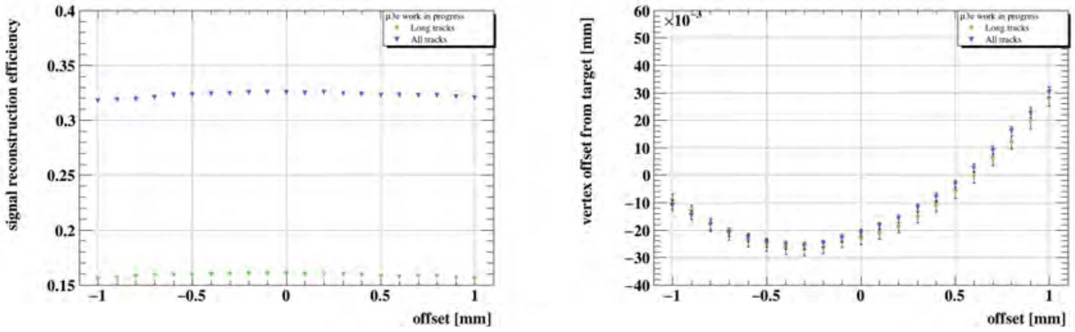

(A) Signal reconstruction efficiency for the signal muon decays.

(B) Absolute offset from reconstructed vertex to target surface.

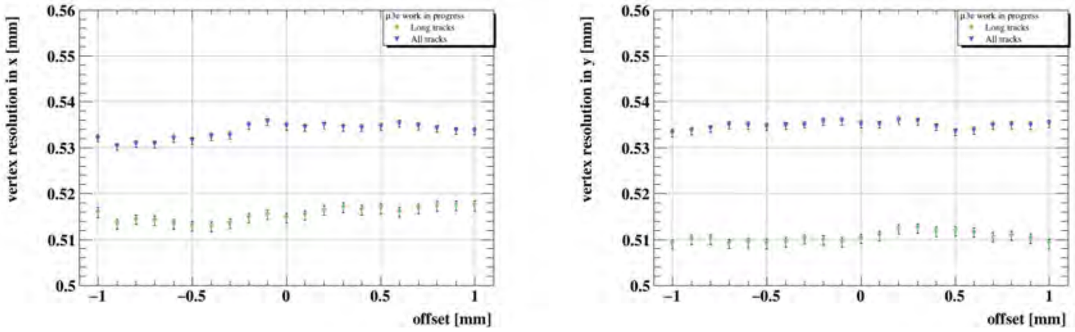

(C) Vertex resolution in x.

(D) Vertex resolution in y.

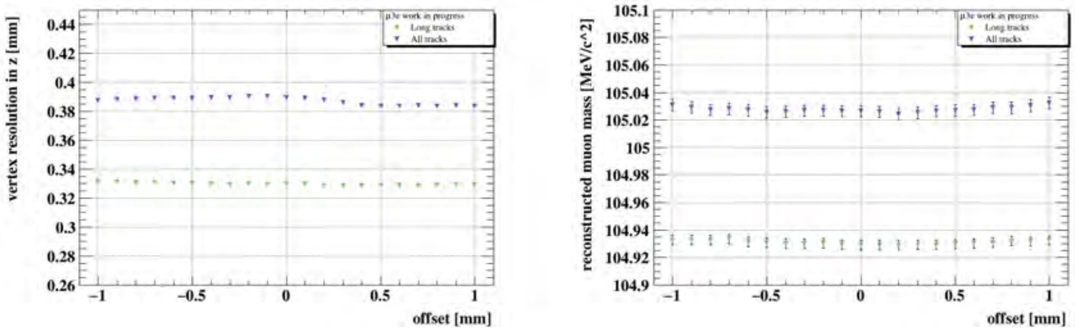

(E) Vertex resolution in z.

(F)) Reconstructed mass of the decayed muon.

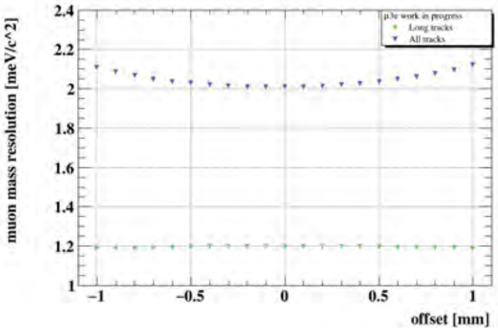

(G) Mass resolution for the decayed muon.

FIGURE B.15: Vertex layers perpendicular to beam direction: Effects on the reconstruction performance for signal decays. Each plot hosts results for utilising only long tracks (green) and for all possible tracks (blue) for reconstruction. The stated offsets correspond to the systematic misplacement of the vertex layers (inner two layers) perpendicular to the beam direction with injecting noise rate per pixel as 20 Hz. The calculation of the vertex resolution in x is compromised due to the large offset of the reconstructed vertex from its nominal position in which the noise rate per pixel is inserted into the perfect detector.

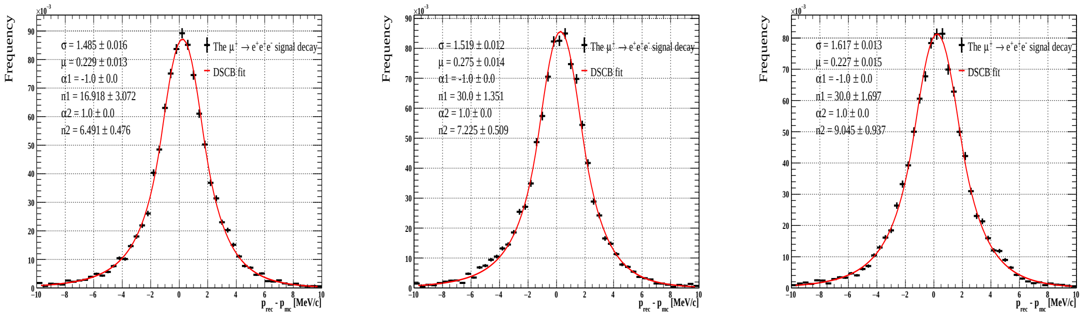

(A) 4,3-hits; 18-20 MeV

(B) 4,3-hits; 20-22 MeV

(C) 4,3-hits; 22-24 MeV

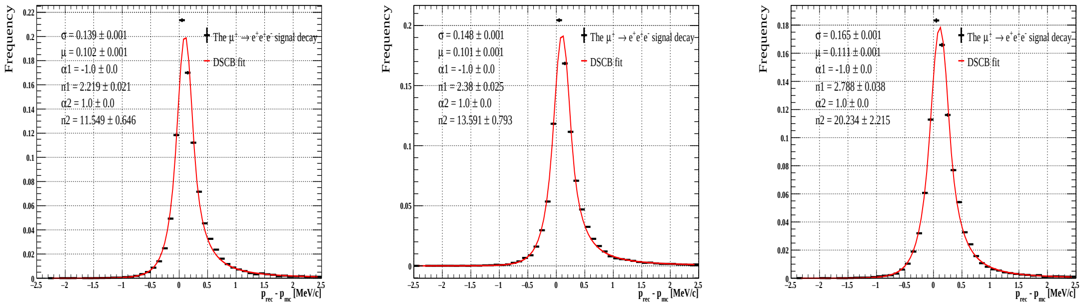

(D) 6,5-hits; 18-20 MeV

(E) 6,5-hits; 20-22 MeV

(F) 6,5-hits; 22-24 MeV

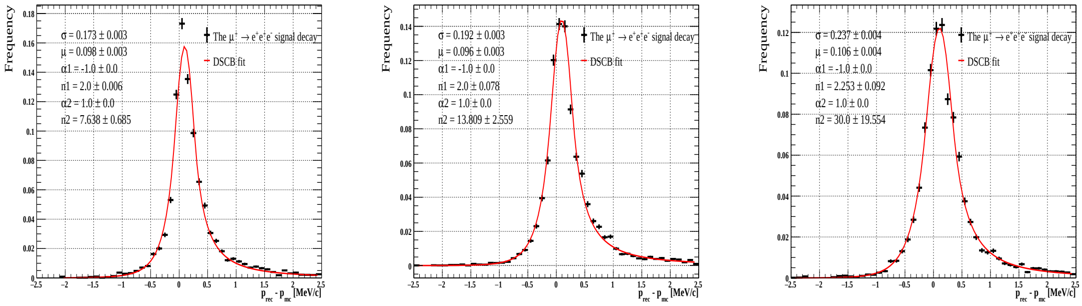

(G) 8,7-hits; 18-20 MeV

(H) 8,7-hits; 20-22 MeV

(I) 8,7-hits; 22-24 MeV

FIGURE B.16: Momentum resolution (with track momenta 18-20, 20-22, 22-24 MeV) for short tracks with 4,3-hit, long tracks with 6,5-hit, and long tracks with 8,7-hit with 5%inefficiency. The fitting function is a Double-sided crystal ball function.

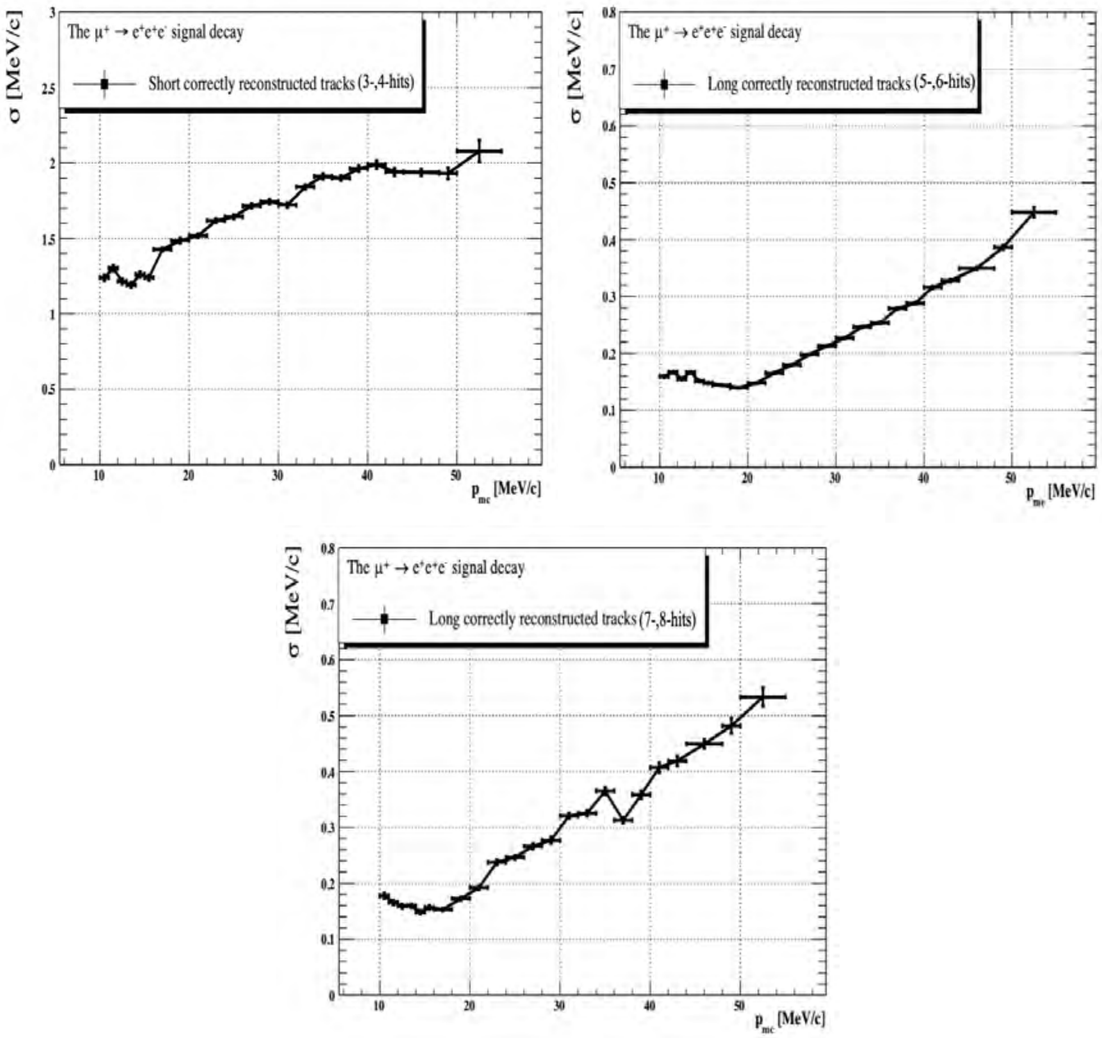

FIGURE B.17: Summary plots for the variations of the momentum resolutions obtained via using Double-sided crystal ball fit as a function of the true track momentum for short tracks with 4,3-hit, long tracks with 6,5-hit, and long tracks with 8,7-hit with 5% inefficiency, respectively from left to right.

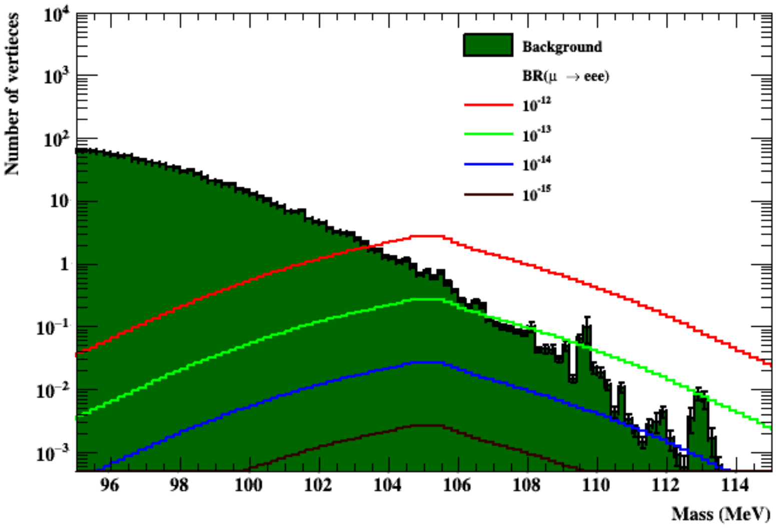

FIGURE B.18: Spectra of the reconstructed invariant three-particle mass of signal decays and background from radiative events with internal conversion in phase I of the Mu3e experiment after the vertex selection cuts. The plot is on a logarithmic y-axis scale. The invariant mass of the three tracks including all short with 3- and 4-hits and long tracks with 5-, 6-, 7-, and 8-hits with 10% inefficiency.

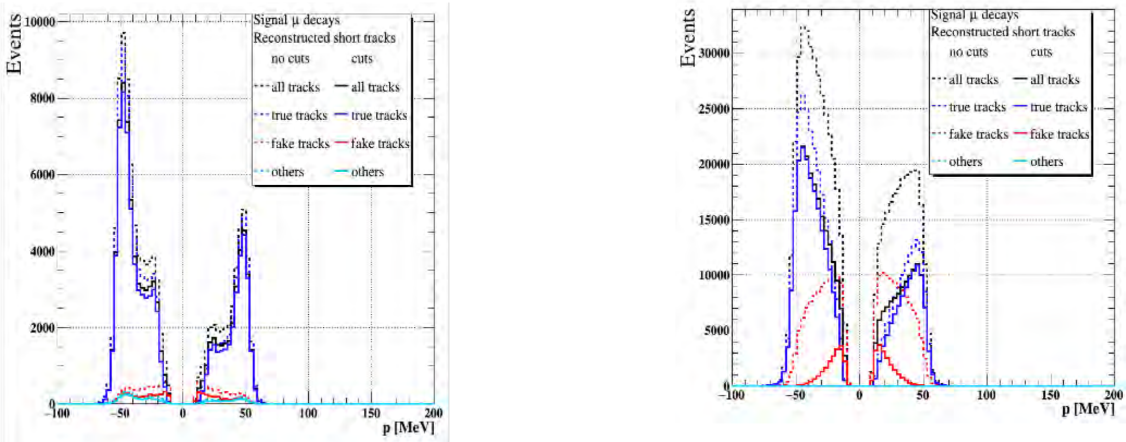

(A) Reconstructed momentum after applying the track reconstruction cuts for perfect short tracks.

(B) Reconstructed momentum after applying the track reconstruction cuts for short tracks with 3-pixel hits if layer 1 is inefficient.

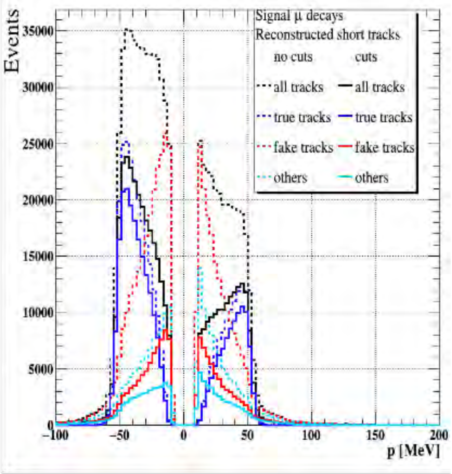

(C) Reconstructed momentum after applying the track reconstruction cuts for short tracks with 3-pixel hits if layer 2 is inefficient.

FIGURE B.19: Reconstructed momentum for signal muon decays after applying the track reconstruction cuts for the short nominal tracks and tracks with missing hits.

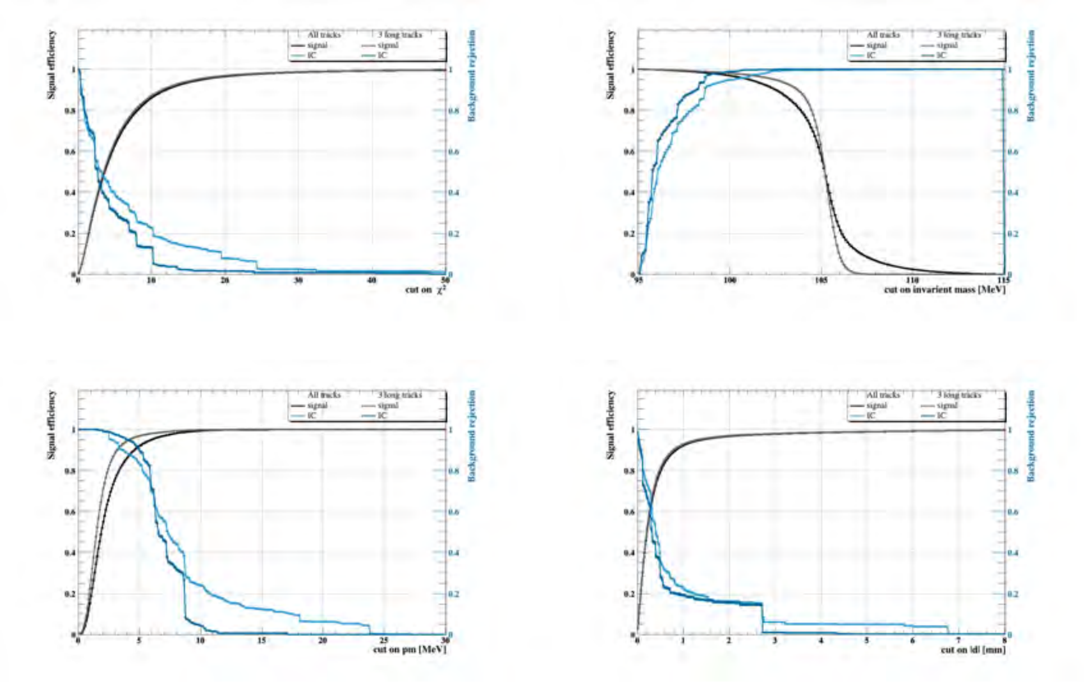

FIGURE B.20: Signal efficiency and background suppression by cuts on the χ^2 of the vertex, the invariant mass $m_{eee}, thetotalmomentump_{eee}$, the target distance |d| of the two positrons and one electron for $\mu^+ \rightarrow e^+e^+e^-$ signal decays and radiative decays with internal conversion $\mu^+ \rightarrow e^+e^+e^-\nu\nu$ (IC). Note that the signal efficiency before applying the vertex cuts.

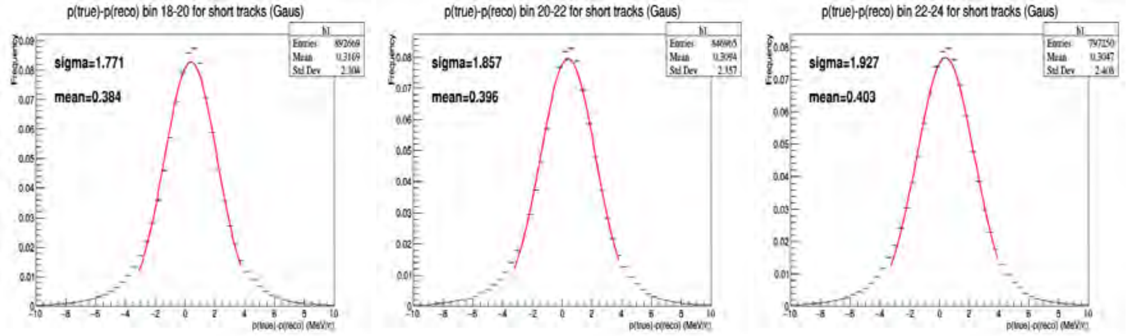

(A) 4-hits; 18-20 MeV (B) 4-hits; 20-22 MeV (C) 4-hits; 22-24 MeV

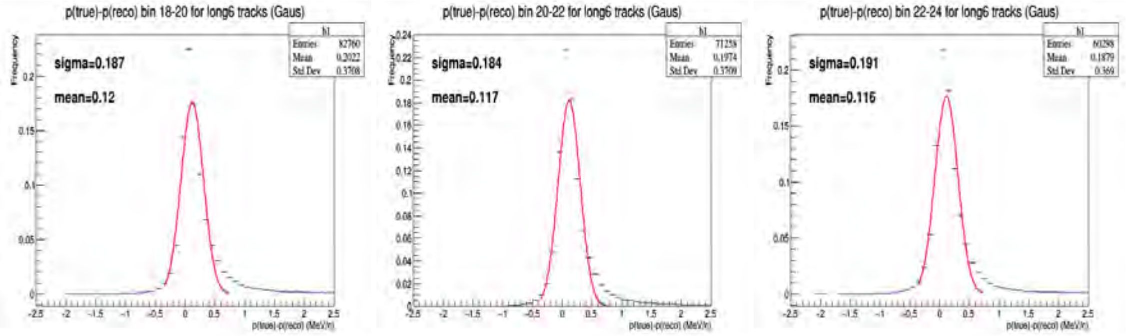

(D) 6-hits; 18-20 MeV (E) 6-hits; 20-22 MeV (F) 6-hits; 22-24 MeV

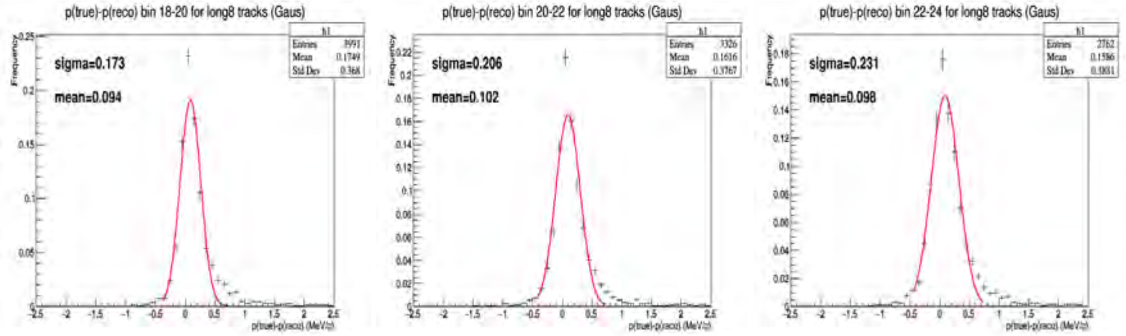

(G) 8-hits; 18-20 MeV (H) 8-hits; 20-22 MeV (I) 8-hits; 22-24 MeV

FIGURE B.21: Momentum resolution for track momenta, 18-20, 20-22, 22-24 MeV for short tracks with 4-hit, long tracks with 6-hit, and long tracks with 8-hit. The fitting function is a Gaussian function..

GUI Graphical User Interface

LFV Lepton Flavour Violation

BR Branching Fraction

SES Single Event Sensitivity

SM Standard Model

QFT Quantum Field Theory

EM Electromagnetic

QCD Quantum ChromoDynamics

QED Quantum Electrodynamics

PSI Paul Scherrer Institute

CMBL Compact Muon beam line

CMS Compact Muon Solenoid

LHC Large Hadron Collider

MS Multiple Scattering

DAQ Data acquisition system

GPU Graphical processing unit

GPUs Graphical processing units

PMNS Pontecorvo–Maki–Nakagawa–Sakata

CLFV Charged Lepton Flavour violation

HV-MAPS High Voltage Monolithic Active Pixel Sensors

TWIST The TRIUMF Weak Interaction Symmetry Test

BSM Beyond Standard Model

PSI Paul-Scherrer Institute

SiPM silicon photo-multiplier

SiPMs silicon photo-multipliers

ASIC Application-specific integrated circuit

CSA	charge sensitive amplifier
LVDS	Low Voltage Differential Signalling
PCB	Printed circuit boards
PCBs	Printed circuit boards
DACs	digital-to-analogue converters
GPU	graphical processing units
IR	Infrared Thermal
TCT	Top-cool technology
MS	Multiple Scattering
DSCB	Double Side Crystal Ball
C.L.	Confidence level
BLUE	Best Linear Unbiased Estimator
SCSI	Small Computer System Interface
SSCB	Single sided crystal ball
DUT	Device under test
PC	Personal computer,
SLM	Stright Line Model
GLM	Broken Line Model
ROI	Region of Interest
FPGA	Field-programmable gate array
PMOS	P-channel metal-oxide-semiconductor
NMOS	N-channel metal-oxide-semiconductor

List of Figures

List of Tables

Bibliography

[1] A. Blondel et al. “ Technical Design of the Phase I Mu3e Experiment”. In: *BSc Thesis. Heidelberg University* (2018).

[2] A. Schöning and S. Schenk. “Linearised Vertex 3D Fit in a Solenoidal Magnetic field with Multiple Scattering”. In: *Mu3e Internal Note* (2013).

[3] A. Affolder, M Andelković, K Arndt, R Bates, A Blue, D Bortoletto, C Buttar, P Caragiulo, V Cindro, D Das, et al. “Charge collection studies in irradiated HV-CMOS particle detectors”. In: *Journal of instrumentation* 11.04 (2016), P04007.

[4] S. Agostinelli et al. “Geant4—a simulation toolkit”. In: *Nuclear Instruments and Methods in Physics Research Section A: Accelerators, Spectrometers, Detectors and Associated Equipment* 506.3 (2003), pp. 250–303. ISSN: 0168-9002. DOI: `https://doi.org/10.1016/S0168-9002(03)01368-8`. URL: `https://www.sciencedirect.com/science/article/pii/S0168900203013688`.

[5] K. Arndt et al. “Technical design of the phase I Mu3e experiment”. In: *Nuclear Instruments and Methods in Physics Research Section A: Accelerators, Spectrometers, Detectors and Associated Equipment* 1014 (2021), p. 165679. DOI: `10.1016/j.nima.2021.165679`. URL: `https://doi.org/10.1016%2Fj.nima.2021.165679`.

[6] JC Ashley. “Energy loss rate and inelastic mean free path of low-energy electrons and positrons in condensed matter”. In: *Journal of electron spectroscopy and related phenomena* 50.2 (1990), pp. 323–334.

[7] A. M. Baldini et al. “Search for the lepton flavour violating decay $\mu^+ \to \mathrm{e}^+\gamma$ with the full dataset of the MEG experiment”. In: *Eur. Phys. J.* C76.8 (2016), p. 434. DOI: `10.1140/epjc/s10052-016-4271-x`. arXiv: `1605.05081 [hep-ex]`.

[8] AM Baldini, F Cei, C Cerri, S Dussoni, L Galli, M Grassi, D Nicolo, F Raffaelli, F Sergiampietri, G Signorelli, et al. “MEG upgrade proposal”. In: *arXiv preprint arXiv:1301.7225* (2013).

[9] Ulrich Benedikt. "Track Based Alignment for the Mu3e Pixel Detector". In: *PhD thesis. Universität Mainz* (2019). URL: `https://www.psi.ch/sites/default/files/2019-05/DissertationHartenstein.pdf`.

[10] Niklaus Berger, Moritz Kiehn, Alexandr Kozlinskiy, and Andre Schöning. "A New Three-Dimensional Track Fit with Multiple Scattering". In: *Nucl. Instrum. Meth.* A844 (2017), p. 135. DOI: `10.1016/j.nima.2016.11.012`. arXiv: `1606.04990 [physics.ins-det]`.

[11] Niklaus Berger, Alexandr Kozlinskiy, Moritz Kiehn, and André Schöning. "A new three-dimensional track fit with multiple scattering". In: *Nuclear Instruments and Methods in Physics Research Section A: Accelerators, Spectrometers, Detectors and Associated Equipment* 844 (2017), pp. 135–140. DOI: `10.1016/j.nima.2016.11.012`. URL: `https://doi.org/10.1016%2Fj.nima.2016.11.012`.

[12] J. Bernabéu, E. Nardi, and D. Tommasini. "-e conversion in nuclei and Z physics". In: *Nuclear Physics B* 409.1 (1993), pp. 69 –86. ISSN: 0550-3213. DOI: `https://doi.org/10.1016/0550-3213(93)90446-V`. URL: `http://www.sciencedirect.com/science/article/pii/055032139390446V`.

[13] Wilhelm H. Bertl et al. "A Search for muon to electron conversion in muonic gold". In: *Eur. Phys. J.* C47 (2006), pp. 337–346. DOI: `10.1140/epjc/s2006-02582-x`.

[14] Monika Blanke, Andrzej J. Buras, Bjoern Duling, Anton Poschenrieder, and Cecilia Tarantino. "Charged Lepton Flavour Violation and (g-2)(mu) in the Littlest Higgs Model with T-Parity: A Clear Distinction from Supersymmetry". In: *JHEP* 05 (2007), p. 013. DOI: `10.1088/1126-6708/2007/05/013`. arXiv: `hep-ph/0702136 [hep-ph]`.

[15] Happy Borgohain and Mrinal Kumar Das. "Lepton number violation, lepton flavor violation, and baryogenesis in left-right symmetric model". In: *Phys. Rev. D* 96 (7 2017), p. 075021. DOI: `10.1103/PhysRevD.96.075021`. URL: `https://link.aps.org/doi/10.1103/PhysRevD.96.075021`.

[16] M. L. Brooks et al. "New limit for the family number nonconserving decay mu+ —> e+ γ". In: *Phys. Rev. Lett.* 83 (1999), pp. 1521–1524. DOI: `10.1103/PhysRevLett.83.1521`. arXiv: `hep-ex/9905013 [hep-ex]`.

[17] R. Brun and F. Rademakers. "ROOT: An object oriented data analysis framework". In: *Nucl. Instrum. Meth.* A389 (1997), pp. 81–86. DOI: `10.1016/S0168-9002(97)00048-X`.

[18] C. Burgard and D. Galbraith. "Standard Model of Physics". In: *CERN Webfest* (2012). URL: `http://davidgalbraith.org/portfolio/ux-standard-model-of-the-standard-model/..`

[19] Lorenzo Calibbi and Giovanni Signorelli. "Charged Lepton Flavour Violation: An Experimental and Theoretical Introduction". In: *Riv. Nuovo Cim.* 41.2 (2018), pp. 71–174. DOI: `10.1393/ncr/i2018-10144-0`. arXiv: `1709.00294 [hep-ph]`.

[20] Chen et al. "MuTRiG: a mixed signal Silicon Photomultiplier readout ASIC with high timing resolution and gigabit data link". In: *Journal of Instrumentation* 12.01 (2017), p. C01043.

[21] Marco Chiappini, Marco Francesconi, Satoru Kobayashi, Manuel Meucci, Rina Onda, Patrick Schwendimann, and MEG II Collaboration. "Towards a New μ eγ Search with the MEG II Experiment: From Design to Commissioning". In: *Universe* 7.12 (2021), p. 466.

[22] Hans Patrick Eckert. "The Mu3e Tile Detector". PhD thesis. U. Heidelberg (main), 2015. DOI: `10.11588/heidok.00018763`.

[23] Martin A Green. "Intrinsic concentration, effective densities of states, and effective mass in silicon". In: *Journal of Applied Physics* 67.6 (1990), pp. 2944–2954.

[24] Particle Data Group et al. "Review of Particle Physics". In: *Progress of Theoretical and Experimental Physics* 2020.8 (Aug. 2020). 083C01. ISSN: 2050-3911. DOI: `10.1093/ptep/ptaa104`. eprint: `https://academic.oup.com/ptep/article-pdf/2020/8/083C01/34673722/ptaa104.pdf`. URL: `https://doi.org/10.1093/ptep/ptaa104`.

[25] Lennart Huth. "A High Rate Testbeam Data Acquisition System and Characterization of High Voltage Monolithic Active Pixel Sensor". In: *Ruperto-Carola-University of Heidelberg, Germany* (2018).

[26] Mitsuru Kakizaki, Yoshiteru Ogura, and Fumitaka Shima. "Lepton flavor violation in the triplet Higgs model". In: *Physics Letters B* 566.3 (2003), pp. 210 –216. ISSN: 0370-2693. DOI: `https://doi.org/10.1016/S0370-2693(03)00833-5`. URL: `http://www.sciencedirect.com/science/article/pii/S0370269303008335`.

[27] Kiehn, Moritz Simon Maria. "Pixel Sensor Evaluation and Track Fitting for the Mu3e Experiment". In: *Dissertation. Heidelberg University* (2016). URL: `http://www.ub.uni-heidelberg.de/archiv/20493`.

[28] M. Kiehn. "Pixel Sensor Evaluation and Track Fitting for the Mu3e Experiment". In: *PhD thesis. Universität Heidelberg* (2016). URL: `https://www.psi.ch/sites/default/files/2019-05/DissertationHartenstein.pdf`.

[29] Andreas Klein. “A generalized kahan-babuška-summation-algorithm”. In: *Computing* 76.3-4 (2006), pp. 279–293.

[30] Jens Kröger. “Readout Hardware for the MuPix8 Pixel Sensor Prototype and a Firmware-based MuPix8 Emulator”. In: *Master thesis. Universität Mainz* (2017). URL: `https://www.psi.ch/sites/default/files/import/mu3e/ThesesEN/MasterKroeger.pdf`.

[31] Yoshitaka Kuno and Yasuhiro Okada. “Muon decay and physics beyond the standard model”. In: *Rev. Mod. Phys.* 73 (1 2001), pp. 151–202. DOI: `10.1103/RevModPhys.73.151`. URL: `https://link.aps.org/doi/10.1103/RevModPhys.73.151`.

[32] Luca Lista. *Statistical methods for data analysis in particle physics*. Springer, 2016.

[33] BG Lowe and RA Sareen. “A measurement of the electron–hole pair creation energy and the Fano factor in silicon for 5.9 keV X-rays and their temperature dependence in the range 80–270 K”. In: *Nuclear Instruments and Methods in Physics Research Section A: Accelerators, Spectrometers, Detectors and Associated Equipment* 576.2-3 (2007), pp. 367–370.

[34] William J Marciano, Toshinori Mori, and J Michael Roney. “Charged lepton flavor violation experiments”. In: *Annual Review of Nuclear and Particle Science* 58 (2008), pp. 315–341. DOI: `10.1146/annurev.nucl.58.110707.171126`.

[35] F. Meier and Mu3e collaboration. “Mu3e Inner Detector Design and Pixel”. In: *Mu3e Internal Note* (2018).

[36] Yasuhiro Okada, Ken-ichi Okumura, and Yasuhiro Shimizu. “$\vec{\mu}\ e\gamma$ and $\vec{\mu}\ 3e$ processes with polarized muons and supersymmetric grand unified theories”. In: *Phys. Rev. D* 61 (9 2000), p. 094001. DOI: `10.1103/PhysRevD.61.094001`. URL: `https://link.aps.org/doi/10.1103/PhysRevD.61.094001`.

[37] C. Patrignani et al. “Review of Particle Physics”. In: *Chin. Phys.* C40.10 (2016), p. 100001. DOI: `10.1088/1674-1137/40/10/100001`.

[38] Ivan Perić. “A novel monolithic pixelated particle detector implemented in high-voltage CMOS technology”. In: *Nuclear Instruments and Methods in Physics Research Section A: Accelerators, Spectrometers, Detectors and Associated Equipment* 582.3 (2007). VERTEX 2006, pp. 876 –885. ISSN: 0168-9002. DOI: `https://doi.org/10.1016/j.nima.2007.07.115`. URL: `http://www.sciencedirect.com/science/article/pii/S0168900207015914`.

[39] HR Philipp and EA Taft. “Optical constants of silicon in the region 1 to 10 eV”. In: *Physical Review* 120.1 (1960), p. 37.

[40] Alexandre Refregier. “Weak Gravitational Lensing by Large-Scale Structure”. In: *Annual Review of Astronomy and Astrophysics* 41.1 (2003), pp. 645–668. DOI: `10.1146/annurev.astro.41.111302.102207`. URL: `https://doi.org/10.1146%2Fannurev.astro.41.111302.102207`.

[41] S. Schenk. “"A Vertex Fit for Low Momentum Particles in a Solenoidal Magnetic Field with Multiple Scattering"”. In: *BSc Thesis. Heidelberg University* (2013).

[42] Helmuth Spieler. *Semiconductor detector systems*. Vol. 12. Oxford university press, 2005.

[43] A. Signer et al. “Matrix Element of the Rare Muon Decay”. In: *Private Communication.* 76.3-4 (2015), pp. 279–293.

[44] A. Hillairet et al. “Precision muon decay measurements and improved constraints on the weak interaction”. In: *Phys. Rev. D* 85 (9 2012), p. 092013. DOI: `10.1103/PhysRevD.85.092013`. URL: `https://link.aps.org/doi/10.1103/PhysRevD.85.092013`.

[45] G. Aad et al. “Observation of a new particle in the search for the Standard Model Higgs boson with the ATLAS detector at the LHC”. In: *Physics Letters B* 716.1 (2012), pp. 1 –29. ISSN: 0370-2693. DOI: `https://doi.org/10.1016/j.physletb.2012.08.020`. URL: `http://www.sciencedirect.com/science/article/pii/S037026931200857X`.

[46] K. Eguchi et al. “First Results from KamLAND: Evidence for Reactor Antineutrino Disappearance”. In: *Phys. Rev. Lett.* 90 (2 2003), p. 021802. DOI: `10.1103/PhysRevLett.90.021802`. URL: `https://link.aps.org/doi/10.1103/PhysRevLett.90.021802`.

[47] P. Adamson et al. “Measurement of the Neutrino Mass Splitting and Flavor Mixing by MINOS”. In: *Phys. Rev. Lett.* 106 (18 2011), p. 181801. DOI: `10.1103/PhysRevLett.106.181801`. URL: `https://link.aps.org/doi/10.1103/PhysRevLett.106.181801`.

[48] Q. R. Ahmad et al. “Measurement of the Rate of $\nu_e + d \to p + p + e^-$ Interactions Produced by ^8B Solar Neutrinos at the Sudbury Neutrino Observatory”. In: *Phys. Rev. Lett.* 87 (7 2001), p. 071301. DOI: `10.1103/PhysRevLett.87.071301`. URL: `https://link.aps.org/doi/10.1103/PhysRevLett.87.071301`.

[49] S Abe et al. “Precision Measurement of Neutrino Oscillation Parameters with KamLAND”. In: *Phys. Rev. Lett.* 100 (22 2008), p. 221803. DOI: `10.1103/PhysRevLett.`

100.221803. URL: https://link.aps.org/doi/10.1103/PhysRevLett.100.221803.

[50] U. Bellgardt et al. "Search for the decay $\mu \to e^+e^-e^+$". In: *Nuclear Physics B* 299.1 (1988), pp. 1 –6. ISSN: 0550-3213. DOI: https://doi.org/10.1016/0550-3213(88)90462-2. URL: http://www.sciencedirect.com/science/article/pii/0550321388904622.

[51] Y. Fukuda et al. "Evidence for Oscillation of Atmospheric Neutrinos". In: *Phys. Rev. Lett.* 81 (8 1998), pp. 1562–1567. DOI: 10.1103/PhysRevLett.81.1562. URL: https://link.aps.org/doi/10.1103/PhysRevLett.81.1562.

[52] B Abelev et al and. "Technical Design Report for the Upgrade of the ALICE Inner Tracking System". In: *Journal of Physics G: Nuclear and Particle Physics* 41.8 (2014), p. 087002. DOI: 10.1088/0954-3899/41/8/087002. URL: https://doi.org/10.1088/0954-3899/41/8/087002.

Acknowledgements

At the end of this work, I would like to express my gratitude towards everyone who supported me to carry out this thesis: First of all, Helen Hayward for her commitment on long-term planning and her advice on software and for critically questioned my methods and strategies. I would like to thank Joost Vossebled for giving me the opportunity to work in the Mu3e group.

My particular appreciation goes to Nikolaos Rompotis, who was a great person and supported me during my whole time in the fist year of my PH.D in the Mu3e group, his valuable support on software and coding. Moreover, I would like to express my appreciation towards the following people in no specific order: Eva Vilella for sharing a lot of time in the clean room and help me to test HV-MAPS and Alexandr Kozlinskiy to help me on some software problems. I would like to thank the rest of the Mu3e group in Liverpool; Andrew, Sean and Carlos for all the assistance.

Finally, I would like to express my deepest gratitude towards my family, especially my husband Ali for always having my back and my son Qusi who allowed me to finish this work on the same time to see him again after a while. Before my viva 11/1/2022, my little girl was born, thanks a lot for you Qamar to remove all my depression and concern on passing my viva. I would like to give my thanks for Gizan University for the financial support during my PH.D years.

Publications

1. Technical design of the phase I Mu3e experiment: https://arxiv.org/abs/2009.11690/
2. The Mu3e Experiment Searching for the Lepton Flavour Violating Decay of a Muon to three Electrons: https://pos.sissa.it/390/898/